LONG-TERM TIMING OF PULSARS IN GLOBULAR CLUSTERS

Dissertation

zur

Erlangung des Doktorgrades (*Dr. rer. nat.*)

der

Rheinischen Friedrich–Wilhelms–Universität, Bonn

vorgelegt von

Alessandro Ridolfi

aus

Rome, Italy

Bonn 2017

Angefertigt mit Genehmigung der Mathematisch-Naturwissenschaftlichen Fakultät der Rheinischen Friedrich–Wilhelms–Universität Bonn

1. Referent: Prof. Dr. Michael Kramer
2. Referent: Prof. Dr. Norbert Langer

Tag der Promotion: 26.07.2017
Erscheinungsjahr: 2017

Diese Dissertation ist auf dem Hochschulschriftenserver der ULB Bonn unter
http://hss.ulb.uni-bonn.de/diss_online elektronisch publiziert

RHEINISCHE FRIEDRICH–WILHELMS–UNIVERSITÄT BONN

Abstract

by Alessandro Ridolfi

for the degree of

Doctor rerum naturalium

Pulsars are fast rotating, magnetized neutron stars that result from the supernova explosion of massive stars. Thanks to their coherent radiation, emitted in the form of collimated beams from the two magnetic poles, pulsars can be exploited as outstanding natural laboratories for fundamental physics. Pulsars can also be part of binary systems where, in most cases, the neutron star is spun-up (or *recycled*) up to rotation periods as low as a few milliseconds, by accreting matter and angular momentum from the companion star. Such *millisecond* pulsars are characterized by an extraordinary rotational stability.

Globular clusters (GCs), spherical groups of stars that are gravitationally bound, are very efficient "factories" of recycled pulsars, thanks to their very high stellar densities, which favour two- or three-body gravitational interactions and the formation of exotic binary systems. This thesis is about the study of the pulsars in 47 Tuc and M15, which are two among the richest GCs for the number of pulsars hosted, having 25 and 8 known such objects, respectively.

After providing an overview of the pulsar phenomenon (Chapter 1), I review in detail the main methods that are used in this thesis to search for and further study radio pulsars (Chapter 2). Particular focus is given to *pulsar timing*, a technique through which it is possible to build a precise model (called *timing solution*) that describes the rotational, astrometric and orbital characteristics of the neutron star and the possible binary system in which it is found. Being pulsars among the most polarized sources in the Universe, *polarimetry* is another major technique, complementary to timing, to investigate some properties of pulsars that would otherwise be inaccessible.

In Chapter 3, I review the main characteristics of globular clusters. The physical conditions found in the latter sharply differ from those found in the Galactic plane. In particular, the extremely crammed cores of GCs are capable of greatly altering the standard evolutionary paths of single stars and binary systems. As a result, the population of pulsars in GCs is very peculiar and very often composed by non-standard end products of binary evolution.

In Chapter 4, I present the results of the analysis of about two decades of data of 47 Tuc, taken with the Parkes radio telescope. All the previously known timing solutions are extended with the inclusion of additional data. For several other pulsars, the timing solutions are instead presented for the very first time since their discovery. For a few particularly faint binary pulsars, I use specific time-domain techniques developed with the goal of maximizing the number of detections and allowing their detailed characterization.

The timing results of all the 25 pulsars of 47 Tuc are then used in Chapter 5 to study the dynamics and other important properties of the cluster. The much more precise

measurements of the pulsar proper motions are used to infer the proper motion of the cluster as a whole. The measured higher-order spin frequency derivatives, instead, are used to derive the cluster distance, which results to be no smaller than 4.69 kpc. All the observed properties of the pulsars can be accounted for without invoking the presence of an intermediate-mass black hole at the core of 47 Tuc, although this hypothesis cannot be ruled out yet. Since almost all the pulsars are located very close to the cluster core, the population of neutron stars in 47 Tuc is likely to have reached a dynamical equilibrium with the stellar population. The only exception is 47 Tuc X, a very peculiar binary system that is much farther away than any other known pulsar of the cluster. This system has probably formed in a three-body exchange encounter that has flung the resulting binary towards the outskirts of the cluster.

A sub-population of the pulsars in 47 Tuc is constituted by the so-called "black widows" and "redbacks". These are pulsars in extremely tight orbits with a very light companion star that is losing mass. Such a mass outflow often causes a change in the gravitational field of the binary, which results in an orbital variability detectable through the timing. In Chapter 6 I present a detailed study of the seven black widows/redbacks of 47 Tuc. I find that, while some of these pulsars show a strong orbital variability, a few others appear remarkably stable.

The pulsars in the other globular cluster, M15, are studied in Chapter 7, primarily through polarimetry. I use recent data taken with the 305-m Arecibo radio telescope to derive the polarimetric properties of five pulsars of the cluster for the first time. One of the pulsars, called M15C, is a binary millisecond pulsar in a double neutron star system and its peculiarity is that it is showing evidence of relativistic spin precession (RSP) occurring, an effect predicted by Einstein's General Relativity. Because of RSP the pulsar spin axis is precessing about the total angular momentum of the binary system, with a full cycle every 275 years. This in turn causes the pulsar radiation beam to change orientation with respect to the distance observer. The variations of the polarimetric properties over time are thus used to model RSP in M15C, and derive constraints on the geometry of the system. I find a large misalignment angle between the pulsar spin axis and the orbital angular momentum, which is not surprising given that the binary has probably formed in a chaotic three-body exchange interaction. The pulsar's visible beam is slowly moving away from our line of sight and it might become undetectable by as early as 2018. On the other hand, the secondary beam (from the other magnetic pole) is approaching our line of sight and could become detectable from around 2041.

Finally, in Chapter 8, I summarize the results and discuss the possible future developments, in the light of the upcoming new generation of radio telescopes.

Acknowledgements

These four years as a PhD student have been an amazing experience and here I would like to thank many people who greatly contributed to make it as such.

My first and biggest thanks is owed to my family, and in particular to my parents, Fabio and Myriam. Ever since I was a kid, they have always encouraged and strongly supported me to follow my passions and dreams. This thesis is a very important achievement for me and it is dedicated to them!

Another very special thanks is for Wonju Kim. In these last two years, she has always stood by me, even in the most stressful moments and has given me invaluable support and motivation in all my pursuits.

I am profoundly grateful to my advisor, Paulo Freire. These few words cannot do justice to how much he contributed to both my scientific and personal growth. I thank him for always being a source of inspiration and a role model, for having taught me the "hidden secrets" of pulsar astronomy and for sharing many enjoyable moments outside of work.

A very special thanks also goes to my supervisor, Michael Kramer. I greatly thank him for his insightful scientific advice, for his constant support and for his dedication. I also thank him for making the MPIfR group such a pleasant and friendly working environment, which I truly enjoyed throughout these years.

Great thanks to our secretary, Kira Kühn, for always promptly helping in many situations and with all the bureaucratic and administrative issues.

Many thanks to Jan Behrend, Markus Krohs, Yusuf Özdilmac and all the MPIfR Rechenzentrum people, for their helpfulness and promptness in solving software and hardware related issues.

During these years, I had the chance to visit (thanks, Paulo!) and observe with the Arecibo radio telescope, until a few months ago the largest radio telescope on Earth! I would like to wholeheartedly thank all the Arecibo staff for the excellent work and support that they have always provided and without which a large part of this thesis could have not been possible. I would like to particularly thank Arun Venkataraman, Chris Salter, Hector Hernandez, Robert Minchin, Angel Vazquez, Andrew Seymour and Giacomo Comes.

Thanks to my fellow PhD and Master's students! In particular I would like to mention Cherry Ng, Pablo Torne, Nicolas Caballero, Jason Wu, Patrick Lazarus, John Antoniadis, Marina Berezina, Joey Martinez, Golam Shaifullah, Eleni Graikou, Nataliya Porayko and Andrew Cameron.

Thanks to all the post-docs and staff members of the Fundamental Physics group for sharing nice scientific discussions as well as very nice and joyful times together. A special mention is owed to Gregory Desvignes, who not only greatly helped me with a large part of my work, he also organized great FIFA tournaments! ;-)

Big thanks to the MPIfR *OpenArena* community of players, for sharing very amusing and nerdy moments between hard work sessions. :-)

I would also like to thank again all my colleagues and friends from the Astronomical Observatory of Cagliari. In particular, I would like to thank my former Master's thesis supervisor Andrea Possenti, as well as Alessandro Corongiu, Noemi Iacolina and Marta Burgay, with whom I had the chance, during my PhD, to continue to collaborate on other exciting scientific projects. I would like to remark how important my Master's thesis experience in Sardinia was and how

the passion, enthusiasm and strong friendships that resulted from it have been great motivations for me to continue in this field. A special mention is for Caterina Tiburzi, who I really thank for her care and strong friendship that has accompanied me throughout these years.

Big thanks to my friend and colleague Vittorio De Falco. Starting our doctoral studies at a very similar times (although in different cities) we shared our experiences and supported each other over the course of our PhD. I also thank his supervisor, Maurizio Falanga, very much for inviting me at ISSI Bern, where I had a great work and leisure time with him, Vittorio and the other nice people of the institute.

Many other people from outside of work have also contributed to make my stay in Bonn so great. Among these, I would like to mention Giulia Mariani, Mariangela Vitale, Marcus Bremer, Moritz Böck and Pietro Pilo Boyl.

Finally, I would very much like to thank Paulo Freire, Michael Kramer, Nicolas Caballero, Ralph Eatough, Gregory Desvignes and Caterina Tiburzi for reading all or part of this thesis, and contributing to significantly improve it.

Contents

Acronyms used in this thesis

ACS	Advanced Camera for Surveys
ADC	Analogue-to-Digital Converter
AFB	Analogue Filterbank
AU	Astronomical Unit
BAT	Barycentric Arrival Time
BB	Binary Barycentre
BH	Black Hole
BIPM	Bureau International des Poids e Mesures
BS	Blue Straggler
BT	Blandford & Teukolsky binary model
BTX	Extended Blandford & Teukolsky binary model
BWP	Black Widow Pulsar
CBR	Caltech Baseband Recorder
CMD	Colour-Magnitude Diagram
CO WD	Carbon-Oxygen White Dwarf
CPU	Central Processing Unit
DADA	Distributed Acquisition and Data Analysis format
DFT	Discrete Fourier Transform
DM	Dispersion Measure
DNS	Double Neutron Star
EoS	Equation of State
EPTA	European Pulsar Timing Array
FAST	Five-hundred-meter Aperture Spherical Telescope
FFT	Fast Fourier Transform
FPGA	Field-Programmable Gate Array
FT	Fourier Transform
FWHM	Full Width at Half Maximum
GC	Globular Cluster
GPS	Global Positioning System
GPU	Graphics Processing Unit
GR	General Relativity
GW	Gravitational Wave
HA	Hour Angle
He WD	Helium White Dwarf
HMXB	High-Mass X-ray Binary
HPC	High-Performance Computer
HST	Hubble Space Telescope
IAU	International Astronomical Union
ICRS	International Celestial Reference System
IEEE	Institute of Electrical and Electronics Engineers
IGM	Intergalactic Medium
IMBH	Intermediate-Mass Black Hole
IMXB	Intermediate-Mass X-ray Binary
IPTA	International Pulsar Timing Array
ISM	Interstellar Medium
JPL	Jet Propulsion Laboratory
LCP	Left-handed Circular Polarization
LIGO	Laser Interferometer Gravitational-wave Observatory
LMXB	Low-Mass X-ray Binary
LNA	Low-Noise Amplifier
LO	Local-Oscillator
MEM	Measurement Equation Modeling
METM	Measurement Equation Template Matching
MJD	Modified Julian Date
MRP	Mildly Recycled Pulsar
MS	Main Sequence
MSP	Millisecond Pulsar
NANOgrav	North American Nanohertz Observatory for Gravitational Waves
NDO	Noise-Diode-Only calibration method
NIST	National Institute of Standards and Technology
NS	Neutron Star
OPM	Orthogonal Polarized Mode
ONeMg WD	Oxygen-Neon-Magnesium White Dwarf
PA	Linear Polarization Position Angle
PFB	Polyphase Filterbank
PK	Post-Keplerian
PMB	Parkes Multi-Beam Receiver
PPTA	Parkes Pulsar Timing Array
PTA	Pulsar Timing Array
PUPPI	Puertorican Ultimate Pulsar Processing Instrument
RBP	Redback Pulsar
RCP	Right-handed Circular Polarization
RFI	Radio Frequency Interference
RG	Red Giant
RM	Rotation Measure
RSP	Relativistic Spin Precession
RV	Radial Velocity
RVM	Rotating Vector Model
S/N	Signal-to-Noise ratio
SAT	Site Arrival Time
SI	International System of Units
SKA	Square Kilometre Array
SMBH	Stellar-Mass Black Hole
SN	Supernova
SNR	Supernova Remnant
SSB	Solar System Barycentre
TAI	International Atomic Time
TCB	Barycentric Coordinate Time
TCG	Geocentric Coordinate Time
TDB	Barycentric Dynamic Time
tMSP	Transitional Millisecond Pulsar
ToA	Time of Arrival
TT	Terrestrial Time
UTC	Universal Coordinated Time
VLBI	Very-Long-Baseline interferometry
WAPP	Wideband Arecibo Pulsar Processors
WD	White Dwarf
WFC	Wide Field Channel
XCOR	Arecibo three-level Autocorrelation Spectrometer

Physical and Astronomical Constants

Speed of light	c	$299\,792\,458$ m s^{-1}
Newton constant of gravitation	G	$6.674\,08(31) \times 10^{-11}$ m^3 kg^{-1} s^{-2}
Planck constant	h	$6.626\,070\,040(81) \times 10^{-34}$ J s
Elementary charge	e	$1.602\,176\,6208(98) \times 10^{-19}$ C
Electron mass	m_e	$9.109\,383\,56(11) \times 10^{-31}$ kg
Proton mass	m_p	$1.672\,621\,898(21) \times 10^{-27}$ kg
Boltzmann's constant	k_B	$1.380\,648\,52(79) \times 10^{-23}$ J K^{-1}
Astronomical unit	AU	$149\,597\,870\,700$ m
Parsec	pc	$3.085\,675\,581\,491\,367\,3 \times 10^{16}$ m
Julian year	yr	$31\,557\,600$ s
Solar mass	$\mathrm{M}_\odot$	$1.988\,55(25) \times 10^{30}$ kg
Solar mass in units of time	$\mathrm{T}_\odot = G\,\mathrm{M}_\odot/c^3$	$4.925\,490\,947 \times 10^{-6}$ s
Nominal Solar radius	$\mathrm{R}_\odot$	$695\,700$ m

Main pulsar data analysis software used in this thesis

Package	Used for	References	Website
`PRESTO`	Pulsar searching	Ransom (2001)	`http://www.cv.nrao.edu/~sransom/presto`
`PSRCHIVE`	Pulsar data reduction	Hotan et al. (2004) van Straten et al. (2012)	`http://psrchive.sourceforge.net`
`DSPSR`	Folding	van Straten & Bailes (2011)	`http://dspsr.sourceforge.net`
`TEMPO`	Timing	–	`http://tempo.sourceforge.net`
`PSRALEX`	T_0-search, orbital variability studies	This thesis	`http://github.com/alex88ridolfi/PSRALEX`
MODELRVM	Modelling of relativistic spin precession	Desvignes et al. (in prep.)	`http://github.com/gdesvignes/modelRVM`

Chapter 1

Introduction

Contents

1.1 The discovery of radio pulsars

The possibility of the existence of extremely dense objects, even denser than white dwarfs (WDs), had already been put forward by many theoreticians in the first half of the XX century. Shortly after the neutron was discovered by James Chadwick in 1932, Baade & Zwicky (1934) proposed that a supernova explosion could result in the formation of a cold and very compact neutron star (NS), whose density could exceed that of nuclear matter (Oppenheimer & Volkoff, 1939). Later, Colgate & White (1966) predicted that, in the explosion, the conservation of magnetic flux and angular momentum would allow the star to retain a strong magnetic field and to reach spin frequencies of tens or hundreds of Hz. This would result in the emission of electromagnetic

waves, as suggested by Hoyle et al. (1964) and Pacini (1967), who proposed this mechanism as the source of energy of the observed X-ray emission in the Crab Nebula.

The confirmation of this picture arrived in the year 1967. At the Mullard Radio Astronomy Observatory in Cambridge (UK), Anthony Hewish and his student Jocelyn Bell were carrying out a survey to study the scintillation in the interplanetary medium, at a frequency of 81.5 MHz. During their analyses, they detected an extremely regular pulsed signal, repeating with a period of $\sim$1.337 s. The signal appeared every day at the same sidereal time, thus suggesting a non-terrestrial origin. Other hints, such as the inability to measure the parallax, pointed towards a position of the source well outside the Solar System. The measurability of some frequency dispersion within the 1-MHz wide band of the receiver further corroborated the hypothesis that the object (named CP 1919) was located at Galactic distance scales. Shortly later, the term "pulsar" (standing for PULSating stAR) was coined by the journalist A. R. Michaelis to refer to the newly discovered class of objects.

CP 1919, presented in the paper by Hewish et al. (1968) and nowadays known as PSR B1919+21, was shortly followed by the discovery of another three pulsating sources with similar properties (Pilkington et al., 1968). This fostered the development of a wealth of different theories to explain the observed properties of these objects. Hewish et al. (1968) already suggested that a pulsed radiation with the periodicity of CP 1919 and with its remarkable stability could have been produced by the radial oscillations of either a WD or a NS. Burbidge & Strittmatter (1968) and Saslaw et al. (1968) proposed that the periodic emission could have derived from an orbital motion, whereas Ostriker (1968) hypothesized hot spots on the surface of a rotating WD as the source of emission. On the contrary, Gold (1968) suggested that the pulsations were originated by a rotating NS.

Over time, the latter model was the only one that survived the new observational evidence that came along with the new discoveries. For instance, the observation of a slow-down in the pulsation rate in several sources was incompatible with the orbital motion scenario, since the latter would rather imply an increase in the rate, as a consequence of the orbital energy loss via emission of gravitational waves. The discoveries of the Vela pulsar (Large et al., 1968) and the Crab pulsar (Staelin & Reifenstein, 1968; Comella et al., 1969), which showed pulse frequencies of $\simeq$ 11 Hz and $\simeq$ 30 Hz, respectively, ruled out all the WD-based models. Indeed, such short periodicities could not be explained by any oscillation modes of a WD. On the other hand, if those frequencies were interpreted as rotational rates, WDs would have to be excluded since they cannot spin that fast without disrupting their outer layers.

In the end, the model of a rotating NS, proposed by Gold (1968), was the only one able to account for all the observed features, including, among other things, the association with supernova remnants (Gold, 1969).

As of today, there is no doubt that pulsars are indeed NSs, although, after exactly fifty years from their discovery, we are still uncertain about the precise mechanism that generates their radio emission.

1.2 The birth of a pulsar

As is now well-known in stellar astrophysics, a NS can be considered as the endpoint of the evolution of a massive ($\gtrsim$ 8 $M_\odot$) main-sequence (MS) star. During its MS phase a star can sustain itself against its own gravity thanks to the radiative pressure generated by nuclear fusion (Vogt, 1926; Russell, 1931). This is achieved by converting hydrogen into helium through

the proton-proton chain reaction, an exothermic process that releases the energy necessary to keep the star structure in a stable equilibrium. When the hydrogen reservoir is depleted, the star first shrinks, causing an increase in the core temperature, until the latter is high enough to ignite the fusion of helium. The larger energy released by this process makes the star expand and enter the so-called giant phase. When helium is also depleted, a new contraction followed by a heating and the burning of heavier elements occurs. For sufficiently heavy stars ($\gtrsim 8$ $M_\odot$) the cycle continues until iron (^{56}Fe) is burned. Contrary to the previous reactions, the fusion of ^{56}Fe is an endothermic process, meaning that there is no associated release of energy. Rather, energy has to be provided to make the process happen. As a result, the star is no longer able to counteract its self-gravity and, therefore, the collapse is unavoidable. In this event, called *core-collapsed supernova*, about 10^{10} times the luminosity of the Sun is released in a tremendous explosion (Arnett, 1996). While the outer layers are violently ejected to form a *supernova remnant* (SNR), the core implodes. If the latter has a mass larger than the Chandrasekhar mass ($\simeq 1.44$ $M_\odot$; Chandrasekhar, 1931, 1935) the collapse will continue until the matter is confined to a radius of ~ 10 km (Lattimer & Prakash, 2001). In such a small volume, the densities reached are of the order of the atomic nuclei, $\sim 10^{14}$ g cm^{-3}. In such conditions, neutrinos, being extremely weakly interacting particles, can still leave the star undisturbed. For protons and electrons, on the other hand, these densities are so high that they fuse together to form neutrons (a process referred to as *neutronization* of matter, or *inverse-β decay*). A new force, quantum in nature because due to the pressure of a degenerate gas of fermions (the neutrons), soon builds up to counteract gravity. A neutron star is born.

1.2.1 The structure of a neutron star

The first attempts to build a consistent model of the interior of a NS were made by Oppenheimer & Volkoff (1939) and Tolman (1939), who first devised the basic equation for building neutron star models, nowadays called the *Tolman-Oppenheimer-Volkoff equation*. Since then, many models have been proposed. Despite that, the exact composition of a NS is still an open astrophysical issue.

Although differing from one another on the details, most models agree on the fact that a NS must be constituted by a number of layers, where matter has different densities and states. Also, by using the inferred NS radius (~ 10 km) and mass (~ 1.4 $M_\odot$) mentioned above and the typical physical properties of the progenitor stars, it is possible to estimate the order of magnitude of some basic characteristics of NSs (and, thus, of pulsars), on which all models agree. In particular, by using the conservation of angular momentum during the supernova explosion, it is easy to show that the resulting NS must rotate much faster than the progenitor star, reaching rotational periods of the order of tens of milliseconds. Similarly, from the conservation of magnetic flux, it is possible to derive a typical NS surface magnetic flux density of the order of 10^{10-12} G. These estimates are in excellent agreement with the observational evidence.

1.3 The pulsar "Standard Model"

Although we are still far from having a deep understanding of all the physical processes underlying the radio pulsar phenomenon, many observed characteristics are excellently explained by a simplified model that is now widely accepted among pulsar astronomers, and that was first developed by Goldreich & Julian (1969) under specific assumptions. Over the years, it has been

further improved, by relaxing some of these assumptions, and today's version of it could be referred to as the current "Standard Model" for pulsars.

In this model, the NS, placed initially in a vacuum, is endowed with a perfectly dipolar magnetic field **B** whose magnetic moment, **m**, is misaligned by an angle $\alpha_{\rm m}$ (called *magnetic inclination*) with respect to the pulsar spin axis, **S** (Fig. 1.1). The fast rotation of the magnetic field induces an electric field that, in turn, exerts a strong force that rips off the charged particles from the NS surface, then forming a dense plasma that surrounds the star. On the other hand, the plasma particles, bound to the magnetic field lines, can co-rotate with the star only up to a distance, called *light cylinder radius* ($R_{\rm LC}$), at which its tangential speed is equal to the speed of light, c, namely:

$$R_{\rm LC} = \frac{cP}{2\pi} \simeq 4.77 \times 10^4 \text{ km} \cdot \left(\frac{P}{\text{s}}\right), \tag{1.1}$$

where P is the pulsar spin period. This radius represents the outer limit of the pulsar magnetosphere, which is the region where the magnetic field lines close within $R_{\rm LC}$, and thus where the charged particles can actually be confined. The coherent radiation that we observe in pulsars, though, is generated in the region just above the two magnetic poles, called *polar gaps*. Here the charged particles are accelerated along the open field lines, producing highly collimated radio "beams" of radiation. If the observer is fortuitously placed in the right position, it will be swept by at least one of the two beams, once per rotation of the NS. Therefore, the pulsar appears to us as a "cosmic lighthouse", as we receive the pulsar radiation with a periodicity that matches the NS rotation period.

1.3.1 Dipole radiation, spin-down and braking index

The ultimate source of energy of a pulsar spinning with angular frequency $\Omega = 2\pi/P$, is its rotational kinetic energy:

$$E_{\rm rot} = \frac{1}{2} I \Omega^2 , \tag{1.2}$$

where I is the NS moment of inertia, typically assumed to be 10^{45} g cm^2. The rate of energy loss, also referred to as *spin-down luminosity*, $L_{\rm sd}$, can be obtained simply by taking the time derivative:

$$L_{\rm sd} = -\frac{\rm d}{{\rm d}t}\left(\frac{1}{2} I \Omega^2\right) = -I \Omega \dot{\Omega} = 4\pi^2 I \frac{\dot{P}}{P^3} . \tag{1.3}$$

This power is released in several ways, such as high-energy emission, a wind of particles and, for a very small fraction, through magnetic dipolar emission. Indeed, from classical electrodynamics (e.g. Jackson, 1962) it is known that a magnetic dipole with magnetic moment **m**, rotating with an angular frequency Ω, radiates power in the form of electromagnetic waves at a rate of:

$$\dot{E}_{\rm dipole} = \frac{2}{3} \frac{|\mathbf{m}|^2 \Omega^4 \sin^2 \alpha_{\rm m}}{c^3} , \tag{1.4}$$

where, again, $\alpha_{\rm m}$ is the angle between **m** and the rotation axis. Although not realistic, it is useful to make the approximation that all the pulsar rotational energy is lost only through the latter mechanism. Under this assumption, we can equate Eq. (1.3) to Eq. (1.4) to derive the pulsar spin-down, $\dot{\Omega}$:

$$\dot{\Omega} = -\left(\frac{2|\mathbf{m}|^2 \sin^2 \alpha_{\rm m}}{3 I c^3}\right) \Omega^3 . \tag{1.5}$$

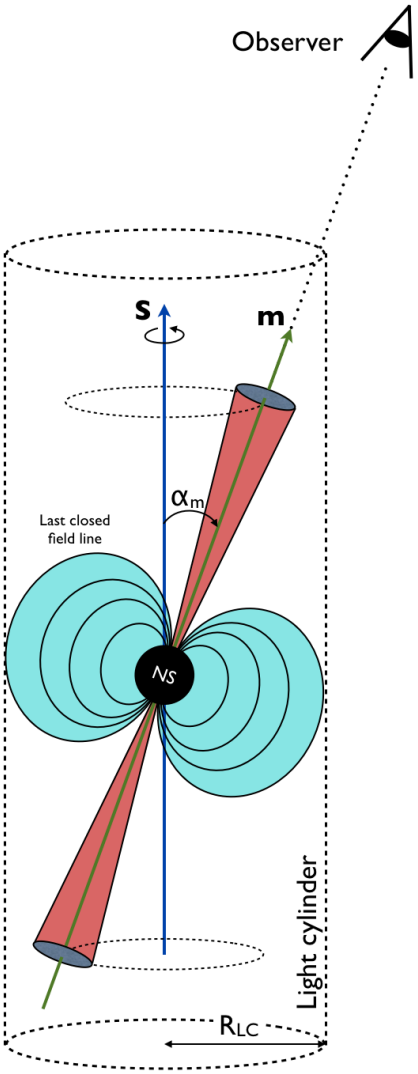

Figure 1.1: Schematic representation of the pulsar "Standard Model": the magnetosphere (light blue) is confined to the last closed line of the dipolar magnetic field. The latter is in turn determined by the light cylinder, an imaginary cylinder of radius $R_{\rm LC}$, namely the distance at which the corotation speed equals the speed of light. The pulsar radiation beam (red) is collimated along the magnetic moment, $\mathbf{m}$, and misaligned with respect to the spin axis, $\mathbf{S}$, by an angle $\alpha_{\rm m}$.

Hence, the spin-down rate is proportional to the third power of the spin frequency. However, this is the case only if the dipole radiation is the only process involved. Because, in reality, this is not true, Eq. (1.5) can be written in a more general form:

$$\dot{\Omega} = -K\Omega^n \quad \Leftrightarrow \quad \dot{f} = -Kf^n \quad \Leftrightarrow \quad \dot{P} = KP^{(2-n)}\,, \tag{1.6}$$

where K is a constant and we have also rewritten the same equation in terms of the spin period $P = \Omega/(2\pi)$ and spin frequency $f = 2\pi/\Omega$. In Eq. (1.6), n is referred to as the *braking index*. This quantity is important because its value depends on the physical processes involved in the emission, and thus is a potential probe for the pulsar energy loss mechanism. Indeed, by further differentiating Eq. (1.6) with respect to time and by using it again to eliminate the constant K, we have:

$$n = \frac{f\ddot{f}}{\dot{f}^2}\,, \tag{1.7}$$

that is, the braking index can be obtained by only measuring the spin frequency and its first two time derivatives. In practice, this is difficult, since $\ddot{f}$ is often dominated by timing noise or it is too small to be measured.

1.3.2 Characteristic age

Another important quantity that can be estimated by simply measuring P and $\dot{P}$ is the age of the pulsar.

Let us take Eq. (1.6) written in terms of P and $\dot{P}$ and let us separate the variables:

$$\frac{{\rm d}P}{{\rm d}t} = KP^{(2-n)} \quad \Rightarrow \; P^{(n-2)}{\rm d}P = K{\rm d}t\,. \tag{1.8}$$

We can now integrate both members, assuming $n \neq 1$, from the birth of the pulsar ($t = 0$) to the current time $\tau_{\rm p}$:

$$\int_{P_0}^{P} P^{(n-2)}{\rm d}P = K\int_0^{\tau_{\rm p}} {\rm d}t\,, \tag{1.9}$$

where $P_0 \equiv P(t = 0)$ is the pulsar spin period at birth.

Solving the integrals, we find:

$$\tau_{\rm p} = \frac{P}{(n-1)\dot{P}}\left[1 - \left(\frac{P_0}{P}\right)^{n-1}\right]. \tag{1.10}$$

If we make the further assumptions that the current pulsar spin period is much larger than its

value at birth ($P_0 \ll P$) and that the only source of energy loss is the magnetic dipole emission ($n = 3$), Eq. (1.10) reduces to:

$$\tau_{\rm p}(P_0 \ll P; n = 3) \equiv \tau_{\rm c} = \frac{P}{2\dot{P}} \quad . \tag{1.11}$$

This quantity is called *characteristic age* and should be considered as an order-of-magnitude estimate of the real age of the pulsar.

1.3.3 Characteristic magnetic field

The strength, B, of a dipolar magnetic field scales with the distance r from the magnetic moment as:

$$B(r) \propto \frac{|\mathbf{m}|}{r^3} \, . \tag{1.12}$$

Under the assumption of magnetic braking as the only spin-down mechanism ($n = 3$) we can solve Eq. (1.4) for $|\mathbf{m}|$ to derive an expression for the magnetic field strength, $B_{\rm s}$, at the surface of a NS of radius R (e.g. Lorimer & Kramer, 2004):

$$B_{\rm s} \equiv B(r = R) = \sqrt{\frac{3c^3}{8\pi^2} \frac{\mathcal{I}}{R^6 \sin^2 \alpha_{\rm m}} P\dot{P}} \simeq \left(\frac{\dot{P}}{10^{-15}}\right)^{1/2} \times \left(\frac{P}{\rm s}\right)^{1/2} \times 10^{12} \ {\rm G} \, , \tag{1.13}$$

where, typically, it is assumed $R \sim 10$ km, $\mathcal{I} \simeq 10^{45}$ g cm^2 and $\alpha_{\rm m} = 90$ deg.

1.4 The pulsar "fauna"

According to the ATNF pulsar catalogue[1] (version 1.55, Manchester et al. 2005a) and including two newly discovered pulsars discussed in this thesis, 2575 rotation-powered pulsars are currently known. Almost all (precisely 97%) are seen in the radio band, whereas the remainder are observed only at higher frequencies.

Many pulsars share some common features that are used to characterize the overall population. A convenient way to do so is to place the pulsars in a graph with P versus $\dot{P}$, which can be seen as the equivalent of the Hertzsprung-Russell diagram for normal stars. Indeed, as the latter, not only does the P-$\dot{P}$ diagram spotlight the different pulsar populations, it also allows us to better understand the evolution of the single objects, as we shall see. The P-$\dot{P}$ diagram for the currently known total pulsar population is shown in Fig. 1.2.

There exist a few main groups of pulsars that differentiate themselves for their values of P and $\dot{P}$, and for this reason they cluster together in different parts of the diagram, some of which are highlighted by ellipses in Fig. 1.2. The groups themselves have fairly fuzzy boundaries that can overlap, so they should not be regarded as definitive, rather just as a guidance. In the following of this section we discuss in more detail only those categories that are relevant for the work of this thesis.

1.4.1 Young pulsars

We regard as *young*, those pulsars that show very small characteristic ages ($\tau_{\rm c} \lesssim 100$ kyr) and that are very likely to have resulted from a recent supernova explosion. Many of these objects are

[1] http://www.atnf.csiro.au/research/pulsar/psrcat

Table 1.1. Main classes of pulsars with corresponding parameter ranges.

Group	P (s)	$\dot{P}$ (s s^{-1})	B_s (G)	τ_c (yr)
Young	$\sim 0.01 - 1$	$\gtrsim 10^{-15}$	$\sim 10^{12} - 10^{14}$	$\lesssim 10^5$
Ordinary	$\sim 0.1 - 5$	$\sim 10^{-17} - 10^{-12}$	$\sim 10^{10} - 10^{13}$	$\sim 10^5 - 10^9$
MRPs	$\sim 0.01 - 0.2$	$\lesssim 10^{-18}$	$\sim 10^9 - 10^{11}$	$\gtrsim 10^8$
MSPs	$\sim 0.001 - 0.1$	$\lesssim 10^{-18}$	$\sim 10^8 - 10^{10}$	$\gtrsim 10^8$
Magnetars	$\sim 2 - 12$	$\sim 10^{-15} - 10^{-9}$	$\sim 10^{13} - 10^{15}$	$\sim 10^4 - 10^7$

indeed located in the middle of a SNR which can be clearly associated with the birth of the pulsar (a striking example is the Crab pulsar, Staelin & Reifenstein 1968). Young pulsars typically have relatively slow spin periods ($P \sim 0.01 - 1$ s) and very large spin period derivatives ($\dot{P} \gtrsim 10^{-15}$), implying very high spin-down luminosities and strong magnetic fields ($B_s \sim 10^{12-14}$ G). Many of them exhibit red noise in their spin-down behaviour, with the occasional occurrence of glitches, i.e. sudden changes in the spin period and spin period derivatives. These pulsars are located around the top-centre region of the P-$\dot{P}$ diagram.

1.4.2 Ordinary pulsars

Because of the energy loss discussed above, a young pulsar will eventually move along a south-east track in the P-$\dot{P}$ diagram, reaching the big cluster of the so-called *ordinary* pulsars[2] in the centre-right region of the P-$\dot{P}$ diagram. As their position suggests, they are characterized by long periods ($P \sim 0.1 - 5$ s), high spin-down rates ($\dot{P} \sim 10^{-17} - 10^{-12}$) and strong magnetic fields ($B_s \sim 10^{10-13}$ G). The transition from a young to an ordinary pulsar can occur over time scales of $10^5 - 10^9$ yr, that are the typical values of the characteristic ages measured for this class of objects.

If not perturbed by other phenomena, an ordinary pulsar continues to spin down, until it crosses the so-called *death line* in the P-$\dot{P}$ diagram. At this point, the physical processes acting in the pulsar magnetosphere become too weak to keep the radio emission active (Chen & Ruderman, 1993). As a consequence, the pulsar becomes undetectable.

1.4.3 Recycled pulsars

Even though pulsars naturally spin down through the emission of electromagnetic radiation, they can also undergo an increase in their rotational speed. This is the case when a pulsar is part of a binary system with a MS companion star that eventually evolves into a giant or supergiant and fills its Roche lobe. When this happens, the pulsar's gravitational pull is predominant at the inner Lagrangian point (L1) of the system. Through this point, the companion starts losing mass from its outer layers. The matter is accreted by the pulsar, which not only gains mass, but also angular momentum, and thus spins faster and faster over time (e.g. Radhakrishnan & Srinivasan, 1982; Podsiadlowski et al., 2002). This process, called *recycling* (e.g. Bhattacharya & van den Heuvel, 1991; Tauris & van den Heuvel, 2006), can last from 10^7 to 10^9 yr and the result is a pulsar with a spin period in the range $\sim 1 - 100$ ms. Recycled pulsars also show a much smaller magnetic field strength, and a consequent spin-down rate of orders of magnitudes smaller than that of ordinary pulsars. Indeed, it is a common belief that the accretion of matter

[2] In the literature, it is also customary to refer to this class with other adjectives, such as "normal" or "canonical" with the same meaning as "ordinary", as used in this thesis.

provokes, among other things, a quenching of the pulsar magnetosphere, although the details of the process are still poorly understood.

Even though they all share the features described above, recycled pulsars can be divided into further sub-classes, of which the most relevant for this thesis are discussed in the following.

Millisecond pulsars

Millisecond pulsars (or MSPs, for short), in the standard formation scenario (e.g. Alpar et al., 1982), are the typical result of a recycling process occurred in a Low-Mass X-ray binary (LMXB), i.e. a binary system consisting of a pulsar and a MS star of mass smaller than ~ 1 $M_\odot$. The low mass implies that the lifetime of the companion star in its evolved giant phase, and thus the lifetime of the accretion process, is of the order of 10^9 yr. This is enough to bring the pulsar spin period down to $\lesssim 10$ ms and its magnetic field to $\sim 10^8$ G. Because of these characteristics, MSPs are located in the bottom-left corner of the P-$\dot{P}$ diagram. Having the smallest spin-down rates among the known pulsar population, and being glitches extremely rare events in this class of objects, MSPs represent the most stable and precise astrophysical clocks in the Universe.

It is also an observational fact that the majority of MSPs are found in binary systems, in most cases with a low-mass WD companion in a circular orbit (attained through tidal circularization processes) as we would naturally expect from the theory of their formation outlined above. Nevertheless, some 40% of them are isolated.

The existence of isolated MSPs is probably related to two other sub-classes of MSPs that have been gaining more and more importance over the last decade, for various reasons. These are the "black widow" pulsars (BWPs) and the "redback" pulsars (RBPs, see Freire 2005; Roberts 2013 for reviews). Both categories, together referred to as "spiders", are characterized by very short orbital periods of the order of a few hours, a very low-mass companion that is undergoing mass loss and the often presence of eclipses in the pulsar radio signal. The distribution of the companion mass in these systems shows a clear bimodality (see e.g. Fig. 1 in Roberts, 2013) that is commonly used as the criterion to distinguish between the two classes: in BWPs the companions have masses of $\lesssim 0.1$ $M_\odot$ and are typically being ablated by the strong wind of the pulsar, which can make them completely stripped stars; on the other hand, in RBPs the companions are heavier ($\sim 0.1 - 0.5$ $M_\odot$) non-degenerate stars and their mass loss occurs via Roche lobe overflow. Also, compared to BWPs, RBPs generally show longer eclipses (which can obscure the pulsar signal for up to 60% of the orbit) and a much stronger orbital variability, very likely due to the gravitational influence of the matter outflowing from the companion.

Since the discovery of PSR B1957+20, the first BWP found by Fruchter et al. (1988), the relevance of the "spiders" in pulsar astrophysics has been constantly increasing, and the reasons are manifold. Originally, it was believed that the strong ablation process seen in PSR B1957+20 and similar objects could eventually make the companion star completely evaporate, thus providing an explanation for the existence of isolated MSPs in the Galaxy. However, it was later realized that the typical timescale for such a process would be too long (more than a Hubble time) to complete and thus the idea was abandoned. A new burst of interest arose in the late 2000's as many new such systems were discovered with the γ-ray *Fermi* satellite (Ray et al., 2012), which more than doubled the total BWP/RBP population in a matter of a few years. In the same years, the redback pulsar PSR J1023+0038, formerly detected as a LMXB (Bond et al., 2002; Thorstensen & Armstrong, 2005; Homer et al., 2006), was seen switching to a radio-MSP state (Archibald et al., 2009), to then switch back to a LMXB state a few years later (Stappers et al., 2014; Deller et al., 2015; Campana et al., 2016). This represented the

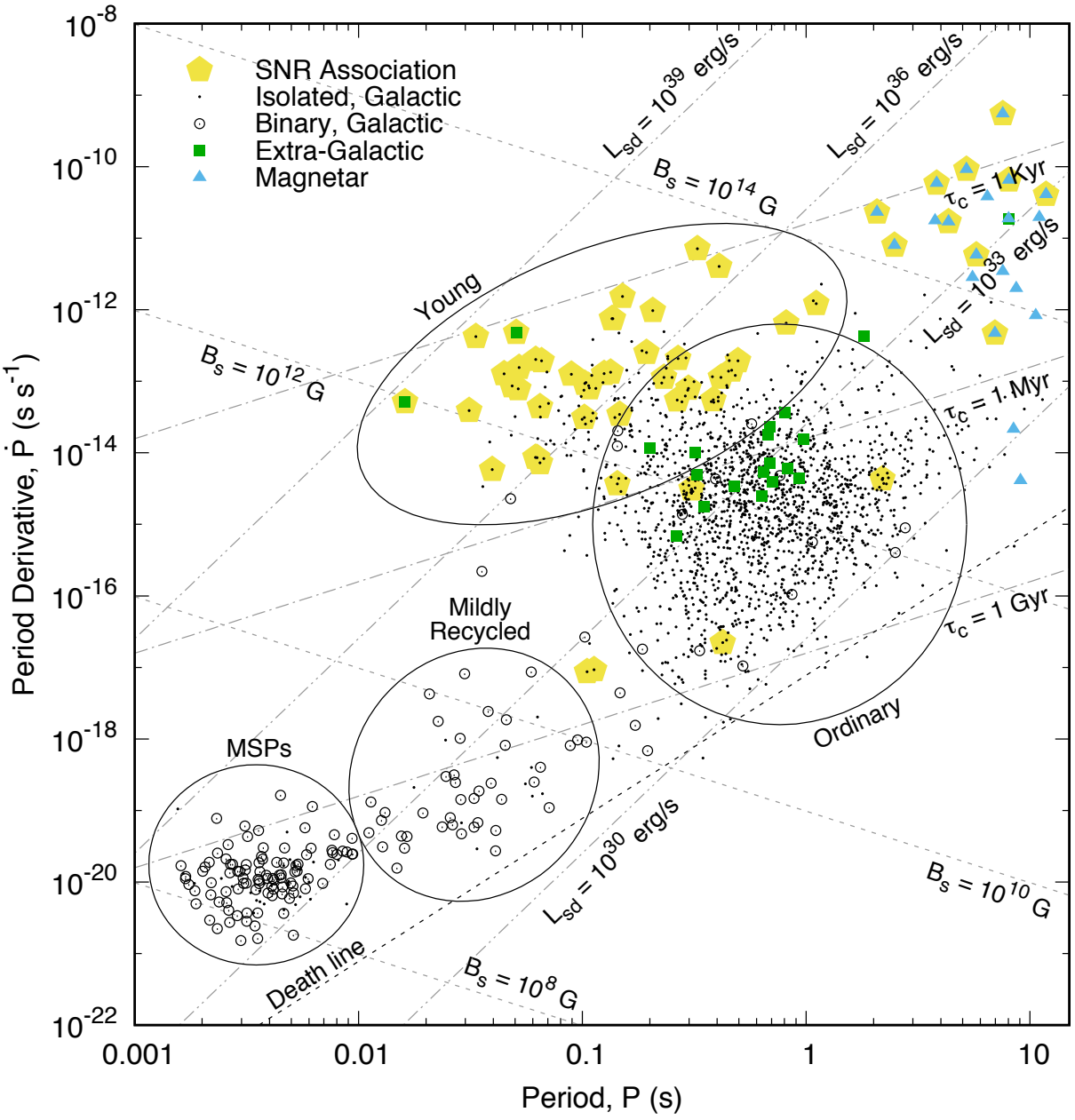

Figure 1.2. Period–Period-derivative (P-$\dot{P}$) diagram for the currently 2021 pulsars (of a total population of 2575) that are not associated with globular clusters and for which both the spin period and the spin period derivative have been measured. The ellipses highlight four among the main classes of pulsars.

first direct evidence of the validity of the recycling model. PSR J1023+0038 is now considered the archetype of a new class of "transitional MSPs" (tMSPs), namely RBPs that swing between LMXB and radio-MSP states. As of today, in addition to PSR J1023+0038, another two tMSPs are known: PSR J1824−2452I in the GC M28 (Papitto et al., 2013) and the newly discovered PSR J1227−4853 (XSS J12270−4859 in its LMXB state, Roy et al., 2014; Bassa et al., 2014; Bogdanov et al., 2014; de Martino et al., 2014; Roy et al., 2015).

In addition to the "spiders", there are also another two sub-groups of MSPs that deserve a particular mention. The first group is that of MSP-WD binaries in eccentric orbits (see Section 1.6.5), two representatives of which are PSR J2234+0511 (Antoniadis et al., 2016) and PSR J1946+3417 (Barr et al., 2017). Even more interesting are the triple systems, i.e. MSPs with two companion stars. To date, two such objects are known, namely PSR B1620−26 (Sigurdsson et al., 2003) and PSR J0337+1715 (Ransom et al., 2014). In both cases the pulsar is part of a hierarchical configuration, that is, the third body revolves around the inner binary system along an orbit that is much wider than those of the other two stars. This is indeed one of the few stable configurations in a three-body problem. For the sake of simplicity, the two triple systems have been plotted as binaries in Fig. 1.2.

Mildly recycled pulsars

When a pulsar forms within either an Intermediate-Mass X-ray Binary (IMXB) or a High-Mass X-ray Binary (HMXB), i.e. systems where the companion star has a mass in the range $\sim 0.1 - 10$ $M_\odot$ and $\gtrsim 10$ $M_\odot$, respectively (Tauris & van den Heuvel, 2006), the fast evolution of the MS star implies a short-lasting accretion phase. As a consequence, the pulsar is only partially spun-up and thus becomes a *mildly recycled pulsar* (MRP), with a spin period in the range $\sim 10 - 200$ ms. In addition to the spin-up, also the magnetic field quenching is only partially fulfilled, as MRPs show surface field strengths between $\sim 10^9 - 10^{11}$ G. If the companion star eventually explodes in a supernova (SN) event, it will leave a second neutron star that will possibly remain bound to pulsar, thus forming a double neutron star system (DNS). These systems are characterized by a large eccentricity, induced by the supernova explosion. Examples of MRPs in a DNS are the Hulse-Taylor pulsar (PSR B1913+16, Hulse & Taylor, 1975) and PSR J0737−3039A/B (Burgay et al., 2003; Lyne et al., 2004). Alternatively, the companion can end its life by ejecting its outer layers in the form of a *planetary nebula* and leaving a massive carbon-oxygen WD (CO WD) or oxygen-neon-magnesium WD (ONeMg WD) companion (Tauris et al., 2000, 2011, 2012). Binary systems so formed are characterized by low orbital eccentricities, but generally not as low as the results of LMXB evolution (MSP-He WD systems).

1.5 Pulsar phenomenology

Radio pulsars are characterized by peculiar phenomenological features that make them very distinctive sources in the sky. Below we review the most important characteristics, easily recognizable in any pulsar observation. For a more complete discussion of the pulsar phenomenon, we refer to Chapter 1 of Lorimer & Kramer (2004).

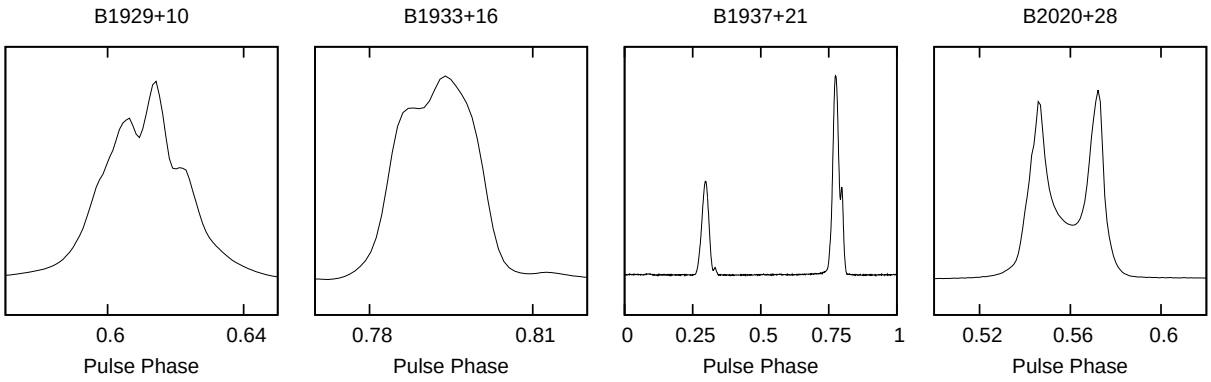

Figure 1.3. Integrated pulse profiles of four extremely bright pulsars as observed at 1.4 GHz with the Arecibo radio telescope. As can be seen, the profile morphology greatly varies from one pulsar to the other. For three pulsars, namely PSR B1929+10, B1933+16 and B2020+28, the profile has been zoomed in on the pulse region to better show the profile complexity. For PSR B1937+21, a full rotation is instead displayed to show the presence of an interpulse separated by about ~ 180 deg from the main pulse.

1.5.1 Single and integrated pulse profiles

The observed signal of a pulsar consists of a train of pulses emitted at intervals as long as the pulsar spin period. The shapes and intensities of the single pulses are generally extremely variable, even between two subsequent rotations of the NS. However, if one adds up a sufficiently high number (normally a few hundreds or thousands, Helfand et al. 1975) of single pulses coherently, the resulting summed (or *integrated*) profile shows a remarkable stability over time, in a given frequency band. The integrated profile can thus be considered as the "fingerprint" of a pulsar, thanks to which the latter is distinctively recognizable.

Fig. 1.3 shows the detail of the integrated profiles of four bright pulsars of the Northern Sky. As can be seen, the shape and the complexity can vary significantly from one pulsar to the other. In some cases, the profile can be the result of the blending of two (as for PSR B2020+28) or more (as for PSR B1929+10) components.

The profile shape and its duty cycle (i.e. the fraction of the pulsar period that shows emission) also depends on the magnetic inclination angle, $\alpha_{\rm m}$. If $\alpha_{\rm m} \simeq 90$ deg, it is very likely for the observer to see the emission coming from both magnetic poles. In this case the profile shows a so-called *interpulse*, that is, a second pulse which is separated by about 180 deg (i.e. half a rotation of the NS) from the main pulse. A clear such example is visible in the integrated pulse profile of PSR B1937+21 (Fig. 1.3), the first MSP ever discovered (Backer et al., 1982). On the other hand, if $\alpha_{\rm m}$ is very small, it is possible that our line of sight will fall within the beam of emission for most of the time, resulting in a profile that occupies most of the pulsar rotation cycle (see e.g. the profile of PSR B0826−34, Fig. 1.2 of Lorimer & Kramer 2004). Observationally, MSPs tend to have pulse profiles with larger duty cycles compared to ordinary pulsars. This suggests that the emission beam in the former is generally wider than in the latter.

Another important characteristic, which is more prominent in young pulsars, is the dependence of the integrated pulse profile on the observing frequency. This phenomenon has been mainly justified by arguing that the emission at different frequencies occurs in the magnetosphere at different heights from the surface, resulting in different profile shapes (Komesaroff, 1970; Cordes, 1978).

1.5.2 Emission spectra

Another quantity that is strongly dependent on the observing frequency, $\nu_{\rm obs}$, is the pulsar mean flux density, $S_{\rm mean}$, that is the integrated intensity of the pulse profile, averaged over one rotation period. For most of the known pulsars, this dependence comes in the form of an inverse power-law relation:

$$S_{\rm mean}(\nu_{\rm obs}) \propto (\nu_{\rm obs})^{\varrho}\,, \tag{1.14}$$

where ϱ is the spectral index. The average measured value for the latter is $\varrho \simeq -1.8 \pm 0.2$ (Maron et al., 2000) with no substantial difference between ordinary pulsars and MSPs (Kramer et al., 1998; Toscano et al., 1998). A small fraction of pulsars show more complex behaviours: for some of them the observed spectrum cannot be fitted by Eq. (1.14) and instead requires a two-component power-law; in some other a spectral turnover is observed, with the emission peaking somewhere between 100 MHz (Sieber, 1973; Kuniyoshi et al., 2015) and about 1 GHz (Kijak et al., 2011; Rajwade et al., 2016), and then decreasing again at lower frequencies.

Excluding magnetars (young pulsars which have very peculiar emission spectra), the current record for the highest-frequency detection of a radio pulsar is the case of pulsar PSR B0355+54, which has recently been detected up to 138 GHz (Torne et al., in prep.).

1.5.3 Polarization

Having a fraction of linear polarization of up to 100% and an average circular polarization of about 10%, pulsars are among the most polarized sources known in the Universe. By using the two orthogonal receptors that virtually all modern radio telescope receivers have, it is also possible to measure the linear polarization position angle (PA), which is of particular interest if used in combination with the *Rotating Vector Model* (RVM, Radhakrishnan & Cooke, 1969; Komesaroff, 1970). Polarization will be thoroughly discussed in Section 2.6.2.

1.6 Scientific applications of pulsars

The ever-increasing interest that pulsar astronomy has generated over the decades is not only due to the fascination that these exotic objects have *per se*, but also because pulsars have proved to be incredibly versatile tools to study a number of astrophysical phenomena. Thanks to their extreme rotational stability, pulsars can literally be used as super-precise clocks in different astrophysical environments. Furthermore, as highlighted in Section 1.5.3, pulsars are highly polarized sources. Polarization is another way of exploiting pulsars in other fields of physics and astrophysics. Here follows a selection of the most relevant scientific applications of pulsars.

1.6.1 Interstellar medium and plasma physics

The pulsar low-frequency radio emission, as well as its large fraction of linear polarization, are ideal tools to probe the ionized component of the Galactic interstellar medium (ISM). The different propagation speed of the pulsar signal, from the source to the Earth, as a function of the observing frequency (a phenomenon called *dispersion*, see Section 2.2.1) allows us to measure the free electron content along the line of sight. Thanks to their large number, people were able to use pulsars to build detailed maps of the electron density distribution in our Galaxy (Cordes et al., 1991; Cordes & Lazio, 2002, 2003; Schnitzeler, 2012; Yao et al., 2016). Similarly, combining such maps with polarimetric measurements of a large set of pulsars, the large-scale

structure of the Galactic magnetic field has been inferred (Noutsos et al., 2008). Very recently, the discovery of *Fast Radio Bursts* and the flourishing of the related research (e.g. Lorimer et al., 2007; Thornton et al., 2013), is making the possibility of applying similar techniques to even the intergalactic medium (IGM) a more concrete prospect for the near future.

Apart from ISM/IGM studies, pulsars are important tools for the study of plasma physics under extreme conditions, as their emission originates near the NS surface, where the gravitational and magnetic field strengths reach exceptional values, unattainable in any laboratory on the Earth. Pioneering studies on the pulsar emission properties were conducted, e.g., by Rankin (1983a,b, 1986, 1990) and Kramer et al. (1997).

1.6.2 Ultra-dense matter and NS equations of state

Even though the exact composition and state of the matter in a NS is still unknown, it is believed that the density at the NS core is higher than that of an atomic nucleus (Lattimer & Prakash, 2004). There exist a number of models that can be indirectly tested through observations of pulsars. This gives us a unique chance to study the physics of matter at supra-nuclear density. By observing pulsar binary systems, sometimes combining radio observations of the pulsar with optical data for the companion, it is possible to measure the mass of the NS. Because the proposed equations of state (EoS) make predictions on what would be the maximum allowed mass for a stable NS, more and more measurements of the masses of new pulsars have constantly raised the value of the maximum observed mass for a NS. This way, a number of models can be ruled out for their inability to account for such large masses. Currently, the most stringent limits are set by the measured mass of $\simeq 2$ $M_\odot$ in the pulsars PSR J1614−2230 (Demorest et al., 2010) and PSR J0348+0432 (Antoniadis et al., 2013).

Recently, however, the discovery of a 2-$M_\odot$ pulsar by Antoniadis et al. (2013) has significantly restricted the number of possibly correct models, ruling out all of those that predict a maximum stable NS mass below that value.

1.6.3 General Relativity and alternative theories of gravity

Pulsars in binary systems, especially those with tight orbits, represent outstanding testbeds for General Relativity (GR). Devised by Albert Einstein around 1915 (e.g. Einstein, 1915), GR is still, one hundred years later, the most successfull theory of gravitation. After successfully passing various tests in the weak-field regime with Solar System experiments in the first half of the XX century (e.g. Eddington 1919; for a comprehensive review see Will 2001), it was not until the discovery of binary pulsars that the same tests, in the strong-field regime, were possible. Fortuitously, the first binary pulsar discovered (i.e. PSR B1913+16; Hulse & Taylor 1975) was a DNS in a very compact orbit with an orbital period of 7.75 h, which implies that relativistic effects are measurable. In this binary, the two NSs can be effectively treated as two point masses, thus making the system an excellent laboratory for GR. The pioneering work done on this system by Barker & O'Connell (1975) and Taylor & Weisberg (1982, 1989) paved the way to a series of analogous tests applied to other binary pulsars in the successive years. The current state of the art is PSR J0737−3039, the only DNS known where both NSs are detected as pulsars (Burgay et al., 2003; Lyne et al., 2004). This binary, with an extremely tight orbit of only 2.4 h, has allowed the most precise test of GR to date, which showed that Einstein's theory is correctly describing gravity up to a precision of at least 0.05% (Kramer et al., 2006).

As has happened for Newtonian gravitation, scientists have good reasons to believe that even GR cannot be the ultimate theory in describing this fundamental force. For this reason,

several alternative theories of gravity have been proposed over the decades (e.g. Brans & Dicke, 1961; Damour & Esposito-Farese, 1992; Hořava, 2009). Some of these theories, such as those that introduce an additional scalar field, have also been tested through the study of a few tight MSP-WD binary systems and very stringent constraints on them have recently been derived (Freire et al., 2012).

Even though binary systems are typically the main tools used to test alternative theories of gravity, it has been shown that even isolated pulsars can provide important insights. As a recent example, Shao et al. (2013) derived the best limits on the isotropic violation of local Lorentz invariance by studying the possible pulse profile variations of two isolated MSPs.

1.6.4 Pulsar Timing Arrays and detection of nHz gravitational waves

Another remarkable application of pulsar astronomy is the detection of Gravitational Waves (GWs), tiny ripples in space-time that propagate at the speed of light, predicted by GR. The first evidence of their existence was indeed obtained by measuring the orbital decay in PSR B1913+16 over a few years (Taylor & Weisberg, 1982). Thirty-four years later, in February 2016, the Laser Interferometer Gravitational-Wave Observatory (LIGO) collaboration announced the first direct detection, through their two ground-based laser interferometers, of a GW coming from a black hole (BH) merger.

Sazhin (1978) was the first to realize that the passage of a GW would also have an effect on the propagation time of the signal of a pulsar. A few years later, Hellings & Downs (1983) pointed out the possibility of detecting very low-frequency (nHz) GWs by studying the cross-correlation in the signals of an array of MSPs located at different sky positions. Such calculations were then further developed by e.g. Jenet et al. (2004, 2005) and Sanidas et al. (2012).

At present, the detection of nHz GWs with pulsars is pursued by three large collaborations: the European Pulsar Timing Array (EPTA, Kramer & Champion, 2013), the Australian Parkes Timing Array (PPTA, Hobbs, 2013) and the North-American Observatory for Gravitational Waves (NANOgrav, McLaughlin, 2013). The data collected are also shared by the three groups in the framework of a worldwide collaboration (the International Pulsar Timing Array, or IPTA, Manchester 2013) with the aim of building the most sensitive GW detector in the nHz regime.

1.6.5 Stellar and binary evolution

Because pulsars are the result of the death of the progenitor star, their study can provide insights into the physics of supernovae. For instance, the space velocity as well as the polarimetry (e.g. Noutsos et al., 2012) of a pulsar can be related to possible asymmetries in the supernova explosion, which give the NS a "kick" (e.g. Spruit & Phinney, 1998; Janka, 2007).

Also, pulsars in binary systems are key tools to understand stellar evolution. The ever-increasing variety of system types, with different companion stars and orbital characteristics, poses a continuous challenge in our attempt to justify their existence within a coherent picture. While the evolutionary paths of the most common types of binary pulsars have mostly been successfully modelled (such as circular pulsar-He WD and pulsar-CO WD binary systems, Tauris & Savonije 1999; Tauris et al. 2000, 2011, 2012) and the recycling model has been confirmed by the discovery of tMSPs (e.g. Papitto et al., 2013), other more exotic, recently found binaries require more complicated explanations. Notable examples are the highly eccentric binary PSR J1903+0327, composed by a MSP and a MS star, whose probable origin from a hierarchical triple system has been discussed by several authors (e.g. Freire et al., 2011; Portegies Zwart

et al., 2011). Similarly, a few newly discovered eccentric pulsar-WD systems have fostered a series of non-standard evolutionary paths that invoke a rotationally-delayed accretion-induced collapse of a spinning WD (Freire & Tauris, 2014), or even the interaction of the binary with a circumbinary disk (Antoniadis, 2014).

1.6.6 Globular cluster studies

The subset of pulsars residing in globular clusters, besides being exploitable individually as any other pulsar, can be used together to provide unique insights into the many characteristics of these groups of stars that are still not fully understood (e.g. Hessels et al., 2015). Being the "protagonists" of this thesis, we refer to Chapter 3 for a detailed discussion of the many peculiar applications of pulsars in GCs.

1.7 Thesis outline

This thesis deals with the study of pulsars in globular clusters, through the application of a wide range of analysis techniques that are also used in other fields of pulsar astronomy. In particular, this work focuses on the pulsars of two well-known GCs, namely 47 Tucanae and M15. Here follows a brief outline of the thesis.

- In **Chapter 2** we give the reader a general overview of the main issues related to the observation of a pulsar. We first discuss the relevant astrophysical phenomena caused by the presence of the interstellar medium that astronomers need to take into account when dealing with pulsar data. With these in mind, we describe the typical instrumentation used to carry out pulsar observations, from the telescope to the data-recording machines. Then, the three main data analysis techniques used in this thesis are discussed in detail. These are: (a) *pulsar searching*, needed to discover new pulsars and/or re-detect the known ones; (b) *pulsar timing*, which is the main tool used to extract information from pulsars and which has been extensively utilized throughout this thesis; (c) *polarimetry*, an indispensable tool to access some specific properties of pulsars and very often complementary to pulsar timing.

- In **Chapter 3** we discuss about pulsars in globular clusters. The currently known GC pulsar population is presented, with a focus on the differences among the different clusters. Then, we examine the many possible scientific applications of GC pulsars, with a particular regard to how their collective properties can tell us a great deal about the GC physics.

- In **Chapter 4** we present the analysis of about two decades of data of the globular cluster 47 Tucanae, taken with the Parkes radio telescope. After a general introduction of the cluster, we present up-to-date timing solutions for all the 25 pulsars. Of these, 23 are phase-connected and several of them are completely new.

- In **Chapter 5** we utilize the derived timing solutions to derive some important physical properties of 47 Tucanae, such as the distance and the proper motion. Among other things, we also confront our results with the hypothesis of having an intermediate-mass black hole at the centre of the cluster.

- In **Chapter 6** we focus on a subpopulation of the pulsars in 47 Tucanae, namely that of the black widows/redbacks. We present a detailed characterization of several of these pulsars and discuss about their strong orbital variability.
- In **Chapter 7** we revisit five of the eigth known pulsars in the globular cluster M15. Thanks to data acquired in full-polarimetry mode from the year 2014, we present, for all the five pulsars, accurately calibrated polarimetric profiles. The same polarization data are used to study the relativistic spin precession effect in the pulsar M15C, a double neutron star system in a very eccentric orbit.
- In **Chapter 8** we summarize our results and discuss possible future prospects, especially in the context of the upcoming next generation of radio telescopes such as FAST, MeerKAT and the SKA.

Chapter 2

Observing a pulsar

Contents

2.1 Introduction

The exploitation of pulsars for scientific purposes requires the utilization of advanced technology, both in hardware and software. In this thesis, a broad range of instrumentation set-ups and analysis techniques have been extensively used. In this chapter, we review in detail the fundamental steps that are needed to do science with pulsars.

In Section 2.2 we discuss the possible impact that the interstellar medium can have on the pulsar signal during its long journey from the neutron star to the Earth. This is of extreme relevance when designing both a telescope data acquisition system and data analysis software.

In Section 2.3 we present the typical instrumentation set-up used for pulsar observations. We describe how the pulsar radiation is collected and then pre-processed in hardware and/or software, before being stored for successive analysis.

In Section 2.4 we show the way new pulsars are typically searched for, which we refer to as *pulsar searching*. This requires the implementation of advanced time- and/or frequency-domain algorithms, of which we describe the most important examples.

In Section 2.5 we thoroughly discuss *pulsar timing*, the most important and most widely used tool to derive the physical parameters of interest of pulsars and their environments.

In Section 2.6 we deal with *pulsar polarimetry*. Since pulsars are typically highly polarized sources, polarimetry provides additional insights into the physics of pulsars and of their surrounding environments.

2.2 Effects of the interstellar medium

Before reaching the observer on the Earth, the electromagnetic waves produced by a pulsar must travel a long distance, very often of the order of a few kpc, within our Galaxy. The latter is permeated with the *interstellar medium* (ISM), mostly ionized gas, which can very often be also inhomogeneous and turbulent. The interaction of the broad-band pulsar radiation with the ISM results in a number of physical effects that cause significant changes in the former. These effects must be taken into consideration and corrected if one wants to recover the original signal.

Dispersion is an effect that always occurs in the presence of a homogeneous plasma. *Faraday rotation*, instead, also requires the plasma to be magnetized. Another two effects, namely *scattering* and *scintillation*, are effective only if the plasma is also inhomogeneous and/or turbulent.

2.2.1 Dispersion

In a vacuum, an electromagnetic wave of any frequency ν propagates at the speed of light, c. On the other hand, it can be shown from Maxwell's equations that, if the radiation travels in a medium, its speed (more precisely, its group velocity, $v_{\rm g}$) will be reduced by a frequency-dependent factor, called *refractive index*, $n(\nu)$, as:

$$v_{\rm g}(\nu) = n(\nu) \cdot c\,. \tag{2.1}$$

The refractive index is always < 1 and its exact value also depends on the physical properties of the medium. Neglecting higher order terms and corrections due to the presence of a magnetic

field, the refractive index of the ionized ISM is (e.g. Lorimer & Kramer, 2004):

$$n(\nu) = \sqrt{1 - \left(\frac{\nu_\mathrm{p}}{\nu}\right)^2} \quad . \tag{2.2}$$

Here ν_p is the so-called *plasma frequency*, defined as:

$$\nu_\mathrm{p} = \sqrt{\frac{e^2 n_\mathrm{e}}{\pi m_\mathrm{e}}} \simeq 8.5 \text{ kHz} \left(\frac{n_\mathrm{e}}{\mathrm{cm}^{-3}}\right)^{1/2}, \tag{2.3}$$

where e is the charge of the electron, m_e its mass, and n_e is the electron number density of the plasma.

Eq. (2.2) tells us that, in a medium, electromagnetic waves propagate faster at higher frequencies. In the limit $\nu \to \infty$, the refractive index $n(\nu) \to 1$ and the propagation speed is the same as in a vacuum ($v_\mathrm{g} = c$). On the other hand, electromagnetic waves with a frequency $\nu < \nu_\mathrm{p}$ do not propagate at all.

From Eq. (2.1) it is possible to calculate the delay $\Delta t_{(\nu,\infty)}$ with which an electromagnetic wave of frequency ν would reach the Earth, compared to another one of infinite frequency:

$$\Delta t_{(\nu,\infty)} = \left[\int_0^d \frac{\mathrm{d}l}{v_\mathrm{g}(\nu)}\right] - \frac{d}{c}, \tag{2.4}$$

where the integral is calculated along the optical path from the radiation source to the Earth and d is the distance between the two. Because for typical pulsar observations $\nu \gg \nu_\mathrm{p}$, it is possible to expand the dispersion relation (Eq. 2.2) as a Taylor series up to the first order and substitute it into Eq. (2.4), thus obtaining:

$$\Delta t_{(\nu,\infty)} \simeq \frac{1}{c}\int_0^d \left[1 + \frac{1}{2}\frac{\nu_\mathrm{p}^2}{\nu^2}\right]\mathrm{d}l - \frac{d}{c} = \frac{e^2}{2\pi m_\mathrm{e} c}\frac{1}{\nu^2}\int_0^d n_\mathrm{e}\,\mathrm{d}l \equiv \mathcal{D}\cdot\frac{\mathrm{DM}}{\nu^2} \quad . \tag{2.5}$$

Here we have defined the quantity $\mathcal{D} \doteq e^2/(2\pi m_\mathrm{e} c)$, called *dispersion constant*, and most importantly the quantity:

$$\mathrm{DM} \doteq \int_0^d n_\mathrm{e}\,\mathrm{d}l\,. \tag{2.6}$$

The latter integral is called *dispersion measure* and represents a measurement of the free electron content along the line of sight between the pulsar and the observer. As we shall see, the knowledge of the DM is of fundamental importance in all pulsar observations and data analyses.

A straightforward way to measure the DM stems from Eq. (2.5) and consists in measuring the difference $\Delta t_{(\nu_1,\nu_2)}$ in the arrival time of the pulsar signal observed at two different frequencies, ν_1 and ν_2 (with $\nu_1 < \nu_2$):

$$\Delta t_{(\nu_1,\nu_2)} = \frac{e^2}{2\pi m_\mathrm{e} c}\cdot\left(\frac{1}{\nu_1^2} - \frac{1}{\nu_2^2}\right)\cdot\mathrm{DM}. \tag{2.7}$$

Once the DM is known, one can integrate Eq. (2.6) to derive the distance of the pulsar, provided that the electron number density distribution, $n_\mathrm{e}(l)$, is known. Although the latter is usually not accurately known, there exist a few models that give a reasonably good estimate of the Galactic electron content distribution. The most used example is the NE2001 model (Cordes &

Lazio, 2002, 2003), which, when used for this purpose, provides distances with a typical relative uncertainty of $\sim 30\%$. More recently, another model (YMW16) has been presented by Yao et al. (2016).

The opposite procedure is also possible: if we have a way to measure the distance of a pulsar (for instance, via the association with a globular cluster or by measuring its parallax), we can use the DM to estimate the electron content along the associated line of sight. This is indeed the method used to refine Galactic models (like the NE2001 and the YMW16), which can thus improve as more and more pulsars are discovered and their DMs and distances are measured.

2.2.2 Faraday Rotation

If the ionized ISM is permeated with a magnetic field with a non-zero component $B_{\parallel}$ along the direction of propagation of an electromagnetic wave travelling through it, the latter will undergo a change in the plane of its linear polarization (see also Section 2.6). This effect is called *Faraday rotation* and can be intuitively explained by the fact that the free electrons, oscillating inside the magnetic field, are subject to a Lorentz force that makes them move circularly in a preferential rotation direction. The circular motion, in turn, induces an additional local magnetic field that superimposes to the external field. This causes the two circular polarization states of light to "experience" a different refractive index and they thus have different propagation speeds. Because a linearly polarized wave can always be seen as the superposition of two circularly polarized waves, the different propagations speeds of the latter two will cause a change in the relative phase, which will translate into a change in the angle of the linear polarization, ψ.

In general, for an electromagnetic wave of frequency ν travelling a distance d in a magnetized and ionized ISM, the phase lag undergone with respect to an infinite-frequency wave, can be expressed as (Lorimer & Kramer, 2004):

$$\Delta\psi(\nu) = -k(\nu)\, d\,, \tag{2.8}$$

where $k(\nu) = 2\pi\nu n(\nu)/c$ is the wavenumber. The refraction index $n(\nu)$, in the presence of a magnetic field, contains an additional term that depends on the circular polarization state of the radiation, namely:

$$n(\nu) = \sqrt{1 - \frac{\nu_{\rm p}^2}{\nu^2} \mp \frac{\nu_{\rm p}^2\, \nu_{\rm B}}{\nu^3}}\,, \tag{2.9}$$

where the "$-$" sign is for a left-handed and the "$+$" sign for a right-handed circularly polarized wave. The quantity $\nu_{\rm B}$ is called *cyclotron* (or *Larmor*) *frequency* and contains the dependence on $B_{\parallel}$:

$$\nu_{\rm B} = \frac{e\, B_{\parallel}}{2\pi m_{\rm e} c}\,. \tag{2.10}$$

Making the reasonable assumptions that $\nu \gg \nu_{\rm p}$ and $\nu \gg \nu_{\rm B}$ (which are true in virtually all pulsar observations), we can use Eq. (2.8)-(2.9) to calculate the differential phase rotation between the two circular polarizations as:

$$\Delta\psi_{\rm F}(\nu) = \int_0^d \big[k_+(\nu) - k_-(\nu)\big]\, {\rm d}l \simeq \frac{e^3}{\pi m_{\rm e}^2 c^2 \nu^2} \cdot \int_0^d n_{\rm e} B_{\parallel}\, {\rm d}l\,, \tag{2.11}$$

where $k_+(\nu)$ and $k_-(\nu)$ is the wavenumber of the right and left circularly polarized wave, respectively.

Because the linear polarization position angle ψ is periodic on π and not 2π, the change in $\psi_{\rm F}$ corresponds to half of the change in ψ:

$$\Delta\psi = \frac{1}{2}\Delta\psi_{\rm F} = \frac{1}{2}\frac{e^3\,\lambda^2}{\pi m_{\rm e}^2 c^4}\cdot\int_0^d n_{\rm e}B_{\parallel}\,{\rm d}l \equiv \lambda^2 \times {\rm RM}\,, \tag{2.12}$$

where λ is the radiation wavelength and we have introduced the *rotation measure*:

$${\rm RM} = \frac{e^3}{2\pi m_{\rm e}^2 c^4}\cdot\int_0^d n_{\rm e}B_{\parallel}\,{\rm d}l\,. \tag{2.13}$$

An interesting application of the measurement of both the DM and the RM of a pulsar is the possibility of inferring the average magnetic field component along the line of sight, $\langle B_{\parallel}\rangle$, by combining Eq. (2.6) and (2.13):

$$\langle B_{\parallel}\rangle = \frac{\int_0^d n_{\rm e}B_{\parallel}\,{\rm d}l}{\int_0^d n_{\rm e}\,{\rm d}l} \equiv 1.23\ \mu{\rm G}\left(\frac{\rm RM}{\rm rad\ m^{-2}}\right)\left(\frac{\rm DM}{\rm pc\ cm^{-3}}\right)^{-1}. \tag{2.14}$$

2.2.3 Scattering

The actual Galactic ionized ISM is far from being a perfectly homogeneous gas. Rather, it very often shows irregularities and turbulence that have a significant impact on the pulsar signal passing through it.

The first relevant effect to be considered is *scattering*. The density irregularities of the local free electron content cause a continuous change in the local refractive index seen by the electromagnetic wave. This makes the different rays have different non-straight optical paths from the pulsar to the observer, translating into longer propagation times. As a result, for any given frequency, while most of the radiation will arrive at once, part of it will arrive at a later time, forming a "tail" in the observed pulse profile.

The simplest way to describe the scattering phenomenon was presented by Scheuer (1968), with the so-called *thin-screen* model. In this model the inhomogeneities are assumed to follow a Kolmogorov spectrum and to be confined within a thin layer located somewhere between the pulsar and the observer. With these simple assumptions, it can be shown (e.g. Lorimer & Kramer, 2004) that the observed intensity of a pulse as a function of time results:

$$I(t) \propto e^{-\Delta t/\tau_{\rm s}}\,, \tag{2.15}$$

where Δt is the time delay due to the longer optical path. Hence, the observed pulse profile emitted by the pulsar will be the intrinsic pulse shape convolved with a one-side exponential function, with a characteristic timescale $\tau_{\rm s}$, which in turn depends on the radiation frequency as:

$$\tau_{\rm s} \propto \nu^{-4}\,. \tag{2.16}$$

Therefore, when observing at low frequencies ($\nu \lesssim 1$ GHz) the scattering effect can be severe and, depending on the specific case, it can cause complete smearing of the pulsed signal.

2.2.4 Scintillation

Closely related to scattering is another phenomenon, called *scintillation*. The same inhomogeneities that are at the origin of the exponential scattering tails, are also responsible for in-

tensity fluctuations of the observed pulsar signal, as first noted by Lyne & Rickett (1968). The distorted wavefronts indeed produce constructive or destructive interference at the location of the observer, within a typical bandwidth (called *scintillation bandwidth*) of size $\Delta\nu$. A condition necessary for the interference to occur is that (Lorimer & Kramer, 2004):

$$2\pi\Delta\nu\tau_{\mathrm{s}} \sim 1. \tag{2.17}$$

Recalling Eq. (2.16), this implies that $\Delta\nu \propto 1/\tau_{\mathrm{s}} \propto \nu^4$. Similarly to scattering, scintillation acts over a timescale that depends on the physical properties of the scattering screen, as well as on the observing frequency.

2.3 Radio telescopes

Historically, the primary way by which astronomers study pulsars is by observing them with single-dish radio telescopes. Because of their characteristics, pulsars are technologically demanding, as they require:

- *large collecting areas*, to build up a signal of sufficient signal-to-noise ratio (S/N) within a reasonably short observing time, in spite of their intrinsic faintness;
- *high time resolution*, in order to resolve their short pulsations due their fast rotational regimes;
- *high frequency resolution*, to correct for the effect of dispersion.
- *large computing power* and *storage capacity*, to properly handle the large amount of data collected.

The functioning scheme of a modern radio telescope can be divided into three main parts, as illustrated in Fig. 2.1:

- The *front-end*, also called *receiver*, is the part of the telescope that collects the astrophysical radiation, amplifies it, and filters out unwanted spurious signals.
- The *down-conversion* consists of a series of devices that electronically manipulate the received signal to make it easier to be transmitted and further processed.
- The *back-end* is the piece of hardware and/or software responsible for the digitization, further processing and final storage of the data.

In the following subsections, these stages will be reviewed in more detail.

2.3.1 Front-end

Typical radio telescopes have reflectors (also dubbed as "dishes") with diameters from a few tens of metres (e.g. 64 m of the Parkes radio telescope) to a few hundred metres (e.g. 305 m for the Arecibo radio telescope). The dish is usually a paraboloid, since this shape has the property of focusing the plane wavefronts coming from infinity onto a single point, called the primary focus. The largest non-steerable telescopes, however, must use different designs, with reflectors that have, for instance, the shape of a spherical cap.

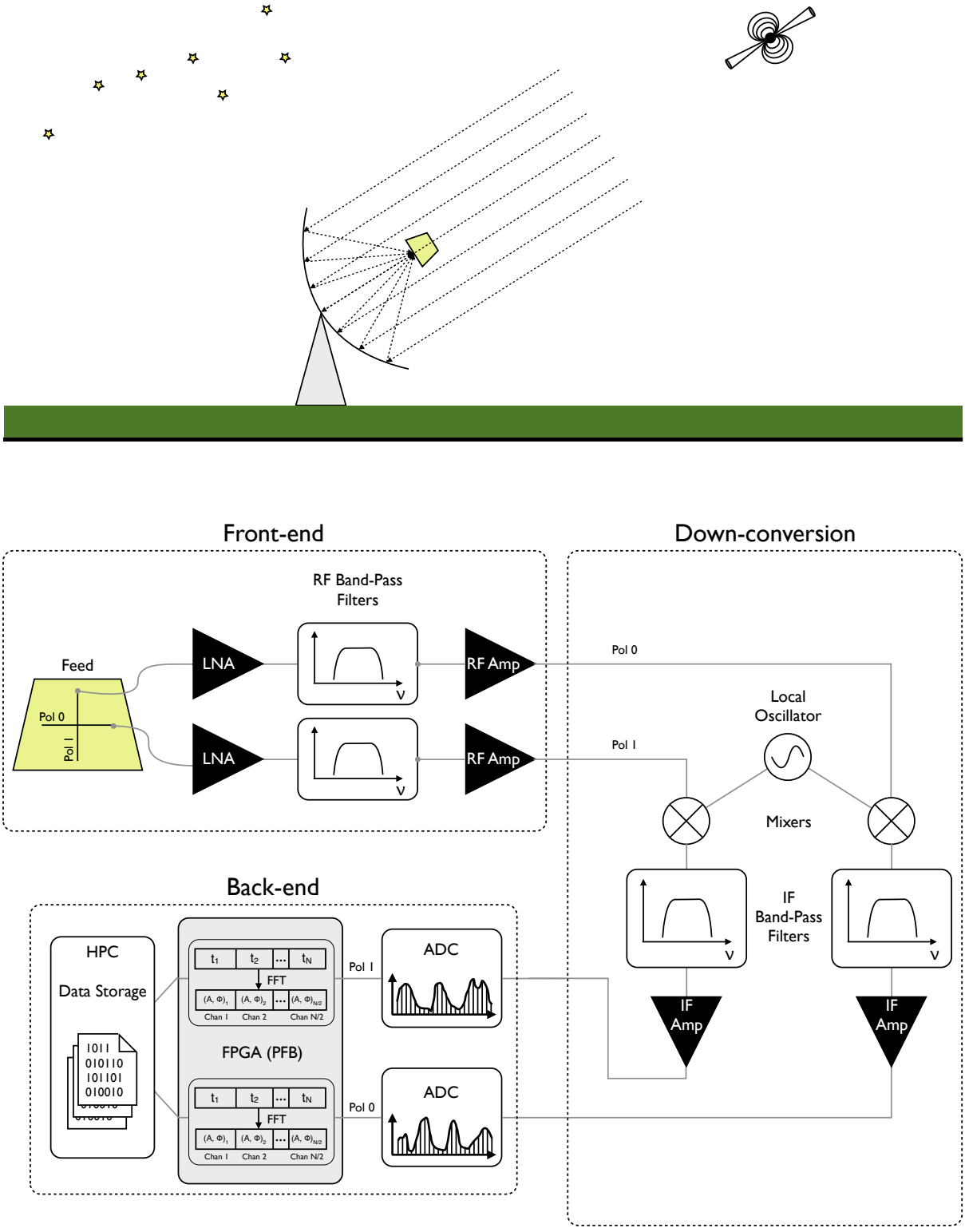

Figure 2.1. Schematic diagram of a modern radio telescope. See text for the detailed description.

At the focus is placed the front-end (or *receiver*), a device that, through a wave guide, collects the incoming radiation. The latter is then converted into electric voltages by means of two receptors that sample the two orthogonal (either linear or circular) polarization states of light (see Section 2.6). The signal of each polarization is then amplified by a Low-Noise Amplifier (LNA), which is cryogenically cooled to minimize the impact of thermal noise on the receiver sensitivity. Then, a band-pass filter removes all the unwanted frequencies outside the range of interest, which might accidentally have been added because of the presence of terrestrial radio frequency interference (RFI) produced by human activities. After this, a further amplification of the signal is usually performed.

2.3.2 Down-conversion

The central radio frequency, ν_{RF}, of the signal at this stage roughly corresponds to the central value of the frequency range to which the receiver is sensitive. However, dealing with a high-frequency electric signal has several downsides: for instance, its transmission is typically accompanied by high power losses; also, despite constantly improving, the hardware available nowadays may still not be fast enough to sample it without loss of information. For this reason, the original signal is converted into another one of lower frequency, but with the same information content. This is achieved by using a Local-Oscillator (LO), a device that produces a monochromatic sinusoidal wave of fixed frequency ν_{LO}. For each polarization, the signal is taken by a *mixer* and multiplied by the LO wave. The result of this operation is the production of two new signals with two new intermediate carrier frequencies $\nu_{\mathrm{IF}} = \nu_{\mathrm{RF}} \pm \nu_{\mathrm{LO}}$. By using another band-pass filter, only the signal at the lower frequency is retained. An additional amplifier may also be used to boost the latter before transmitting it to the back-end.

2.3.3 Back-end

The *back-end* can be regarded as the actual data acquisition system of the telescope. In the back-end, the down-converted analogue signals of the two polarizations are sampled and digitized by two Analogue-to-Digital Converters (ADCs), which, according to the Nyquist-Shannon theorem (Nyquist, 1928; Shannon, 1949), must have a sampling frequency at least two times higher than the signal bandwidth, to retain all the information. Later, the digitized signal is processed by a *polyphase filterbank* (PFB), a piece of hardware (typically a Field Programmable Gate Array, or FPGA) or software that, by performing a Fast Fourier Transform (FFT), takes N samples and translates them into $N/2$ frequency channels. The conversion of time information into frequency information is done with the purpose of later correcting for the dispersion effect, which would otherwise cause smearing of the pulsed signal across the whole band (Fig. 2.2). De-dispersion is generally carried out by a High-Performance Computer (HPC) and can be done with different methods (see Section 2.3.3.1). After de-dispersing, the HPC may further process the data, depending on the observing mode chosen. The final step consists in the storage of the data in a format suitable for successive analysis.

2.3.3.1 Incoherent and coherent de-dispersion

The main purpose of the data stream channelization performed by the polyphase filterbank is the correction of interstellar dispersion. Such correction, called *de-dispersion*, can be applied using two different approaches, one of which does not use the phase information of the Fourier-transformed signal, whereas the other does.

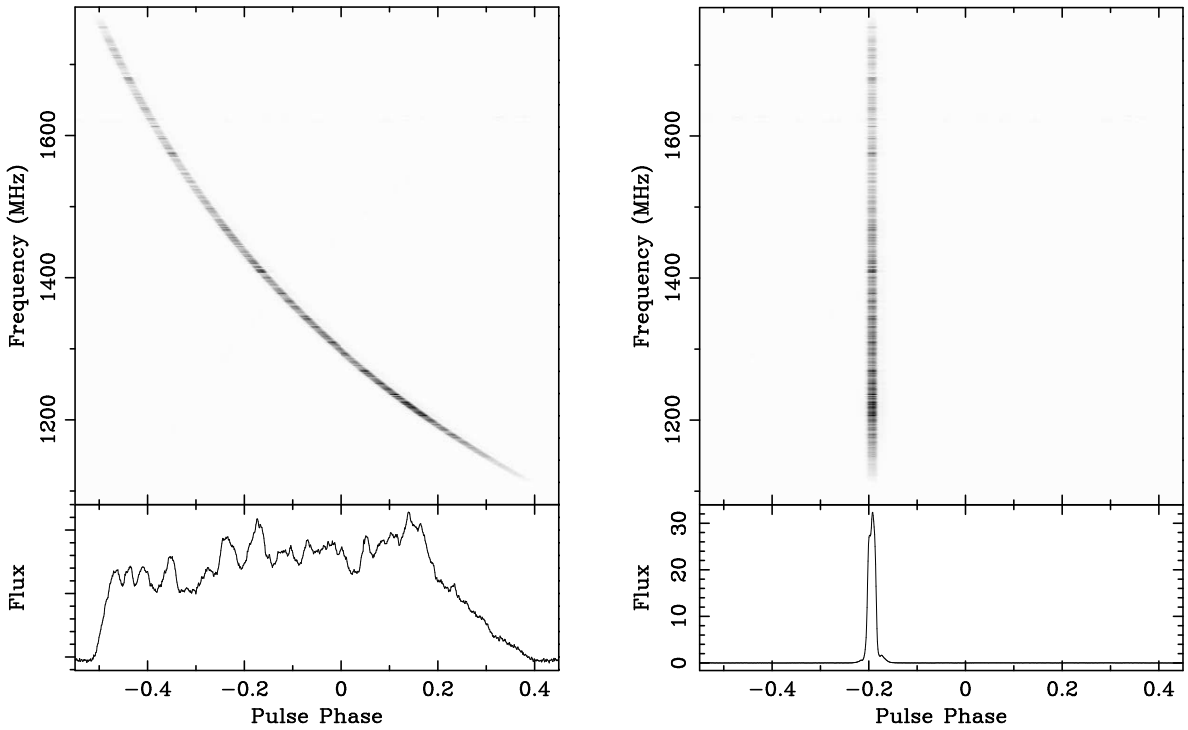

Figure 2.2. Dispersion effect in an example observation of pulsar PSR B1933+16 taken at 1.4 GHz with the Arecibo radio telescope. Left: the pulsed signal shows the characteristic quadratic delay due to the dispersion effect (with a DM of 158.52 pc cm^{-3}) across the observing band (top panel); as a result, the integrated profile is completely smeared out (bottom panel). Right: the same observation after de-dispersing the signal; the pulses in all frequency channels are now aligned (top panel) and the actual integrated pulse profile shape is correctly restored (bottom panel).

In the first approach, called *incoherent de-dispersion*, the total bandwidth is divided into several channels. A proper time shift, calculated from the best available estimate of the DM via Eq. (2.5), is then applied to each channel. This way, the pulsed signal in each channel is aligned across the whole band. This way of de-dispersing the pulsar signal, despite being easy to apply and computationally inexpensive, is limited by the fact that each channel will intrinsically retain some smearing that is proportional to its width.

The way to overcome this issue is by using another approach, called *coherent de-dispersion* (Hankins, 1971; Hankins & Rickett, 1975). In this method, the Nyquist-sampled signal is Fourier-transformed with an FFT and converted into a series of complex voltages (i.e. a sequence of amplitudes and phases) that represent the harmonic content of the electromagnetic wave. For each component of the Fourier spectrum, the relative phase is then rotated by an amount that is proportional to the DM of the pulsar. This is equivalent to applying a time shift equal to the dispersive delay relative to the particular frequency considered. In other words, we are actually doing the same thing as in the case of incoherent de-dispersion, except that this operation is now done in the Fourier domain and we are applying a different shift to every single Fourier components that make up the original signal, and not to a group of them altogether (i.e. a channel). Once the correction is applied, an inverse Fourier transform is performed to recover the real-valued, dispersion-free, original pulsar signal. Because this method involves several FFT operations, it is very costly in terms of computing power. Nowadays, modern back-ends are able

to perform real-time coherent de-dispersion, over a large bandwidth, by implementing it over multiple Graphics Processing Units (GPUs; e.g. De & Gupta, 2016).

2.3.3.2 Observing modes: timing, search and baseband

The format in which the signal is processed and then recorded depends on the chosen observing mode. Modern digital pulsar back-ends are usually capable of working in three different modes, each suitable for specific scientific applications, which we will now briefly review:

- *Timing/Folding mode*: it is used to observe pulsars whose basic characteristics are already known and the data are recorded in a format suitable for pulsar timing (see Section 2.5). The incoming signal is processed in real-time through a procedure called *folding*. When folding, the observing band is first divided into a number of channels and the dispersion effect is removed (coherently or incoherently) according to the value of the DM. After de-dispersing, the time series of each channel is divided into chunks of arbitrary length (from a few seconds to several minutes), called *sub-integrations*. Each sub-integration is further split into intervals of roughly the length of the pulsar spin period. These are then summed coherently in phase according to the pulsar *timing solution*, which is a model that fully describes the rotation of the NS. This way, hundreds or thousands of single pulses are added together to form an *integrated profile* (see Section 1.5.1), one for each sub-integration/frequency-channel pair. The resulting file is called *folded archive* and it is essentially a collection of integrated profiles (see Fig. 2.3), which can either retain or not the full polarimetric information. Further details about timing and folded archives can be found in Section 2.5.

- *Search mode*: it is used to record data in a format suitable for pulsar searching. As for the timing mode, the bandwidth is first divided into a few hundreds or thousands of channels. Usually, no de-dispersion is applied because, when searching for pulsars, the DM is not known a priori (different case is when observing a globular cluster, see below). In the time domain, groups of samples are added together to retain a time resolution of typically a few tens of μs, enough to be sensitive to the fastest MSPs. For search purposes, polarization information is generally not needed, hence the signals of the two polarizations are usually added together. However, as for timing mode, it is also possible to observe in full-Stokes mode, thus retaining the polarization information. The search-mode files so produced can later be folded to obtain folded archives, exactly as in timing mode. For this reason, as we shall see in the next chapters, search mode is also particularly suitable for observations of pulsars in globular clusters, where the same data contain the signals of several pulsars at once. In this case, it is also common to apply de-dispersion with the average DM of the cluster, to minimize the pulse broadening of all the pulsars that reside in it.

- *Base-band mode*: in this mode the signal is down-converted from the actual observing frequency range $[\nu_{\rm lo}, \nu_{\rm lo} + \Delta\nu]$, where $\nu_{\rm lo}$ is the frequency of the lower edge of the observing band and $\Delta\nu$ is the bandwidth, to the base-band, i.e. to the frequency range $[0, \Delta\nu]$. In this case, the recorded data are the actual raw voltages of the two orthogonal receptors, sampled at the Nyquist frequency ($2\Delta\nu$), thus retaining all the information of the signal. This guarantees the maximum flexibility and allows the astronomer to arbitrarily exchange time resolution for frequency resolution in the post-processing

phase. The data are usually stored in the standard DADA format[1]. Because there is no information loss, base-band data are extremely voluminous and hence this mode is used only for very specific scientific applications. For example, base-band data are particularly suitable for studies that require very high time resolution (such as studies of giant radio pulses, see e.g. Karuppusamy 2009) or when the data must be correlated with observations made with other telescopes (like in the *Large European Array for Pulsars* project, Bassa et al. 2016).

2.4 Searching

The search for and discovery of new pulsars clearly represents a fundamental element of pulsar astronomy that also drives the whole field. Since the discovery of the first pulsar, huge advances have been made in both observing systems and analysis software. Nowadays, the two software packages that are most widely used for this purpose are `PRESTO`[2] (Ransom, 2001) and `SIGPROC`[3] (Lorimer, 2011). Both packages allow astronomers to find the periodic signals coming from pulsars with no prior knowledge of their characteristics.

In this section we will review the basic steps that are part of a search pipeline, like the one used for this thesis (see Chapter 4). These are:

- Observations and data acquisition
- RFI removal
- De-dispersion trials
- Search for periodicities
- Candidate selection
- Candidate folding and confirmation

2.4.1 Observations and data acquisition

The search for new pulsars begins by pointing the telescope to a particular region of the sky. According to how such a region is chosen, we can have a *blind* search or a *targeted* search. In the first case, the sky, or a large area of it, is surveyed uniformly by doing a sequence of pointings. In the second case, the telescope is directed towards specific regions or objects, where one or more radio pulsars are very likely to be present (e.g. γ-ray point sources, globular clusters). In both cases, the telescope collects the radiation coming from the chosen target for a certain amount of time that depends on the characteristics of the telescope and of the receiving system, as well as on the chosen search strategy. Because they typically require to cover a much smaller area of the sky, targeted searches can usually afford much longer integration times for the single observations, compared to blind searches. The equation that relates the observing parameters to the corresponding search sensitivity is called *radiometer equation* (Dewey et al., 1984) and,

[1] `http://psrdada.sourceforge.net`
[2] `http://www.cv.nrao.edu/~sransom/presto`
[3] `http://sigproc.sourceforge.net`

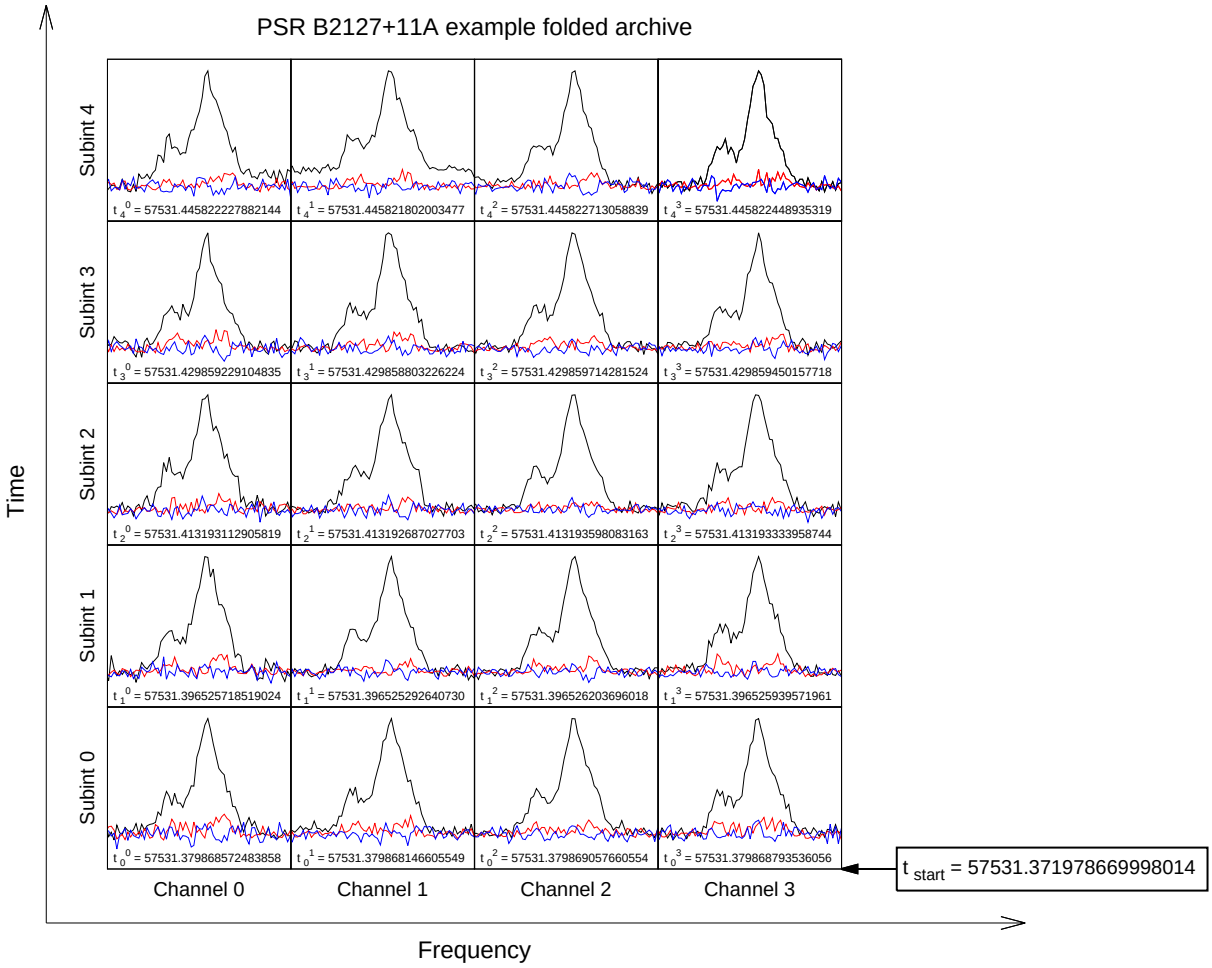

Figure 2.3. Example of an uncalibrated folded archive of pulsar PSR B2127+11A, observed at 1.4 GHz with the Arecibo radio telescope. The archive is a collection of profiles, one for each sub-integration/frequency-channel pair. If the observation is done in full-Stokes mode, as in this example, each profile contains the full polarimetric information: the black line is the total intensity, the red line the linear polarization and the blue line the circular polarization profile.

for a pulsar, it reads:

$$S_{\rm mean} = \frac{({\rm S/N})\,\zeta\,T_{\rm sys}}{\mathcal{G}\sqrt{n_{\rm pol}\,\Delta t_{\rm obs}\,\Delta\nu}}\sqrt{\frac{W}{P-W}}. \tag{2.18}$$

Here $S_{\rm mean}$ is the pulsar mean flux density, S/N the detection signal-to-noise ratio, ζ a correction factor due to the digitization, $T_{\rm sys}$ the system temperature, $\mathcal{G}$ the telescope gain, $n_{\rm pol}$ the number of polarizations, $\Delta t_{\rm obs}$ the observing time, $\Delta\nu$ the receiver bandwidth, P the pulsar spin period and W the pulse width. Given the parameters of the observing set-up, Eq. (2.18) gives us the minimum mean flux density that a pulsar must have to be detected with a signal-to-noise ratio of S/N, when observed for a time $\Delta t_{\rm obs}$.

The data are typically acquired in search mode, retaining a very high time resolution (of the order a few tens of μs), to be able to resolve even the very short pulses of the fastest MSPs, and a very high frequency resolution, to better correct for the effects of interstellar dispersion and identify narrow-band terrestrial RFI.

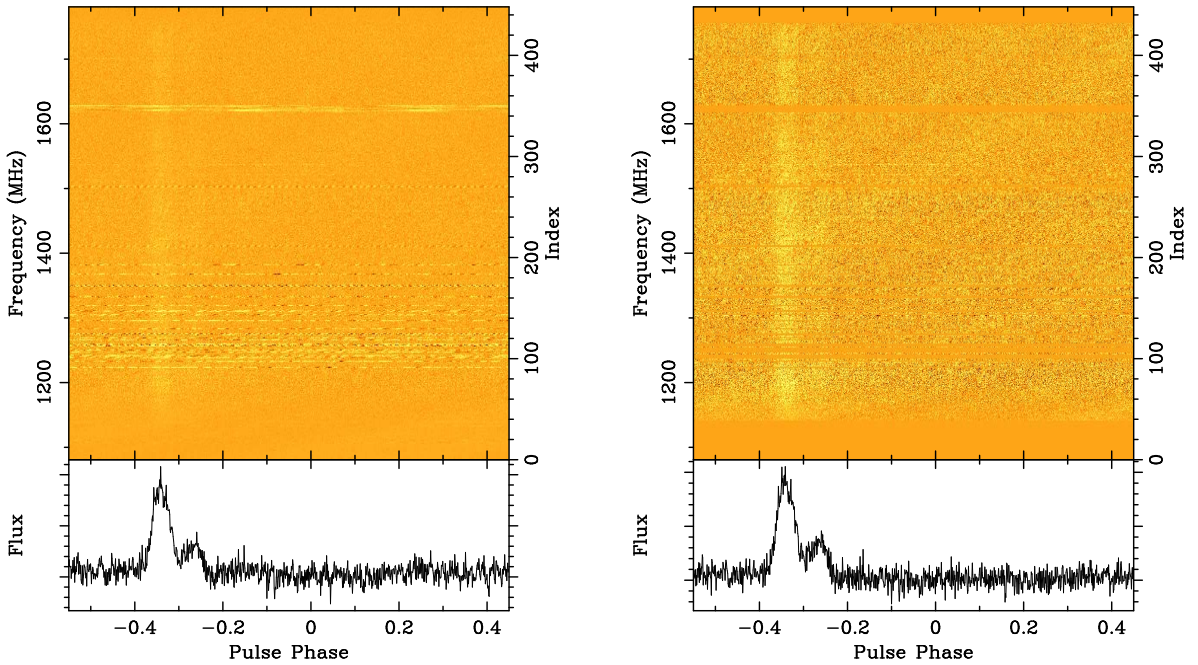

Figure 2.4. Example observation of pulsar PSR B2127+11B, taken at 1.4 GHz with the Arecibo radio telescope. The top panels show the intensity as a function of pulse phase and observing frequency, whereas the bottom panels show the resulting integrated pulse profile, after summing all the frequency channels. On the left, the original folded archive is displayed: prominent narrow-band RFI can be seen between 1200 and 1400 MHz and around 1630 MHz. On the right, the same archive is shown after clipping all the channels affected by RFI.

2.4.2 RFI removal

We regard as RFI all the unwanted non-astrophysical signals that fall within, or close to, the telescope observing band. RFI signals are produced by human activity, through a variety of different devices and, for this reason, their morphology ranges widely. In the time domain, RFI can be persistent, temporary, or even appear as short-lived bursts. In the frequency domain, they are usually narrow-band (Fig. 2.4) but can be broad-band in the case of short bursts. Slow changes in the receiver gain can also produce very low-frequency signals (the so-called *red-noise*, see e.g. Lazarus et al. 2015). RFI is deleterious because, being usually very strong, it can easily hide the astrophysical signals of interest. This is particularly harmful in the case of pulsar searching because, very much like pulsar signals, RFI can be stable periodic signals that may be easily mistaken for promising pulsar candidates.

In the last few decades, with the spread of telecommunication systems, the problem of RFI has grown exponentially. Consequently, a number of techniques have been developed to mitigate the effects. A standard way to identify RFI signals is to exploit the fact that they are terrestrial in origin, and thus they are not dispersed. It is thus common practice to take the acquired data without correcting for dispersion (i.e. DM = 0 pc cm^{-3}) and look for strong periodic signals both in the time and frequency domain (e.g. Eatough et al., 2009). Based on this, we can later ignore (for instance, by creating a *mask*) all the time intervals and frequency channels where RFI was found.

2.4.3 De-dispersion trials

As explained in Section 2.2.1, the signal of a pulsar travels through the ionized component of the ISM and, because of dispersion, it arrives at the observer at different times across the observing band. If not corrected, this effect can make the observed pulsar completely undetectable. When searching for new pulsars, we do not know a priori the associated DM, in most cases[4]. Hence, the DM is treated as a free parameter. A sequence of DM trial values are thus explored within a certain range of interest and, for each DM trial, a time correction calculated with Eq. (2.5) is applied to each frequency channel of the search-mode data.

When searching in DM, it is important to choose an appropriate step size, ΔDM. Choosing too small a step means increasing the total computational cost without gaining in sensitivity. Conversely, if the step is too large, one might miss the actual DM value of the pulsar, causing its signal to be smeared out and, thus, be undetected. The optimal value of ΔDM depends on the observing frequency ν, the total observing bandwidth $\Delta\nu$, as well as the chosen sampling time $t_{\rm samp}$. Lorimer & Kramer (2004) provide an approximate formula to calculate the i-th trial DM value as a function of these three parameters:

$$\mathrm{DM}_i = 1.205 \times 10^{-7}\ \mathrm{pc\ cm^{-3}} (i-1)\, t_{\rm samp}\, (\nu^3/\Delta\nu), \tag{2.19}$$

where $t_{\rm samp}$ is expressed in ms and ν and $\Delta\nu$ in MHz. For each trial value, once the de-dispersion is applied, the frequency channels are summed together to produce an RFI-free de-dispersed time series, which will then be searched for possible pulsar signals. At higher DM values, because of intra-channel smearing, this step is made coarser and the time-series is down-sampled to avoid unnecessary additional computations with no corresponding gain in sensitivity.

2.4.4 Periodicity search

Although there exist multiple methods to search for pulsars, the most commonly used ones are based on Fourier Transforms (FT), which exploit the intrinsic periodicity of pulsar signals. The Fourier theorem states that any function can be represented as the superposition of a (possibly infinite) number of sinusoids, each with a proper amplitude, phase and frequency. The FT is the mathematical tool used to perform such a decomposition. Because the radiation coming from a pulsar has an intrinsic periodicity, while thermal noise does not, the Fourier component with the pulsar period will have a much larger amplitude (and, hence, power) compared to all the other sinusoidal components, and will thus be easily detectable in the Fourier domain.

Because the de-dispersed time series generated as described in Section 2.4.3 are discrete, uniformly sampled sequences of data, the FT is performed in its discrete implementation, called Discrete Fourier Transform (DFT, see e.g. Press et al., 1992). However, the calculation of the DFT of an N-sample time series requires a number of operations of the order $\mathcal{O}(N^2)$ which, for long observations, can easily become prohibitively expensive in terms of computational time even for modern machines. The solution to this problem is the Fast Fourier Transform algorithm (FFT, Cooley & Tukey, 1965), an extremely efficient implementation of the DFT that only requires a $\mathcal{O}(N \log N)$ number of operations. Virtually all modern Fourier-domain analysis software, including `PRESTO` and `SIGPROC`, are based on the FFT.

[4]There are some exceptions, most notably in targeted searches. For instance, pulsars residing in the same globular cluster typically have similar DM values. Hence, if the DM of one pulsar is known, one can greatly narrow the range of DM trials, when searching for new pulsars in the same cluster.

However, despite being periodic, the signal coming from a pulsar is typically not a sinusoidal function. Rather, it is a train of pulses with more or less complex shapes. In the Fourier domain, such a morphology translates into a spectrum where the signal power is shared among the fundamental periodicity and its harmonics (i.e. integer multiples and sub-multiples of the fundamental periodicity). This effect is stronger for smaller pulse duty cycles. In order to correctly recover all the pulsar signal power, it is common practice to do a so-called *harmonic summing*: copies of the Fourier spectrum, each stretched by an integer factor, are created and subsequently summed to the original spectrum. This way, possible harmonically related peaks will be added together, increasing the power of the pulsar signal over the noise level. The method is usually implemented adding up to 1, 2, 4, 8 or 16 harmonics.

2.4.5 Binary pulsars: acceleration search

An additional complication is introduced if the pulsar is part of a binary system. In this case, the neutron star undergoes a time-varying acceleration due to its motion along the orbit, that results in a time-varying observed spin period and spin period derivative:

$$P_{\rm obs}(t) = P\left[1 + \frac{v_l(t)}{c}\right]; \qquad \dot{P}_{\rm obs}(t) = P\,\frac{a_l(t)}{c}\,, \tag{2.20}$$

where P and $\dot{P}$ are the intrinsic spin period and spin period derivative, $P_{\rm obs}$ and $\dot{P}_{\rm obs}$ the observed ones, $v_l(t)$ and $a_l(t)$ the pulsar velocity and acceleration component along the line of sight, respectively. As a consequence, the power of the pulsar signal in the Fourier domain will be spread across several frequency bins, adjacent to the fundamental harmonic. Clearly, the effect will be stronger for pulsars undergoing larger accelerations, as in the case of very tight binaries. Because binary pulsars are very interesting for a number of reasons, people have devised several methods to improve the sensitivity of pulsar searching software for such systems. The most commonly used method is called *acceleration search*. In the acceleration search, the pulsar is assumed to undergo a constant radial acceleration a_l throughout the length $\Delta t_{\rm obs}$ of the considered observation. In `PRESTO`, such an acceleration translates into a maximum number $z_{\rm max}$ of adjacent Fourier bins across which the power of the pulsar signal will be spread, and that can be calculated as (Ransom et al., 2002):

$$z_{\rm max} = \Delta t_{\rm obs}^2 \frac{a_l}{cP}. \tag{2.21}$$

If the Fourier bin has a size $\Delta\nu_{\rm bin}$, all the bins in the interval $[\nu_0 - z_{\rm max}\Delta\nu_{\rm bin}, \nu_0 + z_{\rm max}\Delta\nu_{\rm bin}]$ around a given frequency ν_0 will be considered and properly processed to possibly recover the power spread by the binary motion.

In time-domain based acceleration search software, like `SIGPROC`, the constant acceleration is implemented via a corresponding variable stretching or squeezing of the time series.

However, in both cases, the assumption of a constant acceleration is a valid approximation only for binary systems whose orbital period is about 10 times longer than the observation considered (e.g. Ransom et al., 2003; Ng et al., 2015). Since the pulsar orbit (and thus its radial acceleration) is not known a priori, the acceleration search is performed with several trial values of a_l.

Searches for binary pulsars are very computationally demanding, not only because they add a dimension to the parameter space searched (in addition to the DM and the spin period P), but also because the acceleration search algorithm requires a number of operations that increases

very quickly with the number of acceleration trials. To overcome this issue, people have started implementing this and other search algorithms on modern GPUs (e.g. PRESTO-ON-GPU[5]). Thanks to the high level of parallelization that they allow, GPUs can be tens or even hundreds of times faster than Central Processing Units (CPUs), depending on the specific task considered.

2.4.6 Candidate selection, folding and confirmation

Even after removing the most prominent RFI from the data, the number of periodic signals found per single observation can easily exceed a few thousand, the vast majority of which will turn out to be spurious signals. It is thus of fundamental importance to implement sifting criteria with which to reduce the total number of candidates. For instance, the same periodicity detected at different DMs or acceleration trial values can be considered as a single candidate. Similarly, some candidates can be found to be harmonically related to others and probably originate from the same signal. After filtering out the least significant signals and grouping the likely related ones, the search pipeline folds the most promising pulsar candidates. As explained in Section 2.3.3.2 the folding procedure consists in taking the original observation, de-dispersing it at the candidate DM, and then splitting it into time chunks that will be summed coherently in phase according to the candidate spin period and acceleration (which translates into a spin period derivative, see Eq. 2.20). The folding usually produces a diagnostic plot that contains useful information, such as the integrated pulse profile, the pulse amplitude as a function of pulse phase and time and as a function of pulse phase and frequency, the S/N as a function of trial DM etc. From this plot it is possible to check, for instance, whether the putative pulsar signal is actually broad-band or if it results from RFI. However, the typical number of candidate plots so produced is still prohibitively high to be examined by a human. For this reason, in the last decade, more and more software has been developed to automatically evaluate the goodness of a candidate (Eatough et al., 2010; Lee et al., 2013; Morello et al., 2014; Zhu et al., 2014), in some cases through machine-learning algorithms. If the folded candidate passes all the sanity checks and the final human inspection, it can eventually be re-observed at a later time for the final confirmation.

2.4.7 Determination of the binary orbit

If the newly discovered pulsar shows signs of a changing period (i.e. of binarity), it is necessary to first determine the approximate orbital parameters, before proceeding with its follow-up timing. There are two main ways to do so, that can also be used sequentially. The first way is the *period-acceleration diagram* method, proposed by Freire et al. (2001a), which is particularly suitable for cases in which the detections are very sparse. The method makes use of the measured accelerations, which are plotted as a function of the corresponding period measured in the same detection of the pulsar. This way, the dependence on time is removed. A circular binary will manifest itself in the diagram as a perfect ellipse, whose position and semi-major axes will depend on the physical characteristics of the orbit. An eccentric binary will instead exhibit more complex shapes. The data can then be fitted with codes like CIRCORBIT[6] and ORBITFIT[7] (Freire et al., 2001a) to obtain the orbital parameters through a least-square fitting procedure. Thanks to its independence on the cadence of the detections, the period-acceleration diagram

[5] https://github.com/jintaoluo/presto2_on_gpu

[6] CIRCORBIT, ORBITFIT and FITORBIT are part of a suite of codes developed at Jodrell Bank, whose list can be found at http://www.jb.man.ac.uk/pulsar/Resources/tools.html. The CIRCORBIT code can be downloaded from http://www3.mpifr-bonn.mpg.de/staff/pfreire/programs/circorbit.tar.

method can *always* be used to get a first estimate of the orbital parameters, which can in turn be used as initial guesses for the second method. The latter consists in fitting $P_{\rm obs}(t)$, i.e. the pulsar period values detected from the search pipeline, as a function of time. Indeed, we recall that the observed spin period is expected to vary because of the varying doppler effect due to the orbital motion (Eq. 2.20). In the case of a circular orbit, $P_{\rm obs}(t)$ will be a perfect sinusoid with the period of the binary and with the amplitude corresponding to the projected size of the orbit. In the case of an eccentric binary, the shape of $P_{\rm obs}(t)$ will be more complicated and will also depend on the orientation and on the eccentricity of the orbit. As in the previous method, specific codes (such as e.g. `FITORBIT`[7]) can be used to fit $P_{\rm obs}(t)$ for either a circular or an eccentric orbit, and hence obtain the refined orbital parameters of the system. If the number of detections is large enough in the time range considered, the first step with the period-acceleration diagram method can be skipped.

2.5 Timing

Once a pulsar is discovered, the main tool used for its further study is *pulsar timing*, a technique that exploits the exceptional rotational stability of pulsars. In a nutshell, it consists in precisely measuring the times-of-arrival (ToAs) of the pulses and build a model that, by taking into account all the possible effects that influence the propagation time of the signal from the NS to the observer, is able to correctly describe the pulsar rotation within a given time range. In building the timing model, a series of parameters are fitted. These can be, for instance:

- Rotational: e.g. the spin period and spin period derivative of the pulsar.
- Astrometric: e.g. the position, proper motion and parallax of the pulsar.
- ISM-related: e.g. the dispersion measure.
- Binary: e.g. the projected size of the orbit, the orbital period, the eccentricity etc., if the pulsar is in a binary system.

If the model is good enough to predict each ToA to within a small fraction of the pulsar spin period, we refer to the model as a *phase-connected* (or *phase-coherent*) *timing solution* (or *ephemeris*). A phase-connected timing solution is capable of accounting for every single rotation of the NS, within the time range considered. When this is the case, it means that all the parameters considered in the model are precise enough to not "lose" any rotation of the NS. The measured parameters can thus be used in a wide range of scientific applications (see Section 1.6).

In the following sections we will discuss in detail all the basic steps of pulsar timing, from the data acquisition to the construction of a phase-connected timing solution. A general scheme of the whole procedure is shown in Fig. 2.5. A list of the software packages and relative routines used in this thesis to perform the single steps can be found in Table 2.1.

2.5.1 Observations and data acquisition

The observing set-up and strategy for timing first depends on whether we already have a phase-connected solution or not, for the pulsar considered.

For a newly-discovered pulsar, the only parameters usually known are the position, the spin period and the DM (as well as some of the orbital parameters in the case of a binary system, see

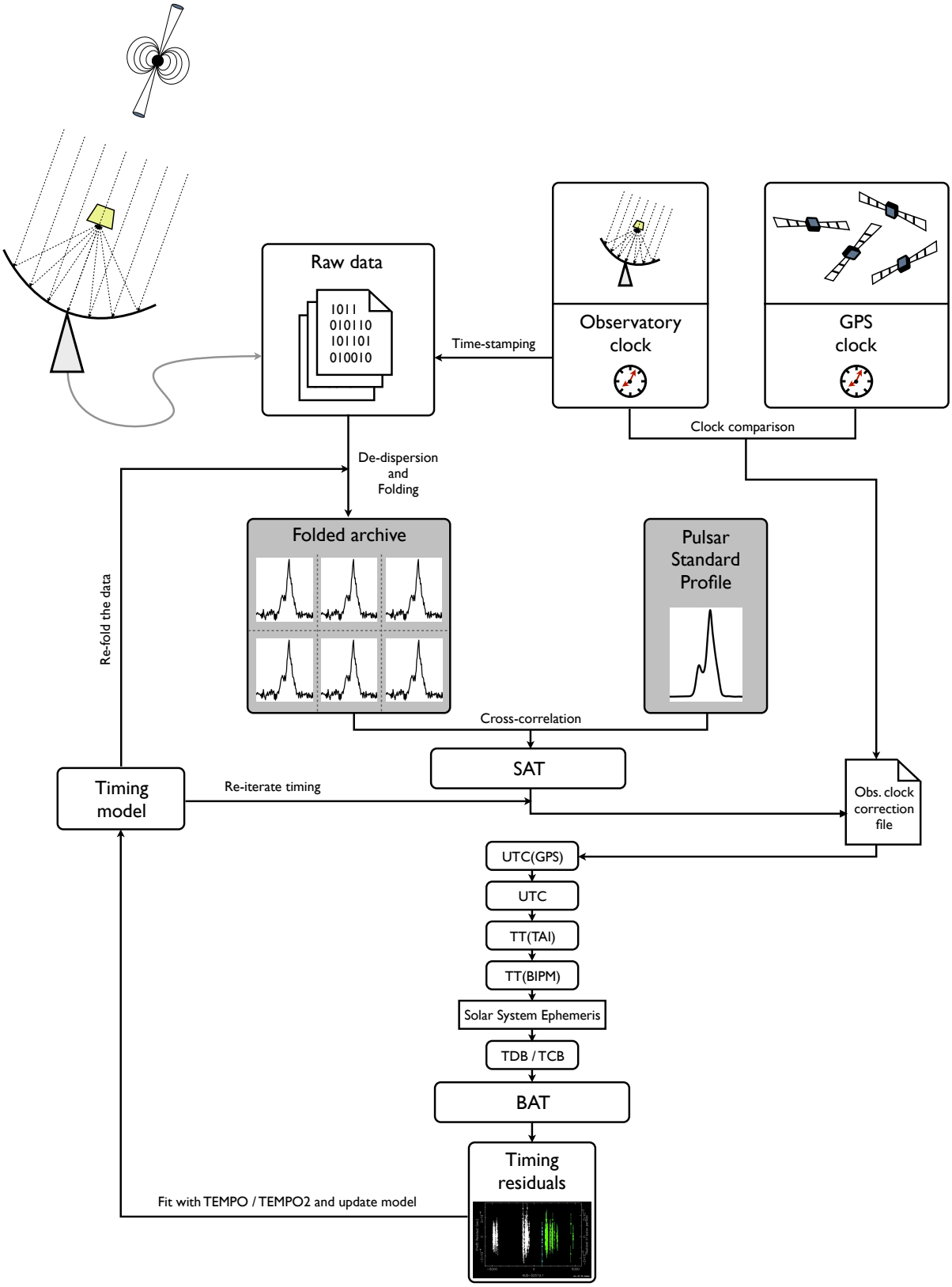

Figure 2.5. General scheme of the pulsar timing procedure. See discussion in Section 2.5 for the details.

Table 2.1. Software packages and relative routines used in this thesis for pulsar timing and polarimetry.

Operation	Routine	Software Package	References
De-dispersion / Folding	`dspsr`	`DSPSR`	van Straten & Bailes (2011)
RFI removal	`pazi`	`PSRCHIVE`	Hotan et al. (2004); van Straten et al. (2012)
Archive manipulation	`pam`	`PSRCHIVE`	Hotan et al. (2004); van Straten et al. (2012)
Standard profile creation	`psradd`	`PSRCHIVE`	Hotan et al. (2004); van Straten et al. (2012)
	`psrsmooth`	`PSRCHIVE`	Hotan et al. (2004); van Straten et al. (2012)
ToA extraction	`pat`	`PSRCHIVE`	Hotan et al. (2004); van Straten et al. (2012)
Timing	`tempo`	`TEMPO`	`http://tempo.sourceforge.net`
	`tempo2`	`TEMPO2`	Edwards et al. (2006); Hobbs et al. (2006)
Polarization calibration	`pac`	`PSRCHIVE`	Hotan et al. (2004); van Straten et al. (2012)
	`pcm`	`PSRCHIVE`	Hotan et al. (2004); van Straten et al. (2012)
RM measurement	`rmfit`	`PSRCHIVE`	Hotan et al. (2004); van Straten et al. (2012)
Flux calibration	`fluxcal`	`PSRCHIVE`	Hotan et al. (2004); van Straten et al. (2012)

Section 2.5.3.3). However, their precision is typically too low to allow a correct real-time folding of new observations made at later times. In this case, even though for the purpose of timing, the pulsar is observed in search-mode. Indeed, thanks to the much finer time resolution, search-mode data can be re-folded at a later time, when the pulsar ephemeris is improved, without any risk of signal loss. This strategy is particularly suitable for binary pulsars (especially redback systems, as we shall see in next chapters), in which inaccurate orbital parameters can easily lead to a loss of phase connection and, thus, to a non-detection of the pulsar when folding the data.

If, instead, the pulsar already has a good timing solution, a typical timing observing campaign will be done using a coherent de-dispersion folding mode of the telescope back-end. The known value of the pulsar DM allows the back-end to completely remove the intra-channel dispersive smearing through coherent de-dispersion. A large number of frequency channels is anyway usually retained, to later allow a better clipping of narrow-band RFI. In the time domain, the sub-integrations are usually chosen to be short, not only to minimize the impact of small errors in the timing parameters, but also to later excise short-lived or impulsive RFI. In most cases, a 10-s sub-integration length represents a good trade-off that permits a successive correction, once the model is updated, without having unnecessarily large data sizes.

In both cases, the data file is time-stamped with the start time of the observation (Fig. 2.3), according to the local observatory clock, which is typically a high-precision hydrogen maser clock. The observatory time is constantly compared to the time kept by an ensemble of atomic clocks located on-board the Global Positioning System (GPS) satellites. The differences between the two times are recorded onto a file that contains the observatory clock corrections, to be applied to the data at a successive step. The proper tagging of the observation is of utmost importance for the correct timing of pulsars, since all the subsequently extracted ToAs are calculated on the basis of the observation start time.

It is also common practice, especially in high-precision pulsar timing, to perform a very short observation of the receiver noise-diode to later calibrate the data in polarization, which can also provide higher timing precision. This topic will be covered in more detail in Section 2.6.

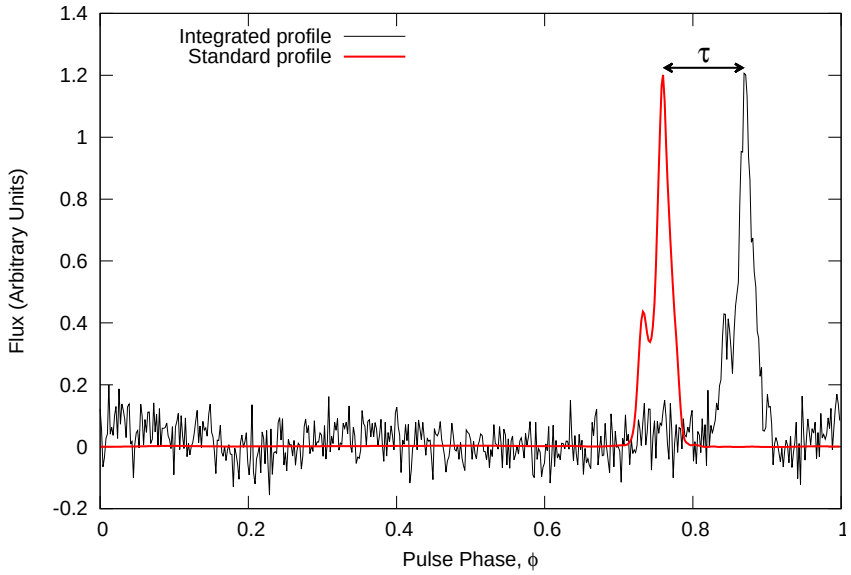

Figure 2.6. Illustration of the ToA determination. A high-S/N, or even noise-less, standard profile (red line), after being scaled, is cross-correlated with the observed integrated profile (black line) to determine the time shift τ.

2.5.2 Extraction of the topocentric Times-of-Arrival

A folded archive is essentially a table containing an integrated profile for each sub-integration / frequency-channel pair (Fig. 2.3). A time-stamp, $t_{\rm start}$, marks the date and time (or *epoch*) at which the observation began. Each integrated profile is also assigned an epoch $t_{\rm int}$, which is referred to some particular *fiducial point* of the profile and it is usually chosen to be referred to the single pulse closest to the mid-point of the sub-integration time interval.

The ToA extraction process is done by using a high-S/N reference profile of the pulsar, usually referred to as the *template*, or *standard profile*. The latter can be just a single high-S/N observation, the addition of several observations together, or even a completely noise-less profile obtained, e.g. by fitting the real profile with analytic functions (Kramer et al., 1994; Kramer, 1994), or by smoothing it with a wavelet transform (Demorest et al., 2013). Each real integrated profile $\mathcal{P}(t)$ is then regarded as a scaled and shifted version of the template $\mathcal{T}(t)$, with some noise $\mathcal{N}(t)$ superimposed (Taylor, 1992; Lorimer & Kramer, 2004):

$$\mathcal{P}(t) = a + b\mathcal{T}(t-\tau) + \mathcal{N}(t). \tag{2.22}$$

The ToA is evaluated by doing a cross-correlation of the template with the integrated profile (Fig. 2.6). Such procedure determines the time shift τ between the fiducial point of the template and that of the integrated profile. The final ToA value will thus be:

$$\text{ToA} = t_{\rm int} + \tau\,. \tag{2.23}$$

Because every ToA determined in this way is topocentric, it is often referred to as *site arrival time* (SAT). Although there exist several different techniques, the cross-correlation itself has typically been done in the Fourier domain with the so-called *Fourier phase gradient* (commonly known as `FFTFIT`) algorithm (Taylor, 1992), which guarantees an accuracy in the ToA determination up to a fraction of the chosen profile bin width, by estimating the relative uncertainty through a χ^2

optimization routine. More recently, other techniques based on one-dimensional Markov-Chain Monte Carlo algorithms have been shown to be preferable in the low-S/N regime (Verbiest et al., 2016).

An important caveat to consider is the possible evolution of the integrated pulse profile as a function of frequency (see Section 1.5.1). If not properly taken into account, this effect can introduce systematic errors when trying to determine ToAs at a frequency which significantly differs from that of the standard profile. This issue has recently become increasingly important because of the development of back-ends capable of processing a very large bandwidth (such as PUPPI at Arecibo, DuPlain et al. 2008) as well as of ultra-wide-band receiving systems (such as the Ultra-Broad-Band receiver[7] at Effelsberg and the Ultra-Wideband Low-frequency receiver at Parkes, Manchester 2015). In the last few years, new sophisticated methods have thus been devised to correctly account for the frequency dependence of the pulse profile when evaluating the ToAs (Liu et al., 2014; Pennucci et al., 2014).

2.5.3 The timing formula

Within the framework of the "Pulsar Standard Model" (see Section 1.3), where the pulsar behaves exactly like a lighthouse, each observed pulse corresponds to a single rotation of the NS. Therefore, between each pair of ToAs, an integer number of rotations of the pulsar must have occurred.

In a reference frame centered on the pulsar and co-moving with it, the number of rotations, N, made by the NS from a reference time t_0 to any given time t, can be modelled by a smooth function, that can be expanded as a Taylor series (Lorimer & Kramer, 2004):

$$N(t) = N_0 + f_0(t-t_0) + \frac{1}{2}\dot{f}_0(t-t_0)^2 + \ldots = N_0 + \sum_{k\geq 0} \frac{1}{(k+1)!} f_0^{(k)}(t-t_0)^{k+1}\,, \tag{2.24}$$

where $f_0 \equiv f(t_0)$ and $f_0^{(k)} \equiv f^{(k)}(t_0)$ are the pulsar spin frequency and the k-th spin frequency derivative at the reference epoch t_0, respectively.

It is important to remark that the time t in Eq. (2.24) is the proper time of the pulse emission as it would be measured by an observer located at the position of the pulsar. Such a reference frame is clearly different from that used to obtain the topocentric ToAs (SATs), which are measured at the telescope site. Therefore, in order to compare the rotational model against real data, we first need to refer each SAT (henceforth, $t_{\rm sat}$) to the pulse emission time (henceforth, $t_{\rm psr}$) as measured at the pulsar centre of mass[8]. This process involves a series of relativistic frame transformations (see Fig. 2.7) and for the general case of a binary pulsar, it can be divided into three steps:

- ($t_{\rm sat} \rightarrow t_{\rm bat}$) The SAT is first referred to the Solar System barycentre (SSB), thus becoming a Barycentric Arrival Time (BAT).
- ($t_{\rm bat} \rightarrow t_{\rm bb}$) The BAT is then referred to the binary system barycentre (BB).
- ($t_{\rm bb} \rightarrow t_{\rm psr}$) The time at the BB is finally converted into the pulsar emission time.

[7] www3.mpifr-bonn.mpg.de/staff/pfreire/BEACON.html

[8] Clearly, the real emission of the pulsar comes from some location near the NS surface, and not from its centre of mass. However, assuming that the true point of emission does not change over the time scale of interest, the difference between the true emission time and that measured from the centre of mass, will be constant and will thus represent an irrelevant offset in Eq. (2.24) (Edwards et al., 2006).

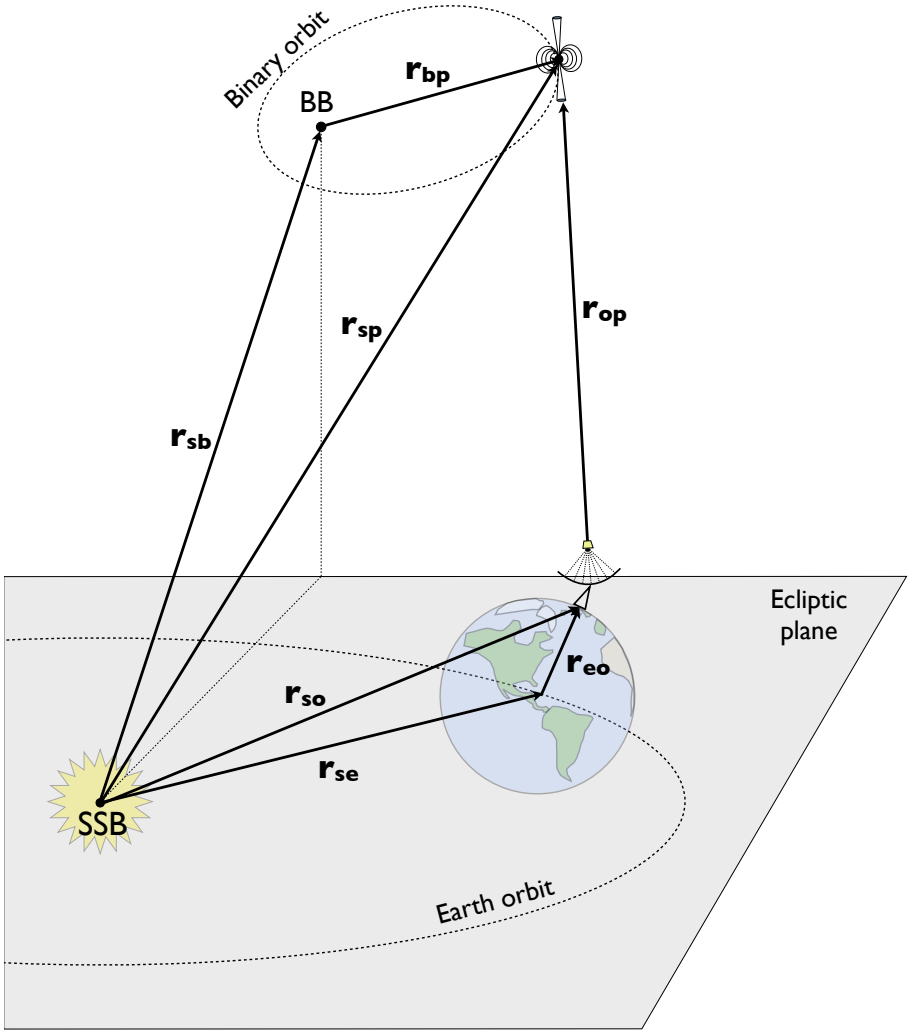

Figure 2.7. Vectors involved in the relativistic frame transformations performed during the timing procedure.

Each of these steps is composed by a series of correction terms that allow us to pass from $t_{\rm sat}$ to $t_{\rm psr}$. Following Edwards et al. (2006), the full equation containing all the contributions from the three steps, can be written as:

$$\begin{aligned} t_{\rm psr} = t_{\rm sat} + \underbrace{\Delta_{\rm Clk} - (\Delta^{\odot}_{\rm R} + \Delta^{\odot}_{\rm D} + \Delta^{\odot}_{\rm E} + \Delta^{\odot}_{\rm S} + \Delta^{\odot}_{\varpi} + \Delta^{\oplus}_{\rm Atm})}_{\text{barycentering terms}} \\ + \underbrace{\Delta^{*}_{\rm VP} + \Delta^{*}_{\rm D} + \Delta^{*}_{\rm E} + \Delta^{*}_{\nu}}_{\text{interstellar terms}} + \underbrace{\Delta^{\rm bin}_{\rm R} + \Delta^{\rm bin}_{\rm E} + \Delta^{\rm bin}_{\rm S} + \Delta^{\rm bin}_{\rm A} + \Delta^{\rm bin}_{\rm K}}_{\text{binary terms}} . \end{aligned} \tag{2.25}$$

In the next subsections each group of contributions will be reviewed in detail.

2.5.3.1 Barycentering terms

The first seven correction terms in Eq. (2.25) are those that allow us to refer the topocentric ToA to the SSB. The SSB is a convenient reference frame because, unlike the Earth, it can

be considered as an inertial frame to a very good approximation. Below follows a detailed description of each contribution.

$\Delta_{\rm Clk}$ The observatory clock used to time-stamp the acquired data is usually stable only over time-scales of a few weeks. For this reason, it is constantly compared to the much more stable GPS-based time and the offsets found are recorded onto a file. $\Delta_{\rm Clk}$ embodies the local observatory clock corrections and the referencing of the time to a much more stable universal time standard, through a series of conversions. Specifically, the local observatory time (SAT) is first converted to the GPS-based Universal Coordinated Time, UTC(GPS), as measured by the *National Institute of Standards and Technology* (NIST) and then to the normal Universal Coordinated Time, UTC. The difference between UTC(GPS) and UTC is that the latter takes into account the ever-decreasing rotation rate of the Earth, whereas the former does not. UTC is then referred to the International Atomic Time (TAI) realization, TT(TAI), of the Terrestrial Time (TT). TT is a theoretical time standard, whose real clocks are only approximations, that is based on the definition of *second* by the International System of Units (SI). TAI, on the other hand, is the most precise real time standard available, as it is based on an ensemble of hundreds of atomic clocks spread across the Earth surface. Because the definition of UTC is based on TAI, the latter is always ahead of UTC by a certain number of so-called *leap seconds* (precisely 37, as of January 2017). Leap seconds are offsets that are artificially added to UTC every few years to account for the irregular changes in the mean solar day length, due to the slowing Earth rotation rate. Despite being the most precise time standard, TAI is also subject to small instabilities. However, once published, TAI is never corrected. For this reason, TT(TAI) is in turn converted to the TT(BIPM) time standard, a retroactively corrected version of the former provided every year by the *Bureau International des Poids e Mesures* (BIPM), and then finally referred to the SSB through either the Barycentric Dynamic Time (TDB) or Barycentric Coordinate Time (TCB). We refer to Hobbs et al. (2012) for a more comprehensive discussion about time standards and pulsars.

$\Delta_{\rm R}^{\odot}$ It is the *Solar System Rømer delay*, which accounts for the difference between the arrival time at the observatory (SAT) with respect to the arrival time as it would be measured at the SSB, assuming that the radiation propagates in a vacuum and ignoring the binary motion of the pulsar (which will be taken into account by another correction term). It is thus just a classical geometrical delay that depends on the relative position of the Earth along its orbit, with respect to the pulsar. The Solar System Rømer delay can be expressed as:

$$\Delta_{\rm R}^{\odot} = -\frac{(\mathbf{r_{se}} + \mathbf{r_{eo}}) \cdot \hat{\mathbf{r}}_{\mathbf{sb}}}{c}\,, \tag{2.26}$$

where $\mathbf{r_{se}}$ is the vector connecting the SSB to the Earth centre, $\mathbf{r_{eo}}$ the vector connecting the Earth centre to the location of the observatory on the Earth surface, and $\hat{\mathbf{r}}_{\mathbf{sb}}$ is the unit vector that from the SSB points to the binary system barycentre.

$\Delta_{\rm D}^{\odot}$ It is the dispersion delay caused by the ionized component of the interplanetary medium. This essentially coincides with the solar wind, whose density profile is modelled with a radial profile that roughly scales with the heliocentric distance r as $\sim r^{-2}$ (Issautier et al., 1998). Keeping in mind the simplifying assumptions made (see Ed-

wards et al., 2006) the associated delay for an electromagnetic wave of frequency ν is then:

$$\Delta_{\rm D}^{\odot} = \frac{\mathcal{D}}{\nu^2} \int_0^{\infty} n_{\rm e}^{\rm sw}(\langle \mathbf{r_{se}} \rangle) \left[\frac{\langle \mathbf{r_{se}} \rangle}{r(l)} \right]^2 {\rm d}l \,, \tag{2.27}$$

where $\mathcal{D}$ is the usual dispersion constant, $n_{\rm e}^{\rm sw}(\langle \mathbf{r_{se}} \rangle)$ is the assumed solar wind free electron number density at the average distance $\langle \mathbf{r_{se}} \rangle = 1$ AU of the Earth from the Sun, and the integral is calculated along the line of sight from the observer to the pulsar. Recent measurements made by Issautier et al. (1998, 2001) and Splaver et al. (2005) agree on a value $n_{\rm e}^{\rm sw}(\langle \mathbf{r_{se}} \rangle) \simeq 4$ cm^{-3}.

$\Delta_{\rm E}^{\odot}$ It is the Solar System *Einstein delay*, i.e. the time dilation associated with the relativistic space-time coordinate frame transformation from the observatory site to the SSB, whose analytical expression is (Irwin & Fukushima, 1999; Edwards et al., 2006):

$$\Delta_{\rm E}^{\odot} = \frac{1}{c^2} \int_{t_0}^{t} \left[U_{\oplus} + \frac{v_{\oplus}^2}{2} + \Delta L_{\rm C}^{\rm (PN)} + \Delta L_{\rm C}^{\rm (A)} \right] {\rm d}t + \frac{\mathbf{r_{eo}} \cdot \mathbf{v}_{\rm gb} + W_0 \, t_{\rm sat}}{c^2} \,. \tag{2.28}$$

Here $U_{\oplus}$ is the gravitational potential at the geocentre given by all the bodies in the Solar System except the Earth; $v_{\oplus}$ is the velocity of the geocentre with respect to the SSB; $\Delta L_{\rm C}^{\rm (PN)}$ and $\Delta L_{\rm C}^{\rm (A)}$ are higher-order relativistic terms and corrections due to the asteroids, respectively (Fukushima, 1995); t_0 is a specific epoch thanks to which Eq. (2.28) correctly relates the measured TT arrival time to the coordinate time scales recommended by the *International Astronomical Union* (IAU), namely TCG (geocentric) and TCB (barycentric, Edwards et al. 2006). The second term accounts for the time dilation and gravitational redshift due to the Earth itself when referring the time from the geocentre to the actual observatory position on the Earth surface, whose positions are related by the vector $\mathbf{r_{eo}}$; $\mathbf{v}_{\rm gb}$ is the relative velocity of the geocentre with respect to the Earth barycentre; W_0 is the approximate spin potential of the Earth at the geoid.

$\Delta_{\rm S}^{\odot}$ It is the Solar System *Shapiro delay* (Shapiro, 1964), i.e. the delay due to the longer optical path that light has to travel when propagating in the curved space-time in proximity of the Solar System bodies. Backer & Hellings (1986) provide an expression that is a first-order approximation:

$$\Delta_{\rm S}^{\odot} = -2 \sum_j \frac{G m_j}{c^3} \ln(\hat{\mathbf{r}}_{\mathbf{op}} \cdot \mathbf{r}_j + |r_j|) + (\mathcal{O}^2) \,, \tag{2.29}$$

where m_j is the mass of the j-th body, $\hat{\mathbf{r}}_{\mathbf{op}}$ is the unit vector from the observatory to the pulsar, and $\mathbf{r}_j$ the vector from the observatory to the j-th body. Higher-order terms are usually negligible and can become important only when the radiation grazes a body at a very short distance. Accurate Solar System ephemerides are regularly provided, e.g., by the *Jet Propulsion Laboratory* (JPL) (e.g. Folkner et al., 2009, 2014).

$\Delta_{\varpi}^{\odot}$ It is the *annual parallax* term. In most cases, the pulsar radiation wavefront is considered to be perfectly plane when it reaches the observatory site. While this is a very good approximation for most pulsars, it might not be adequate for pulsars that are close enough to our Solar System. In the latter cases, the actual curvature of the wavefront

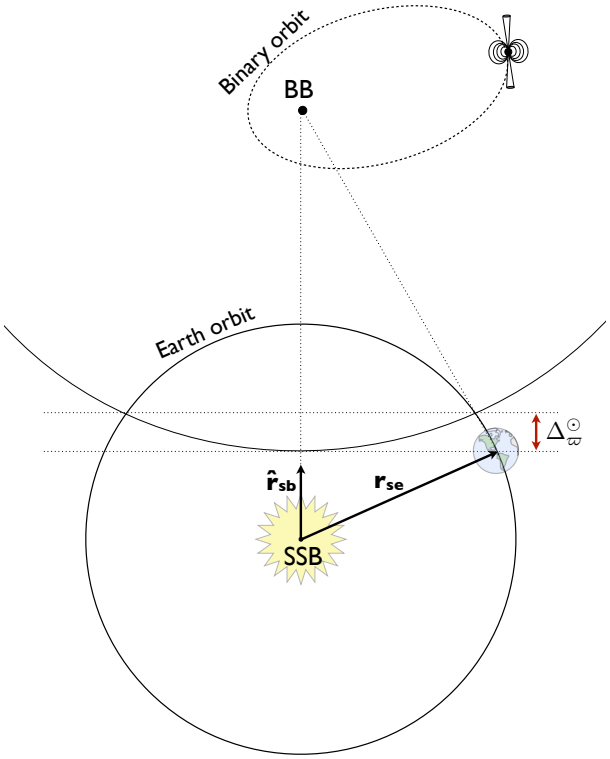

Figure 2.8. Illustration of the parallax effect in its first-order approximation. The curvature of the wavefront is responsible for an extra delay that depends on the position of the Earth along its orbit.

translates into a delay in the arrival time of the radiation at the observatory, compared to the plane-wave approximation case (Fig. 2.8), which depends on the position of the Earth along its orbit. The magnitude of the delay thus varies in a quasi-sinusoidal fashion, with a period of half a year, and can be expressed as (Backer & Hellings, 1986):

$$\Delta_{\varpi}^{\odot} = -\frac{1}{2cd}(\mathbf{r_{so}} \wedge \hat{\mathbf{r}}_{\mathbf{sp}})^2 = -\frac{1}{2cd}[(\mathbf{r_{so}} \cdot \hat{\mathbf{r}}_{\mathbf{sp}})^2 - |\mathbf{r_{so}}|^2]\,, \tag{2.30}$$

where $\mathbf{r_{so}}$ is the vector connecting the SSB to the observatory and $\hat{\mathbf{r}}_{\mathbf{sp}}$ the unit vector connecting the SSB to the pulsar. Clearly, the observable modulation is smaller for pulsars that are far from the ecliptic plane and vanishes for those located at the ecliptic poles.

$\Delta_{\mathrm{Atm}}^{\oplus}$ It is the delay associated with the propagation of the radiation through the Earth atmosphere, where several effects contribute. Firstly, the group velocity of electromagnetic waves in the atmosphere is different from the speed of light in a vacuum. Secondly, the atmosphere refractivity (which also changes between the ionosphere and the non-ionized troposphere) lengthens the optical travel path of the radiation. Thirdly, the ionosphere itself has a small dispersive effect that induces an additional delay, depending on the frequency of the radiation. However, all these effects are usually too small to be measured with the currently available sensitivity and some of them can become relevant only for very low-frequency ($\lesssim 300$ MHz) observations.

2.5.3.2 Interstellar terms

The second block of terms in Eq. (2.25) comes into play when referring $t_{\rm bat}$ to the binary system barycentre (or to the pulsar itself if this is isolated) and are related to the propagation of light through the ISM.

$\Delta^*_{\rm VP}$ It is the *vacuum propagation delay*, i.e. simply the radiation travel time from the BB to the SSB due to the finite speed of light in a vacuum. Its expression is, trivially:

$$\Delta^*_{\rm VP} = \frac{d}{c}\,, \tag{2.31}$$

where d is the distance between the BB and the SSB. Because the actual value of d is hardly ever known[9], most of the time this term cannot actually be calculated. However, it only represents a constant offset. It is therefore relevant only for very specific cases where it is important to know the real time of emission, for instance if we want to relate the pulsar signal to some other phenomenon that occurred at a specific time.

$\Delta^*_{\rm D}$ It is the frequency-dependent *interstellar dispersion delay*, due to the ionized component of the ISM, already discussed in Section 2.2.1. The associated delay is exactly that of Eq. (2.5), taking care of the fact that the radiation frequency as it would be measured at the SSB, $\nu_{\rm SSB}$, differs from the observed one, $\nu_{\rm obs}$, mostly because of the Doppler shift due to the Earth motion (by a factor of up to $\sim 10^{-4}$). The correction term can thus be written as:

$$\Delta^*_{\rm D} = \frac{\mathcal{D}}{\nu^2_{\rm SSB}}\,{\rm DM}\,. \tag{2.32}$$

Another caveat to consider is that, in some pulsars, the DM is seen to vary with time (e.g. Backer et al., 1993; You et al., 2007; Lam et al., 2016). In these cases, more sophisticated models must be used to take these variations into account (Keith et al., 2013; Lee et al., 2014).

Δ^*_{ν} This term accounts for all the possible delays associated with frequency-dependent effects that deviate from the inverse-square law and that cannot thus be absorbed by $\Delta^*_{\rm D}$. This contribution can be expressed as a sum of power laws with different spectral indices α_j, namely:

$$\Delta^*_{\nu} = \sum_j k_j (\nu_{\rm SSB})^{\alpha_j} \qquad \text{with } \alpha_j \neq -2\,, \tag{2.33}$$

where k_j is the scale factor of the j-th contribution.

$\Delta^*_{\rm E}$ It is the *Einstein delay* associated with the relativistic coordinate transformation from the SBB to the BB and it can be calculated in an analogous way to Eq. (2.28).

[9]The actual pulsar distance can be known through the measurement of its parallax, derived either via timing or via very-long-baseline interferometry (VLBI) observations, or through the association of the pulsar with some other object of known distance (e.g. a globular cluster or a supernova remnant).

2.5.3.3 Binary terms

If the pulsar considered is isolated, applying the correction terms described in Sections 2.5.3.1 and 2.5.3.2 will directly give the pulsar emission time, $t_{\rm psr}$. If, instead, the pulsar is part of a binary system, the third block of terms on the right-hand side of Eq. (2.25) must also be taken into account.

Timing models for pulsars in binary systems require a set of additional parameters to describe the orbital motion. In theory, in the case of a purely Keplerian orbit (which is an adequate description for a large number of systems), the 3-D motion of the pulsar along the orbit is fully described by six spatial parameters and one time parameter, namely;

- the *orbital inclination*, i;
- the *longitude of the ascending node*, $\Omega_{\rm p}^{\rm asc}$;
- the *longitude of periastron*, $\omega_{\rm p}$;
- the *semi-major axis*, $a_{\rm p}$;
- the *eccentricity*, e;
- the *orbital period*, $P_{\rm b}$;
- the *epoch of passage at periastron*, T_0;

where the first three parameters specify the orientation of the orbit in the sky, whereas the latter four univocally determine the position of the pulsar along the orbit, as a function of time. The motions of the pulsar and that of its companion are related by the well-known third Kepler's law:

$$\frac{P_{\rm b}^2}{a^3} = \frac{4\pi^2}{G(M_{\rm p}+M_{\rm c})}\,, \tag{2.34}$$

where $M_{\rm p}$ and $M_{\rm c}$ are the masses of the pulsar and of its companion, respectively, and

$$a = a_{\rm p} + a_{\rm c}\,, \tag{2.35}$$

is the *orbital separation*, i.e. the sum of the semi-major axis of the pulsar orbit, $a_{\rm p}$, and the semi-major axis of the companion orbit, $a_{\rm c}$. These quantities are in turn related to each other and to the masses of the bodies as:

$$\begin{cases} a_{\rm p} = a\,\dfrac{M_{\rm c}}{M_{\rm p}+M_{\rm c}} \\ \\ a_{\rm c} = a\,\dfrac{M_{\rm p}}{M_{\rm p}+M_{\rm c}} \end{cases}\,. \tag{2.36}$$

The pulsar motion along the orbit is then conveniently described within a cartesian reference frame $(\mathbf{i},\mathbf{j},\mathbf{k})$ with the origin coinciding with the BB (Fig. 2.9). Following the convention used by Damour & Taylor (1992), $\mathbf{i}$ and $\mathbf{j}$ are chosen to lie on the orbital plane, with the former pointing towards the ascending node of the pulsar orbit, and the latter towards the opposite direction of the observer along the projection of the line of sight; $\mathbf{k} = \mathbf{i} \wedge \mathbf{j}$ is thus orthogonal to the binary orbit and parallel to the orbital angular momentum, $\mathbf{L}$. In this frame, the position of the pulsar can be expressed in polar coordinates in a particularly simple form. Calling $r_{\rm p}$ the

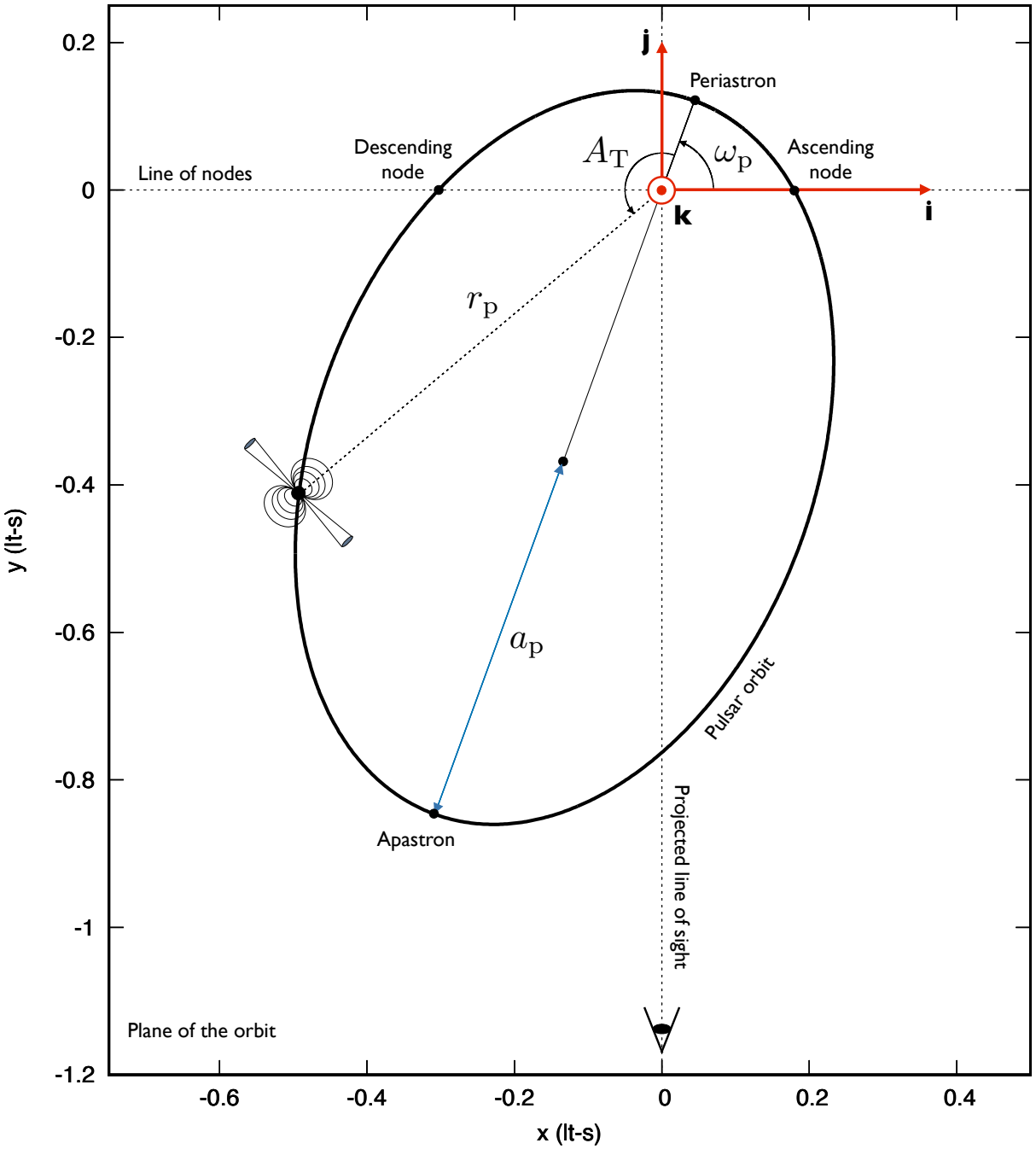

Figure 2.9. Schematic representation of the pulsar orbit in a hypothetical eccentric ($e = 0.75$) binary system with $M_{\rm p} = 1.4$ M$_\odot$, $M_{\rm c} = 2.0$ M$_\odot$, $P_{\rm b} = 3$ h and $\omega_{\rm p} = 70$ deg. The reference frame $(\mathbf{i}, \mathbf{j}, \mathbf{k})$ is highlighted in red.

radial distance of the pulsar and Θ_p the angle measured anti-clockwise from the **i** direction to the pulsar position vector, the trajectory of the pulsar is described by:

$$\begin{cases} \Theta_\mathrm{p} = \omega_\mathrm{p} + A_\mathrm{T} \\ r_\mathrm{p} = \dfrac{a_\mathrm{p}(1-e^2)}{1 + e\cos(A_\mathrm{T} - \omega_\mathrm{p})} \end{cases} . \tag{2.37}$$

Here we have introduced the *true anomaly*, A_T, which is the angle used to identify the pulsar orbital phase, and which is measured exactly like Θ_p, but starting from the periastron direction. The dependence of A_T with time can be obtained with the aid of two auxiliary angles, namely the *eccentric anomaly*, E (see Fig. 2.10), and the *mean anomaly*, M. By definition, in the purely Keplerian case, M is linearly proportional to time t, as:

$$M = \frac{2\pi}{P_\mathrm{b}}(t - T_0)\,. \tag{2.38}$$

The dependence of E on the true anomaly is instead given by a transcendental equation:

$$\tan\left(\frac{A_\mathrm{T}}{2}\right) = \sqrt{\frac{1+e}{1-e}}\,\tan\left(\frac{E}{2}\right). \tag{2.39}$$

It can be shown (see e.g. Capderou, 2005) that M is related to E through the implicit function (known as Kepler's equation):

$$M = E - e\sin E\,, \tag{2.40}$$

which does not have a closed-form solution and must be solved numerically. Solving first Eq. (2.39) and then (2.40) is therefore necessary to pass from A_T to M, and thus be able to express Eq. (2.37) as a function of time.

It is important to remark that, apart from a few exceptional cases, it is generally not possible to fully characterize the orbit through pulsar timing. In other words, timing does not allow us to easily measure all the seven orbital parameters listed above. Rather, only five observables are usually measurable. These are ω_p, P_b, e, T_0 and $x_\mathrm{p} = a_\mathrm{p}\sin i$, the latter being the projected semi-major axis of the pulsar orbit along the line of sight. With only these five parameters measured, we have no information on the system inclination as well as the on masses of the pulsar and its companion. However, by combining Eq. (2.34) with Eq. (2.36), it is possible to obtain a useful relation for these three parameters:

$$f(M_\mathrm{p}) \doteq \frac{4\pi^2}{G}\frac{x_\mathrm{p}^3}{P_\mathrm{b}^2} = \frac{(M_\mathrm{c}\sin i)^3}{(M_\mathrm{p}+M_\mathrm{c})^2}\,. \tag{2.41}$$

The quantity $f(M_\mathrm{p})$ so defined is said to be the *mass function* of the pulsar. Because it depends only on the easily measurable parameters x_p and P_b, it is often used to constrain the companion mass. Indeed, it is easy to see that:

$$f(M_\mathrm{p}) = \frac{M_\mathrm{c}}{\left(\dfrac{M_\mathrm{p}}{M_\mathrm{c}}+1\right)^2}\sin^3 i < M_\mathrm{c}\,\sin^3 i \qquad \Rightarrow \qquad M_\mathrm{c} > \frac{f(M_\mathrm{p})}{\sin^3 i} > f(M_\mathrm{p})\,, \tag{2.42}$$

that is, the pulsar mass function represents a lower limit to the mass of the companion. Also,

because the current range of observed pulsar masses is relatively narrow ($\sim 1-2\,\mathrm{M}_\odot$, Antoniadis et al. 2013), it is possible to use $f(M_\mathrm{p})$ to infer the companion mass for an assumed inclination of the system and a given value of the pulsar mass, typically chosen to be $1.4\,\mathrm{M}_\odot$.

One way to directly measure the inclination and the masses of the pulsar and its companion is by measuring two or more so-called *post-Keplerian* (PK) parameters. As their name suggests, they are parameters used to describe deviations from Newtonian gravity, for instance due to relativistic effects. In General Relativity (GR) and all boost-invariant gravity theories (e.g. Blandford & Teukolsky, 1976; Damour & Deruelle, 1985, 1986; Will & Zaglauer, 1989), the five most important PK parameters are: the rate of advance of periastron, $\dot{\omega}$; the time dilation and gravitational redshift parameter, γ; the orbital decay, $\dot{P}_\mathrm{b}$; the *range*, r, and the *shape*, s, of the Shapiro delay. Their expressions in GR are (Lorimer & Kramer, 2004):

$$\begin{aligned}
\dot{\omega} =& 3\,\mathrm{T}_\odot^{2/3}\left(\frac{P_\mathrm{b}}{2\pi}\right)^{-5/3}\frac{1}{1-e^2}(M_\mathrm{p}+M_\mathrm{c})^{2/3}\,,\\
\gamma =& \mathrm{T}_\odot^{2/3}\left(\frac{P_\mathrm{b}}{2\pi}\right)^{1/3} e\,\frac{M_\mathrm{c}(M_\mathrm{p}+2M_\mathrm{c})}{(M_\mathrm{p}+M_\mathrm{c})^{4/3}}\,,\\
\dot{P}_\mathrm{b} =& -\frac{192\pi}{5}\,\mathrm{T}_\odot^{5/3}\left(\frac{P_\mathrm{b}}{2\pi}\right)^{-5/3}\left[\frac{1+(73/24)e^2+(37/96)e^4}{(1-e^2)^{7/2}}\right]\frac{M_\mathrm{p}M_\mathrm{c}}{(M_\mathrm{p}+M_\mathrm{c})^{1/3}}\,,\\
r =& \mathrm{T}_\odot\, M_\mathrm{c}\,,\\
s \equiv \sin i =& \mathrm{T}_\odot^{-1/3}\left(\frac{P_\mathrm{b}}{2\pi}\right)^{-2/3} x_\mathrm{p}\frac{(M_\mathrm{p}+M_\mathrm{c})^{2/3}}{M_\mathrm{c}}\,,
\end{aligned} \tag{2.43}$$

where $\mathrm{T}_\odot = G\,\mathrm{M}_\odot/c^3 = 4.925490947\ \mu$s and the masses are expressed in solar units.

Hence, in a PK framework, some of the equations seen before will have additional contributions. For example, the mean anomaly M is obtained by integrating the instantaneous orbital frequency $f_\mathrm{b}(t) = [P_\mathrm{b} + \dot{P}_\mathrm{b}\,(t-T_0)]^{-1}$ and Eq. (2.38) thus becomes:

$$M = \int_{T_0}^{t} f_\mathrm{b}(t)\,\mathrm{d}t = \frac{2\pi}{P_\mathrm{b}}(t-T_0)\ -\frac{\pi\dot{P}_\mathrm{b}}{P_\mathrm{b}^2}(t-T_0)^2\,. \tag{2.44}$$

Similarly, the longitude of periastron, ω_p, will also have a time-dependent contribution given by the rate of advance of periastron:

$$\omega_\mathrm{p}(t) = \omega_{\mathrm{p},0} + (t-T_0)\,\dot{\omega}\,, \tag{2.45}$$

where $\omega_{\mathrm{p},0} = \omega_\mathrm{p}(T_0)$.

As can be seen from Eqs. (2.43), the characteristic of the PK parameters (also valid in any boost-invariant theory of gravity) is that they only depend on the usual Keplerian parameters and on the masses of the pulsar and its companion. For this reason, it is possible to plot them in a graph with M_c versus M_p, also called *mass-mass diagram*. Each measured PK parameter will identify a line in the diagram that corresponds to a certain total mass $M_\mathrm{tot} = M_\mathrm{p} + M_\mathrm{c}$ and indicates all the possible combinations of values for M_p and M_c that add up to M_tot. Therefore, when measuring two PK parameters, the intersection of the two corresponding lines in the diagram will give a separate measure of the two masses M_p and M_c. Measuring three or

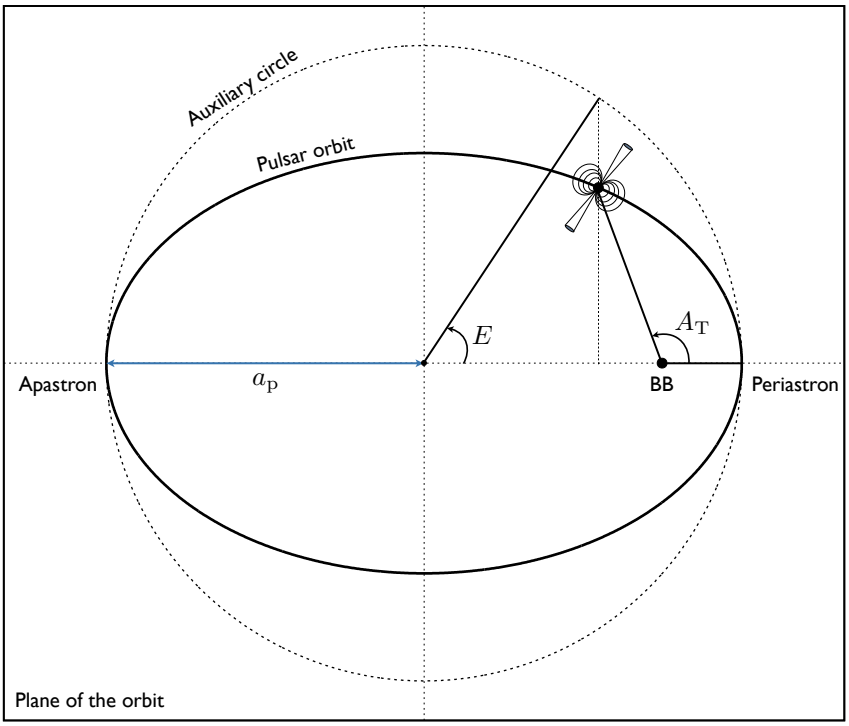

Figure 2.10. Definition of the true anomaly, A_T, and of the eccentric anomaly, E. The true anomaly is defined to be the angle between the vector connecting the BB to the periastron, and the vector connecting the BB to the pulsar. The eccentric anomaly is instead defined through the aid of an auxiliary circle of the same size as the orbital semi-major axis, a_p, onto which the pulsar position is projected.

more PK parameters will instead enable us to test theories of gravity: if the theory considered is correct, all the lines should intersect, within the uncertainties, at one specific point.

With the above discussion in mind, we are finally ready to describe the binary correction terms of Eq. (2.25) in detail:

Δ_R^{bin} It is the *orbital Rømer delay*. Very much like its Solar System equivalent term, it accounts for the difference between the arrival time at the BB and at the actual pulsar position. Its formal expression is (Damour & Taylor, 1992):

$$\Delta_R^{bin} = x_p \left[\cos E - e\,(1+\delta_r)\right] \sin\omega_p + x_p \sin E \sqrt{1-e^2(1+\delta_\Theta)^2}\,\cos\omega_p\,, \tag{2.46}$$

where δ_r and δ_Θ are another two PK parameters that represent relativistic deformations of the orbit (Lorimer & Kramer, 2004) and they vanish in the purely Keplerian case.

Δ_E^{bin} It is the *orbital Einstein delay*. It embodies the delay due to the gravitational redshift caused by the companion star's gravity and the time dilation associated with the coordinate transformation from the reference frame centered to the BB, to that co-moving with the pulsar along its orbit. The contribution can be written as (Lorimer & Kramer, 2004):

$$\Delta_E^{bin} = \gamma \sin E\,. \tag{2.47}$$

$\Delta_{\rm S}^{\rm bin}$ It is the *orbital Shapiro delay* and it accounts for the extra propagation time of the pulsar signal when passing through the curved space-time near the companion star. Its amplitude can be written as:

$$\Delta_{\rm S}^{\rm bin} = -2r \ln \left[1 - e \cos E - s \Big(\sin \omega_{\rm p} (\cos E - e) + \sqrt{1-e^2} \cos \omega_{\rm p} \sin E \Big) \right] . \quad (2.48)$$

Recalling that $s = \sin i$, we see that $\Delta_{\rm S}^{\rm bin}$ depends on the system inclination and on the considered orbital phase, peaking at the pulsar superior conjunction ($\Theta_{\rm p} = \omega_{\rm p} + A_{\rm T} = \pi/2$).

$\Delta_{\rm A}^{\rm bin}$ It is the *aberration* term. It accounts for the change in the direction of the observer, as seen from the pulsar, caused by the Lorentz boost associated with the coordinate transformation from the BB to the pulsar itself. The equation describing the delay is provided, e.g., by Damour & Deruelle (1986):

$$\Delta_{\rm A}^{\rm bin} = \mathcal{X} \Big[\sin(\omega_{\rm p} + A_{\rm T}) + e \sin \omega_{\rm p} \Big] + \mathcal{Y} \Big[\cos(\omega_{\rm p} + A_{\rm T}) + e \cos \omega_{\rm p} \Big] , \quad (2.49)$$

where $\mathcal{X}$ and $\mathcal{Y}$ are parameters that depend on the pulsar spin axis and on the size of the orbit (Edwards et al., 2006).

$\Delta_{\rm K}^{\rm bin}$ It is the so-called *Kopeikin* term and it includes three contributions, namely the change in the viewing angle of the binary due to the proper motion of the system (Kopeikin, 1996), the annual-orbital parallax and the orbital parallax (Kopeikin, 1995). However, it is generally much smaller than the other binary correction terms.

2.5.4 Fit and parameter estimation

For each observed topocentric ToA, once the timing formula (Eq. 2.25) has been used to derive the pulsar proper time of emission, $t_{\rm psr}$, the latter is plugged into Eq. (2.24) to calculate the associated rotation number or, equivalently, the associated rotational phase $\phi(t_{\rm psr})$. The observed phases are then compared against the theoretical values, $\phi^{\rm theo}$, predicted by the timing model, to form the so-called *timing residuals*, which are simply the differences between the two. A statistical estimator is then used to evaluate the goodness of the model in describing the data. The most commonly used estimator is the reduced chi-square, $\chi^2_{\rm red}$ (Taylor & Weisberg, 1989):

$$\chi^2_{\rm red} = \frac{1}{N_{\rm dof}} \sum_i \left(\frac{\phi(t_{{\rm psr},i}) - \phi_i^{\rm theo}}{\sigma_i} \right)^2 , \quad (2.50)$$

where σ_i is the uncertainty associated with the i-th ToA and $N_{\rm dof}$ is the number of degrees of freedom, which is the difference between the number of ToAs and the number of parameters fitted in the model. If the timing model is good enough to predict, on average, the correct rotational phases of the ToA within the uncertainties, we have $\chi^2_{\rm red} \sim 1$. The timing residuals will then be Gaussianly distributed around zero and will not show any kinds of correlation (panel a in Fig. 2.11) . On the contrary, if some effects are not correctly taken into account, or are even completely unmodelled, $\chi^2_{\rm red} > 1$ and the residuals will be highly correlated showing clear trends (panels b, c and d in Fig. 2.11). This often happens when extending the dataset

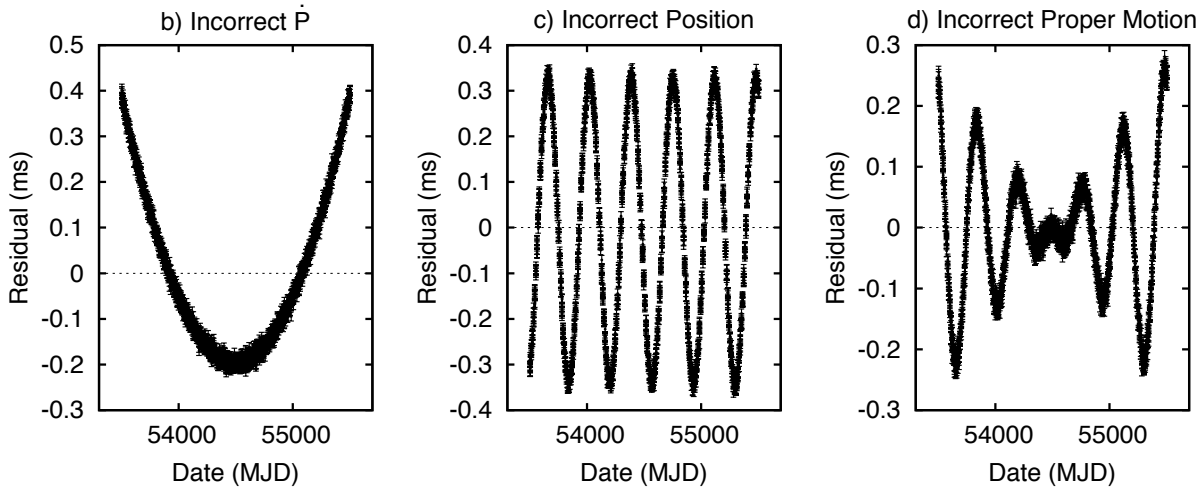

Figure 2.11. Signatures of simulated timing residuals in the case of: a) a good timing model; b) an incorrect spin period derivative; c) an incorrect position; d) an incorrect proper motion.

with newly taken data: as the number of ToAs increases and the time span lengthens, new effects may become apparent and the timing model used may need to be updated. Although the least-squares fit procedure is by far the most widely used technique in pulsar timing (e.g. Hobbs et al., 2006), it relies on several underlying assumptions that can very often be broken down. In particular, strong covariances and non-linearities in the parameters, as well as correlated sources of noise, have led to the development of more advanced techniques that make use of χ^2 mapping (e.g. Lazarus et al., 2014) or Bayesian parameter sampling algorithms (e.g. Lentati et al., 2014; Caballero et al., 2016).

The whole procedure of folding, ToA extraction and timing can be re-iterated several times on the same dataset in order to increase the quality of the ToAs themselves and thus optimize the resulting timing solution.

2.6 Polarimetry

In this section we will give an overview of the property of polarization of electromagnetic waves. Firstly, we will give the mathematical framework within which polarization is usually studied. Secondly, the RVM (introduced in Section 1.5.3) will be described in more detail. Lastly, we will briefly review the main methods used to correctly calibrate pulsar data. In this section, we follow the IAU/IEEE conventions (Hamaker & Bregman, 1996; van Straten et al., 2010) and Rybicki & Lightman (1979) as a reference unless otherwise stated.

2.6.1 Stokes parameters

Let us consider a monochromatic electromagnetic wave of frequency ν (wavelength $\lambda = c/\nu$), propagating along the z-direction of a Cartesian reference frame $(\mathbf{x}, \mathbf{y}, \mathbf{z})$ as shown in Fig. 2.12. The frame is chosen such that the $\mathbf{x}$ and $\mathbf{y}$ axes lie in the plane of the sky, with $\mathbf{x}$ pointing towards the North direction, $\mathbf{y}$ towards East, and $\mathbf{z}$ is directed towards the observer (i.e. it is parallel to the line of sight). The electric field $\mathbf{E}$ of the electromagnetic wave will thus oscillate

in the x-y plane and can therefore be decomposed into the two orthogonal components:

$$\mathbf{E}(z,t) = E_x(z,t)\cdot\hat{\mathbf{x}} + E_y(z,t)\cdot\hat{\mathbf{y}}\,. \tag{2.51}$$

Here $\hat{\mathbf{x}}$ and $\hat{\mathbf{y}}$ are the unit vectors along the x and y direction, respectively, and the components are:

$$\begin{cases} E_x(z,t) = E_{0,x}\cos(\omega t - kz - \varphi_x) \\ E_y(z,t) = E_{0,y}\cos(\omega t - kz - \varphi_y) \end{cases}, \tag{2.52}$$

where $\omega = 2\pi\nu$ is the wave angular frequency, $k = 2\pi/\lambda$ is the wavenumber, $E_{0,x}$ and $E_{0,y}$ are the constant amplitudes of the x and y electric field components, and $\Delta\varphi = \varphi_y - \varphi_x$ is the phase difference between the two components. Because in a monochromatic wave $\Delta\varphi$ is constant, it is easy to verify that Eq. (2.52) represents the parametric form of an ellipse in the x-y plane. The ellipse, as shown in Fig. 2.13, has a semi-major axis that is rotated by an angle ψ with respect to the x-axis and has an eccentricity $\mathcal{E}$ that is related to the angle ξ as $\tan\xi = \sqrt{1-\mathcal{E}^2}$. This is true if we impose the conditions:

$$\begin{aligned} E_{0,x}\cos\varphi_x &= \sqrt{E_{0,x}^2 + E_{0,y}^2}\cos\xi\cos\psi \\ E_{0,x}\sin\varphi_x &= \sqrt{E_{0,x}^2 + E_{0,y}^2}\sin\xi\sin\psi \\ E_{0,y}\cos\varphi_y &= \sqrt{E_{0,x}^2 + E_{0,y}^2}\cos\xi\sin\psi \\ E_{0,y}\sin\varphi_y &= -\sqrt{E_{0,x}^2 + E_{0,y}^2}\sin\xi\cos\psi \end{aligned}\,. \tag{2.53}$$

Fig. 2.14 shows the different possible polarization states of an electromagnetic wave. If, at a given point of the z-axis, the electric field describes an ellipse in the x-y plane as a function of time, the electromagnetic wave is said to be *elliptically polarized*. In the special case in which $\Delta\varphi = 0$ or $\Delta\varphi = \pi$, the ellipse degenerates into a line and the electric field will thus always oscillate along a single particular direction. In this case the radiation is said to be *linearly polarized*. The direction of oscillation is identified by the angle ψ in the x-y plane and it can be calculated as:

$$\psi = \arctan\left(\frac{E_y}{E_x}\right). \tag{2.54}$$

Another special case occurs if $E_{0,x} = E_{0,y}$ and $\Delta\varphi = \pm\pi/2$, when the ellipse reduces to a circumference. If $\Delta\varphi = -\pi/2$ the electric field rotates clockwise, as seen from the observer, and we have a *left-handed* circular polarization (LCP). Conversely, when $\Delta\varphi = +\pi/2$ the electric field rotates counter-clockwise, and we have a *right-handed* circular polarization (RCP).

The polarization state of an electromagnetic radiation is conveniently described by the so-called *Stokes parameters* (Stokes, 1851). These are four quantities, I, Q, U, V, defined as:

$$\begin{cases} I &= E_{0,x}^2 + E_{0,y}^2 &&= E_0^2 \\ Q &= E_{0,x}^2 - E_{0,y}^2 &&= E_0^2\cos(2\xi)\cos(2\psi) \\ U &= 2\,E_{0,x}E_{0,y}\cos\Delta\varphi &&= E_0^2\cos(2\xi)\sin(2\psi) \\ V &= 2\,E_{0,x}E_{0,y}\sin\Delta\varphi &&= -E_0^2\sin(2\xi) \end{cases}, \tag{2.55}$$

where $E_0 = \sqrt{E_{0,x}^2 + E_{0,y}^2}$ is the total amplitude of the electric field. While I is just the total intensity of the electric field, Q, U and V contain the full polarimetric information, as they are

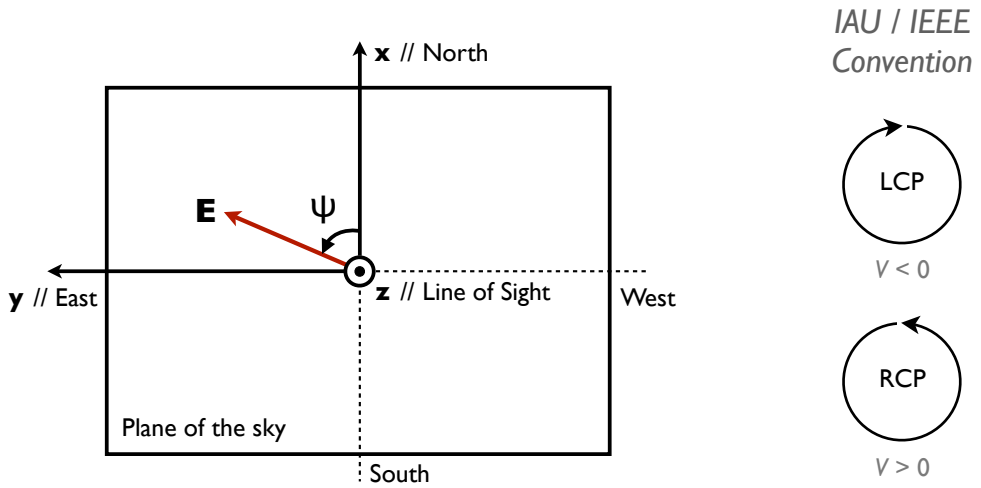

Figure 2.12. Definition of the linear polarization position angle, ψ on the plane of the sky and of the left- (LCP) and right-handed (RCP) circular polarization in the IAU/IEEE conventions.

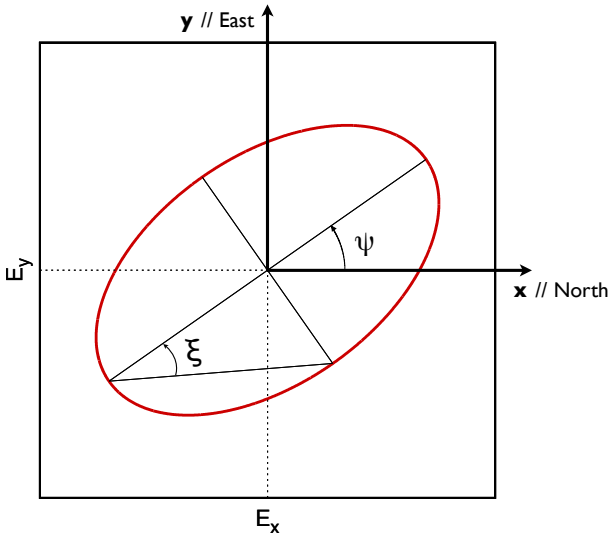

Figure 2.13. Polarization ellipse. The angle ξ determines the polarization state ($\xi = \pm 45$ deg for circularly polarized radiation, $\xi = 0$ deg for linearly polarized radiation), whereas the angle ψ, called *position angle* (or *linear polarization angle*, PA), determines the orientation of the polarization ellipse.

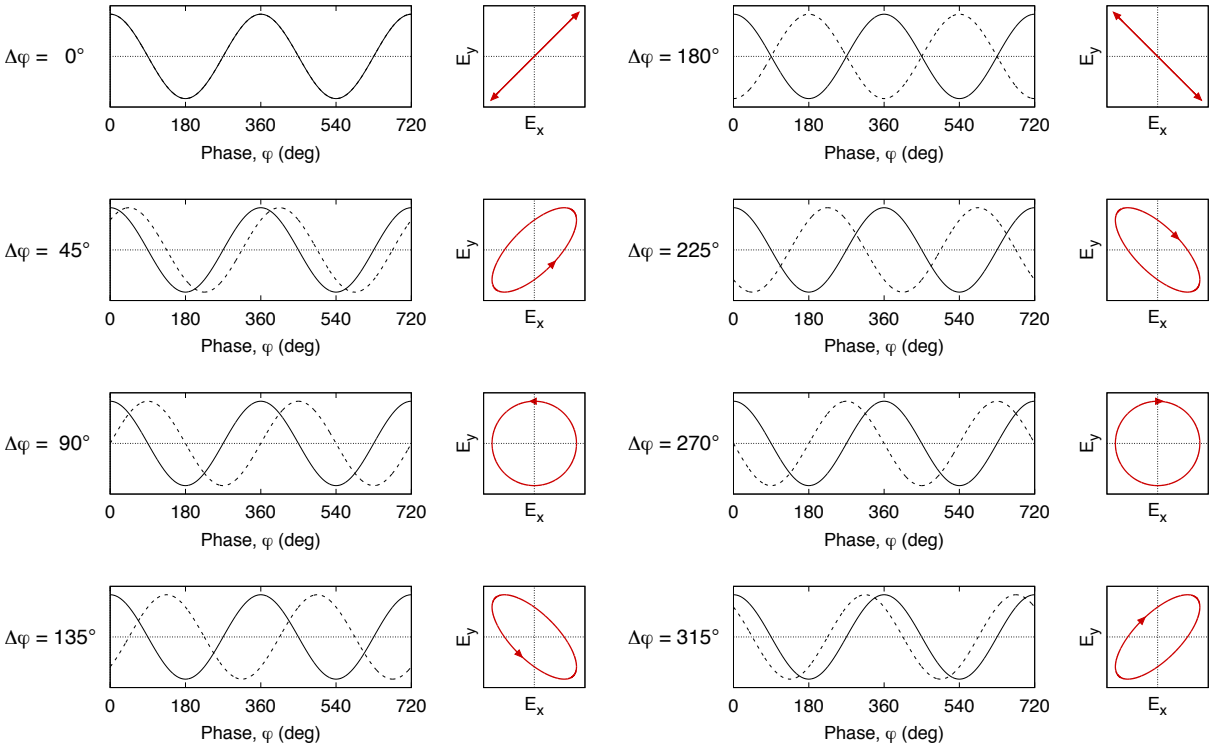

Figure 2.14. The different polarization states of light as a function of the phase shift $\Delta\varphi$ between the component along x (solid black line) and the component along y (dashed black line) of the electric field. The polarization state is linear for $\Delta\varphi = 0$ deg and $\Delta\varphi = 180$ deg, and it is circular for $\Delta\varphi = \pm 90$ deg. All the other values of $\Delta\varphi$ produce an elliptical polarization state.

functions of both amplitudes, $E_{0,x}$ and $E_{0,y}$, of the electric field components and of their phase difference, $\Delta\varphi$. Eqs. (2.55), where the quantities $\Delta\varphi$, $E_{0,x}$ and $E_{0,y}$ are all time-independent, are valid only for a monochromatic wave. The latter is, by definition, 100% polarized. However, in most of real cases, only a fraction $p < 1$ of the radiation is polarized. The Stokes parameters are thus better re-defined as time-averaged quantities:

$$\begin{cases} I &= \langle E_{0,x}^2 + E_{0,y}^2 \rangle &= \langle E_0^2 \rangle & \\ Q &= \langle E_{0,x}^2 - E_{0,y}^2 \rangle &= \langle E_0^2 \cos(2\xi)\cos(2\psi) \rangle &= Ip\cos(2\xi)\cos(2\psi) \\ U &= \langle 2\, E_{0,x} E_{0,y} \cos\Delta\varphi \rangle &= \langle E_0^2 \cos(2\xi)\sin(2\psi) \rangle &= Ip\cos(2\xi)\sin(2\psi) \\ V &= \langle 2\, E_{0,x} E_{0,y} \sin\Delta\varphi \rangle &= \langle -E_0^2 \sin(2\xi) \rangle &= -Ip\sin(2\xi) \end{cases} , \quad (2.56)$$

where $\langle\ \ \rangle$ is the time-average operator. The degree of polarization, p, is thus defined as:

$$p = \frac{\sqrt{Q^2 + U^2 + V^2}}{I} , \quad (2.57)$$

which is 0 for a completely unpolarized radiation, and 1 for a fully-polarized radiation.

For a fully circularly polarized wave, it can be easily seen that $Q = U = 0$, whereas $V = \pm 1$. On the other hand, for a fully linearly polarized radiation, $V = 0$, $I^2 = Q^2 + U^2$ and the

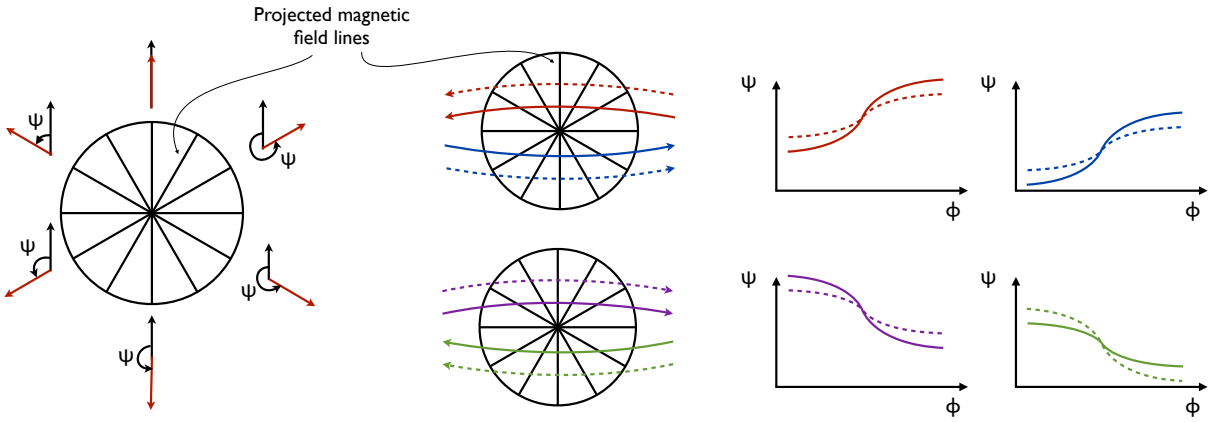

Figure 2.15. Illustration of the Rotating Vector Model (RVM). As the line of sight (coloured curved arrows) cuts the beam at different angular distances from the pulsar magnetic axis, the shape and offset of the linear polarization position angle curve will change accordingly.

previously introduced linear polarization angle (PA), ψ, only depends on Q and U, as:

$$\mathrm{PA} \equiv \psi = \frac{1}{2} \arctan\left(\frac{U}{Q}\right). \tag{2.58}$$

This shows that Q and U only contain information about the linearly polarized component of the electromagnetic wave, whereas V is only related to the circularly polarized component. It is therefore useful to define the *linearly polarized intensity* as:

$$L = \sqrt{Q^2 + U^2}. \tag{2.59}$$

Finally, the polarization of light can be studied within the framework of the Müller calculus (Müller, 1948). In this framework, Stokes parameters can be gathered and treated as a four-vector $\mathcal{S} = (I, Q, U, V)$ with the same mathematical properties of an *event* in relativistic space-time (Britton, 2000). For this reason, we can write $\mathcal{S} = (S_0, \vec{S})$, where $S_0 \equiv I$ is the equivalent of the time-coordinate and $\vec{S} \equiv (Q, U, V)$ is the equivalent of the vector with the spatial components in a Minkowski space-time. In a three-dimensional cartesian reference frame with axes (Q, U, V), the sphere of radius $|\vec{S}| = \sqrt{Q^2 + U^2 + V^2}$ is called *Poincaré sphere*. Each point on this sphere identifies a different polarization state.

Any physical process that can alter the polarization state $\mathcal{S}$, is represented by a 4×4 matrix $\mathbf{M}$ that acts on the Stokes four-vector, such that the new polarization state $\mathcal{S}'$ is given by the matrix product:

$$\mathcal{S}' = \mathbf{M} \cdot \mathcal{S}. \tag{2.60}$$

If, after applying $\mathbf{M}$, the polarization state changes, the three-dimensional vector $\vec{S}$ will move in the Poincaré sphere, which will expand if the polarized fraction increases, or will shrink in case of depolarization.

As we will discuss in Section 2.6.3, Müller calculus is the mathematical tool by which it is possible, among other things, to calibrate pulsar data.

2.6.2 Rotating Vector Model

Pulsars are usually highly polarized sources. In particular, very soon after their discovery, polarimetry measurements showed that, in a significant number of pulsars, the linear polarization angle ψ varies as a function of the rotational phase ϕ with a characteristic S-shaped trend. The explanation to this phenomenon was first given by Radhakrishnan & Cooke (1969), and further developed by Komesaroff (1970), with the so-called *Rotating Vector Model* (RVM). In this model, which assumes a perfectly dipolar pulsar magnetic field, the linear polarization angle corresponds to the direction of the projected magnetic field line in the sky (Fig. 2.15). As our line of sight crosses the beam during the NS rotation, we observe different field lines and thus ψ varies as:

$$\tan(\psi_0 - \psi) = \frac{\sin\alpha_\mathrm{m}\,\sin(\phi-\phi_0)}{\sin(\alpha_\mathrm{m}+\beta_\mathrm{m})\cos\alpha_\mathrm{m} - \cos(\alpha_\mathrm{m}+\beta_\mathrm{m})\,\sin\alpha_\mathrm{m}\,\cos(\phi-\phi_0)}\,. \tag{2.61}$$

Here α_m is the same magnetic inclination as defined in Section 1.3 and ϕ_0 is the rotational phase at which the observer's line of sight is at the smallest angular distance β_m (called *impact parameter*) from the pulsar magnetic axis. The rotational phase $\phi = \phi_0$ also corresponds to the inflection point in the linear polarization angle swing, where $\psi = \psi_0$ and the observer, the pulsar spin axis and the pulsar magnetic axis all lie in the same plane. By fitting Eq. (2.61) to the data, it is in principle possible to infer the orientation of the pulsar spin and magnetic axis (e.g. Everett & Weisberg, 2001). In practice, because ψ is measured only in the on-pulse region of a pulsar profile, α_m and β_m are rather poorly fitted in the majority of cases because of the small pulse duty cycle and, hence, of the small range of ϕ used. In this regard, the presence of an interpulse (which is typically separated by ~ 180 deg from the main pulse) with measurable linear polarization would greatly increase the range of pulse longitudes with a measured value of ψ, which would in in turn significantly help to constrain the fitted model and, hence, the values of the RVM parameters.

Notwithstanding, it is very common to have polarization angle swings that do not follow the prediction of the RVM (e.g. Xilouris et al., 1998; Johnston & Weisberg, 2006; Johnston et al., 2008). In particular, the ψ-curves are often "broken" by abrupt jumps, which in most cases are about 90 deg in magnitude (Backer et al., 1976). Such jumps are thought to be generated by two orthogonal emission states called *Orthogonal Polarized Modes* (OPMs, Manchester et al. 1975).

2.6.3 Polarization calibration

The data recorded by the telescope back-end do not contain the *intrinsic* polarization properties of the observed pulsar. This is because the incoming radiation is modified by a number of effects. These include the Faraday rotation and a series of other effects that occur in the hardware chains, from the signal reception to the data output. Ignoring for the moment the Faraday rotation, the measured Stokes vector $\mathcal{S}_\mathrm{obs}$ of the pulsar can be written as:

$$\mathcal{S}_\mathrm{obs} = \mathbf{M}_\mathrm{tot}\cdot\mathcal{S}_\mathrm{in}\,, \tag{2.62}$$

where $\mathcal{S}_\mathrm{in}$ is the intrinsic Stokes vector of the pulsar and $\mathbf{M}_\mathrm{tot}$ is the Müller matrix that accounts for the effects of the hardware chains. $\mathbf{M}_\mathrm{tot}$ can in turn be expressed as the product of four matrices, each accounting for a different effect (e.g. Heiles et al., 2001; Lorimer & Kramer, 2004):

$$\mathbf{M}_\mathrm{tot} = \mathbf{M}_\mathrm{Amp}\cdot\mathbf{M}_\mathrm{CC}\cdot\mathbf{M}_\mathrm{Feed}\cdot\mathbf{M}_\Pi\,, \tag{2.63}$$

where, because of the non-commutative nature of the matrix product, the order is important. The four matrices involved are:

$\mathbf{M}_{\Pi}$ It accounts for the change in the *parallactic angle* (Π), which is defined as the angle between the great circle passing through the source and the Zenith and the great circle passing through the source and the celestial poles. The parallactic angle changes as a function of the source position in the observatory sky and can be calculated via the simple formula (Lorimer & Kramer, 2004):

$$\Pi = \arctan\left(\frac{\sin \mathrm{HA}\cos l_{\oplus}}{\sin l_{\oplus}\cos\delta - \cos l_{\oplus}\sin\delta\cos \mathrm{HA}}\right), \tag{2.64}$$

where HA is the source Hour Angle, $l_{\oplus}$ is the latitude of the observatory on the Earth and δ is the source declination. In modern radio telescopes with alt-azimuthal mounts, this causes an apparent rotation of the source with respect to the telescope feed, by an angle Π, as the source is being tracked. The effect on the Stokes parameters is described by the matrix (Heiles et al., 2001; Lorimer & Kramer, 2004):

$$\mathbf{M}_{\Pi} = \begin{pmatrix} 1 & 0 & 0 & 0 \\ 0 & \cos 2\Pi & \sin 2\Pi & 0 \\ 0 & -\sin 2\Pi & \cos 2\Pi & 0 \\ 0 & 0 & 0 & 1 \end{pmatrix}, \tag{2.65}$$

which represents a rotation in the Poincaré space about the V-axis by an angle 2Π, resulting in a mixing between the Q and the U components and, hence, in a rotation in the observed linear polarization angle, ψ.

$\mathbf{M}_{\mathrm{Feed}}$ It describes the geometry of the telescope feed in the ideal case, and corresponds to the basis used to represent the incoming electric field. Currently, the vast majority of radio telescope receivers have either two orthogonal linear or circular receptors, although elliptical receptors can in principle also be used. The matrix describing the feed geometry is (Heiles et al., 2001; Lorimer & Kramer, 2004):

$$\mathbf{M}_{\mathrm{Feed}} = \begin{pmatrix} 1 & 0 & 0 & 0 \\ 0 & \cos 2\Upsilon & 0 & \sin 2\Upsilon \\ 0 & 0 & 1 & 0 \\ 0 & -\sin 2\Upsilon & 0 & \cos 2\Upsilon \end{pmatrix}. \tag{2.66}$$

For a feed that samples the two orthogonal linear polarizations of the incoming signal (*dual linear feed*), $\Upsilon = 0$ deg and thus $\mathbf{M}_{\mathrm{Feed}} = \mathbb{1}$, where $\mathbb{1}$ is the identity matrix. For a feed that samples the two orthogonal circular polarizations (*dual circular feed*), $\Upsilon = 45$ deg. All the other values of Υ, instead, represent possible dual elliptical configurations.

$\mathbf{M}_{\mathrm{CC}}$ While $\mathbf{M}_{\mathrm{Feed}}$ describes the geometry of an ideal feed, $\mathbf{M}_{\mathrm{CC}}$ accounts for possible imperfections that cause cross-coupling effects, i.e. the unwanted spillover of power from one receptor to the other. This can be due, for instance, to electric power leakage

or imperfections in mounting the two receptors, which may not be perfectly orthogonal (Heiles et al., 2001). If the imperfections are small, the associated matrix is, to the first order:

$$\mathbf{M}_{\mathrm{CC}} = \begin{pmatrix} 1 & 0 & A & B \\ 0 & 1 & C & D \\ A & -C & 1 & 0 \\ B & -D & 0 & 1 \end{pmatrix}, \tag{2.67}$$

where A, B, C, D are defined as:

$$\begin{cases} A &= \epsilon_0 \cos\phi_0 + \epsilon_1 \cos\phi_1 \\ B &= \epsilon_0 \sin\phi_0 + \epsilon_1 \sin\phi_1 \\ C &= \epsilon_0 \cos\phi_0 - \epsilon_1 \cos\phi_1 \\ D &= \epsilon_0 \sin\phi_0 - \epsilon_1 \sin\phi_1 \end{cases}. \tag{2.68}$$

The quantities ϵ_0 and ϵ_1 are the amplitudes (also called *ellipticities*) of the cross-coupling of the two receptors, whereas ϕ_0 and ϕ_1 are the relative phases.

$\mathbf{M}_{\mathrm{Amp}}$ It accounts for the *differential gain* and the *differential phase* between the signals of the two receptors (Fig. 2.16). The former arises from the different amplification chains associated with the two receptors. The latter, instead, is mostly due to the different lengths l_0 and l_1 of the cables carrying the two polarization signals; to the first order, this causes a relative phase delay $\delta_\phi = 2\pi c\nu(l_1 - l_0)$, which is thus linearly proportional to the signal frequency ν. The matrix describing both effects, in the approximation that the differential gain δ_Γ is small, is (Heiles et al., 2001):

$$\mathbf{M}_{\mathrm{Amp}} = \begin{pmatrix} 1 & \delta_\Gamma/2 & 0 & 0 \\ \delta_\Gamma/2 & 1 & 0 & 0 \\ 0 & 0 & \cos\delta_\phi & -\sin\delta_\phi \\ 0 & 0 & \sin\delta_\phi & \cos\delta_\phi \end{pmatrix}. \tag{2.69}$$

Calibrating pulsar data in polarization means determining all the six unknown parameters (δ_Γ, δ_ϕ, ϵ_0, ϵ_1, ϕ_0, ϕ_1) of the $\mathbf{M}_{\mathrm{tot}}$ matrix. These parameters (optionally together with the absolute gain Γ, necessary if we want to calibrate also in flux) represent the full *reception model* of the system (Table 2.2). After the latter is determined, the intrinsic Stokes parameters of the pulsar can be derived by inverting $\mathbf{M}_{\mathrm{tot}}$ and applying it to the observed Stokes four-vector:

$$\mathcal{S}_{\mathrm{in}} = (\mathbf{M}_{\mathrm{tot}})^{-1}\, \mathcal{S}_{\mathrm{obs}}\,. \tag{2.70}$$

The accurate polarization calibration is of great importance not only because it is necessary to correctly interpret the data in polarimetric studies of pulsars, but also because it can actually improve the precision of pulsar timing (van Straten, 2006). Indeed, by looking at Eq. (2.65)-(2.69) it can be seen that some effects can also have an impact on the Stokes parameter I, which represents the total intensity profile of the pulsar, typically used for generating the ToAs. If not properly calibrated, data of highly polarized pulsars can be affected by distortions in the pulse profile shape that can easily translate into systematic timing errors as a function of the

parallactic angle (Britton, 2000).

In the following sections, we will review the main techniques used for calibrating the polarization in astronomical pulsar data.

2.6.3.1 NDO: Noise-Diode only

The most basic way to perform polarization calibration involves the use of an artificial signal that is generated by a device (often called *noise-diode*, sometimes also *cal-probe*) and injected directly into the two receiver receptors (e.g. Lorimer & Kramer, 2004). The noise-diode is usually designed to produce a signal that is 100% linearly polarized and that illuminates both receptors equally (Fig. 2.16). In the case of a dual linear feed ($\mathbf{M}_{\rm Feed} = \mathbb{1}$), this means that the signal has a position angle of 45 deg, and hence its polarization state is represented by the Stokes vector:

$$\mathcal{S}_{\rm cal} = \begin{pmatrix} I_{\rm cal} \\ 0 \\ I_{\rm cal} \\ 0 \end{pmatrix} , \tag{2.71}$$

where $I_{\rm cal}$ is the intensity of the noise-diode signal. However, because of the differential gain and phase of the response of the two receptors, the observed Stokes vector will be:

$$\mathcal{S}_{\rm obs} = \mathbf{M}_{\rm Amp} \cdot \mathcal{S}_{\rm cal} , \tag{2.72}$$

where the cross-coupling effects have been neglected and the parallactic angle effect is not present since the signal is not astronomical ($\mathbf{M}_{\rm CC} = \mathbf{M}_{\Pi} = \mathbb{1}$). Explicitly:

$$\begin{pmatrix} I_{\rm obs} \\ U_{\rm obs} \\ Q_{\rm obs} \\ V_{\rm obs} \end{pmatrix} = \begin{pmatrix} 1 & \delta_\Gamma/2 & 0 & 0 \\ \delta_\Gamma/2 & 1 & 0 & 0 \\ 0 & 0 & \cos\delta_\phi & -\sin\delta_\phi \\ 0 & 0 & \sin\delta_\phi & \cos\delta_\phi \end{pmatrix} \begin{pmatrix} I_{\rm cal} \\ 0 \\ I_{\rm cal} \\ 0 \end{pmatrix} \Rightarrow \begin{cases} I_{\rm obs} = I_{\rm cal} \\ U_{\rm obs} = \dfrac{\delta_\Gamma}{2} I_{\rm cal} \\ Q_{\rm obs} = I_{\rm cal} \cos\delta_\phi \\ V_{\rm obs} = I_{\rm cal} \sin\delta_\phi \end{cases} . \tag{2.73}$$

This is a system of four linear equations in the three unknowns, $I_{\rm cal}$, δ_ϕ and δ_Γ, that, once solved, relates the differential gain and phase to the observed parameters:

$$\begin{cases} \delta_\phi = \arctan\left(\dfrac{V_{\rm obs}}{Q_{\rm obs}}\right) \\ \\ \delta_\Gamma = \dfrac{2U_{\rm obs}}{I_{\rm obs}} \end{cases} . \tag{2.74}$$

As previously stated, the above treatment is valid in the ideal case in which the noise-diode signal is 100% linearly polarized at 45 deg, which hardly ever corresponds to a real case. In reality, the noise-diode signal is not fully polarized and it is likely illuminating the two receptors not equally. If the two assumptions are relaxed, the noise-diode input Stokes vector can be

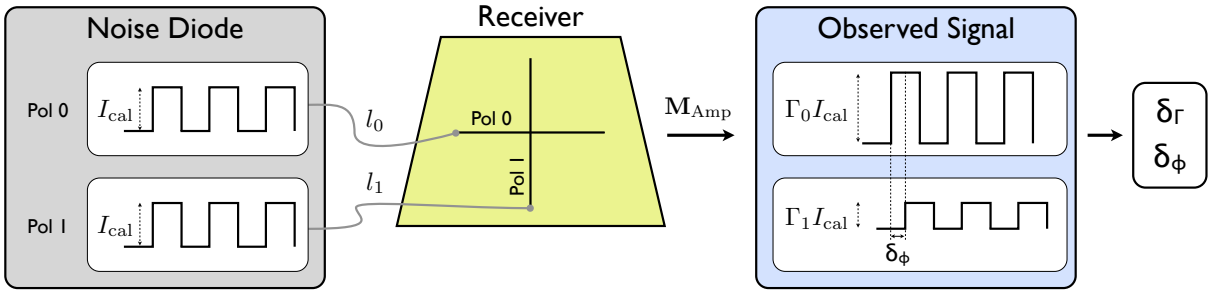

Figure 2.16. Scheme of the procedure used in the NDO polarization calibration method. An artificial square wave, 100% linearly polarized, illuminates the two receptors equally. By measuring the output signal it is then possible to determine the differential gain, δ_Γ, and the differential phase δ_ϕ of the two receptors. See Section 2.6.3.1 for details.

written as:

$$\mathcal{S}_{\rm cal} = \begin{pmatrix} I_{\rm cal} \\ Q_{\rm cal} \\ U_{\rm cal} \\ 0 \end{pmatrix} , \tag{2.75}$$

where it is still assumed that the signal is injected in-phase into both receptors and thus $V_{\rm cal} = 0$. In this case, Eq. (2.73) becomes:

$$\begin{pmatrix} I_{\rm obs} \\ U_{\rm obs} \\ Q_{\rm obs} \\ V_{\rm obs} \end{pmatrix} = \begin{pmatrix} 1 & \delta_\Gamma/2 & 0 & 0 \\ \delta_\Gamma/2 & 1 & 0 & 0 \\ 0 & 0 & \cos\delta_\phi & -\sin\delta_\phi \\ 0 & 0 & \sin\delta_\phi & \cos\delta_\phi \end{pmatrix} \begin{pmatrix} I_{\rm cal} \\ Q_{\rm cal} \\ U_{\rm cal} \\ 0 \end{pmatrix} \Rightarrow \begin{cases} I_{\rm obs} = I_{\rm cal} + \dfrac{\delta_\Gamma}{2} Q_{\rm cal} \\ U_{\rm obs} = \dfrac{\delta_\Gamma}{2} I_{\rm cal} + Q_{\rm cal} \\ Q_{\rm obs} = U_{\rm cal} \cos\delta_\phi \\ V_{\rm obs} = I_{\rm cal} \sin\delta_\phi \end{cases} . \tag{2.76}$$

This is a system of four equations in the five unknowns $I_{\rm cal}$, $Q_{\rm cal}$, $U_{\rm cal}$, δ_Γ, δ_ϕ. The way to solve it is by obtaining an independent measure of $I_{\rm cal}$ through the observation of a source of known flux, typically a quasar (Lorimer & Kramer, 2004). This procedure allows us to remove an unknown in Eq. (2.75), and thus to solve the system of equations.

2.6.3.2 MEM: Measurement Equation Modelling

Because it takes only a few seconds to observe the noise-diode signal, and possibly a few extra minutes to observe a flux calibrator, the NDO method described above is very straightforward and easy to carry out. However, it is limited by the fact that it does not account for the possible feed cross-coupling, which can be very important for high-precision polarimetry studies.

One way to overcome this limitation is to use the *Measurement Equation Modelling* (MEM) method, described in van Straten (2004) and shown schematically in Fig. 2.17. In addition to the noise-diode signal, the MEM method requires the observation of a strongly polarized pulsar over a wide range of parallactic angles, as well as of a (possibly unpolarized) source with a well-determined degree of circular polarization (e.g. a quasar). If the pulsar is observed at N_Π different parallactic angles and, for each pointing, there is a measurement of the pulsar polarization at N_ϕ different pulse longitudes, then we end up with a system of equations that

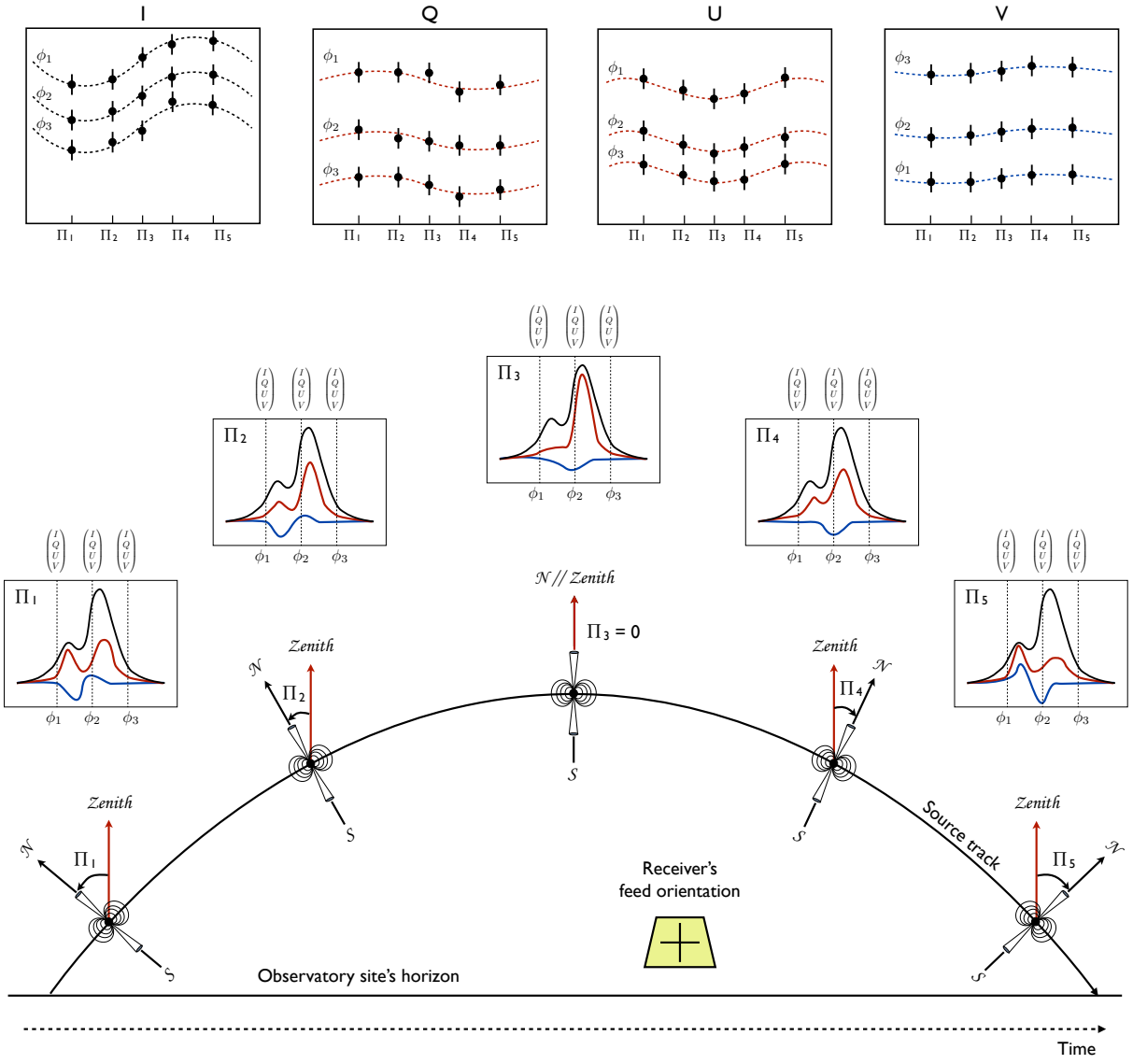

Figure 2.17. Schematic representation of the MEM polarization calibration method. See text for the details.

can be written as:

$$\begin{cases} \mathcal{S}^{\bullet}_{\mathrm{obs},\,k}(\Pi_j) = \mathbf{M}_{\mathrm{tot}}(\Gamma, \delta_\Gamma, \delta_\phi, \epsilon_0, \epsilon_1, \theta_0, \theta_1;\, \Pi_j) \cdot \mathcal{S}^{\bullet}_{\mathrm{in},\,k}(\Pi_j) \qquad \text{with} \quad \begin{matrix} k = 1, \ldots, N_\phi \\ j = 1, \ldots, N_\Pi \end{matrix} \\ \mathcal{S}^{\mathrm{cal}}_{\mathrm{obs}} = \mathbf{M}_{\mathrm{Amp}}(\Gamma, \delta_\Gamma, \delta_\phi) \cdot \mathbf{M}_{\mathrm{CC}}(\epsilon_0, \epsilon_1, \theta_0, \theta_1) \cdot \mathcal{S}^{\mathrm{cal}}_{\mathrm{in}} \\ \mathcal{S}^{*}_{\mathrm{obs}} = \mathbf{M}_{\mathrm{tot}}(\Gamma^*, \delta^*_\Gamma, \delta^*_\phi, \epsilon^*_0, \epsilon^*_1, \theta^*_0, \theta^*_1;\, \Pi_j) \cdot \mathcal{S}^{*}_{\mathrm{in}} \end{cases} . \tag{2.77}$$

Here $\mathcal{S}^{\bullet}_{\mathrm{obs},\,k}$ and $\mathcal{S}^{\bullet}_{\mathrm{in},\,k}$ are the observed and intrinsic Stokes four-vectors of the k-th pulse longitude of the pulsar, respectively, whereas $\mathcal{S}^{*}_{\mathrm{obs}}$ and $\mathcal{S}^{*}_{\mathrm{in}}$ are the observed and intrinsic Stokes four-vectors of the quasar, respectively. The dependence of the Müller matrices on the seven parameters of the full reception model (Table 2.2) have been made explicit.

We point out that the reception model parameters describing the quasar observation (marked with the asterisk in their superscripts) are in general different from those of the pulsar and noise-diode observations (with no superscripts). The reason is that, when switching between the quasar and the pulsar, the system attenuation levels can be changed, because of the large difference in the fluxes of the two sources. Eq. (2.77) is thus a system of $4 + 4 + 4\,N_\phi\,N_\Pi$ equations and $14 + 4 + 4 + 4\,N_\phi$ unknowns, and it is thus usually overdetermined. The determination of the 14 parameters can then be achieved via a least-square fitting algorithm (van Straten, 2004).

It is important to note that, if the absolute orientation of the pulsar in the sky is not known, it is not possible to measure the absolute orientations of the receptors, θ_0 and θ_1, but only their relative orientation. All the position angles will be thus measured with respect to the direction of one of the receptors.

2.6.3.3 METM: Measurement Equation Template Matching

The MEM method is undoubtedly the most complete and accurate way to characterize the observing system response and, hence, to calibrate the data. However, it is very time consuming, since it requires to observe a test pulsar along a large portion of its track in the sky. Hence, it is usually not possible to apply the MEM method with a high cadence.

A good compromise between calibration accuracy and time cost is represented by the *Measurement Equation Template Matching* (METM) method, proposed by Athanasiadis et al. (2003) and van Straten (2013). Apart from the noise-diode signal, the METM method requires at least one uncalibrated observation of a highly polarized reference pulsar (good candidates are PSR B1937+21 and PSR B1929+10) and a well-calibrated observation of the same pulsar[10], that will be regarded as a *template*. Given N_{obs} observations of the reference pulsar, the system of equations to solve is:

[10]The well-calibrated observation of the reference pulsar could have been obtained, for instance, with the MEM method at a preceding epoch.

Table 2.2. Parameters involved in a complete calibration, in polarization and flux, of the data.

Parameter	Symbol	Units	Matrix	Value for ideal linear feed	Model
Absolute Gain	Γ	-	$\mathbf{M}_{\rm Amp}$	N/A	{NDO, MEM, METM} + Flux
Differential Gain	δ_Γ	-	$\mathbf{M}_{\rm Amp}$	0	NDO, MEM, METM
Differential Phase	δ_ϕ	deg	$\mathbf{M}_{\rm Amp}$	0	NDO, MEM, METM
Ellipticity of receptor 0	ϵ_0	deg	$\mathbf{M}_{\rm CC}$	0	MEM, METM
Ellipticity of receptor 1	ϵ_1	deg	$\mathbf{M}_{\rm CC}$	0	MEM, METM
Orientation of receptor 0	θ_0	deg	$\mathbf{M}_{\rm CC}$	0	MEM, METM
Orientation of receptor 1	θ_1	deg	$\mathbf{M}_{\rm CC}$	0	MEM, METM

$$\begin{cases} \mathcal{S}^{\bullet}_{{\rm obs},\,k}(\Pi_n) = \mathbf{M}_{\rm tot}(\Gamma, \delta_\Gamma, \delta_\phi, \epsilon_0, \epsilon_1, \theta_0, \theta_1;\, \Pi_n) \cdot \mathcal{S}^{\bullet}_{{\rm template},k} \qquad \text{with} \quad \begin{matrix} k = 1, \ldots, N_\phi \\ n = 1, \ldots, N_{\rm obs} \end{matrix} \\ \\ \mathcal{S}^{\rm cal}_{\rm obs} = \mathbf{M}_{\rm Amp}(\Gamma, \delta_\Gamma, \delta_\phi) \cdot \mathbf{M}_{\rm CC}(\epsilon_0, \epsilon_1, \theta_0, \theta_1) \cdot \mathcal{S}^{\rm cal}_{\rm in} \end{cases} \tag{2.78}$$

where $\mathcal{S}^{\bullet}_{{\rm template},k}$ is the *known* Stokes four-vector of the k-th pulse longitude of the reference pulsar template observation and all the other variables have the same meaning as for Eq. (2.77). The METM technique finds the best instrumental response parameters such that each observation of the reference pulsar can match the template through the application of the inverse of $\mathbf{M}_{\rm tot}$. Similarly to the case of MEM, this is achieved through a least-square fitting algorithm.

2.6.4 RM measurement and correction for Faraday effect

Even after a proper correction for the instrumental response, the polarization properties of a pulsar are often not directly visible in the data. The main reason for this is the Faraday rotation effect. As explained in Section 2.2.2, a non-zero RM causes a rotation of the linear polarization angle ψ as a function of the radiation frequency. Hence, if not properly taken into account, the effect will lead to the so-called *bandwidth depolarization*: because every frequency channel has a different value of ψ, the linear polarization will appear severely reduced, when summing all the channels incoherently (Fig. 2.18).

The solution is thus to obtain a measurement of the RM and then apply an adequate counter-rotation to each frequency channel, according to Eq. (2.12), before summing all the frequency channels. Several methods have been developed to estimate the RM in pulsar data. One straightforward way is to do a brute-force search for the value of the RM, and look for the value that maximizes the intensity of the linear polarization of the pulsar. Another way is to fit the observed ψ as a function of frequency for Eq. (2.12).

After these steps, the data will be finally containing the real intrinsic polarimetric properties of the pulsar, which can thus be used for further scientific investigations.

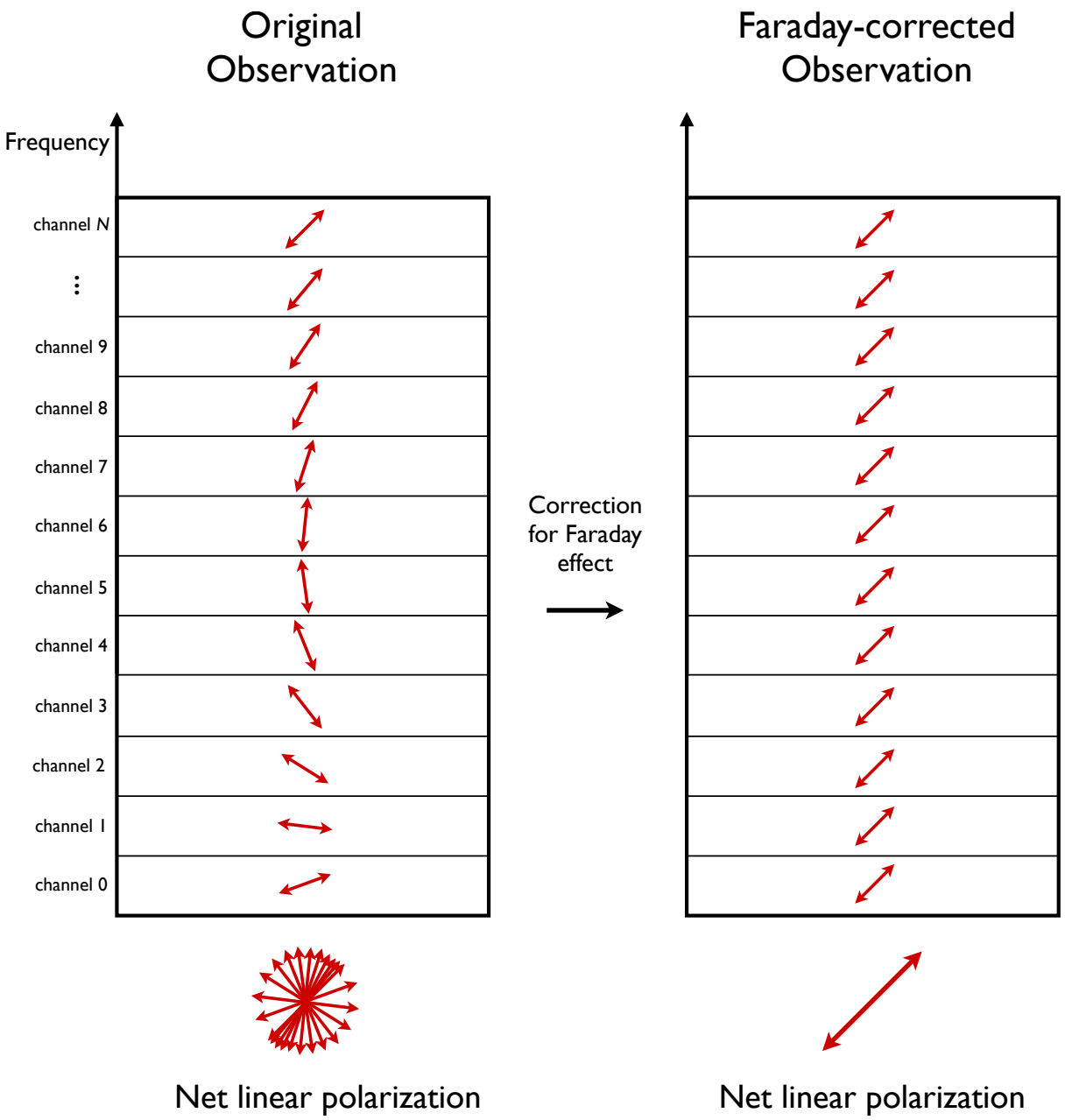

Figure 2.18. Left: effect of the Faraday rotation on the linear polarization (red double-headed arrows). The angle of the linear polarization is different for each channel across the observing band. As a result, when summing all the channels together, the linear polarization will be added incoherently, resulting in depolarization. Right: after correcting for the Faraday effect according to the measured RM, the linear polarization will be coherent across the whole band and it will thus be retained when adding the channels together.

Chapter 3

Pulsars in Globular Clusters

Contents

3.1 Introduction

Of the total currently known pulsar population, a non-negligible fraction is known to be hosted by globular clusters (GCs). Pulsars in globular clusters show striking differences when compared to the population of the Galaxy, mainly due to the very peculiar characteristics of their surrounding environment. In this chapter, we give an overview of the science of pulsars in GCs.

In Section 3.2 we introduce globular clusters, discussing their physical characteristics and origin.

In Section 3.3 we analyze the currently known population of pulsars in globular clusters, highlighting its peculiar properties and differences with respect to that of the Galaxy.

In Section 3.4 we review the most important scientific applications for which pulsars in globular clusters are particularly suitable.

3.2 Globular clusters

Globular clusters are self-gravitating groups of $10^4 - 10^6$ stars, confined in a volume of a few pc across, that orbit the bulge of a host galaxy, exactly like a satellite.

GCs exhibit extremely high stellar densities. In their cores, these can reach $10^2 - 10^6$ stars per cubic parsec, thus exceeding those of the Galactic field by several orders of magnitude.

The first discovery of a GC in our Galaxy dates back to 1665, when the German astronomer Abraham Ihle observed what would later be referred to as the M22 cluster. Due to the limited sizes of the telescopes available at that time, the number of clusters known slowly increased to 34 over the next century or so. A major advance was made in 1782 by William Herschel who, using telescopes with larger apertures, began an extensive survey that led to the discovery of 36 new clusters. In 1789, he also coined the term *globular cluster*, which he used to refer to these objects in his second *"Catalogue of a Second Thousand New Nebulae and Clusters of Stars"*. As of 2010, according to the Harris Catalogue[1] (Harris, 1996), we know 157 GCs in the Milky

[1] http://physwww.physics.mcmaster.ca/~harris/mwgc.dat

Way, while another few tens are very likely to be present but invisible because of obscuration by Galactic dust. The number of GCs in other galaxies can greatly differ from that of the Milky Way and it seems to be higher in giant elliptical galaxies. For instance, the cD-type M87 supergiant elliptical galaxy is estimated to be populated by $\gtrsim 10000$ GCs (Tamura et al., 2006; Harris, 2009).

The way GCs form is still rather poorly understood and is thus object of debate. Over the last decades, several theories have been proposed, and they are commonly divided into three main categories: *primary*, *secondary* and *tertiary*. The difference is in the fact that they hypothesize that GCs formed *before*, *together with* and *after* the formation of their host galaxy, respectively (Fall & Rees, 1988).

Although the actual formation process is still a mystery, observations show that the Milky Way GCs are certainly among the oldest stellar systems in the Universe, with ages of the order of a few billion years, i.e. as old or older than the Galaxy. The first evidence for this is that there is no sign of active star formation in any known cluster. Secondly, all the stars that belong to a specific cluster show very similar chemical composition, in particular in their iron content (Gratton et al., 2004); hence, all the stars must have formed together. Lastly, all GCs are constituted by population-II stars, which contain a very small fraction of elements heavier than helium (i.e. they have a low metallicity).

The primary way to study the stellar population of a GC is the *Colour-Magnitude Diagram* (CMD, also known as *Hertzsprung-Russell Diagram*) which, in most of Galactic GCs, shows very distinctive features (see Fig. 3.1). In particular we can always distinguish:

- The *main-sequence* (MS) branch, where all the low-mass stars that are still in the hydrogen-burning stage of their life are located. In GCs, the MS branch is interrupted at the so-called *main-sequence turn-off point* where it bends and joins the *red giant* (RG) branch. This is a clear sign of the fact that all the stars in the cluster have roughly the same composition and age, and the only difference is their birth mass.
- The *red giant branch* (RG), where are found the stars that have left the main sequence phase, and have thus expanded in size and become cooler.
- The *horizontal branch* (HB), namely a group of stars that, after passing through a giant phase, have ignited helium fusion in their hot and dense cores. A subclass of HB stars is represented by the *RR Lyrae*, which are stars that undergo periodic radial oscillations and hence show a variable luminosity.
- The *blue stragglers* (BS). These are stars that are more luminous and bluer than the stars at the turn-off point, thus they appear to the left of the latter. For this reason, if they were born together with all the other stars of the clusters, they seem to violate the standard stellar evolutionary models. To explain their characteristics, astronomers hypothesized that they may be the result of mass transfer, merger, or even collision of binaries (e.g. Knigge et al., 2009; Perets & Fabrycky, 2009; Ferraro et al., 2015), which may in turn have allowed them not to evolve off the main sequence yet.
- The *white dwarf* (WD) island. Here we can find all those stars that were born massive enough to evolve quickly, such that they have already stopped their fusion processes and have become WDs.

The interpretation of the peculiar shape of the CMD of GCs is that the more massive stars have already exhausted the hydrogen in their cores, and thus they have already left the main

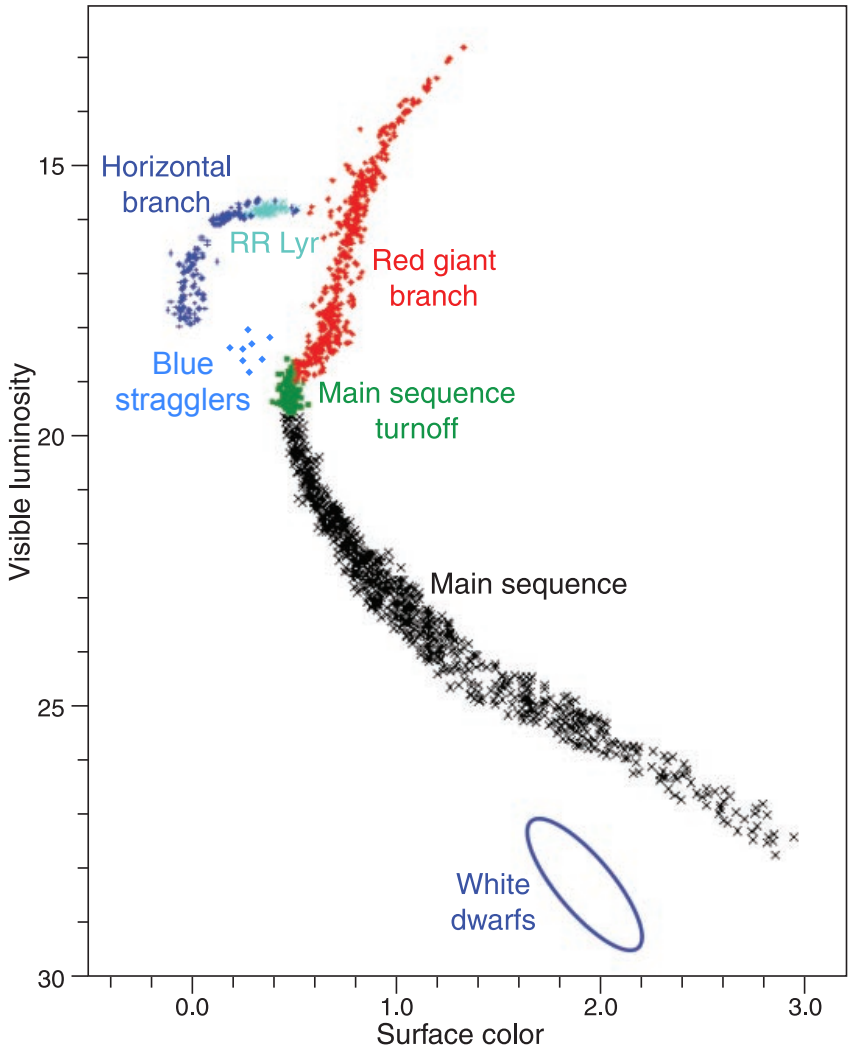

Figure 3.1. Scheme of the typical Colour-Magnitude Diagram of a GC. Figure adapted from Krauss & Chaboyer (2003).

sequence and migrated towards the RG branch. Since we have very precise models for the evolution of a MS star, the turn-off point can hence be used to measure the age of the GC: the older the cluster, the more stars will have had time to evolve and leave the MS branch, and thus the position of the turn-off point will have moved down, towards stars of lower mass and later spectral type.

Although not directly detectable at visible wavelengths and thus not present in the CMD, GCs are also populated by a number of NSs and stellar-mass black holes (SMBHs), which resulted from the explosion of the most massive born MS stars. As we shall see, NSs and BHs have a central role in the dynamical evolution of a GC.

3.2.1 Static models

A globular cluster can be studied, to a very good approximation, as a self-gravitating spherically-symmetric N-body system. In other words, it can be treated as a classical collisional gas with

the stars acting like the gas particles.

The structure of a GC is conveniently described by means of three characteristic radii that are related to its physical parameters. Following Spitzer (1987), these are:

- The *core radius*, $r_{\rm core}$, defined as the distance from the core at which the cluster surface brightness is half of its central value.
- The *half-mass radius*, $r_{\rm hm}$, defined as the radius within which half of the mass of the cluster is contained.
- The *tidal radius*, $r_{\rm tid}$, defined as the radius beyond which the gravitational pull of the host galaxy becomes higher than that of the cluster itself. A star located at a distance $r > r_{\rm tid}$ would thus be ripped off from the cluster.

.

Propaedeutic to the study of the dynamical evolution of a GC is the derivation of a static model, in which the cluster main physical properties (such as the density) remain constant over time and which provides a zero-order solution for the equations that govern the cluster dynamics (Spitzer, 1987). A fundamental assumption underlying this approach is that the granularity of the cluster due to the presence of self-gravitating masses (i.e. the stars) is ignored, and the gravitational potential throughout the cluster can hence be considered as a continuous smooth function of the position. The validity of a static model is legitimated by the consideration that all the internal and external processes that drive the evolution of a GC act over time-scales that are normally far longer than the so-called *crossing time*, $t_{\rm cross}$, which is the typical time-scale that takes for a star to cross the cluster. The simplest class of static cluster models is the one that assumes an isotropic distribution for the velocities of the stars. Examples of solutions of this kind are the *Plummer model* and the *isothermal sphere*. Both models have the advantage of having a particularly simple analytic solution for the cluster radial density profile, $\rho(r)$. On the other hand, it is known from observations that these two model are not a good representation of real GCs, for their behaviour at large and short distances from the centre, respectively.

A way to overcome these issues is to assume a so-called *lowered Maxwellian* energy distribution for the cluster stars, which is a Maxwellian with a cut-off applied to its high-velocity tail (Spitzer, 1987). This assumption is justified by the fact that GCs are always under the gravitational influence of the host galaxy, which will capture all the stars that are farther away than the tidal radius from the cluster core. Models with such an energy distribution are called *King* models (King, 1962, 1966). Extensions of them are the *King-Michie* models (Michie, 1963), which also account for a possible anisotropy of the velocity distribution. Both King and King-Michie models can be solved via numerical integration. For practical purposes, it is sometimes convenient to use some analytic approximations to the King model. An example is the one used by Freire et al. (2005), derived from King (1962) and in which $\rho(r)$ has the simple form:

$$\rho(r) = \frac{\rho_0}{\left[1 + (r/r_{\rm core})^2\right]^{3/2}}\,, \tag{3.1}$$

where $\rho_0 \equiv \rho(r = 0)$ is the central density.

3.2.2 Evolution and stellar dynamics

Static models are very useful tools that can be applied to several different case studies. However, we know that GCs do evolve over time. The difficulty in modelling the evolution of GCs is mainly

related to the many different time-scales involved, from the orbital periods of tight binaries of the order of a few hours, to the several billions of years of the ages of most of the clusters known. This means that, in general, a very high number of steps in numerical integrations are needed.

As a zero-order approximation, the evolution of the GC can in principle be obtained as a sequence of static solutions resulting from dynamical effects that are treated as perturbations. However, much more advanced and realistic methods are available nowadays, among which the four most important ones are (e.g. Davies, 2013):

- *Gas models*: the GC is treated as a spherically-symmetric self-gravitating gas and its structure is represented by the density $\rho(r)$ and temperature $T(r)$, where the latter takes the role of the velocity dispersion of the stars (e.g. Larson, 1970a,b; Lynden-Bell & Eggleton, 1980; Heggie & Hut, 2003). Thermal conduction drives the evolution of the cluster.

- *Fokker-Planck models*: the cluster is described through a distribution function $\mathcal{F}(\mathbf{r}, \mathbf{v}, t)$ that depends on the position $\mathbf{r}$, on the velocity $\mathbf{v}$, and on time, t. The evolution of the cluster is thus modelled by evolving $\mathcal{F}(\mathbf{r}, \mathbf{v}, t)$ via the collision-less Boltzmann equation (Binney & Tremaine, 2008), which can be solved numerically using finite-difference methods (Cohn, 1979; Chernoff & Weinberg, 1990; Drukier, 1995).

- *Monte-Carlo models*: the cluster stars having similar orbits are considered as a single particle. At every step, a couple of particles are chosen randomly, their mutual interaction is calculated and their orbits are modified accordingly (e.g. Hénon, 1971a,b; Fregeau et al., 2003; Giersz & Heggie, 2009).

- *N-body models*: all the stars of the cluster are treated individually and their motion is integrated numerically: at every step, the force undergone by each star is calculated and all the positions and velocities are updated accordingly (e.g. Aarseth, 1999, 2003; Hurley et al., 2005). They are the most realistic way of modelling a GC but they are also the most computationally challenging.

In all cases, the main driver of the long-term evolution of a GC is the *two-body relaxation*, namely the exchange of kinetic energy between two stars due to their mutual gravitational interaction, whose effect eventually provokes major changes in the cluster structure. A characteristic time-scale associated with this process is the *relaxation time*, $t_{\rm rlx}$, which can be defined as the time it takes for the velocity of a star to change by an order of magnitude comparable to its initial value (e.g. Binney & Tremaine, 2008). For a typical GC, $t_{\rm rlx}$ is of the order of $10^8 - 10^9$ yr and the exact value depends on the considered location of the cluster, with the denser inner regions having shorter relaxation times compared to cluster outskirts. Therefore, the core of the cluster typically evolves much faster than the outer parts.

The two-body relaxation is responsible for one of the most important processes in the evolution of a GC: the so-called *mass segregation*. The repeated encounters and consequent scattering will indeed make the total kinetic energy be evenly distributed among all the stars of each particular location of the cluster, with the more massive stars thus ending up to have slower velocities. As a consequence, the lighter stars will likely be flung towards the cluster outskirts, whereas the heavier ones will tend to sink towards the core. Over the time-scale a few $t_{\rm rlx}$, the core can hence reach extremely high densities.

The core of a GC is also a strongly self-gravitating system, whose temperature T is defined

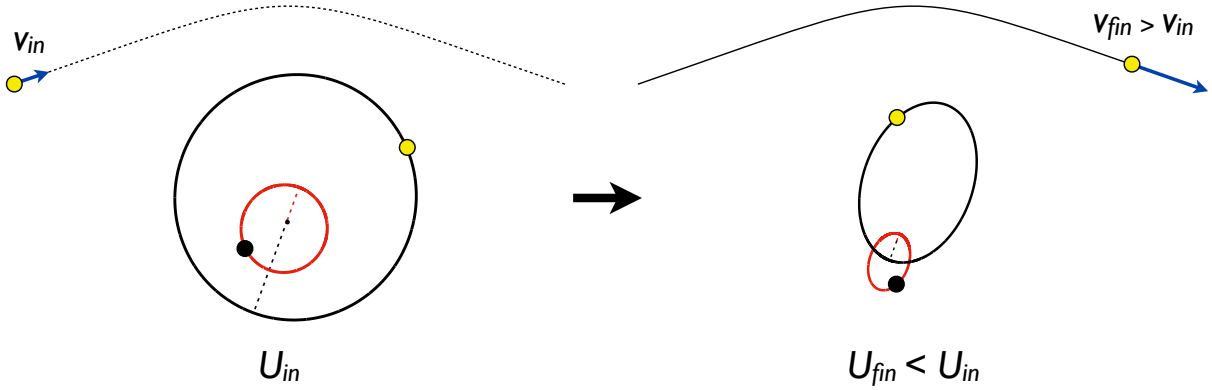

Figure 3.2. Illustration of the *binary hardening*, namely the mechanism by which the collapse of a GC core is eventually halted. A single star passes in the vicinity of a binary system and gets deflected by its gravitational pull. The binary system transfer some of its binding energy U to the single star. As a result, the single star will increase its kinetic energy, whereas the binary will become more bound, i.e. it will shrink. In this process the binary eccentricity is typically increased.

as for an ideal gas (Binney & Tremaine, 2008):

$$\frac{1}{2}\mathcal{M}\langle v^2\rangle = \frac{3}{2}k_{\rm B}T\,, \tag{3.2}$$

where $k_{\rm B}$ is the Boltzmann constant, $\mathcal{M}$ is the stellar mass and $\langle v^2\rangle$ is the mean square velocity of the stars. For N stars, the total kinetic energy is $\mathcal{K} = (3/2)Nk_{\rm B}\langle T\rangle$, with $\langle T\rangle$ being the mass-weighted mean temperature. On the other hand, the virial theorem (e.g. Binney & Tremaine, 2008) states that, for a system of particles bound by potential forces, the total energy of the system is $E_{\rm tot} = -\mathcal{K}$, and hence:

$$E_{\rm tot} = -\frac{3}{2}Nk_{\rm B}\langle T\rangle. \tag{3.3}$$

The system heat capacity:

$$\mathcal{C} = \frac{{\rm d}E_{\rm tot}}{{\rm d}\langle T\rangle} = -\frac{3}{2}Nk_{\rm B} \tag{3.4}$$

is therefore negative. This has a strong impact on the GC evolution. A negative heat capacity means that, as the system (i.e. the cluster core) loses energy via the two-body scattering, it will continuously shrink, therefore increasing its temperature, which will lead to an even larger energy loss. This positive-feedback process, called *gravothermal catastrophe* (Antonov, 1962), makes the core reach extremely high densities, an event called *core-collapse*. Core-collapsed clusters can be recognized by the fact that their radial density profiles (derived by optical observations) do not become flat around $r = 0$, but rather show a cusp. A classic example is the globular cluster M15 (Guhathakurta et al., 1996), which is an object of study of this thesis (see Chapter 7).

Although in theory unstoppable, the collapse of a GC can in fact be halted by the injection of energy into the core, which balances the natural energy loss. This energy is typically provided by scattering involving binary systems: when an isolated star has a close encounter with a tight binary, the latter will transfer part of its orbital energy to the former. The result is a tighter (and, in most cases, more eccentric) binary with a more negative binding energy, and a scattered star with an increased kinetic energy and, thus, higher velocity (Fig. 3.2, see e.g. Heggie 1975; Hut & Bahcall 1983; Sigurdsson & Phinney 1995). Even if the cluster core is originally empty of binary systems, these can be formed over time in a number of ways, the most important of

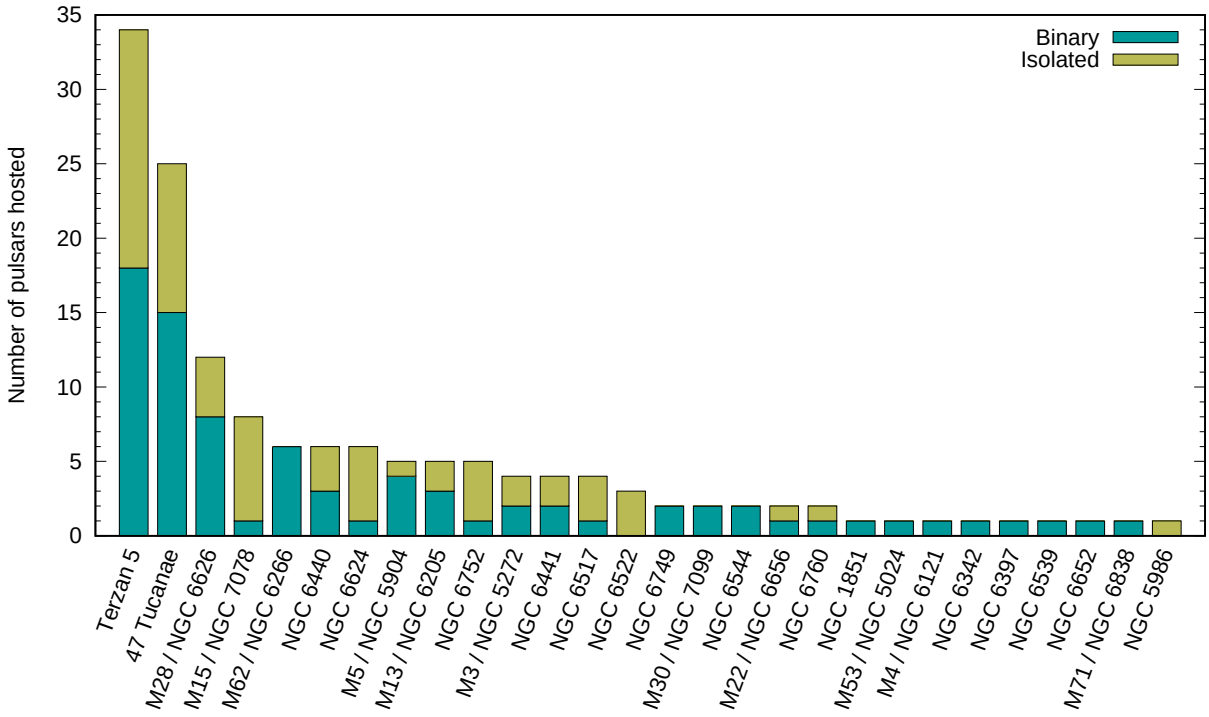

Figure 3.3. Histogram of the 28 globular clusters currently known to host radio pulsars, as of January 2017.

which are tidal captures (e.g. Fabian et al., 1975; Press & Teukolsky, 1977), and three-body encounters, where three initially unbound stars result in a binary and a runaway star.

3.3 The population of pulsars in globular clusters

As of today, 146 pulsars have been discovered[2] in 28 different Galactic GCs (Fig. 3.3), representing $\sim 6\%$ of the overall currently known pulsar population[3]. However, the estimated total number of GC pulsars that are potentially observable (i.e. with the beam pointing towards us) in our Milky Way is in fact much larger, with the most recent calculations done by Turk & Lorimer (2013) indicating a value of a few thousands. Currently, the two richest clusters are Terzan 5 and 47 Tucanae, with 34 and 25 pulsars known, respectively.

Because of the characteristics above described, the crammed GC environments greatly foster dynamical interactions between stars. These result in very high rates of formation and disruption of binaries, with the creation of exotic systems where a NS can be recycled by a companion star during one or multiple events. These conditions are absolutely unattainable in the low-density Galactic field, where the probability of close encounters is orders of magnitudes lower than in GCs (Hills, 1975). As a result, the population of pulsars in GCs shows striking differences with respect to that of the Galaxy.

For instance, the vast majority of GC pulsars are very fast spinning, with 82% classifiable as MSPs ($P < 10$ ms), to be compared with a value of $\sim 7\%$ for the Galactic field pulsars. Indeed, the frequent close encounters involving stars and binaries is believed to be the reason

[2]See `http://www.naic.edu/~pfreire/GCpsr.html` for the most up-to-date GC pulsar catalogue.
[3]According to the ATNF pulsar catalogue, version 1.55.

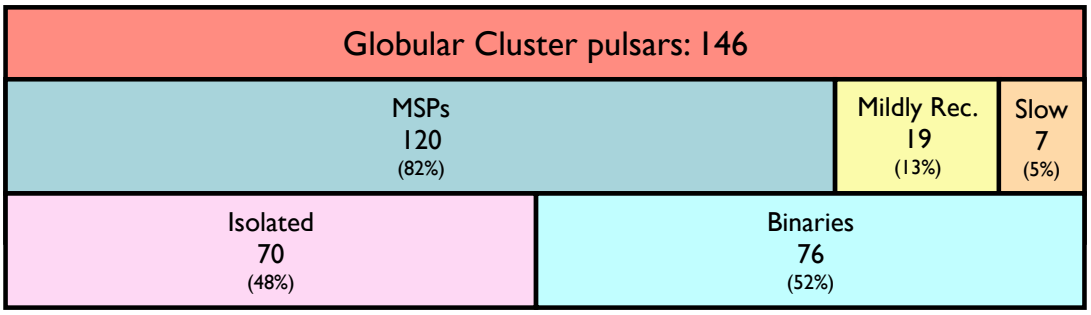

Figure 3.4. Scheme of the total known globular cluster population, as of January 2017.

for the copiousness of X-ray binary systems (composed by a NS and a MS companion star) in GCs (Clark, 1975). Such X-ray binaries are the places where NSs can be spun-up and eventually turned into MSPs.

A similar comparison can be applied to the fraction of binaries, which is $\sim 52\%$ in GCs compared to $\sim 7\%$ in the field. Restricting to MSPs, the fraction of those found in binary systems is $\sim 52\%$ for GCs (Fig. 3.4), compared to $\sim 66\%$ in the Galaxy.

In addition to the different relative fractions of the pulsar sub-classes, GCs are host of exotic systems that do not follow the canonical evolutionary paths and would then be extremely difficult (if not impossible) to see in the Galaxy. These include young pulsars, partially recycled pulsars, and binary systems that are clearly the result of secondary exchange encounters. Verbunt & Freire (2014) noted that the properties of the pulsar population of a GC are strongly related to the *encounter rate per binary*, γ_b. The latter in turn depends on the physical characteristics of the cluster, specifically the density and the radius of its core. In GCs with a low γ_b (such as 47 Tuc) the binaries that are formed have a low probability of being perturbed, hence they are likely to follow a standard evolutionary path. This may include a complete mass-transfer phase in which the NS can be fully recycled. On the contrary, in those cluster where γ_b is higher, it is more likely to find exotic objects. Examples of this case are PSR B2127+11C in M15 (Prince et al., 1991), PSR B1718−19A in NGC 6342 (Lyne et al., 1993) and J1807−2459A in NGC 6544 (Lynch et al., 2012), all of which are clearly products of one or multiple exchange encounter events.

3.4 Science with globular cluster pulsars

Pulsars in GCs can be exploited in a wide range of scientific applications, the most important of which will be reviewed in this section. As pointed out by Hessels et al. (2015), GC pulsars can be used individually, for instance to perform studies of fundamental physics, or as an ensemble of objects that can act as probes for the physical properties of the host cluster.

Two single-pulsar applications suitable for GCs are:

- *NS masses and equation of states.* The high eccentricities of many binaries found in GCs can greatly help the measurement of the pulsar masses. For these systems, the relativistic precession of periastron is indeed much easier to measure with respect to the highly circular systems that are mostly found in the Galaxy and it is thus a PK parameter that gives immediate access to the total mass of the binary (e.g. Freire et al., 2008). In this case, the masses of the individual bodies can be derived by measuring a

second PK parameter or, when possible, through optical spectroscopy of the companion star. As explained in Section 1.6.2, measurements of NS masses are very valuable to constrain the various equation of states proposed for the structure of NSs. Additional constraints can be provided by the fastest-spinning pulsars which, as explained above, are much more likely to be present in GCs thanks to the possible repeated recycling events that they can undergo (e.g. Hessels et al., 2006).

- *Physics of accretion and the link between LMXBs and MSPs.* The high number (a couple of dozens, to date) of BWPs and RBPs found in GCs provides an excellent opportunity to study the physical processes underlying the eclipses that are often seen in such systems. By studying the properties of the eclipses one can infer important details about the rate of mass loss undergone by the companion. As discussed in Section 1.4.3, this is particularly important since some RBPs, so-called *transitional* have been seen swinging between the two states (e.g. Papitto et al. 2013, see also Section 6.4) and thus represent a unique chance to understand the relationship between LMXBs and MSPs.

Belonging to the second class of studies, it is worth mentioning:

- *GC potential and dynamics.* As explained by Phinney (1992, 1993) the gravitational potential of a GC imparts non-negligible accelerations to the pulsars in the cluster, which in turn affect the observed pulsar spin and orbital period derivatives. Therefore, by measuring the latter, it is possible to directly probe the GC potential. This is particularly true for those pulsars that are closest to the GC cores, where the effect is stronger. The opposite approach is also possible: if we know the GC physical properties, in particular the maximum expected acceleration at the cluster centre, we can obtain an upper limit on the intrinsic spin-down of the pulsars (Freire et al., 2001b). The measurement of the pulsar proper motions via pulsar timing can also be used to infer several important properties of the cluster. Firstly, they can be used in combination with optical observations to infer the global proper motion of the cluster and the latter can be used to extrapolate its orbit in the Galaxy (Hessels et al., 2015). Secondly, if both the proper motions of the pulsars and that of the GC are known with enough precision, it is possible to derive the trajectories of the pulsars inside the cluster, once a model for the GC potential is assumed. This can in turn have a significant impact for the study of the dynamics of the cluster and the formation of the pulsars that reside in it. Thirdly, the population itself of a single cluster, with its peculiar fraction of binaries and isolated pulsars, carries important information that can be used to study the structure and the history of the cluster (Verbunt & Freire, 2014).

- *Intra-cluster medium.* Even though GCs, being very old, contain a very small quantity of gas, the effects of the latter can be observable in pulsar data. By accurately measuring the DMs of the various pulsars and combining this information with their positions, it is indeed possible to detect the ionized component of the intra-cluster medium. This has been successfully done by (Freire et al., 2001b) for the first time for the globular cluster 47 Tucanae. If the RMs are also measured through polarimetry observations, it is then possible to also probe the intra-cluster magnetic field (Ho et al. 2014, Abbate et al., in prep.).

Chapter 4

Finding pulsars, orbits and timing solutions in 47 Tuc

The work presented in this chapter is published in the following articles:

- Pan, Z.; Hobbs, G.; Li, D.; **Ridolfi, A.**; Wang, P.; Freire, P.; *"Discovery of Two New Pulsars in 47 Tucanae (NGC 104)"*; MNRAS: Letters, 2016, Volume 459, Issue 1, p.L26-L30
- **Ridolfi, A.**; Freire, P. C. C.; Torne, P.; Heinke, C. O.; van den Berg, M.; Jordan, C.; Kramer, M.; Bassa, C. G.; Sarkissian, J.; D'Amico, N.; Lorimer, D.; Camilo, F.; Manchester, R. N.; Lyne, A., *"Long-term observations of the pulsars in 47 Tucanae - I. A study of four elusive binary systems"*; MNRAS, 2016, Volume 462, Issue 3, p.2918-2933
- Freire, P. C. C.; **Ridolfi, A.**; Kramer, M; Jordan, C.; Manchester, R. N.; Torne, P.; Sarkissian, J.; D'Amico, N.; Camilo, F.; Lorimer, D. R.; Lyne, A. G.; *"Long-term observations of the pulsars in 47 Tucanae - II. Proper motions, accelerations and jerks"*; Submitted to MNRAS

My contribution was the reduction of the Parkes data, the re-detection and the timing analysis for all the previously known pulsars, and the determination of refined orbital parameters for the faintest elusive binary systems.

Contents

4.1 Introduction

In this chapter we present new results derived from the analysis of about two decades of data of the globular cluster 47 Tucanae taken with the Parkes radio telescope in New South Wales (Australia).

47 Tucanae (also known as NGC 104 or 47 Tuc, for short) is a well-known GC visible in the Southern Sky. With its diameter of about 37 pc, it is one of the largest clusters known. Although it is massive ($\sim 10^6$ $M_\odot$, Pryor & Meylan 1993) and has a fairly high central density ($\sim 10^5$ $M_\odot$ pc^{-3}, Pryor & Meylan 1993), it is not a core-collapsed cluster (Harris, 1996). The centre of 47 Tuc is located at a right ascension $\alpha = 00^h\,24^m\,5^s.67$ and declination $\delta = -72°\,04'\,52''.62$, whereas its core radius is $\theta_c = 0.347$ arcmin (McLaughlin et al., 2006). For the cluster distance, d, we use 4.69 kpc[1] (Woodley et al., 2012). These values will be used throughout the text.

The previous observations of 47 Tuc with the Parkes radio telescope have provided outstanding scientific results that include the discovery of 25 radio MSPs (Manchester et al., 1990, 1991; Robinson et al., 1995; Camilo et al., 2000; Knight, 2007; Pan et al., 2016), all of which have spin periods smaller than 8 ms. This is a very exceptional population, since only $\sim$7% of the non-cluster pulsars in the Galaxy have spin periods of less than 8 ms. As expected from a GC with a relatively low encounter rate per binary (Verbunt & Freire, 2014), a large fraction (60%) of the pulsars in 47 Tuc are part of binary systems. This is similar to that of the Galactic *non-cluster* MSP population ($\sim$66%), but very different from the general pulsar population, where the number in binaries is $\sim$7%. The binary pulsar population of 47 Tuc is composed by eight pulsar-WD binaries, five "black widow" pulsars (BWPs), with orbital periods of $P_b \sim 0.06 - 0.4$ days and companion masses of $M_c \sim 0.02 - 0.05$ $M_\odot$, and two eclipsing "redback" pulsars (RBPs) with $P_b \sim 0.1 - 0.2$ days and $M_c \sim 0.1 - 0.5$ $M_\odot$ (see Section 1.4.3).

Until now, 16 pulsars had published timing solutions (Robinson et al., 1995; Camilo et al., 2000; Freire et al., 2001b, 2003). These have allowed exceptional scientific results, among which are the study of the stellar evolution in GCs (Rasio et al., 2000), a detailed study of the dynamics of the cluster (Freire et al., 2001b) and the very first detection of ionized gas in a globular cluster (Freire et al., 2001c). Additionally, all the pulsars with a measured position have been detected at X-ray wavelengths (Grindlay et al., 2001, 2002; Heinke et al., 2005; Bogdanov et al., 2005, 2006, Bhattacharya et al., in prep.) and six WD companions (of pulsars 47 Tuc Q, S, T, U, W and Y; Edmonds et al., 2001, 2002; Cadelano et al., 2015; Rivera-Sandoval et al., 2015) have been detected at optical wavelengths.

Here, we present complete phase-connected timing solutions for seven previously unsolved pulsars, of which four are in binaries (47 Tuc R, W, X, Y) and three are isolated (47 Tuc Z, aa, ab). For another two binary systems (47 Tuc P and V), where this was not possible, we present very accurate orbital parameters. For all the other pulsars, we extend their timing solutions (last updated by Freire et al. 2003) with an additional 10 years of data. The much longer timing baseline has allowed us to obtain much more precise parameters for all the pulsars, enabling us to investigate new and previously inaccessible properties of the pulsars and their host cluster.

[1] A more recent assessment places 47 Tuc at a slightly smaller distance, 4.53 kpc (Bogdanov et al., 2016). The distance of the cluster and its impact on the study of its dynamics will be discussed in Chapter 5.

4.2 The 47 Tuc dataset

The 20-cm 47 Tuc dataset used consisted of 519 pointings to the cluster done with the 64-m Parkes radio telescope, at 414 different epochs[2], between October 1997 and August 2013. All the observations together amount to a total of $\sim$1770 hours. Of the 519 pointings, 438 were longer than 1 hour, whereas 30 were shorter than 10 minutes, the latter mostly being the result of accidental failures in the observing system or stops imposed by adverse weather conditions.

The observing setup was mostly the same as described in Freire et al. (2003). The vast majority of the observations were carried out at a frequency of $\simeq$1.4 GHz using the central beam of the Parkes Multi-Beam Receiver (PMB, Staveley-Smith et al., 1996), whose size (full-width half-maximum, FWHM) is 14.4 arcmin. Occasionally, when the PMB was not available, we observed 47 Tuc with the H-OH receiver at the same frequency. Another handful of observations were made with other receivers, namely the "436-MHz", the "660-MHz", the "10-50cm" and the METH6 receiver. Until August 1999 we used the PMB filterbank as back-end. When using the PMB receiver, we had a central observing frequency $f_c = 1374$ MHz, a bandwidth of 288 MHz divided into 96, 3-MHz wide, channels and a sampling time of 125 μs. At that frequency, for a pulsar with the average DM of 47 Tuc ($\simeq$ 24.4 pc cm^{-3}), the dispersive smearing is 234 μs across a single channel, resulting in an effective time resolution of 265 μs. From August 1999 we switched to a different configuration, and most of the observations were carried out with the Analogue Filter Bank (AFB) back-end, with a central frequency $f_c = 1390$ MHz, 256 MHz of bandwidth divided into 512, 0.5-MHz wide, channels and a sampling time of 80 μs. For this observing system the dispersive smearing of the 47 Tuc pulsars is only 37 μs across a single channel, which gives an effective time resolution of 88 μs. After summing the signals of the two polarizations and integrating for the time of the chosen sampling interval, all the data were 1-bit digitized and recorded onto magnetic tapes as *filterbank* (Lorimer, 2011) search-mode files.

4.3 Updated timing solutions for 18 pulsars in 47 Tuc

For 16 pulsars in 47 Tuc, namely 47 Tuc C, D, E, F, G, H, I, J, L, M, N, O, Q, S, T and U, phase-connected timing solutions had already been published (Robinson et al., 1995; Camilo et al., 2000; Freire et al., 2001b, 2003). For another two, i.e. pulsars R and Y, the timing solutions were already derived in 2006, but had not as yet been published.

Hence, for each pulsar, we started by using the most up-to-date ephemeris available to de-disperse and fold all our dataset anew with `DSPSR`[3] (van Straten & Bailes, 2011), producing as many folded archives as the number of observations, among which we looked for those where the pulsar was detected. After that, we selected the best detections to built a high-S/N template. The latter was then cross-correlated with the integrated profiles of all the detections found, using the `PSRCHIVE`[4] pulsar software package (Hotan et al., 2004; van Straten et al., 2012), to extract topocentric times-of-arrival (ToAs, see Section 2.5.2 for details). After applying the clock corrections of the Parkes radio telescope, the ToAs were referred to the Solar System barycentre (SSB) by `TEMPO`. This was achieved by first correcting for the Earth rotation using data from the

[2]We call "pointing" a single, continuous observation of 47 Tuc, that hence corresponds to a single recorded data file. An "epoch" is instead used as a synonym for "day". The full list of pointings with the relative observing parameters can be found at: `http://www3.mpifr-bonn.mpg.de/staff/pfreire/47Tuc/Observations_Table.html`

[3]`http://dspsr.sourceforge.net`

[4]`http://psrchive.sourceforge.net`

Table 4.1. Number of detections of the four "elusive" binary pulsars of 47 Tuc obtained with the three different search methods as well as by refolding the whole dataset with the relative timing solutions (reported in Table 4.5).

Pulsar	PRESTO (20-min)	PRESTO (60-min)	T_0-search	Folding (Timing)
47 Tuc P	0	0	4	4
47 Tuc V	0	0	7	19
47 Tuc W	1	1	23	34
47 Tuc X	12	16	–	312

International Earth Rotation Service, and then correcting for the Earth motion around the SSB using the JPL DE421 Solar System Ephemeris (Folkner et al., 2009). The differences between the observed ToAs and the values predicted by our ephemeris were then fitted by `TEMPO` through a weighted χ^2 minimization for the astrometric, rotational and possibly orbital parameters. When doing so, we fixed the parallax to a value corresponding to the assumed distance of 47 Tuc, 4.69 kpc (Woodley et al., 2012). This procedure allowed us to extend the timing solution of each of the 18 pulsars, meaning that all the pulsar ephemerides are now capable of accounting for every single rotation of the relative pulsars at least until the date of the latest ToAs, around the year 2013. The updated timing solutions derived for these pulsars are presented in Tables 4.2-4.4, whereas the post-fit timing residuals are shown in Fig. 4.3.

4.4 47 Tuc P, V, W and X: four elusive binaries

Among the pulsars known to reside in 47 Tuc, there are four extremely faint binaries, namely 47 Tuc P, V, W and X. The combination of very low fluxes, orbital characteristics and scintillation, makes these pulsars remarkably elusive. For this reason, neither a phase-connected timing solution nor a well-determined orbit was previously available for any of them. Therefore, we implemented more sophisticated techniques in order to obtain as many detections of the pulsars as possible, which in turn enabled us to perform a more thorough analysis of these poorly studied binaries. For two of these pulsars, as we shall see, this allowed us to obtain phase-connected timing solutions for the very first time since their discovery.

4.4.1 Acceleration search

We have carried out a deep search of the whole dataset using a machine endowed with two NVIDIA K20 and two NVIDIA K40 GPUs and a search pipeline that made use of the GPU-based version of `PRESTO` (see Section 2.4.5). Each observation was split into chunks of both 20 and 60 minutes of length. On each chunk we first ran the `rfifind` routine to look for bursts of RFI, creating a mask and filtering out bad frequency channels or time intervals. Then, again for each chunk, a 0-DM (i.e. without correcting for the dispersion effect due to the interstellar medium) time series was created and searched for prominent persistent terrestrial low-level RFI (dubbed "birdies") with a Fast Fourier Transform. The periodicities found were marked as interference, to be ignored during the analysis, and stored in a so-called "zaplist" file. After that, nine de-dispersed time series were created for an assumed DM of 23.90 pc cm^{-3} to 24.70 pc cm^{-3}

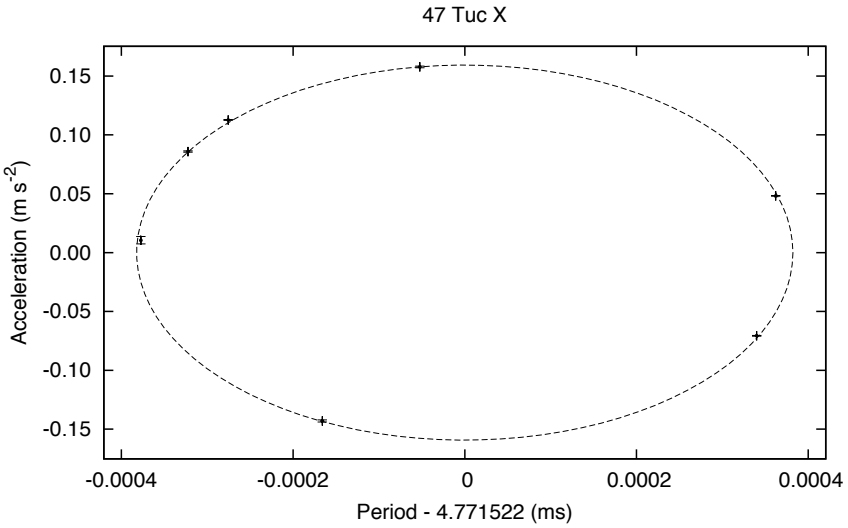

Figure 4.1. Period-acceleration diagram for the binary pulsar 47 Tuc X. The fit returned an orbital period of $P_{\rm b} \simeq 10.9$ days and a projected semi-major axis of $x_{\rm p} \simeq 11.9$ lt-s for the pulsar orbit.

with steps[5] of 0.10 pc cm^{-3}. The time series were then searched in the Fourier domain by the `accelsearch` routine, summing up to 8 harmonics, with a $z_{\rm max}$-value (see Eq. 2.21) ranging from 0 (absence of acceleration) up to 1200 for the 60-minute chunks and up to 200 for the 20-minute chunks. All the candidate pulsar-like signals with a detection significance of $\sigma \geq 2.0$ were recorded onto files, one for each chunk and each DM.

Once the search was done, we looked for all the candidates with the highest σ values that were detected at periods close to the known barycentric spin periods of the pulsars of our sample of interest (namely 47 Tuc P, V, W and X) and that appeared at multiple adjacent DM values. Table 4.1 shows the number of detections that we obtained for each pulsar.

4.4.2 Orbital solution for 47 Tuc X

47 Tuc X is a formerly known, but unpublished, millisecond pulsar that had been discovered in previous searches of the cluster. The pulsar had already been found with non-zero accelerations, indicating the occurrence of a binary motion. Our `PRESTO` 20- and 60-minute search pipelines produced a sufficiently large number of new detections of this pulsar to allow us to estimate its orbital parameters with the *period-acceleration diagram* method (Freire et al., 2001a, see also Section 2.4.7). Among the 16 different epochs at which the pulsar was detected, we selected the 7 best ones. We then used `TEMPO` to fit the latter for the barycentric spin period, P, and its first derivative, $\dot{P}$, thus finding a local timing solution for each epoch. After converting the $\dot{P}$ values into radial accelerations a_l (through the relation $a_l = c\dot{P}/P$, where c is the speed of light), we fitted for the orbital period, $P_{\rm b}$, and projected semi-major axis of the pulsar orbit, $x_{\rm p}$, via Eq. (7) and (8) of Freire et al. (2001a), using `CIRCORBIT` (see Section 2.4.7). The data points and best-fit curve are shown in Fig. 4.1. The fit revealed that the pulsar is in a circular orbit with $P_{\rm b} \simeq 10.9$ days and $x_{\rm p} \simeq 11.9$ lt-s.

[5]Such an interval more than covered the DM range of the pulsars known in 47 Tuc when the search was done. However, a newly discovered pulsar, 47 Tuc aa, has a DM of $\simeq 24.94$ pc cm^{-3} (Pan et al., 2016). This implies that the range of DM's in 47 Tuc is larger than what we assumed in the present work.

4.4.3 T_0-search

As shown in Table 4.1, pulsars P, V and W were either detected once or not at all in our PRESTO searches. The reasons for the very low rate of detection are manifold: these pulsars are all intrinsically very faint, their orbital periods are very short (reducing the maximum possible integration time where the constant acceleration approximation is effective, see e.g. Ransom et al. 2003) and two of them (V and W) are eclipsed for a large fraction of the orbit. Only when both the scintillation and the observed orbital phase interval were favourable, did we have the chance of detecting these pulsars. Because of their very compact orbits, comparable with the length of a single observation, the orbital parameters of pulsars P, V, and W were already known at the time of their discovery with a reasonable degree of accuracy. However, the uncertainties on their orbital periods, together with the large orbital variability that some of them show (see Chapter 6), prevented us from predicting their correct orbital phases at a later time. Unlike the uncertainty associated with the projected semi-major axis, the uncertainty $\Delta\phi_{\rm b}(t)$ on the orbital phase $\phi_{\rm b}$ at any time t, grows linearly with time, as:

$$\Delta\phi_{\rm b}(t) = \frac{\Delta P_{\rm b} \cdot (t - t_0)}{P_{\rm b}^2}\,, \tag{4.1}$$

where t_0 is the epoch at which the orbital period $P_{\rm b}$ and its uncertainty $\Delta P_{\rm b}$ were estimated. The uncertainty on $\phi_{\rm b}$ translates into an uncertainty in T_0, the epoch of passage at periastron[6], in the pulsar ephemeris. This is the reason why, even knowing the spin periods and the rough values of the orbital parameters of the three pulsars at the epoch of their discoveries, we could not simply fold the more recent data to look for possible new detections: the correction for the Rømer delay due to the binary motion would be applied with a wrong orbital phase, thus smearing out the signal.

What we did instead was a search in orbital phase, or, equivalently, in the value of T_0. For this reason we will refer to it as T_0-search throughout the rest of this thesis.

First, we created a full-length (i.e. this time we did not split the observations into chunks) de-dispersed time series for each observation of our 47 Tuc dataset, at a DM of 24.40 pc cm^{-3}. We chose to use a single value of the DM since, for the purpose of just detecting the pulsars, a more precise value is unimportant. Then, for each pulsar, we folded all the de-dispersed time series with an ephemeris that had all the known parameters fixed, with the exception of T_0. The latter was instead searched, allowing its value to vary between the epoch of the beginning of the observation, $t_{\rm start}$, and $t_{\rm start} + P_{\rm b}$, where $P_{\rm b}$ was the (rough) value of the orbital period of the pulsar considered. This procedure has been implemented in the `alex_T0_search` routine of the PSRALEX[7] software package, which we used to perform the search. The choice of using de-dispersed time series instead of the original search-mode files is justified, apart from the fact that we know the DMs of the pulsars very precisely, by the huge advantage in computational speed that the former have over the latter, when folding. To further minimize the computational costs without degrading the sensitivity of our search, the choice of the step size was also crucial and will be now discussed in detail.

[6] For circular orbits (as is the case for all the pulsars discussed in this chapter), where the periastron is not defined, T_0 is conventionally chosen to coincide with $T_{\rm asc}$, the epoch of passage at the ascending node.

[7] http://github.com/alex88ridolfi/PSRALEX

4.4.3.1 Choice of the step size

Let us consider the case of a perfectly circular orbit (as is practically the case for pulsars P, V and W) and let us assume to know the exact orbital period, P_b, and projected size of the orbit, x_p. Then, if the orbital phase predicted by an incorrect ephemeris differs from the actual phase ϕ_b by a quantity $\Delta\phi_\mathrm{b}$, the correction applied for the orbital Rømer delay at a time t will be wrong by the quantity:

$$\begin{aligned}
&x_\mathrm{p}\sin[\phi_\mathrm{b}(t)+\Delta\phi_\mathrm{b}]-x_\mathrm{p}\sin[\phi_\mathrm{b}(t)]= \\
&=x_\mathrm{p}\Big\{\sin[\phi_\mathrm{b}(t)+\Delta\phi_\mathrm{b}]-\sin[\phi_\mathrm{b}(t)]\Big\}= \\
&=x_\mathrm{p}\left\{2\cos\left[\frac{\phi_\mathrm{b}(t)+\Delta\phi_\mathrm{b}+\phi_\mathrm{b}(t)}{2}\right]\sin\left[\frac{\phi_\mathrm{b}(t)+\Delta\phi_\mathrm{b}-\phi_\mathrm{b}(t)}{2}\right]\right\}= \\
&=2\,x_\mathrm{p}\sin\left(\frac{\Delta\phi_\mathrm{b}}{2}\right)\cos\left[\phi_\mathrm{b}(t)+\frac{\Delta\phi_\mathrm{b}}{2}\right]= \\
&=\mathcal{A}\,\cos\left[\frac{2\pi}{P_\mathrm{b}}(t-T_0)+\frac{\Delta\phi_\mathrm{b}}{2}\right],
\end{aligned} \tag{4.2}$$

where we used the Prosthaphaeresis formulas and the amplitude of the sinusoid is:

$$\mathcal{A}=2x_\mathrm{p}\sin(\Delta\phi_\mathrm{b}/2)\,. \tag{4.3}$$

When folding, the integrated pulse profile will have a width $W\sim\mathcal{A}$. If $\mathcal{A}\gtrsim P$, where P is the pulsar spin period, the residual orbital modulation will completely smear out the pulsar signal, resulting in a non-detection.

For this reason, we imposed that the step size in our T_0-search be sufficiently small such that, in the case of the best trial value, $A\leq P/4$, which translates into the condition:

$$\Delta\phi_\mathrm{b}\leq 2\arcsin\left(\frac{P}{8x_\mathrm{p}}\right). \tag{4.4}$$

The resulting total number of steps is thus:

$$N=\frac{2\pi}{\Delta\phi_\mathrm{b}}=\frac{\pi}{\arcsin(P/8x_\mathrm{p})}. \tag{4.5}$$

For pulsars P, V and W, the latter amounts to 262, 4441 and 2601, respectively.

As already mentioned, this calculation is valid under the assumption of knowing the correct values for P_b and x_p. In general, this is not the case, since our goal is in fact to *obtain* a better value for P_b. Incorrect starting values of P_b and x_p introduce additional errors to the applied Rømer delay corrections, which further degrade our sensitivity. This degradation can be partly compensated by using a finer grid of values in the T_0-search. In our work, in the case of pulsars P and W, we started with good values of P_b and x_p, precise enough to fold an observation correctly, once the exact value of T_0 was determined; for V, instead, the values were not as precise. In our analysis, in order to maximize our sensitivity, we decided to use a number of steps which was ~ 2 times larger than the values reported above for all the three pulsars.

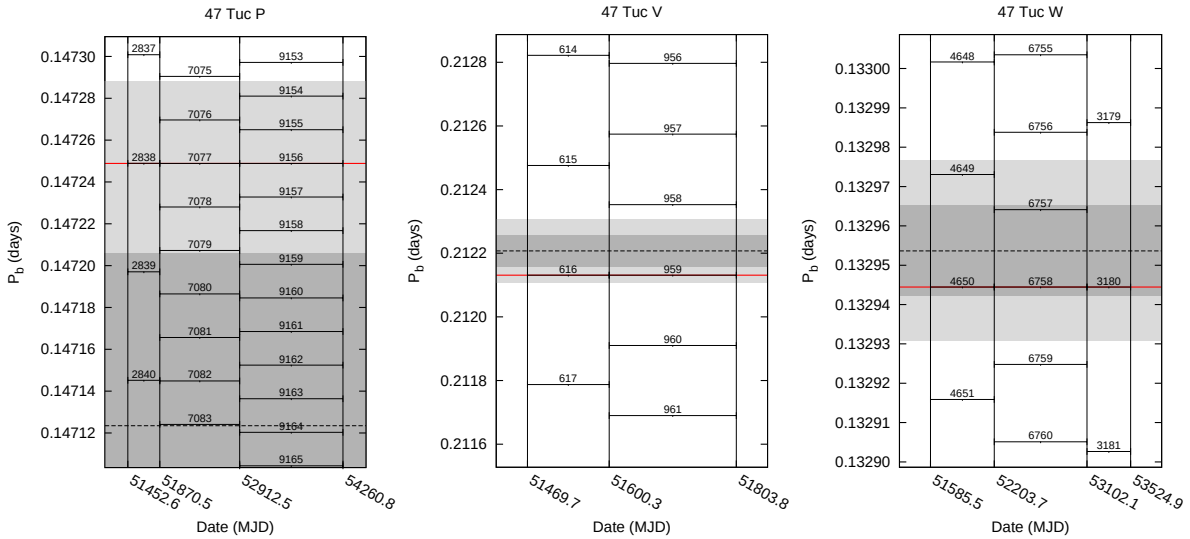

Figure 4.2. Periodograms for pulsars 47 Tuc P, V and W. In each plot the dashed line marks the initial guess of P_b, corresponding to the best-fit value derived by running `TEMPO` on the best detection obtained from our T_0-search; the dark grey and light grey areas represent the relative formal 1-σ and 2-σ uncertainties, respectively. The solid vertical lines indicate the measured T_0 values that we used. The horizontal segments indicate the orbital period obtained by dividing the time interval that they connect by the integer number reported above them. In each plot, the red line highlights the orbital period that is an integer submultiple of all time intervals.

4.4.4 Periodograms and improved orbital periods for 47 Tuc P, V and W

After folding all the observations with all the trial values of T_0, we ordered by signal-to-noise ratio (S/N) the resulting archives, which were then inspected visually. From every archive where we clearly detected the pulsar (see Table 4.1 for the number of detections obtained with the T_0-search for each pulsar), we extracted the topocentric ToAs and fitted for T_0 only with `TEMPO`, to obtain a refined value of it for each epoch. The latter were in turn used to improve the measurement of the orbital period using the periodogram method described by Freire et al. (2001a), which essentially consists in finding a value of P_b that fits an integer number of times between any pair of measured values of T_0. Fig. 4.2 shows the periodograms for 47 Tuc P, V and W.

4.4.5 Timing of the elusive binaries

Differently from the case of the 18 pulsars discussed in Section 4.3, for these four elusive binaries we did not have a phase-connected timing solution from where to start. Therefore, we proceeded differently, as described in the following.

For each pulsar, we started by constructing a first ephemeris that included the average barycentric spin period, the nominal position and proper motion of the cluster, as well as a simple Keplerian (BT, Blandford & Teukolsky, 1976) binary model with the refined orbital parameters obtained through the period-acceleration diagram for pulsar X, and through the T_0-search and the periodogram method for P, V and W. We then used the ephemeris to re-fold the entire dataset with `DSPSR`. This occasionally allowed us to obtain a few additional detections. After that, we proceeded similarly to the case of the previous 18 pulsars. We first used `PSRCHIVE` to extract the topocentric ToAs, by cross-correlating the pulse profiles against a high-S/N template

that we had previously built from the best detections (the template profiles used for all the 25 pulsars of 47 Tuc are shown in Fig. 4.4). The ToAs were then converted by `TEMPO` and referred to the SSB. In this case, because our preliminary ephemeris was not phase-connected, we let `TEMPO` fit not only for the astrometric, rotational and orbital parameters, but also for arbitrary jumps between groups of ToAs belonging to different epochs. This produced a more refined, but still non-coherent, timing solution. The latter was then used to refold the data again, often yielding new detections of the pulsar and, thus, more ToAs that were then included in the fit. In doing this, we tried to remove as many arbitrary jumps as possible by trying to guess the exact number of rotations between the ToAs that they separated. The whole procedure was iterated a few times until we converged to the best (presumably phase-connected) solution. For two of the pulsars (namely 47 Tuc W and X) we were able to remove all the arbitrary jumps and thus to obtain a fully phase-connected timing solution, capable of unambiguously account for every single rotation of the NS. The best-fit timing parameters for all the four elusive binary pulsars of 47 Tuc are reported in Table 4.5.

4.5 The new isolated pulsars 47 Tuc Z, aa, ab

47 Tuc Z was first discovered by Knight (2007) as a 4.55-ms pulsar without signs of acceleration. The relatively good amount of detections allowed the author to confirm the isolated nature of the NS, and to build a first good, but not phase-connected, ephemeris. 47 Tuc aa and ab were instead discovered as a 1.84- and 3.70-ms isolated pulsar, respectively, with a stacked-search technique by Pan et al. (2016).

Our `PRESTO`-based search pipeline described in Section 4.4.1 allowed us to obtain additional detections for all the three pulsars. Starting from these detections, we built a first ephemeris for each pulsar and we proceeded as described in the previous section. By extracting ToAs and fitting them with `TEMPO`, we were able to obtained refined ephemerides, which in turn allowed to increase the number of detections. This process was re-iterated until phase-connected solutions were obtained (reported in Table 4.2). Because of the scarcity and sparsity of its detections, 47 Tuc aa could not be solved manually and required the use of a code developed by P. Freire for the automatic finding of timing solutions. This code will be presented in Freire (in prep.).

Table 4.2. Timing parameters of the ten isolated pulsars in 47 Tuc. The associated 1-σ uncertainties were calculated using a Monte-Carlo bootstrap routine implemented in `TEMPO`. For all the pulsars, a fixed parallax value of 0.2132 mas was assumed; the time units are TDB; the assumed terrestrial time standard is UTC(NIST); the Solar System ephemeris used is the JPL DE421.

Pulsar	47 Tuc C	47 Tuc D	47 Tuc F	47 Tuc G	47 Tuc L
Phase-connected? ...	Yes	Yes	Yes	Yes	Yes
Reference Epoch (MJD)	51600.000	51600.000	51600.000	51600.000	51600.000
Start ToA (MJD) ...	47857.439	47716.842	48494.790	48600.489	50686.683
End ToA (MJD) ...	56508.971	56508.976	56466.879	56466.879	56388.208
Number of ToAs ...	6225	3607	1785	594	411
Residuals RMS (μs) ..	12.33	8.74	7.83	11.25	17.02
α (J2000) (hh:mm:ss) .	00:23:50.3546(1)	00:24:13.88092(6)	00:24:03.85547(10)	00:24:07.9603(1)	00:24:03.7721(3)
δ (J2000) (dd:mm:ss) .	−72:04:31.5048(4)	−72:04:43.8524(2)	−72:04:42.8183(2)	−72:04:39.7030(5)	−72:04:56.923(2)
μ_α (mas yr^{-1})	5.2(1)	4.24(7)	4.52(8)	4.5(1)	4.4(2)
μ_δ (mas yr^{-1})	−3.1(1)	−2.24(5)	−2.50(5)	−2.9(1)	−2.4(2)
f (Hz)	173.708218965958(4)	186.651669856731(3)	381.158663656311(5)	247.501525096385(8)	230.08774629142(2)
$\dot{f}$ (Hz s^{-1})	$1.50421(6)\times10^{-15}$	$1.1922(3)\times10^{-16}$	$-9.3711(1)\times10^{-15}$	$2.5825(1)\times10^{-15}$	$6.4611(2)\times10^{-15}$
$\ddot{f}$ (Hz s^{-2})	$1.3(4)\times10^{-27}$	$-1.2(2)\times10^{-27}$	$6.8(7)\times10^{-27}$	$6.0(9)\times10^{-27}$	$-13(13)\times10^{-28}$
DM (pc cm^{-3})	24.600(4)	24.732(3)	24.382(5)	24.436(4)	24.40(1)
Derived Parameters					
θ_α (arcmin)	−1.1784	+0.6316	−0.1396	+0.1762	−0.1460
θ_δ (arcmin)	+0.3520	+0.1460	+0.1634	+0.2151	−0.0719
$\theta_\perp$ (arcmin)	1.2298	0.6483	0.2149	0.2781	0.1627
$\theta_\perp$ (core radii)	3.5442	1.8683	0.6194	0.8014	0.4689
$r_\perp$ (pc)	1.6778	0.8845	0.2932	0.3794	0.2220
P (ms)	5.7567799955164(1)	5.35757328486572(7)	2.62357935251262(3)	4.0403791435651(1)	4.3461679994616(3)
$\dot{P}$ (10^{-21} s s^{-1}) ...	−49.850(2)	−3.4219(9)	64.5031(7)	−42.159(2)	−122.0406(10)
$\dot{a}_l$ (10^{-21} m s^{-3}) ...	−2.3(7)	1.98(26)	−5.3(5)	−7.3(1.1)	1.7(1.7)

Table 4.2 – *continued*

Pulsar	47 Tuc M	47 Tuc N	47 Tuc Z	47 Tuc aa	47 Tuc ab
Phase-connected? ...	Yes	Yes	Yes	Yes	Yes
Reference Epoch (MJD)	51600.000	51600.000	51600.000	51600.000	51600.000
Start ToA (MJD) ...	48491.694	48515.534	51003.792	51413.635	51000.785
End ToA (MJD) ...	55526.513	55648.110	54645.852	54816.499	56388.135
Number of ToAs ...	315	436	107	49	210
Residuals RMS (μs) ..	20.15	12.98	58.78	26.41	24.85
α (J2000) (hh:mm:ss) .	00:23:54.4899(3)	00:24:09.1880(2)	00:24:06.041(2)	00:24:07.2783(8)	00:24:08.1615(5)
δ (J2000) (dd:mm:ss) .	−72:05:30.756(2)	−72:04:28.8907(7)	−72:05:01.480(6)	−72:05:19.521(4)	−72:04:47.602(2)
μ_α (mas yr^{-1})	5.0(3)	6.3(2)	4(2)	4.6(8)	4.2(6)
μ_δ (mas yr^{-1})	−2.0(4)	−2.8(2)	1(2)	−5(1)	−2.9(5)
f (Hz)	271.98722878874(2)	327.44431861739(1)	219.5656060346(1)	541.8936549490(1)	269.93179806134(4)
$\dot{f}$ (Hz s^{-1})	$2.8421(4)\times10^{-15}$	$2.3435(2)\times10^{-15}$	$2.19(3)\times10^{-16}$	$1.3475(4)\times10^{-14}$	$-7.155(6)\times10^{-16}$
$\ddot{f}$ (Hz s^{-2})	$7(2)\times10^{-27}$	$-9(2)\times10^{-27}$	$8(25)\times10^{-27}$	$7(3)\times10^{-26}$	$-8(3)\times10^{-27}$
DM (pc cm^{-3})	24.43(2)	24.574(9)	24.45(4)	24.941(7)	24.37(2)
Derived Parameters					
θ_α (arcmin)	−0.8594	+0.2707	+0.0286	+0.1237	+0.1917
θ_δ (arcmin)	−0.6354	+0.3955	−0.1479	−0.4484	+0.0838
$\theta_\perp$ (arcmin)	1.0688	0.4793	0.1506	0.4651	0.2092
$\theta_\perp$ (core radii)	3.0801	1.3812	0.4340	1.3403	0.6028
$r_\perp$ (pc)	1.4581	0.6539	0.2054	0.6345	0.2854
P (ms)	3.6766432176002(3)	3.0539543462608(1)	4.554447383906(3)	1.8453805296800(5)	3.7046394947985(5)
$\dot{P}$ (10^{-21} s s^{-1}) ...	−38.418(5)	−21.857(2)	−4.56(1)	−45.89(1)	9.820(8)
$\dot{a}_l$ (10^{-21} m s^{-3}) ...	−8.0(2.6)	8.5(1.5)	−11(33)	−39(16)	8.7(3.6)

Parameters: α: right ascension; δ: declination; μ_α: proper motion in right ascension; μ_δ: proper motion in declination; f: spin frequency; $\dot{f}$: 1st spin frequency derivative; $\ddot{f}$: 2nd spin frequency derivative; DM: dispersion measure; x_p: projected semi-major axis of the pulsar orbit; e: eccentricity; η: first Laplace-Lagrange parameter; κ: second Laplace-Lagrange parameter; ω: longitude of periastron; T_0: epoch of passage at periastron; T_asc: epoch of passage at the ascending node; P_b: orbital period; $\dot{P}_\mathrm{b}$: orbital period derivative; f_b: orbital frequency; $f_\mathrm{b}^{(n)}$: n-th orbital frequency derivative; $\dot{\omega}$: rate of periastron advance; θ_α: angular offset from cluster centre in right ascension; θ_δ: angular offset from cluster centre in declination; $\theta_\perp$: total angular offset from cluster centre; $r_\perp$: projected distance from cluster centre; P: spin period; $\dot{P}$: observed spin period derivative; $a_{l,\mathrm{GC}}$: line-of-sight acceleration from cluster field; $\dot{P}_\mathrm{int}$: intrinsic spin period derivative; B_s: surface magnetic field; L_sd: spin-down luminosity; τ_c: characteristic age; $\dot{a}_l$: jerk; $f(M_\mathrm{p})$: pulsar mass function; $M_\mathrm{c,min}$: minimum companion mass; $M_\mathrm{c,med}$: median companion mass; M_tot: total system mass.

Table 4.3. Timing parameters for seven of the eight MSP-WD binaries in 47 Tuc. The associated 1-σ uncertainties were calculated using a Monte-Carlo bootstrap routine implemented in `TEMPO`. For all the pulsars, a fixed parallax value of 0.2132 mas was assumed; the time units are TDB; the assumed terrestrial time standard is UTC(NIST); the Solar System ephemeris used is the JPL DE421.

Pulsar	47 Tuc E	47 Tuc H	47 Tuc Q	47 Tuc S
Phase-connected? ...	Yes	Yes	Yes	Yes
Reference Epoch (MJD)	51600.000	51600.000	51600.000	51600.000
Start ToA (MJD) ...	48464.854	48517.512	50689.700	50686.683
End ToA (MJD) ...	56508.948	56508.972	56388.178	56466.879
Number of ToAs ...	1812	1073	697	577
Residuals RMS (μs) ..	6.06	17.04	12.73	9.50
α (J2000) (hh:mm:ss) .	00:24:11.10528(5)	00:24:06.7032(2)	00:24:16.4909(1)	00:24:03.9794(1)
δ (J2000) (dd:mm:ss) .	−72:05:20.1492(2)	−72:04:06.8067(6)	−72:04:25.1644(6)	−72:04:42.3530(4)
μ_α (mas yr^{-1})	6.15(3)	5.1(2)	5.2(1)	4.5(1)
μ_δ (mas yr^{-1})	−2.35(6)	−2.8(2)	−2.6(1)	−2.5(1)
f (Hz)	282.779107035000(3)	311.49341784423(1)	247.943237418920(9)	353.306209385356(9)
$\dot{f}$ (Hz s^{-1})	$-7.87728(4)\times10^{-15}$	$1.775(1)\times10^{-16}$	$-2.0907(2)\times10^{-15}$	$1.50466(1)\times10^{-14}$
$\ddot{f}$ (Hz s^{-2})	$2.9(2)\times10^{-27}$	$1.60(2)\times10^{-25}$	$7(11)\times10^{-28}$	$-7.8(8)\times10^{-27}$
DM (pc cm^{-3})	24.236(2)	24.369(8)	24.265(4)	24.376(4)
Binary Parameters				
Binary Model	DD	DD	ELL1	ELL1
$x_{\rm p}$ (lt-s)	1.9818427(4)	2.152813(2)	1.4622043(9)	0.7662686(8)
e	$3.159(4)\times10^{-4}$	$7.0558(1)\times10^{-2}$	–	–
η	–	–	$6.2(1)\times10^{-5}$	$9.1(3)\times10^{-5}$
κ	–	–	$-5.1(2)\times10^{-5}$	$3.87(2)\times10^{-4}$
ω (deg)	218.6(1)	110.603(1)	–	–
T_0 (MJD)	51001.7900(8)	51602.186289(7)	–	–
$T_{\rm asc}$ (MJD)	–	–	51600.2842078(2)	51600.6250241(2)
$P_{\rm b}$ (days)	2.2568483(9)	2.357696895(10)	1.1890840496(4)	1.2017242354(6)
$\dot{P}_{\rm b}$ (10^{-12} s s^{-1}) ...	4.8(2)	−0.7(0.6)	1.0(2)	−4.9(4)
$\dot{\omega}$ (deg/yr)	$9(2)\times10^{-2}$	$6.73(2)\times10^{-2}$	–	0.33(9)
Derived Parameters				
θ_α (arcmin)	+0.4179	+0.0795	+0.8326	−0.1301
θ_δ (arcmin)	−0.4587	+0.7636	+0.4578	+0.1712
$\theta_\perp$ (arcmin)	0.6205	0.7677	0.9502	0.2150
$\theta_\perp$ (core radii)	1.7882	2.2123	2.7383	0.6196
$r_\perp$ (pc)	0.8465	1.0473	1.2963	0.2933
P (ms)	3.53632915276243(3)	3.2103407093504(1)	4.0331811845726(2)	2.83040595787912(7)
$\dot{P}$ (10^{-21} s s^{-1}) ...	98.5103(5)	−1.830(1)	34.0076(6)	−120.541(1)
$a_{l,\rm GC}$ (10^{-9} m s^{-2})..	+7.31(32)	−1.0(0.9)	+3.0(0.7)	−14.2(1.1)
$\dot{P}_{\rm int}$ (10^{-21} s s^{-1}) ..	11.9(3.7)	9(9)	−6(9)	13(10)
$B_{\rm s}$, (10^8 G)	2.07	2.31	< 1.96	1.94
$L_{\rm sd}$ (10^{33} erg s^{-1}) ..	10.62	19.82	−0.72	23.17
$\tau_{\rm c}$ (Gyr)	4.7	> 1.9	> 5.0	> 1.3
$\dot{a}_l$ (10^{-21} m s^{-3}) ...	−3.10(26)	−154.5(2.2)	−0.9(1.3)	6.6(6)
$f(M_{\rm p})$ ($M_\odot$)	0.0016409130(15)	0.001927197(6)	0.002374007(5)	0.0003345154(10)
$M_{\rm c,min}$ ($M_\odot$)	0.159	0.168	0.181	0.091
$M_{\rm c,med}$ ($M_\odot$)	0.185	0.196	0.212	0.105
$M_{\rm tot}$ ($M_\odot$)	2.3(7)	1.665(7)	–	3.1(1.1)

Parameters: see Table 4.2

Table 4.3 – *continued*

Pulsar	47 Tuc T	47 Tuc U	47 Tuc Y
Phase-connected? ...	Yes	Yes	Yes
Reference Epoch (MJD)	51600.000	51600.000	51600.000
Start ToA (MJD) ...	50683.712	48515.506	50739.663
End ToA (MJD) ...	56466.934	56466.919	56508.973
Number of ToAs ...	554	1309	804
Residuals RMS (μs) ..	54.36	9.68	8.11
α (J2000) (hh:mm:ss) .	00:24:08.5491(5)	00:24:09.8366(1)	00:24:01.4026(1)
δ (J2000) (dd:mm:ss) .	−72:04:38.932(3)	−72:03:59.6882(4)	−72:04:41.8363(4)
μ_α (mas yr^{-1})	5.1(6)	4.6(2)	4.4(1)
μ_δ (mas yr^{-1})	−2.6(7)	−3.8(1)	−3.4(1)
f (Hz)	131.77869947406(2)	230.264772211776(6)	455.23717843241(1)
$\dot{f}$ (Hz s^{-1})	$-5.1021(2) \times 10^{-15}$	$-5.04916(9) \times 10^{-15}$	$7.2891(2) \times 10^{-15}$
$\ddot{f}$ (Hz s^{-2})	$-3(2) \times 10^{-27}$	$1.88(6) \times 10^{-26}$	$-2.11(9) \times 10^{-26}$
DM (pc cm^{-3})	24.41(2)	24.337(4)	24.468(4)
Binary Parameters			
Binary Model	ELL1	ELL1	ELL1
$x_{\rm p}$ (lt-s)	1.338501(5)	0.5269494(7)	0.6685965(7)
η	$3.55(7) \times 10^{-4}$	$-2.9(4) \times 10^{-5}$	$-3(3) \times 10^{-6}$
κ	$1.85(7) \times 10^{-4}$	$1.43(2) \times 10^{-4}$	$7(224) \times 10^{-8}$
$T_{\rm asc}$ (MJD)	51600.5692696(7)	51600.3893516(1)	51554.8340067(2)
$P_{\rm b}$ (days)	1.126176771(1)	0.42910568324(8)	0.5219386107(1)
$\dot{P}_{\rm b}$ (10^{-12} s s^{-1}) ...	2.5(1.1)	0.66(5)	−0.82(7)
$\dot{\omega}$ (deg/yr)	–	1.2(3)	–
Derived Parameters			
θ_α (arcmin)	+0.2215	+0.3207	−0.3283
θ_δ (arcmin)	+0.2280	+0.8821	+0.1799
$\theta_\perp$ (arcmin)	0.3179	0.9386	0.3743
$\theta_\perp$ (core radii)	0.9160	2.7049	1.0788
$r_\perp$ (pc)	0.4336	1.2805	0.5107
P (ms)	7.5884798073671(9)	4.3428266963923(1)	2.19665714352124(6)
$\dot{P}$ (10^{-21} s s^{-1}) ...	293.80(1)	95.228(2)	−35.1720(8)
$a_{l,\rm GC}$ (10^{-9} m s^{-2}) .	7.7(3.5)	5.31(38)	−5.4(4)
$\dot{P}_{\rm int}$ (10^{-21} s s^{-1}) ..	99(89)	18(5)	4.7(3.3)
$B_{\rm s}$, (10^8 G)	8.67	2.81	1.02
$L_{\rm sd}$ (10^{33} erg s^{-1}) ..	8.94	8.79	17.48
$\tau_{\rm c}$ (Gyr)	>0.43	3.8	>3.1
$\dot{a}_l$ (10^{-21} m s^{-3}) ...	7.8(3.7)	−24.4(8)	13.9(6)
$f(M_{\rm p})$ ($M_\odot$)	0.002030139(25)	0.0008532200(35)	0.0011779754(37)
$M_{\rm c,min}$ ($M_\odot$)	0.171	0.126	0.141
$M_{\rm c,med}$ ($M_\odot$)	0.200	0.146	0.164
$M_{\rm tot}$ ($M_\odot$)	–	1.7(7)	–

Parameters: see Table 4.2

Table 4.4. Timing parameters of four of the five "black widow" systems of 47 Tuc. The associated 1-σ uncertainties were calculated using a Monte-Carlo bootstrap routine implemented in `TEMPO`. For all the pulsars, a fixed parallax value of 0.2132 mas was assumed; the time units are TDB; the assumed terrestrial time standard is UTC(NIST); the Solar System ephemeris used is the JPL DE421.

Pulsar	47 Tuc I	47 Tuc J	47 Tuc O	47 Tuc R
Phase-connected? ...	Yes	Yes	Yes	Yes
Reference Epoch (MJD)	51600.000	51600.000	51600.000	51600.000
Start ToA (MJD) ...	47859.462	47717.894	50683.712	50742.607
End ToA (MJD) ...	56466.878	56388.106	56508.991	55362.896
Number of ToAs ...	1201	10135	1903	449
Residuals RMS (μs) ..	18.26	4.89	9.70	10.81
α (J2000) (hh:mm:ss) .	00:24:07.9347(2)	00:23:59.4077(1)	00:24:04.65254(6)	00:24:07.5851(2)
δ (J2000) (dd:mm:ss) .	−72:04:39.6815(7)	−72:03:58.7908(5)	−72:04:53.7670(2)	−72:04:50.3954(5)
μ_α (mas yr^{-1})	5.0(2)	5.27(6)	5.01(5)	4.8(1)
μ_δ (mas yr^{-1})	−2.1(2)	−3.59(9)	−2.58(8)	−3.3(2)
f (Hz)	286.94469953049(1)	476.04685844061(1)	378.308788360098(6)	287.31811946930(1)
$\dot{f}$ (Hz s^{-1})	$3.7771(2)\times10^{-15}$	$2.2190(2)\times10^{-15}$	$-4.34352(8)\times10^{-15}$	$-1.22467(2)\times10^{-14}$
$\ddot{f}$ (Hz s^{-2})	$-3.35(9)\times10^{-26}$	$2.0(1)\times10^{-26}$	$4.38(5)\times10^{-26}$	$-8.5(1.5)\times10^{-27}$
DM (pc cm^{-3})	24.43(1)	24.588(3)	24.356(2)	24.361(7)
		Binary Parameters		
Binary Model	ELL1	BTX	BTX	ELL1
$x_{\rm p}$ (lt-s)	$3.8446(1)\times10^{-2}$	$4.04058(6)\times10^{-2}$	$4.51533(3)\times10^{-2}$	$3.3363(1)\times10^{-2}$
e	–	0	0	–
η	0	–	–	$-10(6)\times10^{-5}$
κ	0	–	–	$-3(7)\times10^{-5}$
ω (deg)	–	0	0	–
T_0 (MJD)	–	51600.1084250(6)	51600.0757563(3)	–
$T_{\rm asc}$ (MJD)	51600.002421(2)	–	–	51600.0029871(6)
$P_{\rm b}$ (days)	0.2297922489(4)	–	–	$6.623147751(6)\times10^{-2}$
$\dot{P}_{\rm b}$ (10^{-12} s s^{-1}) ...	−0.8(2)	–	–	0.19(4)
$f_{\rm b}$ (s^{-1})	–	$9.59191153(1)\times10^{-5}$	$8.511956725(6)\times10^{-5}$	–
$f_{\rm b}^{(1)}$ (s^{-2})	–	$-21(34)\times10^{-22}$	$-7.3(1)\times10^{-20}$	–
$f_{\rm b}^{(2)}$ (s^{-3})	–	$-19(21)\times10^{-29}$	$-10(2)\times10^{-29}$	–
$f_{\rm b}^{(3)}$ (s^{-4})	–	$3.9(5)\times10^{-35}$	$33(15)\times10^{-37}$	–
$f_{\rm b}^{(4)}$ (s^{-5})	–	$-15(24)\times10^{-44}$	–	–
$f_{\rm b}^{(5)}$ (s^{-6})	–	$-5.5(8)\times10^{-50}$	–	–
$f_{\rm b}^{(6)}$ (s^{-7})	–	$58(23)\times10^{-59}$	–	–
$f_{\rm b}^{(7)}$ (s^{-8})	–	$55(10)\times10^{-66}$	–	–
$f_{\rm b}^{(8)}$ (s^{-9})	–	$-89(20)\times10^{-74}$	–	–
$f_{\rm b}^{(9)}$ (s^{-10})	–	$-3.9(8)\times10^{-80}$	–	–
$f_{\rm b}^{(10)}$ (s^{-11})	–	$86(15)\times10^{-89}$	–	–
$f_{\rm b}^{(11)}$ (s^{-12})	–	$15(37)\times10^{-96}$	–	–
$f_{\rm b}^{(12)}$ (s^{-13})	–	$-42(8)\times10^{-104}$	–	–
		Derived Parameters		
θ_α (arcmin)	+0.1742	−0.4821	−0.0783	+0.1473
θ_δ (arcmin)	+0.2156	+0.8972	−0.0192	+0.0371
$\theta_\perp$ (arcmin)	0.2772	1.0185	0.0806	0.1519
$\theta_\perp$ (core radii)	0.7989	2.9352	0.2322	0.4378
$r_\perp$ (pc)	0.3782	1.3895	0.1099	0.2072
P (ms)	3.4849920616629(1)	2.10063354535248(6)	2.64334329724356(4)	3.4804627074933(2)
$\dot{P}$ (10^{-21} s s^{-1}) ...	−45.873(2)	−9.7919(9)	30.3493(6)	148.351(3)
$a_{l,\rm GC}$ (10^{-9} m s^{-2}) .	−11.8(3.7)	–	–	10.1(1.9)
$\dot{P}_{\rm int}$ (10^{-21} s s^{-1}) ..	92(43)	–	–	31(22)
$B_{\rm s}$, (10^8 G)	5.65	–	–	3.29
$L_{\rm sd}$ (10^{33} erg s^{-1}) ..	85.55	–	–	29.04
$\tau_{\rm c}$ (Gyr)	0.60	–	–	> 0.73
$\dot{a}_l$ (10^{-21} m s^{-3}) ...	35(1)	−12.5(9)	−34.68(37)	8.9(1.5)
$f(M_{\rm p})$ (M$_\odot$)	0.0000011555(1)	0.0000048646(2)	0.0000053461(1)	0.0000090898(10)
$M_{\rm c,min}$ (M$_\odot$)	0.0132	0.0214	0.0221	0.0264
$M_{\rm c,med}$ (M$_\odot$)	0.0153	0.0248	0.0256	0.0306

Parameters: see Table 4.2

Table 4.5. Timing parameters for the four "elusive" binary pulsar systems of 47 Tuc discussed in Section 4.4. The associated 1-σ uncertainties are the nominal values calculated by `TEMPO`. For all the pulsars, a fixed parallax value of 0.2132 mas was assumed; the time units are TDB; the assumed terrestrial time standard is UTC(NIST); the Solar System ephemeris used is the JPL DE421.

Pulsar	47 Tuc P	47 Tuc V	47 Tuc W	47 Tuc X
Phase-connected? ..	No	No	Yes	Yes
Reference epoch (MJD)	51000.000	51000.000	50000.000	54000.000
Start ToA (MJD) ...	50689.609	51012.862	51214.216	50981.881
End ToA (MJD) ...	54260.850	56508.781	54934.047	56508.949
Number of ToAs ...	28	99	199	719
Residuals RMS (μs) .	10.43	25.32	10.20	14.51
α (J2000) (hh:mm:ss)	00:24:20(29)	00:24:05.359[a]	00:24:06.058(1)	00:24:22.38565(9)
δ (J2000) (dd:mm:ss) .	−72:04:10(62)	−72:04:53.20[a]	−72:04:49.088(2)	−72:01:17.4414(7)
μ_α (mas yr^{-1})	4.9[a]	4.9[a]	6.1(5)	5.8(1)
μ_δ (mas yr^{-1})	−2.7[a]	−2.7[a]	−2.6(3)	−3.3(2)
f (s^{-1})	274.49748(2)	207.892963(3)	425.10779625320(5)	209.576694635350(2)
$\dot{f}$ (Hz s^{-2})	$-5(3)\times10^{-14}$	–	$1.56415(2)\times10^{-14}$	$-8.0646(3)\times10^{-16}$
$\ddot{f}$ (Hz s^{-2})	–	–	$1.5(7.4)\times10^{-27}$	$1.3(7.8)\times10^{-28}$
DM (pc cm^{-3})	24.29(3)	24.105(8)	24.367(3)	24.539(5)
Binary Parameters				
Binary Model	BT	BTX	BTX	ELL1
x_p (lt-s)	0.038008(4)	0.74191(2)	0.243443(2)	11.9170570(9)
e	0	0	0	–
η	–	–	–	$4(1)\times10^{-7}$
κ	–	–	–	$-2(2)\times10^{-7}$
ω (deg)	0	0	0	–
T_0 (MJD)	52912.5481(1)	51803.775137(2)	51585.3327393(2)	–
T_{asc} (MJD)	–	–	–	53278.0247041(2)
P_b (days)	0.147248891(7)	–	–	10.921183545(1)
$\dot{P}_b$ (10^{-12} s s^{-1}) ..	–	–	–	6(2)
f_b (s^{-1})	–	$5.45609205(4)\times10^{-5}$	$8.70594798(3)\times10^{-5}$	–
$f_b^{(1)}$ (s^{-2})	–	$-2.34(4)\times10^{-18}$	$-1.26(4)\times10^{-18}$	–
$f_b^{(2)}$ (s^{-3})	–	$2.34(6)\times10^{-26}$	$4.0(2)\times10^{-26}$	–
$f_b^{(3)}$ (s^{-4})	–	$2.31(6)\times10^{-33}$	$6.3(3)\times10^{-33}$	–
$f_b^{(4)}$ (s^{-5})	–	$-6.7(2)\times10^{-41}$	$-9.2(4)\times10^{-40}$	–
$f_b^{(5)}$ (s^{-6})	–	$5.6(1)\times10^{-49}$	$6.3(3)\times10^{-47}$	–
$f_b^{(6)}$ (s^{-7})	–	–	$-2.7(1)\times10^{-54}$	–
$f_b^{(7)}$ (s^{-8})	–	–	$7.4(3)\times10^{-62}$	–
$f_b^{(8)}$ (s^{-9})	–	–	$-1.22(5)\times10^{-69}$	–
$f_b^{(9)}$ (s^{-10})	–	–	$9.3(4)\times10^{-78}$	–
Derived Parameters				
θ_α (arcmin)	1.1289	-0.0239	+0.0299	+1.2899
θ_δ (arcmin)	+0.7063	-0.0097	+0.0589	+3.5863
$\theta_\perp$ (arcmin)	1.3314	0.0258	0.0660	3.8105
$\theta_\perp$ (core radii)	3.8368	0.0744	0.1902	10.9813
$r_\perp$ (pc)	1.8163	0.0352	0.0901	5.1986
P (ms)	3.6430207(2)	4.81016762(7)	2.3523445319370(3)	4.77152291069355(5)
$\dot{P}$ (10^{-21} s s^{-1}) ...	683(419)	–	-86.553(1)	18.3609(7)
$a_{l,GC}$ (10^{-9} m s^{-2}) .	–	–	–	1.7(7)
$\dot{P}_{int}$ (10^{-21} s s^{-1}) ..	–	–	–	< 2
B_s, (10^8 G)	–	–	–	< 3
L_{sd} (10^{33} erg s^{-1}) ..	–	–	–	< 7
τ_c (Gyr)	–	–	–	> 4
$\dot{a}_l$ (10^{-21} m s^{-3}) ...	–	–	−1(5)	−0.2(1.1)
$f(M_p)$ ($M_\odot$)	2.7188×10^{-6}	9.743×10^{-3}	8.764×10^{-4}	1.524×10^{-2}
M_c^{min} ($M_\odot$)	0.0176	0.3048	0.1269	0.3616
$M_{c,med}$ ($M_\odot$)	0.0204	0.3594	0.1479	0.4279

[a] The proper motion was set to the average value of the 22 pulsars with a phase-connected timing solution available at the time of the analysis.

Parameters: see Table 4.2

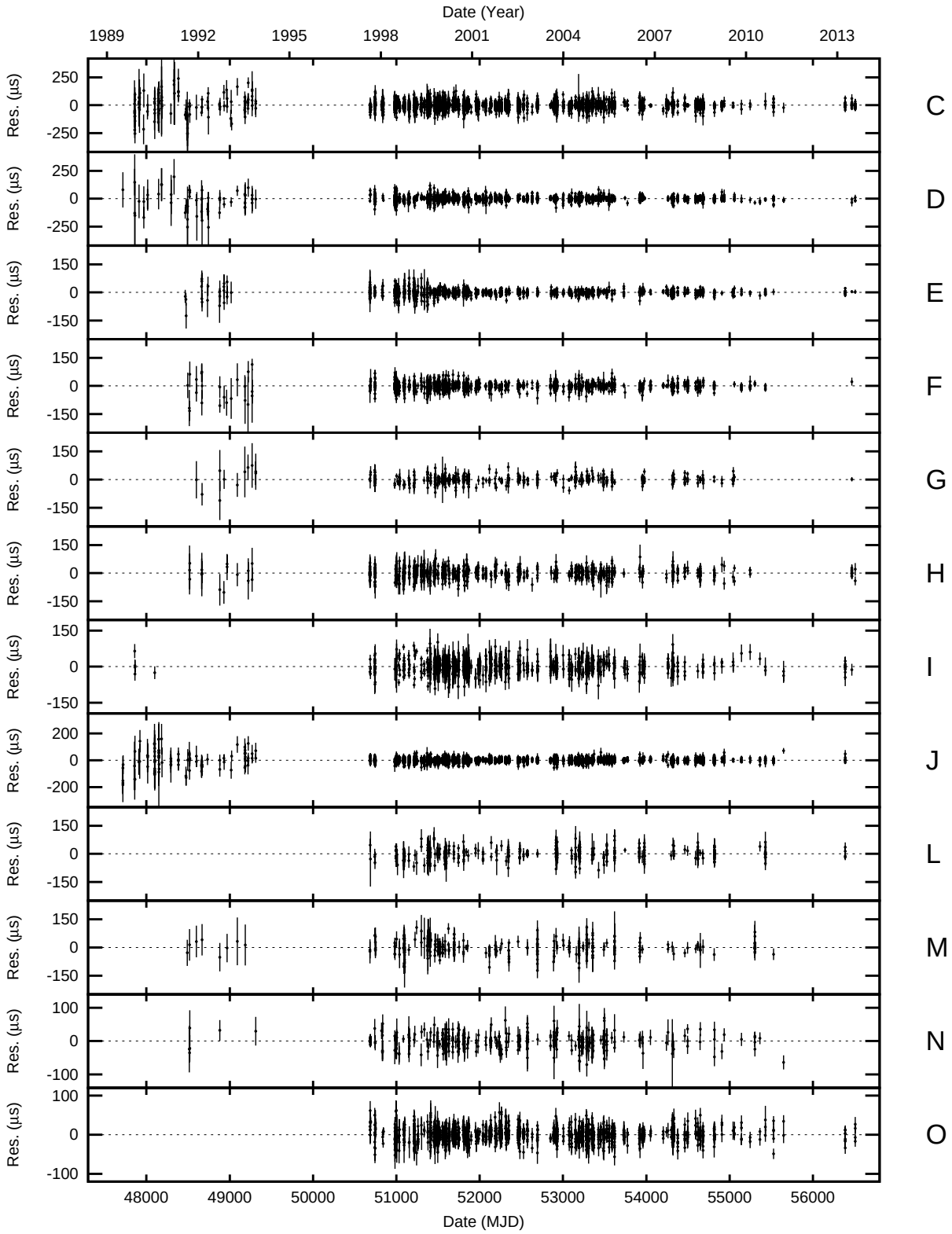

Figure 4.3. Timing residuals of all the 23 pulsars in 47 Tuc with a phase-connected timing solution determined.

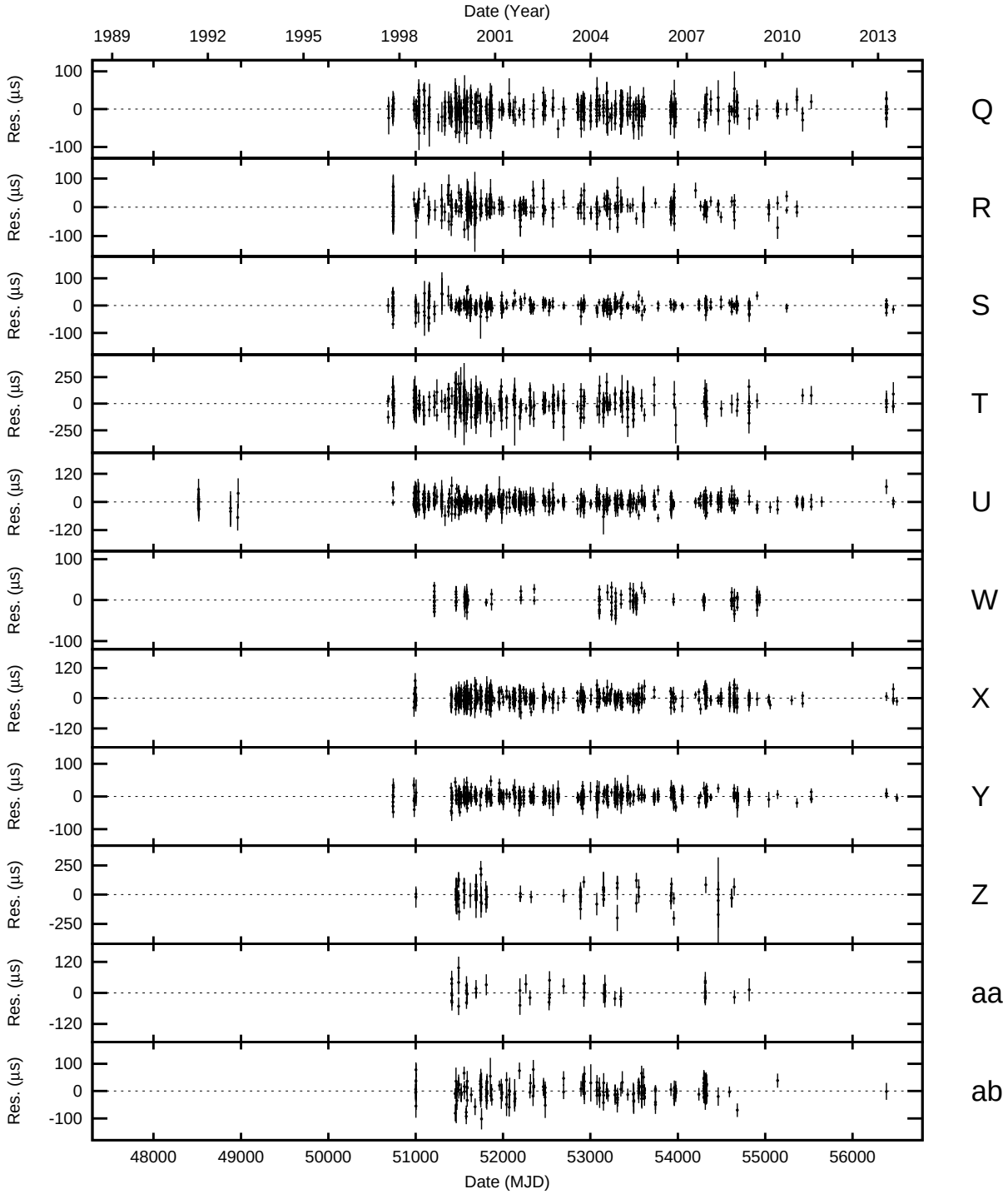

Figure 4.3 – *continued*

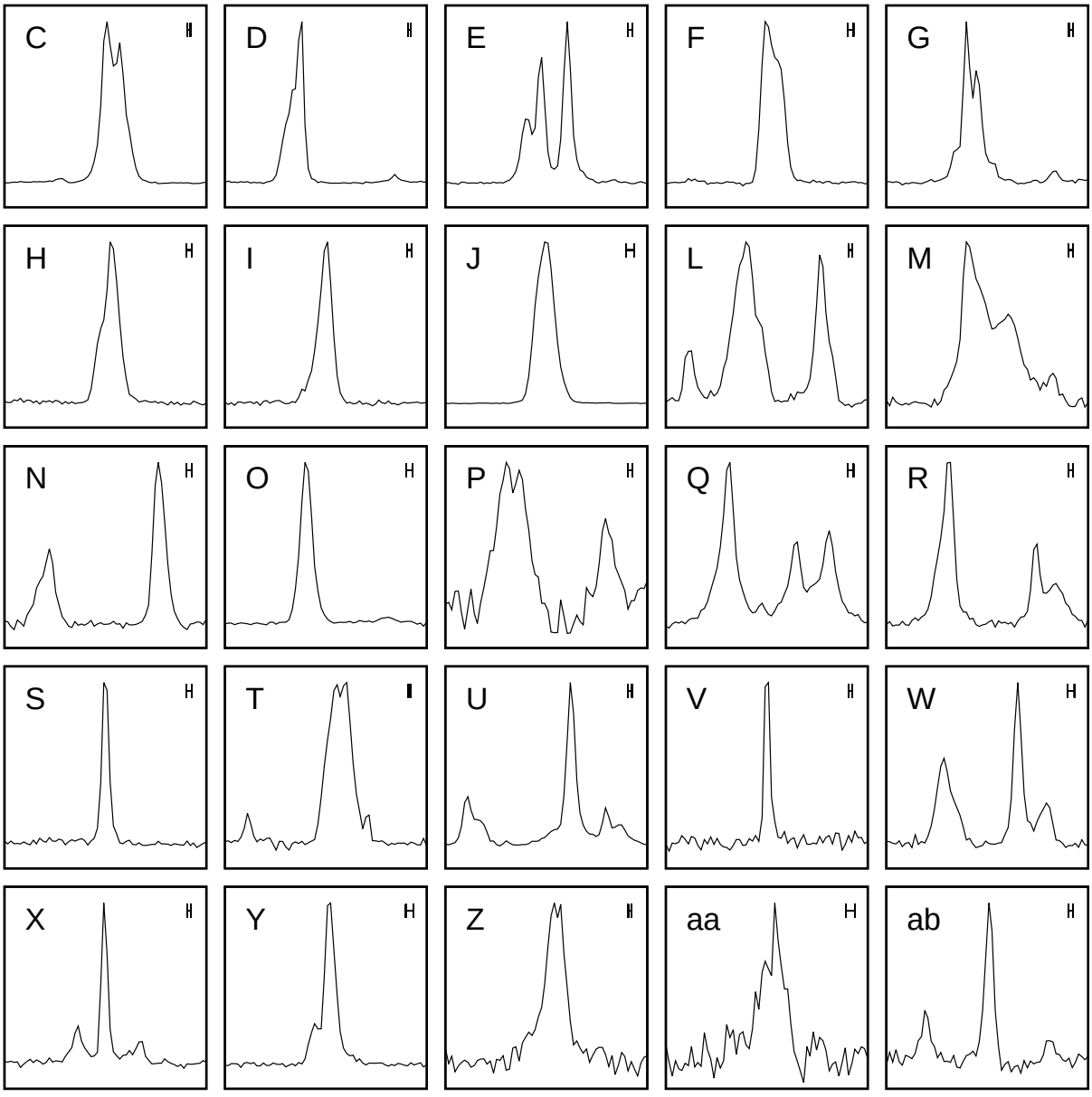

Figure 4.4. High-S/N integrated pulse profiles (used as templates in our timing analysis) for all the 25 pulsars known in 47 Tuc. Each profile has 64 bins and is shown over one full rotation. The horizontal bar on the top right of each panel shows the nominal AFB back-end sampling interval (80 μs).

Chapter 5

Implications on the dynamics of 47 Tucanae

The work presented in this chapter is published in the following articles:

- **Ridolfi, A.**; Freire, P. C. C.; Torne, P.; Heinke, C. O.; van den Berg, M.; Jordan, C.; Kramer, M.; Bassa, C. G.; Sarkissian, J.; D'Amico, N.; Lorimer, D.; Camilo, F.; Manchester, R. N.; Lyne, A., *"Long-term observations of the pulsars in 47 Tucanae - I. A study of four elusive binary systems"*; MNRAS, 2016, Volume 462, Issue 3, p.2918-2933
- Freire, P. C. C.; **Ridolfi, A.**; Kramer, M; Jordan, C.; Manchester, R. N.; Torne, P.; Sarkissian, J.; D'Amico, N.; Camilo, F.; Lorimer, D. R.; Lyne, A. G.; *"Long-term observations of the pulsars in 47 Tucanae - II. Proper motions, accelerations and jerks"*; Submitted to MNRAS

My main contribution for this chapter was the reduction of the radio data and the derivation of the observed parameters through the timing analysis. The reduction and analysis of the X-ray and optical data for the pulsar 47 Tuc X were carried out by co-authors.

Contents

5.1 Introduction

The timing results presented in the previous chapter are relevant not only for the characterization of the individual pulsars of 47 Tuc, but also because they enable a series of additional investigations of the cluster itself.

Here, we discuss the results shown in Chapter 4 in detail and use them to constrain some dynamical properties of 47 Tuc, obtaining significant improvements over the previously published models of the cluster (Freire et al., 2003).

5.2 Cluster parameters

In the analysis presented in this chapter, we benefit greatly from the new studies of *Hubble Space Telescope* (*HST*) data that have become available since the last study of the cluster potential (Freire et al., 2003). These data provide much more precise cluster parameters and in some cases entirely new information. As already anticipated in Section 4.1, McLaughlin et al. (2006) place the centre of 47 Tuc at right ascension $\alpha = 00^{\rm h}\,24^{\rm m}\,5.67^{\rm s}$ and declination $\delta = -72^\circ\,04'\,52''.62$; they also measure the core radius: $\theta_{\rm c} = 0.347$ arcmin. A newly available measurement, which will be of great importance for this work, is the 1-D proper motion dispersion for stars at the cluster centre obtained from differential *HST* astrometry: $\sigma_{\mu,0} = 0.573\,{\rm mas\,yr^{-1}}$ (Watkins et al., 2015a).

From Eq. (1)-(34) in Spitzer (1987), which is accurate to ∼0.5% for clusters where the tidal radius, $r_{\rm tid}$, is much larger than the core radius, $r_{\rm core}$ (such as 47 Tuc, where $\log_{10}(r_{\rm tid}/r_{\rm core}) = 2.07$, see Harris 1996), we derive the following expression for the central density:

$$\rho(0) = \frac{9\,\sigma_{\mu,0}^2}{4\pi G\,\theta_{\rm c}^2}\,, \tag{5.1}$$

where we have replaced the spectroscopic radial velocity (RV) dispersion σ_0 with $\sigma_{\mu,0}\,d$ (where d is the distance to 47 Tuc) and the core radius $r_{\rm core}$ with $\theta_{\rm c}\,d$. The distance terms then cancel out; this means that the central density can be determined solely from the aforementioned angular measurements, independently of d. For the value of $\sigma_{\mu,0}$ and $\theta_{\rm c}$ of 47 Tuc, Eq. (5.1) yields $\rho(0) = 1.20 \times 10^5\ {\rm M_\odot\,pc^{-3}}$.

For the distance d, we use 4.69 kpc (Woodley et al., 2012). Other recent assessments placed the cluster at very similar distances; for instance, using the (relatively well-trusted) WD cooling track model, Hansen et al. (2013) derived a distance of 4.6 ± 0.2 kpc. Using other methods, like the self-consistent isochrone fits to colour-magnitude diagrams and the eclipsing binary star V69, Brogaard et al. (2017) derived a slightly smaller distance of 4.4 ± 0.2 kpc. Averaging several recent measurements, Bogdanov et al. (2016) obtained a distance of $4.53^{+0.08}_{-0.04}$ kpc.

However, not all distance estimates match: by comparing their measurement of $\sigma_{\mu,0}$ to their best estimate of σ_0, Watkins et al. (2015b) derived a kinematic distance of 4.15 ± 0.08 kpc, consistent with the earlier estimate of McLaughlin et al. (2006) ($d = 4.02 \pm 0.35$ kpc).

A possible explanation of this discrepancy is that the σ_0 measurements (generally close to 11 km s^{-1}), are biased towards smaller values. Likely reasons for this are discussed in detail in Bogdanov et al. (2016). Briefly, those authors pointed out that the RV measurements used for comparison were intended to be of single stars, but *HST* images show that a number of the targeted "stars" actually comprise more than one star of similar brightness. The RV measurements of combined stars tend to be closer to the cluster mean than single stars, so

this has the effect of reducing the inferred velocity dispersion, and the resultant distance to the cluster. Indeed, when Watkins et al. (2015b) included a larger sample of RV measurements that extend further out from the core of 47 Tuc to compare with their proper motions, they found a distance of $4.61^{+0.06}_{-0.07}$ kpc (see their Appendix A, Fig. 9), consistent with the larger distances mentioned above.

This issue is crucial for the interpretation of our results. As we will see in Sections 5.5 and 5.6, our results also favour this large distance, in detriment of the smaller kinematic distance estimates. This is also crucial for addressing the question of the presence of an intermediate mass black hole in the centre of 47 Tucanae, which has been repeatedly raised in the literature.

5.3 Positions

Fig. 5.1 shows the positions of all the 23 pulsars in 47 Tuc with a phase-connected timing solution, with their numerical values being listed in Tables 4.2 to 4.5.

The first striking evidence is that all the pulsars, with the exception of one, are well within the distance of 47 Tuc C to the centre of the cluster, namely 1.22 arcmin. Since the Parkes beam at 20 cm has a FWHM of 14.4 arcmin, this is not a selection effect. Rather, it is a clear consequence of the mass segregation produced by dynamical friction. Indeed, closer to the core, the relaxation time is much shorter, hence the pulsars are likely to have reached dynamical equilibrium with the stellar population there.

The only exception to this is represented by the binary system 47 Tuc X, which stands out for its distance of ~ 3.8 arcmin from the nominal cluster centre, more than three times farther than pulsar C. The system is very interesting not only for its unusual location, but also for other reasons that will be thoroughly discussed in Section 5.8.

5.4 Proper motions

One of the main benefits of long-term timing is a better determination of the proper motions. In Freire et al. (2001b), the number and precision of the proper motions was small and only the motion of the GC as a whole was detectable. With a few more years of intense timing with the high-resolution AFB data, some of the proper motions were measured precisely enough to detect relative motions, particularly for 47 Tuc D, E and J (Freire et al., 2003).

Because of the increased timing baselines, the proper motions presented here are significantly more precise. In Fig. 5.2, we display the 17 pulsars for which both the proper motion 1-σ Monte Carlo uncertainties (in ecliptic longitude and ecliptic latitude) are smaller than 0.3 mas yr^{-1}. Although the proper motions themselves are displayed in J2000 equatorial coordinates, the error ellipses are aligned according to ecliptic coordinates, where the measurement uncertainties are least correlated. For these pulsars, the (unweighted) average proper motion is $\mu_\alpha = 5.00$ mas yr^{-1} and $\mu_\delta = -2.84$ mas yr^{-1}, and is depicted by the solar symbol in Fig. 5.2. This represents the simplest estimate for the proper motion of the cluster as a whole, and it is consistent with the estimate presented in Freire et al. (2003): $\mu_\alpha = 5.3 \pm 0.6$ mas yr^{-1} and $\mu_\delta = -3.3 \pm 0.6$ mas yr^{-1}. The standard deviations of the proper motions around this average (σ_μ) are 0.59 mas yr^{-1} in α and 0.49 mas yr^{-1} in δ. At a distance of 4.69 kpc (Woodley et al., 2012), these standard deviations correspond to 13.2 and 10.9 km s^{-1} respectively. The uncertainty in the mean value is given by $\sigma_\mu/\sqrt{N}$, where N is the number of measurements (17, in

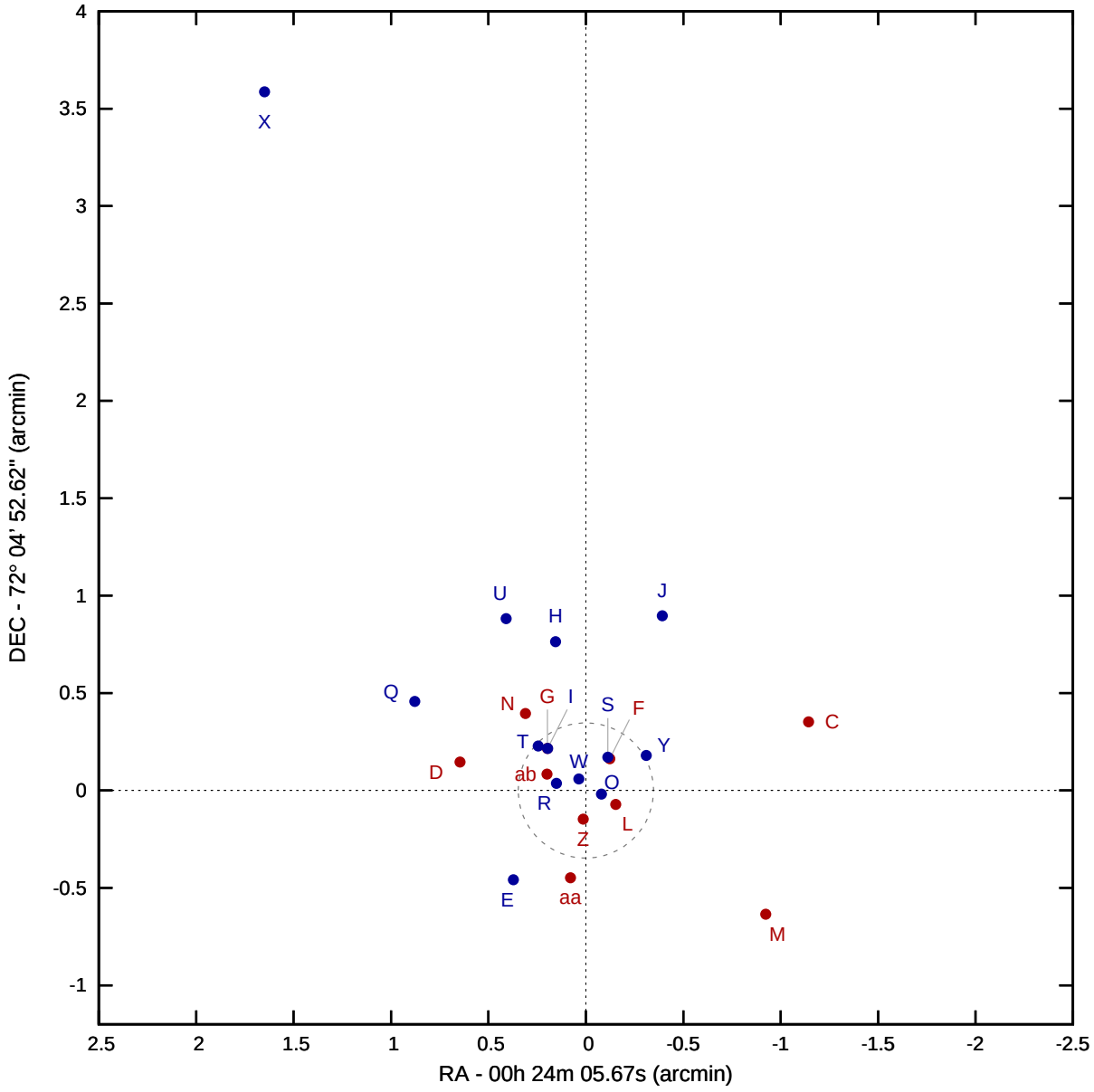

Figure 5.1. Positions of the 23 pulsars in 47 Tuc with a phase-connected timing solution determined. The blue dots and the red dots indicate the binary and the isolated pulsars, respectively. The grey dashed circle marks the cluster core radius, placed at a distance of 0.347 arcmin (McLaughlin et al., 2006). The distance of pulsar 47 Tuc X from the nominal cluster centre is ~ 3.8 arcmin, more than three times that of pulsar C, the second farthest in 47 Tuc.

this case). Thus our uncertainties for the mean cluster motion are $\sigma_{\mu_\alpha} = 0.14$ mas yr^{-1} and $\sigma_{\mu_\delta} = 0.12$ mas yr^{-1}.

An alternative method to estimate the overall motion of the cluster is to require that all observed pulsar proper motions fit within the smallest possible velocity envelope. This corresponds to finding the centre of a circle defined by the proper motions of the three outermost pulsars in the proper motion plot, namely 47 Tuc D, E and U (alternatively we can use 47 Tuc D, N and U; we prefer the former set because the proper motion for 47 Tuc E is known much more precisely). This minimal proper motion envelope is represented by the dashed circle and has a radius of 1.10 mas yr^{-1}; at 4.69 kpc this represents a velocity of 24.5 km s^{-1}, or about half of the escape velocity from the centre of the cluster ($\sim$ 50 km s^{-1}, e.g. McLaughlin et al. 2006). The centre of this minimal envelope is at $\mu_\alpha = 5.16$ mas yr^{-1} and $\mu_\delta = -2.85$ mas yr^{-1}, represented by a solid dot at the centre of Fig. 5.2. This μ_α is nearly 1-σ consistent with the average estimated above, the μ_δ is practically identical to the average.

5.4.1 Comparison with optical proper motions

We now compare these numbers with previous literature. Regarding the absolute proper motion, the latest relevant study combines *HIPPARCHOS* and *GAIA* positions to derive absolute proper motions for five Galactic globular clusters, among which is 47 Tuc (Watkins & van der Marel, 2016). The values they obtain ($\mu_\alpha = 5.50 \pm 0.70$ mas yr^{-1} and $\mu_\delta = -3.99 \pm 0.55$ mas yr^{-1}) are consistent with our measurement of the average proper motion in α, but in δ the deviation is -2.1-σ, i.e. only marginally consistent. In Section 3.1 of that paper they list previous measurements of the proper motion of 47 Tuc and discuss their consistency, and it is clear that there is some disagreement between the proper motion estimates obtained by different methods. The situation will likely improve significantly with the second release of *GAIA* data.

Our 1-D standard deviations for the proper motions is consistent with the $\sigma_{\mu,0}$ obtained by Watkins et al. (2015a). This result agrees qualitatively with the observation by McLaughlin et al. (2006) that the observed velocity dispersion is largely constant across magnitude range, i.e. it appears to be the same for stellar populations of different masses.

5.4.2 Proper motion pairs?

Given the extreme proximity of 47 Tuc I and G in the plane of the sky and in acceleration, there is a suggestion that these pulsars could be in a bound system, with a semi-major axis a_p of at least 600 AU (Freire et al., 2001b). Such systems are not stable in 47 Tuc, since their cross section for violent interactions is too large, but they can exist temporarily. If this were the case, then the maximum relative orbital velocity should be of the order of $v \sim \sqrt{GM_\mathrm{tot}/a_\mathrm{p}} = 2$ km s^{-1}. At the distance of 47 Tuc, this translates to an upper limit on the difference of proper motions of about 0.09 mas yr^{-1}. As we can see from Fig. 5.2, the difference is of the order of 1 mas yr^{-1}, ten times larger. We conclude therefore that, despite their proximity, these two pulsars are not in a bound system.

Two other pulsars, 47 Tuc F and S, are also remarkably close to each other and have DMs that are 1-σ compatible. In this case the minimum separation is 3700 AU (Freire et al., 2003), requiring a maximum relative orbital velocity of $v \sim 0.8$ km s^{-1} and a maximal proper motion difference of 0.036 mas yr^{-1}. Interestingly, this is not excluded by our measurements: as we can see in Fig. 5.2, the proper motion of 47 Tuc F falls within the 1-σ contour for the proper motion of 47 Tuc S. The latter covers 1.1% of the proper motion surface within the velocity envelope

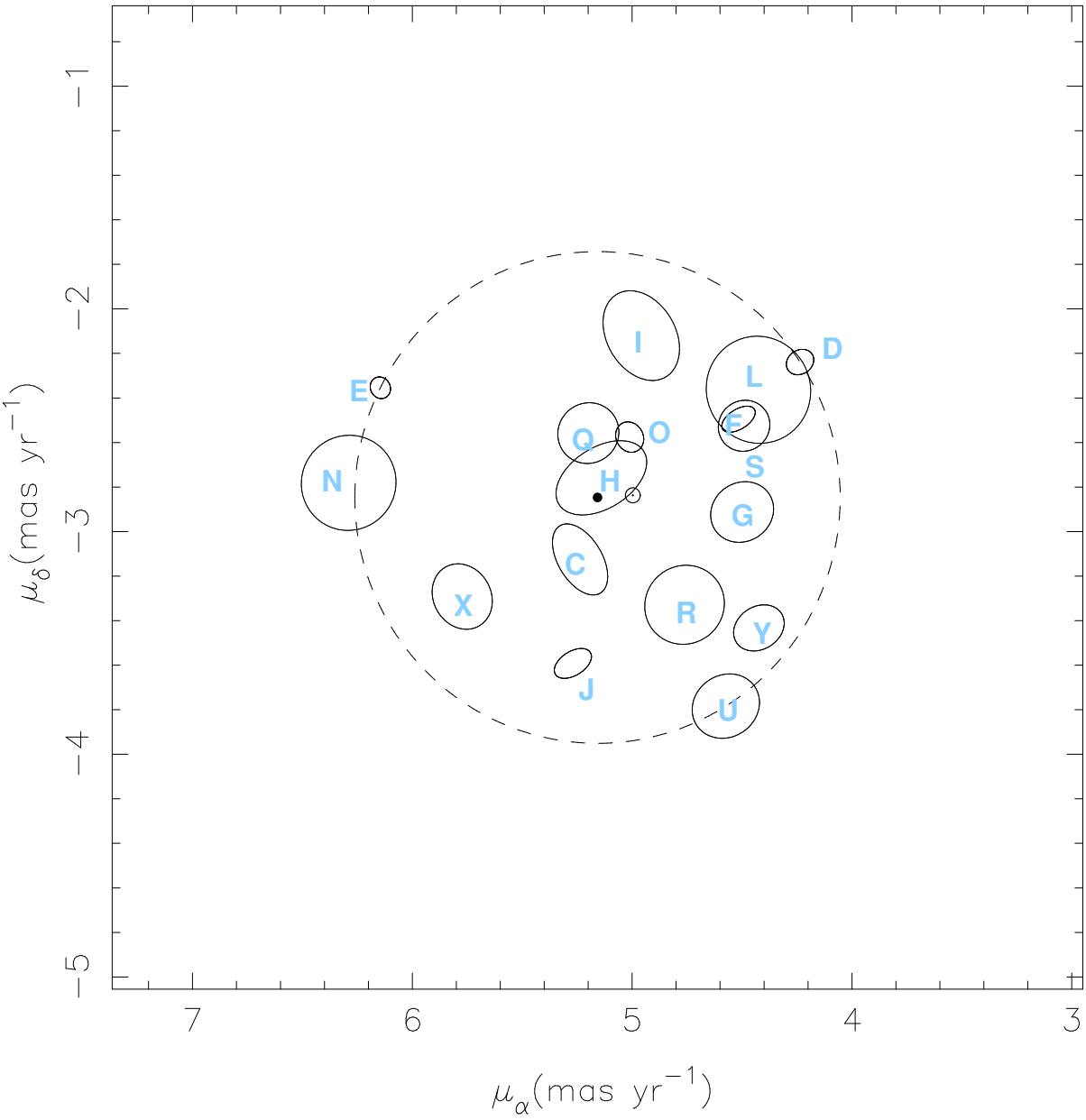

Figure 5.2. Proper motions for the 17 pulsars in 47 Tuc where the 1-σ uncertainties are smaller than 0.3 mas yr^{-1}. The proper motions are displayed by their 1-σ error ellipses, where the axes are aligned along ecliptic coordinates (where the positional and proper motion uncertainties are well defined). The differences in transverse velocity between the pulsars is highly significant, particularly for precisely timed pulsars like 47 Tuc D, E, F, J and O. The average of all proper motions in α and δ ($\mu_\alpha = 5.00$ mas yr^{-1} and $\mu_\delta = -2.84$ mas yr^{-1}) is given by the solar symbol near the centre of the plot. The dashed circle represents the minimal possible velocity envelope for these pulsars, its centre (the solid dot at the centre of the plot, at $\mu_\alpha = 5.16$ mas yr^{-1}, $\mu_\delta = -2.85$ mas yr^{-1}) represents an estimate of the proper motion of the globular cluster. This circle has a radius of 1.10 mas yr^{-1}. At the assumed distance to 47 Tuc (4.69 kpc) this is a velocity difference of 24.5 km s^{-1}, or about half of the escape velocity.

determined above, so that is the probability of coincidence for any given pulsar. Given their spatial proximity, the proper motion coincidence is suggestive of a temporarily bound status.

As mentioned in Freire et al. (2001b), another test of the bound nature of these systems would be the detection of changes in their line-of-sight accelerations, which will produce a second derivative of the spin frequency, $\ddot{f}$, also referred to as *jerk*. However, as we shall see in Section 5.5, the $\ddot{f}$'s of these pulsars (with the possible exception of 47 Tuc I) can be accounted for by their movement in the cluster potential.

5.5 Spin period/frequency derivatives

We will now discuss the measurements of the spin frequency (or, equivalently, spin period) derivatives of the pulsars in 47 Tuc. Like those of other pulsars in GCs (and unlike the spin frequency derivatives observed in the Galactic disk) the first spin frequency derivatives for the pulsars in 47 Tuc are *mostly* caused by dynamical effects. Higher spin frequency derivatives are, within our timing precision, instead caused *entirely* by dynamical effects.

5.5.1 First spin period derivative and upper limits on the cluster acceleration

The observed variation of spin period, $\dot{P}_{\rm obs}$, is generally given by the following equation:

$$\frac{\dot{P}_{\rm obs}}{P} = \frac{\dot{P}_{\rm int}}{P} + \frac{\mu^2 d}{c} + \frac{a_{l,\rm GC}}{c} + \frac{a_{\rm Gal}}{c}, \tag{5.2}$$

where P is the observed pulsar spin period, $\dot{P}_{\rm obs}$ is the observed spin period derivative, $\dot{P}_{\rm int}$ is the *intrinsic* spin period derivative, μ is the composite proper motion, d is the distance to the cluster (the term $\mu^2 d/c$ is known as the Shklovskii effect, see Shklovskii 1970), c is the speed of light, $a_{l,\rm GC}$ is the line-of-sight acceleration of the pulsar in the gravitational field of the cluster and $a_{\rm Gal}$ is the difference between the accelerations of the Solar System and 47 Tuc in the field of the Galaxy, projected along the direction to 47 Tuc ($a_{\rm Gal} = -1.172 \times 10^{-10}\,{\rm m\,s^{-2}}$, calculated using the Reid et al. 2014 model for the Galactic rotation). In principle, this equation could have other contributions, in particular accelerations caused by nearby stars; however, as shown by Phinney (1993), even in dense clusters those are very rarely relevant. As we shall see, the dominant term for the pulsars in 47 Tuc is $a_{l,\rm GC}$.

For most pulsars, we can only derive an upper limit, $a_{l,\rm max}$, on this dominant term from $\dot{P}_{\rm obs}/P$, since $\dot{P}_{\rm int}$ is generally not known but is always positive:

$$a_{l,\rm max} \doteq a_{l,\rm GC} + \frac{\dot{P}_{\rm int}}{P} c = \frac{\dot{P}_{\rm obs}}{P} c - \mu^2 d - a_{\rm Gal}. \tag{5.3}$$

These limits, calculated for all the pulsars, are displayed graphically in Fig. 5.3 as triangles pointing down (to emphasize that they represent an upper limit on the cluster acceleration). The black solid lines, instead, represent the maximum line-of-sight acceleration due to the cluster potential ($a_{l,\rm GC,\,max}$) for the analytical model of the cluster described in Freire et al. (2005). This uses the mass distribution described in King (1962) for the case where we are near (within ~ 4 core radii) the centre of the cluster:

$$\rho(x) = \frac{\rho(0)}{(1+x^2)^{3/2}}, \tag{5.4}$$

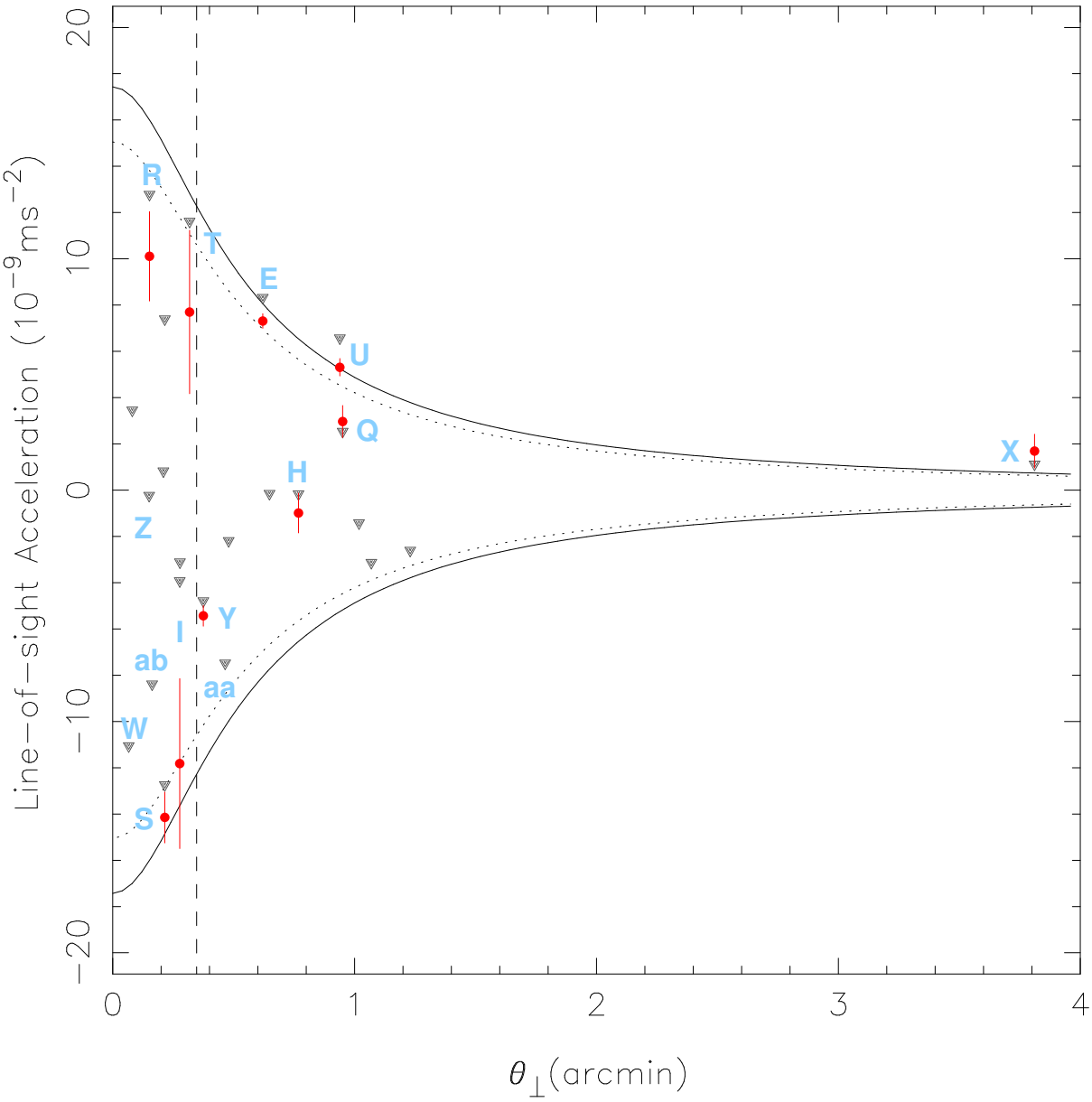

Figure 5.3. Line of sight accelerations (a_l) as a function of the total angular offset from the centre of the cluster ($\theta_\perp$) for the pulsars in 47 Tuc. The inverted triangles represent, for each pulsar system, an upper limit for its acceleration in field of the cluster, as determined from $\dot{P}_{\rm obs}$ via $a_{l,\rm max}$ (see discussion in Section 5.6). This is not a measurement of the real acceleration in the field of the cluster because of a contribution from the intrinsic spin period derivative of each pulsar ($\dot{P}_{\rm int}$). The red error bars represent measurements of the line-of-sight accelerations of 10 binary pulsars (47 Tuc E, H, I, Q, R, S, T, U, X and Y, which are named), determined from their orbital period derivatives, $\dot{P}_{\rm b,obs}$. We also plot the maximum and minimum theoretical accelerations along each line of sight using an analytical model of the cluster described in Section 5.5, with distances of 4.69 kpc (solid lines) and 4.15 kpc (dotted lines). We also name the systems with recently determined timing solutions (R, W, Z, aa, ab). The core radius is indicated by the vertical dashed line.

where x is the distance to the centre divided by the core radius $r_{\rm core} = \theta_{\rm c}\, d$. Here we use the $\rho(0)$ defined in Eq. (5.1). Since this is independent of distance, the mass of the cluster within a particular angular distance (i.e. within x core radii, $M_{\rm GC}(x)$) is proportional to d^3, so the acceleration at that x is proportional to $M_{\rm GC}(x)/d^2$, i.e., proportional to d:

$$a_{\rm GC}(x) = \frac{9\sigma^2_{\mu,0}\, d}{\theta_{\rm c}} \frac{1}{x^2} \left(\frac{x}{\sqrt{1+x^2}} - \sinh^{-1} x \right). \tag{5.5}$$

The line-of-sight component of this acceleration, $a_{l,\rm GC}(x)$, can be obtained by multiplying $a_{\rm GC}(x)$ by l/x, where l is the distance (also in core radii) to the plane of the sky that passes through the centre of the cluster (Σ), such that $x = \sqrt{l^2 + x^2_\perp}$ and $x_\perp = \theta_\perp/\theta_{\rm c}$. For each of the pulsar line-of-sight distances to the centre of the cluster, $\theta_\perp$, we calculate $a_{l,\rm GC}(x)$ for a variety of values of l, recording the maximum values found, $a_{l,\rm GC,max}$. These are the solid lines displayed in Fig. 5.3. For the line of sight going through the centre, we obtain the largest possible acceleration induced by the field of the cluster:

$$a_{l,\rm GC,max}(0) = 1.5689 \frac{\sigma^2_{\mu,0}\, d}{\theta_{\rm c}}; \tag{5.6}$$

the numerical factor matches the more general expectation of 1.50 ± 0.15 from Eq. (3.6) in Phinney (1993). The latter was used to constrain the cluster parameters in Freire et al. (2003).

Apart from d, the predicted $a_{l,\rm GC,max}(x_\perp)$ depends only on unambiguous angular measurements, meaning that the measurements of pulsar accelerations can be used to constrain d, i.e., this is a second kinematic distance measurement.

None of the pulsars, including those with recently found solutions (47 Tuc R, W, X, Y, Z, aa and ab, all named in Fig. 5.3), has a value of $a_{l,\rm max}$ that is significantly larger than the model $a_{l,\rm GC,\,max}$ for its line of sight: the magnitude of $a_{l,\,\rm GC}$ must be significantly larger than the contribution from $\dot{P}_{\rm int}$, otherwise a majority of $\dot{P}_{\rm obs}$ would be positive, while in fact similar numbers of pulsars have negative and positive $\dot{P}_{\rm obs}$. For three pulsars, 47 Tuc E, U and X, the $a_{l,\rm max}$ is slightly larger than $a_{l,\rm GC,\,max}$. For 47 Tuc E and U, this is caused by the contribution of their $\dot{P}_{\rm int}$; as we will see in Section 5.6, their line-of-sight accelerations are (just about) consistent with the cluster model. For 47 Tuc X, it is likely that the same is happening, although in that case the $\dot{P}_{\rm b,\,obs}$ is not yet precise enough to reach any definite conclusions. However, it is unlikely that the analytical acceleration model described above is still entirely valid at its large $\theta_\perp$.

5.5.2 Second spin frequency derivative (jerk)

In the absence of substantial timing noise (as is the case for most MSPs), the second spin frequency derivative ($\ddot{f}$) reflects the rate of change of a_l, known as the jerk. Rearranging Eq. (2) in (Joshi & Rasio, 1997), we obtain:

$$\frac{\dot{a}_l}{c} = \left(\frac{\dot{f}}{f}\right)^2 - \frac{\ddot{f}}{f} \simeq -\ddot{f}P, \tag{5.7}$$

where the approximation is valid since the first term, $(\dot{f}/f)^2$, is many orders of magnitude smaller than $\ddot{f}/f$. According to Phinney (1992), $\dot{a}_l$ has two main physical contributions. The first ($\dot{a}_{l,\rm GC}$) arises from the movement of the pulsar in the potential of the cluster: different positions in the cluster will generally have a different $a_{l,\rm GC}$; the movement of the pulsar from one position to the other will therefore cause a variation of this quantity. The second contribution

to $\dot{a}_l$ is due to the gravity of nearby stars; this is more significant for denser clusters.

Freire et al. (2003) detected the second spin frequency derivative for only one pulsar, 47 Tuc H ($\ddot{f} = 1.6 \pm 0.2 \times 10^{-25}\,\mathrm{Hz\,s^{-2}}$). They then estimated the maximum jerk induced by the motion of the pulsar in the mean field of the cluster ($\dot{a}_{l,\,\mathrm{GC,\,max}}$) and the corresponding $\ddot{f}$ ($\ddot{f}_{\mathrm{max}}$) using a slightly modified version of Eq. (4.3) in Phinney (1993):

$$\frac{\dot{a}_{l,\,\mathrm{GC,\,max}}(0)}{c} = -\frac{\ddot{f}_{\mathrm{max}}}{f} = -\frac{4\pi}{3} G\rho(0)\,\frac{v_{l,\mathrm{max}}}{c}, \tag{5.8}$$

where $v_{l,\mathrm{max}}$ is the maximum velocity of the pulsar relative to the cluster, in this case assumed to be moving along the line of sight; in Freire et al. (2003) this was assumed to be $\sigma_0 \sim 13\,\mathrm{km\,s^{-1}}$. The sign depends on the direction of $v_{l,\mathrm{max}}$, if the latter is positive (i.e., the pulsar is moving away from us), then $\dot{a}_{l,\,\mathrm{GC,\,max}}(0)$ is negative. The $\ddot{f}$ of 47 Tuc H is much larger than the estimated $\ddot{f}_{\mathrm{max}}$, from this they concluded that this system is being perturbed by a nearby stellar companion.

However, that estimate of $\dot{a}_{l,\,\mathrm{GC,\,max}}$ (and $\ddot{f}_{\mathrm{max}}$) is not very precise: first, because Eq. (5.8) applies only to the centre of the cluster; second because, as we have seen in Section 5.4, individual pulsars can have velocities along any direction that are almost twice as large as σ_0. Furthermore, and owing to our larger timing baseline T, we are now able to measure $\dot{a}_l$ precisely for almost all MSPs in 47 Tuc (see Tables 4.2-4.4). This improvement in measurements of $\dot{a}_l$ must be matched by an improvement in the prediction of $\dot{a}_{l,\,\mathrm{GC,\,max}}$.

This prediction is obtained from the gradient of $a_{l,\,\mathrm{GC}}$ along the radial direction $r \equiv l\,r_{\mathrm{core}}$ where it reaches a maximum, at $r = l = 0$ (i.e. in the plane Σ) and then multiplying it by $v_{l,\,\mathrm{max}}$. Near this plane l is small, so $x = \sqrt{l^2 + x_\perp^2} \simeq x_\perp$ is basically independent of l. In that case, the line-of-sight accelerations can be derived trivially from Eq. (5.5) multiplied by the projection factor $l/x_\perp$:

$$a_{l,\mathrm{GC}}(x_\perp) = \frac{9\,\sigma_{\mu,0}^2\,d}{\theta_\mathrm{c}}\,\frac{l}{x_\perp^3}\left(\frac{x_\perp}{\sqrt{1+x_\perp^2}} - \sinh^{-1} x_\perp\right). \tag{5.9}$$

Being proportional to l in the vicinity of Σ, these line-of-sight accelerations are zero for any object in Σ, so the only non-zero spatial derivative of $a_{l,\mathrm{GC}}$ in that plane is along its normal: the radial direction r. This derivative is trivial since Eq. (5.9) is linear on l. Using $\mathrm{d}l/\mathrm{d}r = \mathrm{d}l/(d\,\theta_\mathrm{c})\mathrm{d}l = 1/(d\,\theta_\mathrm{c})$, we obtain, for $l = 0$ (not forgetting $v_{l,\,\mathrm{max}}$):

$$\dot{a}_{l,\,\mathrm{GC,max}}(x_\perp) = \frac{9\,\sigma_{\mu,0}^2}{\theta_\mathrm{c}^2}\,\frac{1}{x_\perp^3}\left(\frac{x_\perp}{\sqrt{1+x_\perp^2}} - \sinh^{-1} x_\perp\right) v_{l,\,\mathrm{max}}. \tag{5.10}$$

For the line of sight going through the centre ($x_\perp = \theta_\perp = 0$), Eq. (5.10) cannot be evaluated directly, but the limit of the terms with $x_\perp$ is $-1/3$. Thus, in that limit, we recover the result of Eq. (5.8) (with the central density from Eq. 5.1) for the most extreme $\dot{a}_{l,\,\mathrm{GC,max}}$:

$$\dot{a}_{l,\,\mathrm{GC,max}}(0) = -\frac{3\sigma_{\mu,0}^2}{\theta_\mathrm{c}^2} v_{l,\,\mathrm{max}}. \tag{5.11}$$

Apart from $v_{l,\,\mathrm{max}}$, these predictions for $\dot{a}_{l,\,\mathrm{GC,max}}$ depend only on angular measurements. In our calculations, we used $v_{l,\,\mathrm{max}} = v_\mathrm{e}$, i.e., the velocity envelope derived in Section 5.4.

The comparison between this prediction and the measured jerks is displayed graphically in

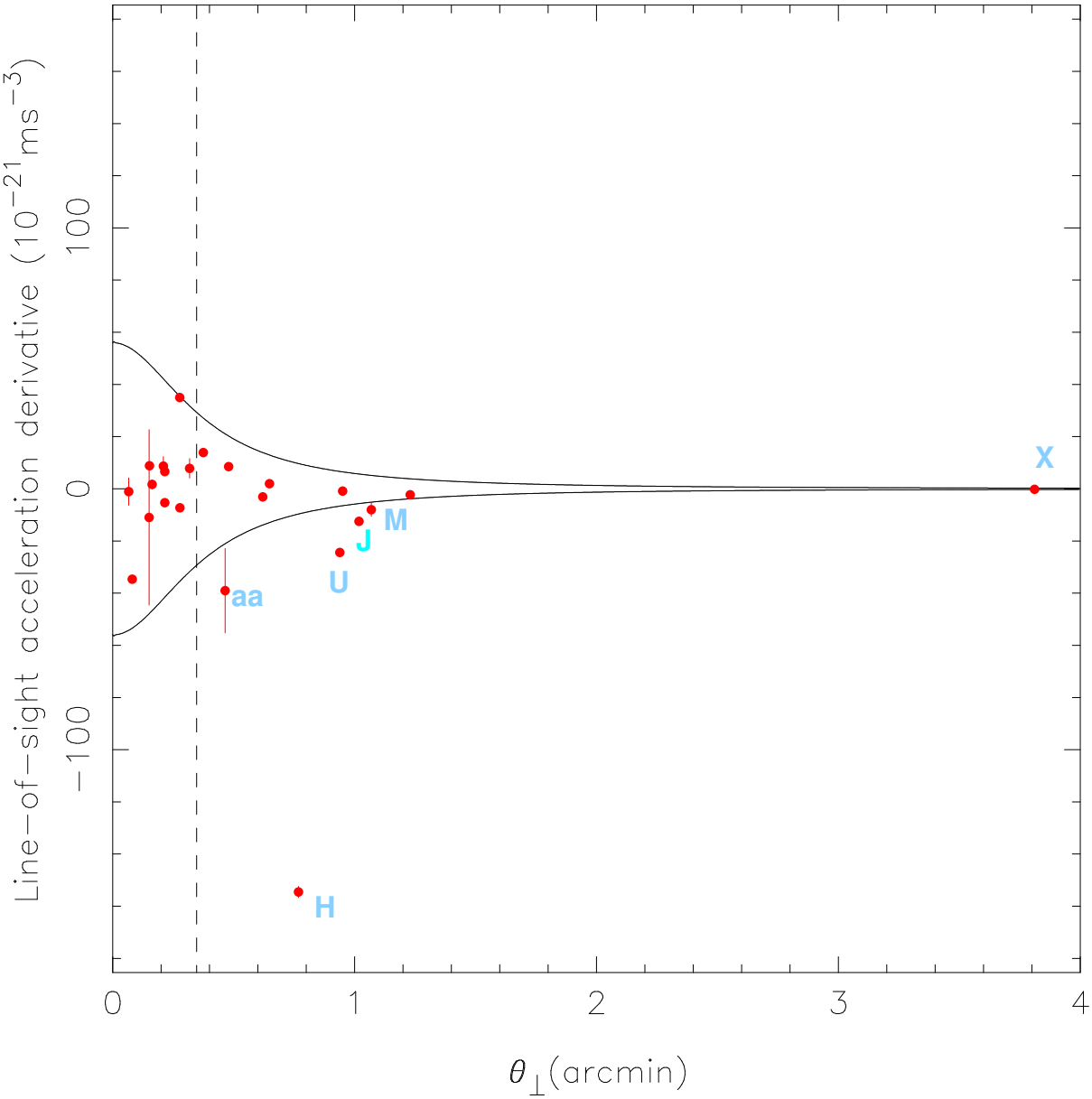

Figure 5.4. Line of sight acceleration derivatives ($\dot{a}_l$) as a function of the total angular offset from the centre of the cluster ($\theta_\perp$) for the pulsars in 47 Tuc. The red error bars represent measurements of the line-of-sight acceleration derivatives for all the pulsars. We also plot the maximum and minimum values of $\dot{a}_{l,\,\mathrm{GC}}$ ($\dot{a}_{l,\,\mathrm{GC,max}}$) predicted by Eq. (5.10) (solid lines). For some pulsars (47 Tuc H and U and possibly 47 Tuc J), the observed $\dot{a}_l$ is larger than $\dot{a}_{l,\,\mathrm{GC,max}}$; this is likely due to the presence of a nearby star. The core radius is indicated by the vertical dashed line.

Fig. 5.4. The red dots and red vertical error bars depict the measurements of the jerks and associated uncertainties. We also plot (in solid black lines) the $\dot{a}_{l,\,\mathrm{GC},\,\mathrm{max}}$ predicted for each line of sight by our cluster model.

Most pulsars have jerks that are smaller than our estimate of $\dot{a}_{l,\,\mathrm{GC},\,\mathrm{max}}$ for their lines of sight; such jerks can therefore be attributed to the movement of the pulsars in the mean field of the cluster. However, a few stand out. For 47 Tuc H, the observed $\ddot{f}$ is consistent with that reported in 2003, but 10 times as precise: $\ddot{f} = 1.60 \pm 0.02 \times 10^{-25}\,\mathrm{Hz\,s^{-2}}$; the corresponding jerk ($\dot{a}_l = -1.545(22) \times 10^{-19}\,\mathrm{m\,s^{-3}}$) is much larger (in absolute terms) than $|\dot{a}_{l,\,\mathrm{GC},\,\mathrm{max}}|$ for that pulsar's line of sight (or any in the cluster), so we come to the same conclusion as Freire et al. (2003): this system must have a nearby companion. We can now see that this is also true for 47 Tuc U and J. For 47 Tuc M and aa the observed jerks are only ~ 1-σ away from the $\dot{a}_{l,\,\mathrm{GC,max}}$ for their lines of sight.

An intriguing observation is that the systems with jerks larger than the cluster mean-field expectation lie preferably at distances from the core of about 1 arcmin. This is counter-intuitive since the stellar density is larger nearer the core – those pulsars are the most likely to be perturbed by nearby stars. The fact that none is being unambiguously perturbed by nearby stars suggests that the probability for a stellar interaction inducing a measurable $\ddot{f}$ is quite small, at least in this cluster. If this probability is small near the core, it should be even smaller at 1 arcmin from the centre, where the pulsars with larger-than-expected jerks lie. This suggests that these systems are not really just passing nearby stars, but they are being orbited by other objects, as in the case for the triple system PSR B1620−26, which is also found in an environment with lower stellar density (Thorsett et al., 1999; Sigurdsson et al., 2003). These orbits must have significantly larger orbital periods than our timing baseline, since we do not yet measure a full orbital period. Such wide orbits would not be stable in the vicinity of the cluster centre, thus explaining the lack of significant stellar jerk for the pulsars nearer the core.

5.5.3 Third spin frequency derivative

Unlike for the lower spin frequency derivatives, the third and higher spin frequency derivatives, $f^{(n)}$, can only be caused by the gravitational field of nearby objects.

The idea that 47 Tuc H is being influenced by a nearby stellar companion is supported by the fact that it is the pulsar in the cluster for which the measurement of $f^{(3)}$ is most significant, $f^{(3)} = (3.8 \pm 1.7) \times 10^{-35}\,\mathrm{Hz\,s^{-3}}$, a 2.3-$\sigma$ "detection". Most of the black widow systems also appear to have a non-zero $f^{(3)}$, but in no case is the measurement more significant than 2-σ. For the other main candidate for a stellar companion, 47 Tuc U, we measure $f^{(3)} = (-1.0 \pm 1.3) \times 10^{-35}\,\mathrm{Hz\,s^{-3}}$; we therefore did not fit for this parameter in the derivation of its timing solution (Table 4.3).

Since the uncertainty in the measurement of $f^{(3)}$ scales with $T^{-9/2}$, continued timing will improve these measurements very quickly. The rate of improvement will be even faster for higher frequency derivatives. The measurement of five such derivatives allows a unique determination of the five Keplerian orbital parameters (Joshi & Rasio, 1997); we would then know whether 47 Tuc H and its companion are bound or not.

5.6 Orbital period derivatives

Another quantity that greatly benefits from prolonged timing is the measurement of the variation of the orbital period, $\dot{P}_\mathrm{b}$. For most of the eclipsing binaries like 47 Tuc V, W, J and O (see

Chapter 6), there are unpredictable variations in the orbital period with time, similar to those observed for other eclipsing binaries in the Galaxy (e.g. Shaifullah et al. 2016); in these cases we need many orbital frequency derivatives to describe the evolution of orbital phase with time. For the remaining binary pulsars, namely the MSP-WD systems (47 Tuc E, H, Q, S, T, U, X and Y) and two of the black widow systems (47 Tuc I and R), the phase evolution of the orbit can be described with a period and a period derivative only.

5.6.1 Measurements of cluster accelerations

If the orbital period, $P_{\rm b}$, in the reference frame of the binary is stable, then we will not be able to measure orbital frequency derivatives higher than 1$^{\rm st}$ order (unless the system is in a triple, in which case the effects will be much more obvious in the spin frequency derivatives). At the Earth, the observed orbital period derivative will then be given by (Damour & Taylor, 1991):

$$\frac{\dot{P}_{\rm b,obs}}{P_{\rm b}} = \frac{\dot{P}_{\rm b,int}}{P_{\rm b}} + \frac{\mu^2 d}{c} + \frac{a_{l,\rm GC}}{c} + \frac{a_{\rm Gal}}{c}, \tag{5.12}$$

where all parameters are as in Eq. (5.2), except that $\dot{P}_{\rm b,obs}$ is the observed orbital period derivative and $\dot{P}_{\rm b,int}$ is the intrinsic orbital period derivative. For the MSP-WD systems, the intrinsic variation of the orbital period, $\dot{P}_{\rm b,int}$, should be dominated by energy loss due to the emission of gravitational waves. This is expected to be a very small quantity: for the MSP-WD system with the shortest orbital period, 47 Tuc U ($P_{\rm b} = 0.42911$ days), the expected orbital decay is -1.36×10^{-14} s s^{-1} (this assuming that the MSP has a mass of 1.4 M$_\odot$ and an orbital inclination $i = 90$ deg), which is a factor of 2 smaller than the current measurement uncertainty for the $\dot{P}_{\rm b,obs}$ for that pulsar. The cases of 47 Tuc I and R are discussed in detail in Section 6.4.

Re-writing Eq. (5.12), and ignoring the intrinsic term, we can, for each pulsar, calculate the cluster acceleration, since the remaining terms are also known, in particular the proper motion (see Section 5.4):

$$a_{l,\rm GC} = \frac{\dot{P}_{\rm b,\,obs}}{P_{\rm b}} c - \mu^2 d - a_{\rm Gal}. \tag{5.13}$$

These accelerations are presented in Tables 4.3 and 4.5, and depicted graphically as the vertical red error bars in Fig. 5.3. Like the values of $\dot{P}_{\rm obs}/P$, they represent important constraints on the dynamics of the cluster. As we can see in Fig. 5.3, the accelerations for 47 Tuc S, E and U can (just about) be accounted for by the mass model for the cluster described in Section 5.5 with a distance of 4.69 kpc. With the kinematic distance (4.15 kpc, represented by the dotted line in Fig. 5.3), this model cannot account for these accelerations.

We conclude therefore that our acceleration measurements are not compatible with a distance d significantly smaller than 4.69 kpc, in agreement with most published distance estimates; they appear to be incompatible with the kinematic distance of 4.15 kpc. A more robust probabilistic estimate of the cluster distance most favoured by our measurements will be presented elsewhere.

5.6.2 Intrinsic spin period derivatives

As we can see from Fig. 5.3, the measured values of $a_{l,\rm GC}$ tend to be similar, but slightly smaller than $a_{l,\rm max}$. The difference, as evident from Eq. (5.3), is due to the contribution from $\dot{P}_{\rm int}$. The values of $\dot{P}_{\rm int}$ can be obtained directly from the observables by subtracting Eq. (5.12) from

Eq. (5.2) and re-arranging the terms (and taking into account the fact that the $\dot{P}_{\rm b,int}$ are small):

$$\dot{P}_{\rm int} = P_{\rm obs}\left[\left(\frac{\dot{P}}{P}\right)_{\rm obs} - \left(\frac{\dot{P}_{\rm b}}{P_{\rm b}}\right)_{\rm obs}\right]. \tag{5.14}$$

The intrinsic values of $\dot{P}$ and resulting estimates for the characteristic age, $\tau_{\rm c}$, are also presented in Tables 4.3 and 4.4. For most of the other pulsars, less constraining upper limits for $\dot{P}_{\rm b,int}$ were derived assuming the largest possible negative value of $a_{\rm GC}$ for the line of sight of the pulsar (see Freire et al. 2001b and Freire et al. 2003).

Although the estimates of $\dot{P}_{\rm int}$ are not measured with high significance (only a couple of cases, 47 Tuc E and U, are measured with 3-σ significance), they already allow a comparison with the MSPs in the Galaxy. Putting the limits in a P-$\dot{P}$ diagram (Fig. 5.5), we see that these pulsars have characteristics similar to the majority of MSPs in the disk of the Galaxy. They are very different from some of the "young" globular cluster pulsars (depicted in red), for which the $\dot{P}_{\rm obs}$ are too large to be explained by cluster accelerations (for a discussion, see e.g., Freire et al. 2011, Johnson et al. 2013, Verbunt & Freire 2014 and references therein).

As discussed in detail below, these $\tau_{\rm c}$ estimates agree qualitatively with the total ages (τ_o) estimated for the WD companions that have been detected by the *HST* (Edmonds et al., 2001, 2002; Rivera-Sandoval et al., 2015; Cadelano et al., 2015), i.e., we find no case where $\tau_{\rm c} \ll \tau_o$. A similar comparison was done in Rivera-Sandoval et al. (2015) and Cadelano et al. (2015) using preliminary numbers from our timing program. It is interesting to note that the two apparently oldest WD companions, 47 Tuc Q and Y, are those that have the largest lower limits for $\tau_{\rm c}$.

5.6.2.1 47 Tuc Q

For 47 Tuc Q, $\dot{P}_{\rm int} = (-5.8 \pm 9.3) \times 10^{-21}\,{\rm s\,s^{-1}}$. This means that we cannot specify an upper limit for the characteristic age $\tau_{\rm c} = P/(2\dot{P}_{\rm int})$, since $\dot{P}_{\rm int}$ could be very small. Its 2-σ upper limit, $1.28 \times 10^{-20}\,{\rm s\,s^{-1}}$, implies a minimum $\tau_{\rm c}$ of 5.0 Gyr.

For a variety of reasons, the τ_o for the WD companion of this pulsar is highly uncertain: the cooling age ranges from 0.3 to 5 Gyr (this value depends very sensitively on the mass of the WD), plus $\sim$ 1 Gyr for the proto-WD phase (Rivera-Sandoval et al., 2015). We thus find that an age close to 6 Gyr is preferred for this system.

5.6.2.2 47 Tuc S

For 47 Tuc S, $\dot{P}_{\rm int} = (1.3 \pm 1.0) \times 10^{-20}\,{\rm s\,s^{-1}}$. Again, no reliable upper age can be derived, but a lower limit for $\tau_{\rm c}$ of 1.3 Gyr can be derived from the 2-σ upper limit of $\dot{P}_{\rm int}$. The cooling age for the WD companion ranges from 0.1 to 0.4 Gyr, to this we should add up to 0.4 Gyr for the time the companion spent as a proto-WD (Rivera-Sandoval et al., 2015). This suggests that τ_o is not larger than 0.8 Gyr. This is fine since $\tau_{\rm c}$ assumes a starting spin period that is much shorter than the present spin period. This is clearly not the case for most MSPs, particularly those with shorter spin periods, meaning that the real age will generally be smaller than $\tau_{\rm c}$.

5.6.2.3 47 Tuc T

For 47 Tuc T, the timing constraints are not so precise and we get $\dot{P}_{\rm int} = (9.9 \pm 8.9) \times 10^{-20}\,{\rm s\,s^{-1}}$. This implies a 2-$\sigma$ lower limit $\tau_{\rm c} > 0.43\,{\rm Gyr}$. The estimated τ_o is from 0.1 and 0.8 Gyr (Rivera-Sandoval et al., 2015), consistent with $\tau_{\rm c}$.

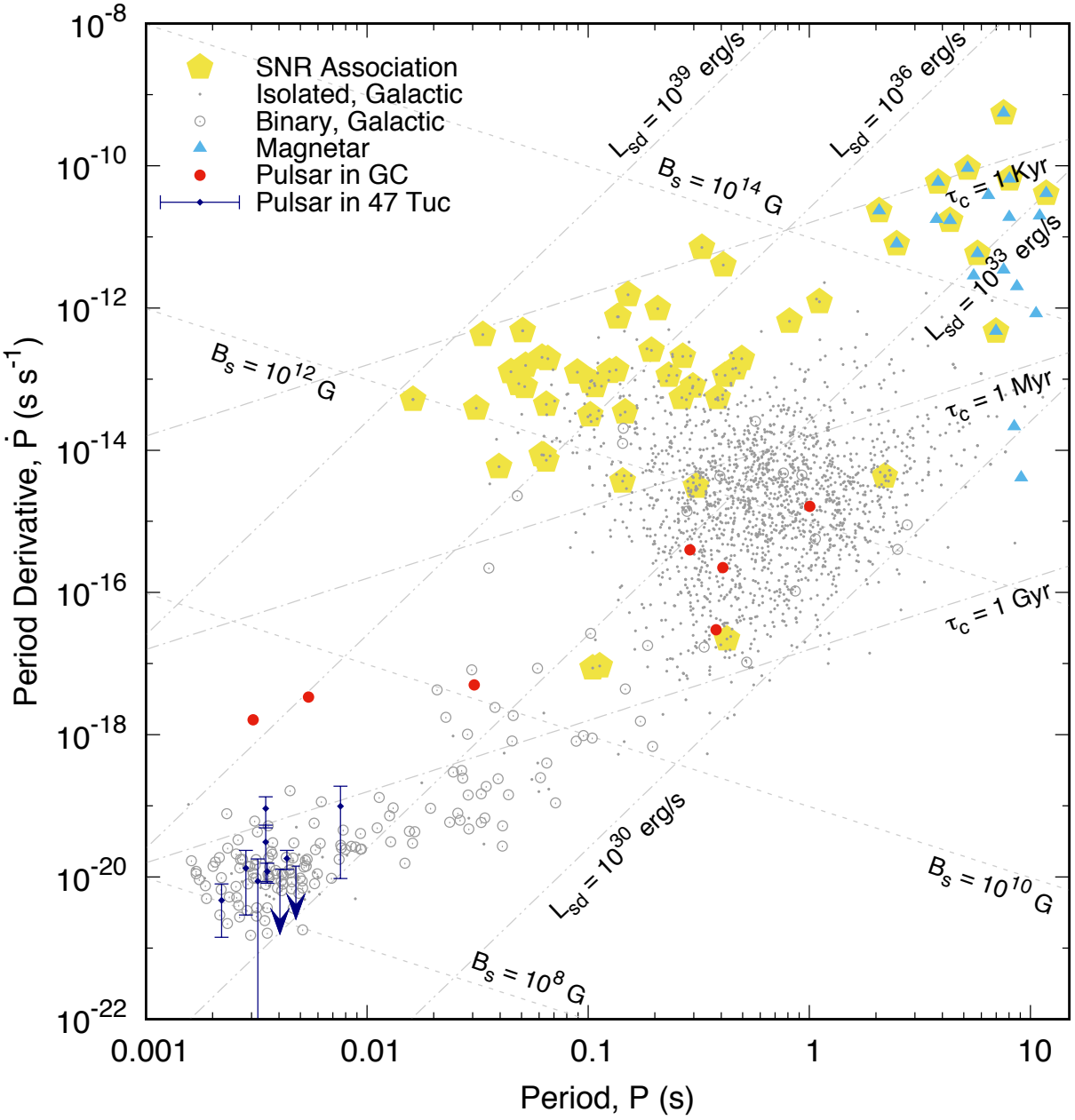

Figure 5.5. Period-period derivative (P-$\dot{P}$) diagram for the pulsars in the ATNF Pulsar Catalogue. The newly derived period derivatives for the MSPs in 47 Tuc (in dark blue) place them in the same region of the diagram where the majority of Galactic MSPs occur, i.e., they appear to be normal millisecond pulsars. Based on this sample, we conclude that 47 Tuc does not appear to have young pulsars like some seen in some other globular clusters (red dots).

5.6.2.4 47 Tuc U

For 47 Tuc U, $\dot{P}_{\rm int} = (1.82 \pm 0.55) \times 10^{-20}\,{\rm s\,s^{-1}}$. This means we can establish solid lower *and* upper limits for $\tau_{\rm c}$ from the 2-σ upper and lower limits of $\dot{P}_{\rm int}$: $2.4 < \tau_{\rm c} < 9.4\,{\rm Gyr}$. For the WD companion Rivera-Sandoval et al. (2015) derive a τ_o between $1.6 - 2.1$ Gyr, slightly lower than $\tau_{\rm c}$. As for 47 Tuc S, this is fine since $\tau_{\rm c}$ represents an upper limit on the age that assumes a very small initial spin period.

5.6.2.5 47 Tuc X

For 47 Tuc X, we obtain $\dot{P}_{\rm int} = (-1 \pm 3) \times 10^{-20}$ at the 3-σ level. Because the pulsar must be spinning down, the real value must be positive. Hence we can put an upper limit and say that $\dot{P}_{\rm int} \lesssim 2 \times 10^{-20}$ with $\sim 99\%$ probability. This implies a characteristic age of $\tau_{\rm c} \gtrsim 4$ Gyr at the 3-σ level.

5.6.2.6 47 Tuc Y

For this pulsar $\dot{P}_{\rm int} = (4.7 \pm 3.3) \times 10^{-21}\,{\rm s\,s^{-1}}$, from the 2-$\sigma$ upper limit of $\dot{P}_{\rm int}$ we derive a lower limit for $\tau_{\rm c}$ of 3.1 Gyr. Rivera-Sandoval et al. (2015) derive a τ_o between 3.1 to 3.9 Gyr, in agreement with $\tau_{\rm c}$.

5.7 New detections of the rate of advance of periastron

Another measurement that substantially benefits from a much extended timing baseline is the rate of advance of periastron, $\dot{\omega}$. For a binary system consisting of two point masses (a reasonable approximation for the MSP-WD binaries in 47 Tuc), this is solely an effect of relativistic gravity. In General Relativity, and to leading post-Newtonian order, it depends only on the Keplerian parameters and the total mass of the system $M_{\rm tot}$ (Eq. 2.43).

To measure this effect, we need a system with a significant orbital eccentricity (e), otherwise it is impossible to measure the longitude of periastron ($\omega_{\rm p}$) with enough precision to detect its variation with time. For most MSP-WD systems in the Galaxy, e is too small for such a measurement to be feasible. In globular clusters, on the other hand, the stellar density is so high that binary pulsars are perturbed by close encounters with other members of the cluster; this will generally increase their orbital eccentricity (Phinney, 1992, 1993). The large eccentricities of many binaries in GCs has allowed the measurement of their $\dot{\omega}$ and, consequently, of the binary masses (see e.g., Özel & Freire 2016 and references therein). However, the perturbations (and corresponding increases in e) are larger for the wider binaries; this implies that, generally, when we are able to measure $\dot{\omega}$ well, then the wide orbit makes it hard to measure other relativistic parameters (these would be useful for determining the individual masses of the components of the binary). There are only two exceptions to date, both products of exchange interactions located in core-collapsed clusters (PSR J1807−2500B in NGC 6544, Lynch et al. 2012, and PSR B2127+11C in M15, Jacoby et al. 2006, see Chapter 7).

Among the known binary pulsars in 47 Tuc, the most eccentric by far is 47 Tuc H ($e = 0.0705585 \pm 0.0000007$), which is also the second widest known in the cluster ($P_{\rm b} = 2.3577\,{\rm days}$). This orbital eccentricity is $4 - 5$ orders of magnitude larger than observed in MSP-WD systems of similar $P_{\rm b}$ in the Galactic disk. For this system, Freire et al. (2003) measured $\dot{\omega} = 0.0658 \pm 0.0009\,{\rm deg\,yr^{-1}}$ (where the uncertainty is the 1-σ error returned by `TEMPO`). This allowed an estimate of the total mass of the system of $M_{\rm tot} = 1.61 \pm 0.03\,{\rm M_\odot}$ (1-σ). Our current value is

a factor of five better: $\dot{\omega} = 0.06725 \pm 0.00019$ degyr^{-1}; this implies $M_{\rm tot} = 1.665 \pm 0.007$ M$_\odot$ (1-σ). No other relativistic orbital effects are detectable, so it is not possible to determine the individual masses in this binary. However, combining this constraint with the constraint $\sin i \leq 1$, we obtain $M_{\rm p} < 1.49$ M$_\odot$ and $M_{\rm c} > 0.175$ M$_\odot$, for the mass of the pulsar and of the companion, respectively.

Although much lower, the eccentricities of most of the MSP-WD systems in 47 Tuc are also orders of magnitude larger than observed among MSP-WD systems with similar orbital periods in the Galactic disk. Because of this, we have made significant (> 3-σ) detections of $\dot{\omega}$ in 3 other systems: 47 Tuc E ($\dot{\omega} = 0.090 \pm 0.016$ deg yr^{-1}, $M_{\rm tot} = 2.3 \pm 0.7$ M$_\odot$), 47 Tuc S ($\dot{\omega} = 0.311 \pm 0.075$ deg yr^{-1}, $M_{\rm tot} = 3.1 \pm 1.1$ M$_\odot$) and 47 Tuc U ($\dot{\omega} = 1.17 \pm 0.32$ deg yr^{-1}, $M_{\rm tot} = 1.7 \pm 0.7$ M$_\odot$). These measurements are, however, not yet precise enough to derive any astrophysically interesting values of the total masses for these systems. Improving them is important, because if we can determine precise total masses for these systems, then we will have good estimates for the masses of these pulsars, since their WD companion masses are relatively well known from optical photometry (Edmonds et al., 2002; Rivera-Sandoval et al., 2015; Cadelano et al., 2015).

Another two systems where $\dot{\omega}$ might be detectable in the future are 47 Tuc Q (0.46 ± 0.22 deg yr^{-1}) and 47 Tuc T (0.30 ± 0.28 deg yr^{-1}), again two systems for which we have good optical detections of the WD companions. For the remaining MSP-WD systems (47 Tuc X and Y), the orbital eccentricities are too low for a measurement in the foreseeable future.

5.8 The exceptional binary system 47 Tuc X

In Section 5.3 we have already mentioned 47 Tuc X as a peculiar system for its unusual location compared to the other pulsars in the cluster. However, the binary has other interesting characteristics that make it unique. For this reason, we have conducted a very detailed study of 47 Tuc X, also using wavelengths other than the radio. Here we present our results and the most relevant implications will be discussed in Section 5.9.

Astrometric parameters and dispersion measure

The first remarkable feature of 47 Tuc X is its position of $\simeq 3.81$ arcmin away from the cluster centre, equivalent to $\simeq 10.98$ core radii. This is more than three times the distance of 47 Tuc C, the previous farthest pulsar known in 47 Tuc. The corresponding projected linear distance, for the assumed cluster distance of 4.69 kpc (Woodley et al., 2012), is $r_\perp \sim 5.20$ pc. Using the measured DM of 24.539 ± 0.005 pc cm^{-3}, and the linear relation by Freire et al. (2001c), we can also infer the distance component along the line of sight $r_\parallel \simeq 2.37$ pc. Such an estimate should not be considered as very robust, since the Freire et al. (2001c) model is only known to work well in the central regions of the cluster.

Orbit and mass function

Given the high circularity of the 47 Tuc X orbit and the absence of strong orbital variability, we opted for the ELL1 binary model (Lange et al., 2001, N. Wex, unpublished), which is particularly suitable for systems with very low eccentricities. The measured values for the first and second Laplace-Lagrange parameters are $\eta \equiv e \sin \omega_{\rm p} = (4.1 \pm 1.4) \times 10^{-7}$ and $\kappa \equiv e \cos \omega_{\rm p} = (-2.4 \pm 1.5) \times 10^{-7}$, respectively, corresponding to an eccentricity $e = \sqrt{\eta^2 + \kappa^2} = (4.8 \pm 1.5) \times 10^{-7}$.

As we shall see in Section 5.9, this is among the smallest eccentricities ever measured in a binary pulsar. The measured orbital period and projected semi-major axis of the pulsar orbit translate into a mass function $f(M_c) = 1.52 \times 10^{-2}$ $M_\odot$. For an assumed pulsar mass of 1.4 $M_\odot$, this implies a minimum ($i = 90$ deg) companion mass of $M_c = 0.36$ $M_\odot$ and a median ($i = 60$ deg) value of $M_c = 0.43$ $M_\odot$.

X-ray detection

47 Tuc has been studied repeatedly by the *Chandra X-ray Observatory*, but no list of *Chandra* X-ray sources outside the half-mass radius has been published. We utilized the deepest *Chandra* observations of 47 Tuc that cover the position of 47 Tuc X and retain spectral information. These were 4 ∼65-kilosecond observations done in 2002 using the ACIS-S array in full-frame mode, described by Heinke et al. (2005) (the short interleaved subarray observations do not cover the position of 47 Tuc X). Note that these observations, with a 3.2-s frame readout time, are not sensitive to pulsations at the X-ray spin period. We downloaded the Level 2 reprocessed event lists provided by the *Chandra* X-ray Center pipeline reprocessing[1], which applied the latest calibration files to the data. We reprojected the 4 event files to a common tangent point, constructed an image of the S3 CCD chip in the 0.3−6 keV energy band, and ran the `wavdetect` source detection algorithm. An X-ray source was clearly detected at the coordinates $\alpha = 00^h{:}24^m{:}22.416^s$, $\delta = -72°{:}01'{:}17\farcs29$, with astrometric uncertainty of 0.6 arcsec (90% confidence), consistent with the radio timing position of 47 Tuc X. At this distance from the cluster core (3.81 arcmin) source crowding is low, with a 0.1% probability of a chance coincidence based on the local density of detected sources, so we are confident that this is the true X-ray counterpart.

We extracted source and local background spectra and constructed response files for each of the four observations, and combined them. Only 35 counts were attributed to 47 Tuc X, after subtracting a local background of 12.3±4.6 counts (the low count rate and relatively high background were due in part to 47 Tuc X's position significantly off-axis, reducing the detector sensitivity and increasing the size of the point spread function). Therefore, we grouped the spectra by 10 counts/bin (retaining the last underfilled bin) and fitted only simple spectral models with the `XSPEC` X-ray spectral fitting program (Arnaud, 1996). In each fit, we included photoelectric absorption by the interstellar medium (the `XSPEC` model `tbabs`) using Wilms et al. (2000) abundances and Verner et al. (1996) cross-sections, with the hydrogen column density, N_H, fixed to 1.3×10^{20} cm^{-2} (Gratton et al., 2003; Predehl & Schmitt, 1995). We also performed fits to the unbinned spectra using the C-statistic (Cash, 1979), with consistent results. A simple absorbed power-law fit is statistically acceptable, with an inferred photon index of $2.4^{+0.5}_{-0.4}$. Such a soft value for the photon index would be unusual for magnetospheric emission from radio pulsars, where the index is typically between 1 and 2 (e.g. Becker & Aschenbach, 2002). It is also rather softer than the photon index (1.1−1.7) measured in cases where the emission is thought to be powered by a shock between a wind from the donor star, and a pulsar wind (e.g. Bogdanov et al., 2005, 2010). Thus, it seems likely that part or all of the X-rays are produced by emission from one or both heated polar caps, as seen in many MSPs with similar spin properties and X-ray luminosities (Zavlin et al., 2002; Zavlin, 2006; Bogdanov et al., 2006). We therefore fitted the spectrum with blackbody (for consistency with previous works) and hydrogen neutron star atmosphere (NSATMOS, Heinke et al. 2006) models, both of which were good fits. The X-ray spectrum with the fitted NSATMOS model is shown in Fig. 5.6. For the blackbody fit, the

[1] `http://cxc.harvard.edu/cda/repro4.html`

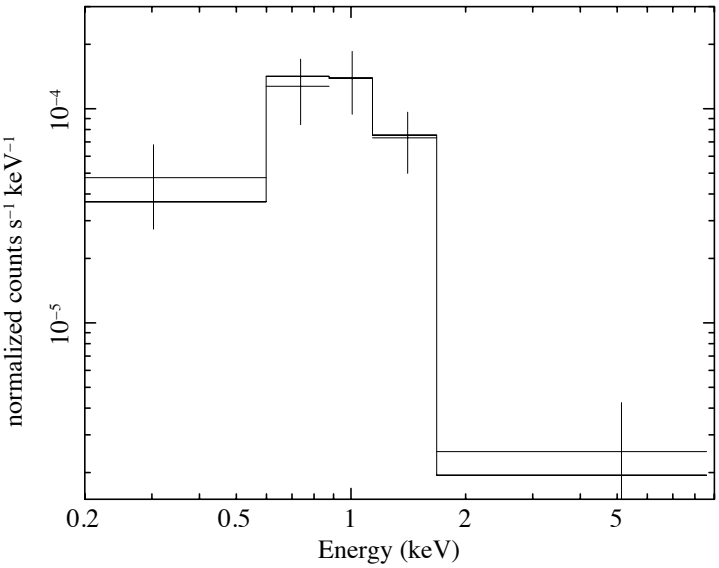

Figure 5.6. *Chandra* X-ray spectrum of 47 Tuc X, fit with a hydrogen atmosphere neutron star model: observed data binned by 10 counts/bin (crosses), and best-fit model folded through instrumental response (solid line).

inferred temperature is $3.0^{+1.0}_{-0.8} \times 10^6$ K with an inferred equivalent radius of 0.07±0.05 km. For the NSATMOS model, we fixed the neutron star mass to 1.4 $M_\odot$, the radius to 10 km, and the distance to 4.69 kpc (Woodley et al., 2012; Hansen et al., 2013), and allowed the normalization to vary. In this case, the inferred temperature was $1.9^{+1.0}_{-0.7} \times 10^6$ K, and the inferred radius was $0.2^{+0.4}_{-0.1}$ km. In either case, the inferred 0.5−10 keV luminosity was $2.0 \pm 0.6 \times 10^{30}$ erg s^{-1}.

Comparing the spectral fits to the X-ray spectrum of 47 Tuc X with those for other MSPs, we see that the best-fit temperatures tend to be higher than those for the other MSPs in 47 Tuc (Bogdanov et al., 2006), while the best-fit emitting radii are smaller. However, 3 of the 5 MSPs in NGC 6752 have higher fitted blackbody temperatures, and smaller best-fit radii, than 47 Tuc X (Forestell et al., 2014). The remarkably high temperature of 47 Tuc X, as for those in NGC 6752, could be due to the presence of an undetected non-thermal spectral component, in addition to the predominating thermal component. The limited statistics preclude a definite answer.

Characteristic age, magnetic field and spin-down luminosity

Our radio timing precision was enough to detect the orbital period derivative, which amounts to $\dot{P}_\mathrm{b} = 6 \pm 2 \times 10^{-12}$ s s^{-1}. As discussed in Section 5.6.2, this opens the possibility of constraining the intrinsic spin down of the pulsar, and thus other relevant quantities that depend upon it.

From this we can also give limits for the spin-down luminosity of the pulsar, L_sd, its characteristic age, τ_c, and its surface magnetic field, B_s using equations (3.5), (3.12) and (3.15), respectively, from Lorimer & Kramer (2004). We find $L_\mathrm{sd} \lesssim 7 \times 10^{33}$ erg s^{-1}, $B_\mathrm{s} \lesssim 3 \times 10^8$ G and $\tau_\mathrm{c} \gtrsim 4$ Gyr at the 3-σ level.

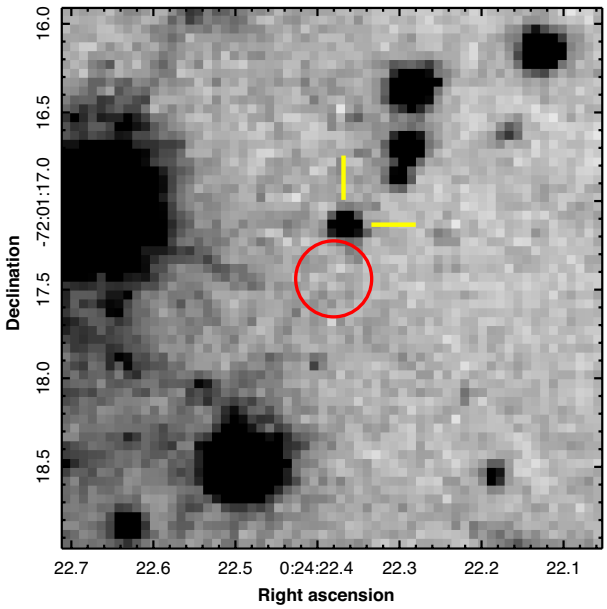

Figure 5.7. A section of the stacked ACS/WFC F435W image centered on the radio position of 47 Tuc X, which is marked with a red circle. The radius of the circle is equal to the 3-σ positional error (0.21 arcsec). The star that is indicated with tick marks is the closest detection to the radio position at a separation of 0.3 arcsec. The size of the image is $3'' \times 3''$. North is up, East to the left.

Search for the optical counterpart

The location of 47 Tuc X, being almost 4 arcmin away from the centre of 47 Tuc, was observed with *HST* on only one occasion. The four images that include the position of 47 Tuc X were taken with the Wide Field Channel (WFC) on the Advanced Camera for Surveys (ACS) as part of program GO-12971 (PI: H. Richer). These observations were obtained on 2013 February 26 between 05:32 and 7:19 UT, and include two exposures (one of 290 s and one of 690 s) in the F435W filter, and another two (of 360 s and 660 s) in the F555W filter. We retrieved these images from the *HST* archive and started our data reduction with the flat-fielded `flc` images, which are corrected for the degradation of the charge transfer efficiency by the CALACS pipeline version 8.3.0. We processed the images with the `DRIZZLEPAC` software (Gonzaga et al., 2012) to remove the geometric distortion and create stacks for each filter. The resulting master images have a pixel scale of 0.05 arcsec pixel^{-1}. Next, we tied the absolute astrometry to the same reference system as the radio coordinates, i.e. the International Celestial Reference System (ICRS), using stars in the UCAC2 catalogue (Zacharias et al., 2004). As the UCAC2 stars in the ACS images are all saturated, we employed the following method. Based on the cataloged coordinates of 140 UCAC2 stars, we first derived an astrometric solution for a 30-s V-band image of the cluster taken on 2002 October 29 with the Wide Field Imager on the ESO/2.2-m telescope at La Silla, Chile. The resulting solution has r.m.s. residuals of $\sim$ 0.026 arcsec in both right ascension and declination. From this image we selected 24 unsaturated and relatively isolated stars in the vicinity of 47 Tuc X to astrometrically calibrate the 290-s F435W exposure of GO-12971, resulting in a r.m.s. residuals of 0.035 arcsec in right ascension and 0.045 arcsec in declination. Finally, we transferred this solution to the stacked F435W and F555W images of the field around 47 Tuc X with $\sim$500 stars and negligible r.m.s. residuals ($\sim$0.01 arcsec). We used `DAOPHOT` to extract photometry; the resulting magnitudes in the F435W and F555W

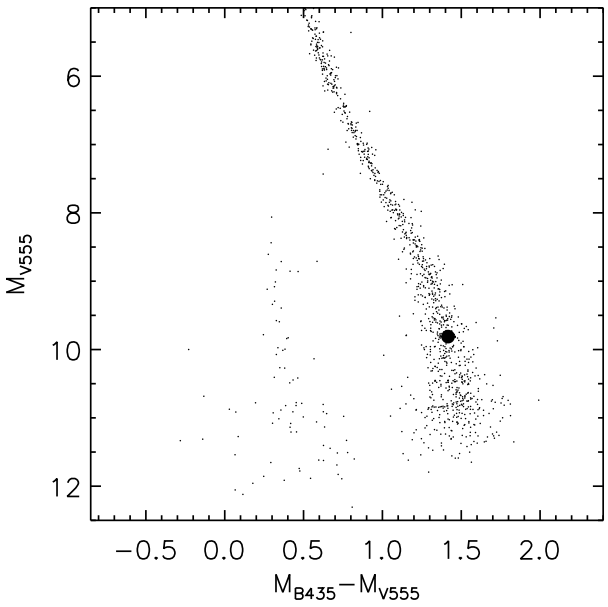

Figure 5.8. $B_{435} - V_{555}$ versus V_{555} colour-magnitude diagram extracted from a $\sim$1 arcmin^2 section of the ACS/WFC images around 47 Tuc X. The nearest detection to 47 Tuc X is marked with a large filled circle, and has typical main-sequence−star colors. Photometry is given in the Vega-mag system and has been converted to absolute magnitudes using an unreddened distance modulus of $(m - M)_0 = 13.36$ (Woodley et al., 2012) and a reddening of $E(B - V) = 0.024$ (Gratton et al., 2003). Errors on the photometry are comparable to the symbol size, and include the `DAOPHOT` errors, and the errors on $(m - M)_0$ and $E(B - V)$. The sequence of stars with $M_{V_{555}} \gtrsim 8$ and $0.2 \lesssim M_{B_{435}} - M_{V_{555}} \lesssim 0.7$ are stars in the Small Magellanic Cloud.

filters (denoted with B_{435} and V_{555}, respectively) were calibrated to the Vega-mag system using the zeropoints provided by the STScI[2]. Fig. 5.7 shows a section of the F435W image around the radio position of 47 Tuc X, which is marked with a circle. The radius of the circle represents the 3-σ error on the absolute astrometry of the image. Here, $\sigma = 0.072$ arcsec and equals the quadratic sum of all the astrometric errors mentioned above, plus the systematic error in the alignment of the UCAC2 coordinates to the ICRS (about 0.010 arcsec; Zacharias et al. 2004). The errors on the radio position are negligible. The star that is closest to 47 Tuc X is located at a separation of 0.3 arcsec (4.1-σ). In the colour-magnitude diagram of Fig. 5.8, this star falls right on the main sequence. We consider its angular offset from 47 Tuc X too large to make this star a convincing counterpart. Also, the evolutionary path for such a companion would exclude such a low eccentricity as we measure (see below).

For example, the He WD companions of five 47 Tuc MSPs that Rivera-Sandoval et al. (2015) identified with the same method as used here, were all excellently aligned to the radio positions, with a maximum offset of 0.016 arcsec (0.2-σ).

From the faintest detection with S/N $\gtrsim$ 3 we estimated the detection limit in the F435W band. We find that it corresponds to an absolute magnitude of $M_{B_{435}} \simeq 13.7$, where we adopted the unreddened distance modulus $(m - M)_0 = 13.36 \pm 0.02 \pm 0.06$ (random and systematic error, respectively) from Woodley et al. (2012) and the reddening $E(B - V) = 0.024 \pm 0.004$ from Gratton et al. (2003). In the standard MSP formation scenario, the companion to the MSP is a low-mass WD, which is all that is left of the original donor star after it has lost most of

[2] `http://www.stsci.edu/hst/acs/analysis/zeropoints`

its envelope during the mass-transfer stage. Based on the theoretical relation between the WD mass and the orbital period of the MSP-WD binary, the measured orbital period of 10.92 days for 47 Tuc X implies a WD mass between $\sim$0.22 and 0.27 $M_\odot$ (Tauris & Savonije, 1999; De Vito & Benvenuto, 2010). Based on our non-detection of a WD near 47 Tuc X and the cooling tracks of $0.2 - 0.3$ $M_\odot$ WDs computed for the metallicity of 47 Tuc (see Rivera-Sandoval et al., 2015), we find that the lower limit to the age of the WD must be $\sim$ 1.7 Gyr for it to remain undetected, assuming the companion is indeed a low-mass WD.

5.9 What the pulsars tell us about cluster dynamics

Thanks to the large timing baseline and uniform time coverage provided by the high-resolution AFB observations made at Parkes, we were able to obtain great improvements in the measurement of several key parameters for the pulsars in 47 Tuc. This is particularly true for those parameters that are relevant for the study of the dynamics of the cluster: the proper motions, the real line-of-sight accelerations as determined from the orbital period derivatives, and the jerks. From these physical quantities, we can already derive some preliminary conclusions.

The first one is about the distance of 47 Tuc. As already mentioned in Section 5.6.1, based on the stellar proper motion dispersion near the centre of the cluster and the analytic cluster acceleration model presented in Section 5.5, the measurements of acceleration derived from $\dot{P}_{\rm b,obs}$ can only be accounted for by this model if the distance to the cluster is close to 4.69 kpc. If we instead use the smaller distances suggested by kinematic studies, then the cluster model is unable to predict the line-of-sight accelerations of three binary pulsars, 47 Tuc E, S, and U. The distance that our model favours coincides with most photometric and spectroscopic distances published to date (see e.g. Woodley et al. 2012 and references therein); this suggests that the kinematic distances are too small. As discussed by Bogdanov et al. (2016), this is likely to be due to systematic under-estimates of σ_0 and our results support this conclusion.

Other important considerations can be made based on the characteristics of the pulsar population of the cluster. 47 Tuc is known to have one of the largest total stellar interaction rates ($\Gamma_{\rm GC}$) among clusters in the Milky Way system (Verbunt & Hut, 1987; Bahramian et al., 2013). A consequence of this is that, following the frequent exchange encounters, many old, "dead" neutron stars end up binding themselves in binaries with main sequence companions. Subsequent evolution of these companions cause transfer of gas to the NSs, i.e. the system becomes a low-mass X-ray binary (LMXB). After this, the companion typically becomes a low-mass WD, and the NS becomes a radio MSP. The large number of MSPs in 47 Tuc can therefore be understood primarily as a consequence of the large $\Gamma_{\rm GC}$.

The characteristic ages of the binary MSPs in 47 Tuc and the optical ages of their WD companions suggest that these systems have been forming at a near-constant rate throughout the age of the cluster, i.e., there is no indication of an early burst of MSP formation (which would make all pulsars look very old). There are also no signs of an ongoing burst of MSP formation either, since none of the pulsars in the cluster has a large $\dot{P}_{\rm int}$ that cannot be accounted for by the cluster acceleration model, and none have characteristic ages smaller than about 0.33 Gyr (the lower limit for the age of 47 Tuc I). In this respect, the situation in 47 Tuc offers a stark contrast to that observed in some of the core-collapsed clusters, in particular NGC 6624, where at least three pulsars (out of the six known in that cluster) have characteristic ages smaller than 0.2 Gyr (Lynch et al., 2012), and in a particular case (PSR B1820−30A) as small as 25 Myr (Freire et al., 2011).

Table 5.1. Populations of pulsars in 47 Tuc.

Class	# of pulsars	Pulsar names
Isolated	10	C, D, F, G, L, M, N, Z, aa, ab
MSP-WD	8	E, H, Q, S, T, U, X, Y
Black Widow	5	I, J, O, P, R
Redback	2	V, W

The difference between the populations of these clusters reflects fundamentally different dynamics. Although both types of clusters have a similar $\Gamma_{\rm GC}$, the interaction rate *per binary*, $\gamma_{\rm b}$ (Verbunt & Freire, 2014) is much higher in NGC 6624 than in 47 Tuc. The fundamental reason for this is the fact that NGC 6624 has a collapsed core. Instead, the pulsar population in 47 Tuc has the characteristics one would expect for a GC with a low $\gamma_{\rm b}$: any newly formed LMXBs evolve undisturbed to their normal outcomes (MSP-WD binaries, black widows and isolated MSPs, as observed in the Galactic disk). All systems have large $\tau_{\rm c}$ the moment they form. There are no mildly recycled pulsars − there are currently no companion stars in GCs massive enough (and evolving fast enough) to result in mild recycling, as seen for instance in double neutron star systems and pulsars with massive WD companions in the Galactic disk. This is the likely reason for the remarkably small range of spin periods ($1.8 < P < 7.6$ ms) for the pulsars in 47 Tuc.

On the contrary, in clusters with higher $\gamma_{\rm b}$, we can find a higher percentage of isolated pulsars (from the disruption of MSP-WD systems), mildly recycled - and apparently young - pulsars (from the disruption of X-ray binaries, which leaves the recycling process incomplete) and products of *secondary* exchange interactions, i.e. exchange interactions that happen after the formation of the MSP. None of the MSPs in 47 Tuc is clearly the product of such an interaction.

Furthermore, in high-$\gamma_{\rm b}$ GCs we find many pulsars very far from the cluster core. An extreme example is NGC 6752 (D'Amico et al., 2002; Corongiu et al., 2006), a core-collapsed cluster where two of the five known pulsars lie at more than 14 core radii from the centre. This phenomenon is common in other core-collapsed GCs and is caused by chaotic binary interactions, which typically have a strong recoil that can propel MSPs to the outer reaches of the cluster. In 47 Tuc, all pulsars but one appear to lie close to the core, their radial distribution being as expected from mass segregation of a dynamically relaxed population (Heinke et al., 2005). Even for the exceptional system, 47 Tuc X, it is not clear whether there was a recoil in the past (see below).

Another important consideration can be made by observing that all the binary systems in 47 Tuc have relatively small orbital eccentricities compared to what we see in denser clusters, like Terzan 5 and M28 (for even denser clusters, binary destruction sets in, but we do see a few very eccentric survivors) and the only "eccentric" binary in 47 Tuc, 47 Tuc H, might have gained its eccentricity from an object orbiting it, not from interactions with other stars.

In this regard, a particular mention goes to 47 Tuc X, by far the binary with the lowest measured eccentricity in the cluster. Ranking 3rd among the most circular systems with a measurable non-zero eccentricity (after PSR J1909−3744 and PSR J1738+0333), the circularity of 47 Tuc X is even more remarkable when related to its long orbital period and to the fact that it resides in a globular cluster. Indeed, pulsar X is by far the most circular system ever found in a GC and, more generally, it is the binary with the lowest eccentricity-to-orbital-period ratio known, with a value of $e/P_{\rm b} = 4.4 \times 10^{-8}$ days^{-1} (compared to 7.4×10^{-8} days^{-1} of PSR

J1909−3744 and 9.6×10^{-7} days^{-1} of PSR J1738+0333). The eccentricity and the position of 47 Tuc X can give us important clues about how this system may have formed. Here we discuss two possible formation hypotheses, where the main difference is the orbit of the system in the cluster.

In the first scenario, an unrecycled NS near the core of the GC has a close encounter with a main sequence (MS) binary, with subsequent chaotic interactions. In such encounters, the most likely outcome is the high-speed ejection of the lightest star among the three (likely one of the light MS stars); by conservation of momentum, the newly formed NS-MS binary will also recoil. Its orbit around the cluster will become eccentric, and it will spend most of its time in the outskirts of the cluster. Such an exchange interaction would induce a residual eccentricity. The extremely low eccentricity of the orbit implies that the circularization occurred *after* the formation of the current binary, hence the current companion star must be the former donor that spun up the pulsar. This is similar to the case of pulsar PSR J1911−5958A in NGC 6752 (Bassa et al., 2006; Corongiu et al., 2012). We also note that, if the system has actually been ejected from the core but is still bound to the cluster, it will be making many more periodic visits to the central regions of 47 Tuc. Even though the relaxation timescale at the projected distance of 47 Tuc X is more than 3 Gyr, because the orbits within the cluster are non-Keplerian, the system will spend a fairly long time in proximity of the core, thus significantly reducing the relaxation timescale and, equivalently, increasing the probability of dynamically interacting with other bodies. This would in turn increase the eccentricity of the binary (Phinney, 1992). Because 47 Tuc X instead has an extremely circular orbit, the system must be relatively young. There is nothing unusual in this formation path − this is the normal evolution for all MSPs in globular clusters. Most other systems formed in this way eventually sink back to the core of the cluster, because of dynamical friction, and eventually reach an equilibrium configuration dictated by mass segregation (Heinke et al., 2005). This is the reason why all other MSPs apart from 47 Tuc X lie, at least in projection, within 1.2 arcmin from the centre of the cluster. The fact that 47 Tuc X is found in the outskirts would suggest that, since recycling, it has had no time to sink back to the core, which would in turn indicate that it was recycled later than the other MSPs in the cluster.

However, despite these two indications that the system must be young, the optical non-detection introduced a lower limit on the age of the system of $\sim$1.7 Gyr. This problem is avoided in the second possible formation scenario, where the system was born directly in the outskirts. In this case, 47 Tuc X may have formed in two ways: either from a primordial MS−MS star that naturally evolved first into a LMXB and then into the current pulsar-WD binary we see today, or again from a dynamical encounter that set the system to a nearly circular orbit around the cluster. In both ways, the motion in the cluster would be such that the system never approached the central regions, the probability of dynamical encounters was low and thus the evolution of 47 Tuc X would resemble that which happens in the Galactic field, which naturally retains the low eccentricity obtained after the end of the recycling phase.

In both scenarios, it is difficult to tell whether the companion is a He WD or a Carbon-Oxygen (CO) WD. The median mass of the companion, inferred from the mass function, $M_{\rm WD} \simeq 0.43$ M$_\odot$, lies roughly at the border that discriminates the two types. However, as already mentioned at the end of Section 5.8, the companion mass range predicted by the $P_{\rm b} - M_{\rm WD}$ relation for He WDs (Tauris & Savonije, 1999) is somewhat lower than the minimum mass derived from the mass function, thus making a CO WD type more likely.

Regardless of the formation history and the nature of its companion, 47 Tuc X does not belong to any of the groups of pulsars so far discovered in the cluster (see Table 5.1). However,

this is quite understandable: its position in the outskirts of 47 Tuc enables it to maintain a long orbital period for a long time without binary destruction, while the other pulsars, closer in, would likely be ionized (thus leaving isolated MSPs) by stellar encounters. 47 Tuc X looks just like many other MSPs in the field, which are in wide orbits together with a He WD companion. The dense and ionizing dynamical environment, generally prevents us from seeing such systems in globular clusters.

A detailed characterization of the pulsar populations of other GCs will be very important for testing the whole picture described in this section. In particular, the pulsar populations in low-γ_b GCs (like M3, M5, M13, M22, M53, M62, NGC 6749 and NGC 6760) should have characteristics similar to 47 Tuc, thus different from those in the high-γ_b clusters. This appears to be true (Freire et al., 2005; Hessels et al., 2007; Lynch et al., 2011, 2012), but it could be refuted (or further confirmed) by timing more of the pulsars in those clusters − and finding new ones.

5.9.1 An intermediate mass black hole in the centre of 47 Tuc?

Recently, the possibility of a 2200-$M_\odot$ intermediate mass black hole (IMBH) at the centre of 47 Tuc has been raised considering only the $\dot{P}_{\rm obs}$ of the pulsars (Kızıltan et al., 2017), which give us upper limits on the pulsar accelerations ($a_{l,\,\rm max}$) via Eq. (5.3). In this work, we consider not only the $a_{l,\,\rm max}$, but also measurements of jerk along the line of sight ($\dot{a}_l$), and actual measurements of the line-of-sight accelerations in the field of the cluster ($a_{l,\,\rm GC}$) for 10 binary pulsars, as discussed in previous sections. This is important because these accelerations are more constraining than the $a_{l,\,\rm max}$ taken into account in Kızıltan et al. (2017).

The simple analytical cluster model described in Section 5.5 can account for all the $a_{l,\,\rm GC}$ despite the fact that these are more constraining than the $a_{l,\,\rm max}$. In the cases where these are missing, the cluster model can account for all the $a_{l,\,\rm max}$ (from the $\dot{P}_{\rm obs}$) as well. Furthermore, the model also accounts for the jerks observed for all the pulsars that lie (in projection) in the core. Thus, considering all the available observations, we come to the conclusion that we have no evidence for the existence of an IMBH at the centre of the cluster: its gravity is not necessary to explain our results.

Let us first elaborate further on the issue of the predicted accelerations. As mentioned in Section 5.5 and 5.6, if we accept (against the arguments presented in the literature listed before) the standard deviation of the spectroscopic velocity measurements ($\sigma_0 = 11.0\,{\rm km\,s^{-1}}$) then $d \sim 4\,{\rm kpc}$. The latter value is the estimate used in Kızıltan et al. (2017). In this case, our model also under-predicts the $\dot{P}_{\rm obs}$ of 47 Tuc S. This issue has already been discussed in detail by Freire et al. (2003), who concluded that the cluster as a whole must be more massive than suggested by this measurement of σ_0. Our measurement of $\dot{P}_{\rm b,\,obs}$ for this binary system (which was not taken into account by any previous studies) further increases the disagreement with the prediction of our $d \sim 4.15$ kpc model. Hence, such a model is unlikely to be correct.

Let us accept for the time being that the explanation for the large acceleration of 47 Tuc S is the pull from a central IMBH. In this case, the accelerations would be enhanced within its radius of influence, about 10 arcsec from the centre (see Fig. 2 in Kızıltan et al. 2017); farther away they would still be the accelerations predicted by a normal cluster model with $\sigma_0 = 11.0\,{\rm km\,s^{-1}}$ and $d \sim 4.15\,{\rm kpc}$. However, as we can see in Fig. 5.3, such a model cannot account for the measured accelerations (from $\dot{P}_{\rm b,\,obs}$) of 47 Tuc E and U: these systems lie, in projection, at 37.2 and 56.3 arcsec from the centre, respectively. A model with $d = 4.69\,{\rm kpc}$ can, as discussed above, account for all these accelerations without an IMBH.

Furthermore, within the inner 10 arcsec, an IMBH would produce greatly enhanced jerks to any nearby pulsar. However, as we have seen above, the cluster model with $d = 4.69$ kpc can also account for all jerks in this region. It is only for a few pulsars well outside the core (47 Tuc H, U and J) that additional contributions (very likely from nearby stars) are needed.

To summarise, a model with $d = 4.69$ kpc and no central IMBH can account for all measured accelerations, while a model with $d = 4.15$ kpc and an IMBH cannot. Also, the distance of 4.69 kpc is in much better agreement with all (non-kinematic) distance measurements (and, as previously discussed, even kinematic distance measurements when we use stars slightly outside the core, where the possibility of pairs of stars falling within the same pixel decreases). Such a model, we find, is far more likely to be an accurate description of the cluster.

Despite the fact that pulsar measurements provide no positive evidence in favour of a central IMBH at the centre of 47 Tuc, we cannot exclude such a possibility, particularly if the mass is much smaller than 2200 $M_\odot$. A probabilistic estimate of the mass of this hypothetical IMBH will be presented elsewhere.

Chapter 6

The population of "black widow" and "redback" pulsars of 47 Tuc

The work presented in this chapter is published in the following articles:

- **Ridolfi, A.**; Freire, P. C. C.; Torne, P.; Heinke, C. O.; van den Berg, M.; Jordan, C.; Kramer, M.; Bassa, C. G.; Sarkissian, J.; D'Amico, N.; Lorimer, D.; Camilo, F.; Manchester, R. N.; Lyne, A., *"Long-term observations of the pulsars in 47 Tucanae - I. A study of four elusive binary systems"*; MNRAS, 2016, Volume 462, Issue 3, p.2918-2933
- Freire, P. C. C.; **Ridolfi, A.**; Kramer, M; Jordan, C.; Manchester, R. N.; Torne, P.; Sarkissian, J.; D'Amico, N.; Camilo, F.; Lorimer, D. R.; Lyne, A. G.; *"Long-term observations of the pulsars in 47 Tucanae - II. Proper motions, accelerations and jerks"*; Submitted to MNRAS

For all the pulsars discussed in this chapter, I reduced the radio data, and carried out the timing analysis and the study of the orbital variability. The reduction and analysis of the X-ray and optical data for the pulsar 47 Tuc V was carried out by co-authors.

Contents

6.1 Introduction

In this chapter, we focus on one sub-population of the pulsars in 47 Tuc, namely that of the black widow and redback binary systems (of which we have discussed the main differences in Section 1.4.3). Currently, there are five black widows (pulsars I, J, O, P, R) and two redbacks (pulsars V and W) known in 47 Tuc. In Chapter 4 we have derived very precise orbital parameters for 47 Tuc P, V and W and, for the latter, we have also obtained a phase-connected timing solution. For the other black widows and redbacks, we have extended the previously known timing solutions.

Here we review the main characteristics of all the black widow and redback pulsars in 47 Tuc: for the previously studied pulsars, we highlight the improvements obtained by our extended timing, whereas for pulsars P, V and W, we present a more thorough analysis.

Finally, we discuss the intrinsic orbital variability, a phenomenon that is very evident in some of these pulsars, but seems to be absent in others.

6.2 Characterization of the orbital variability

Both black widows and redbacks are known for their orbital variability: the orbital period (and sometimes the projected semi-major axis) of these pulsars changes unpredictably with time, as seen in long-term timing of some black widow systems (see e.g. Shaifullah et al., 2016). For such cases, a simple Keplerian (BT) model is inadequate to correctly describe the orbit. Instead, it is necessary to use a BTX model (D. Nice, unpublished; `http://tempo.sourceforge.net`), which allows a description of the orbital behaviour through the use of multiple orbital frequency derivatives, although only within the time range spanned by the data. In short, the number of orbits $N_{\rm b}^{\rm BTX}$ at any given time t is given by a Taylor expansion:

$$N_{\rm b}^{\rm BTX}(t) = N_0 + \sum_{k=0}^{N_{\rm d}} \frac{1}{(k+1)!} f_{\rm b}^{(k)} (t - T_0)^{(k+1)} \tag{6.1}$$

where N_0 is an arbitrary constant, $N_{\rm d}$ is the number of orbital frequency derivatives, T_0 is the time of passage at periastron (or at the ascending node, in the case of a circular orbit), and $f_{\rm b}^{(k)}$ is k-th orbital frequency derivative calculated at the time $t = T_0$. As a rule, we choose the number of orbital frequency derivatives to be the minimum such that the reduced chi-square $\chi^2 \sim 1$ in the timing residuals.

As we shall see in the next section, some of the black widows and redbacks in 47 Tuc required the used of the BTX model. To study how well the model was describing our data, we followed a method similar to the one used by Ng et al. (2014) for PSR J1731−1847. For each group of ToAs (that is, for each detection), we calculated the epoch of passage at periastron, $T_0^{\rm pred}$, closest to the mid-point $\langle T_{\rm obs} \rangle$ of the observation, that a simple Keplerian model would predict. This is equivalent to finding t closest to $\langle T_{\rm obs} \rangle$ in Eq. (6.1), after setting to zero all the orbital frequency derivatives. Then, we fitted the ToAs with `TEMPO` for T_0 only, using a simple Keplerian model (i.e., setting all the $f_{\rm b}^{(k)}$ to zero) in the ephemeris, and keeping all the other parameters fixed, thus obtaining a measured value $T_0^{\rm obs}$. The difference $\Delta T_0 = T_0^{\rm pred} - T_0^{\rm obs}$ was then plotted against the sum of the terms with $k \geq 1$ of Eq. (6.1), which represents the deviation from the Keplerian model. This procedure has been coded in the `alex_orbital_variability` routine of the `PSRALEX` software package, which we used for the actual analyses of the 47 Tuc pulsars.

6.3 The black widow and redback pulsars in 47 Tuc

In this section we present the seven black widow/redback pulsars of 47 Tuc in more detail. For those systems that have already been thoroughly studied in the past literature, we recall their main characteristics and point out the improvements obtained with our long-term timing over the previously published solutions. For the other systems, we report the detailed analyses that we have made.

6.3.1 47 Tuc I

47 Tuc I is a 3.48-ms binary pulsar in a 5.5-h orbit, discovered by Manchester et al. (1991) and further studied by different authors (Robinson et al., 1995; Camilo et al., 2000; Freire et al., 2001b, 2003). Its mass function, $f(M_{\rm p}) = 1.555 \times 10^{-6}$ M$_\odot$, implies a median companion mass of $M_{\rm c} = 0.015$ M$_\odot$, hence it belongs to the black widow class. Since it does not show radio eclipses, it may have a low orbital inclination.

Our extended timing, compared to the latest publication, improved all the previously measured parameters and allowed us to detect the second spin frequency derivative as well as the first orbital frequency derivative.

6.3.2 47 Tuc J

47 Tuc J is a 2.10-ms eclipsing binary pulsar in a 2.9-h orbit. As pulsar I, it was discovered by Manchester et al. (1991) and further studied by several authors (Camilo et al., 2000; Robinson et al., 1995; Freire et al., 2001b, 2003). Its mass function, $f(M_{\rm p}) = 4.86 \times 10^{-6}$ M$_\odot$, implies a median companion mass of $M_{\rm c} = 0.025$ M$_\odot$, so it is also a black widow.

Thanks to its very high intrinsic brightness, pulsar J features the best timing precision among all the 47 Tuc pulsars, with a timing residual r.m.s. of only 4.89 μs.

With our timing, we improved all the previously measured parameters and measured the second spin frequency derivative, $\ddot{f}$. Furthermore, we detected a strong intrinsic orbital variability. The orbital period appears to vary by a fraction of a ms in a quasi-sinusoidal fashion (Fig. 6.1). A BTX binary model with twelve orbital frequency derivatives was thus necessary to correctly describe this behaviour within the timing baseline considered.

6.3.3 47 Tuc O

47 Tuc O is a 2.64-ms eclipsing binary pulsar in a 3.3-h orbit. It was discovered by Camilo et al. (2000) and further studied by Freire et al. (2001b) and Freire et al. (2003). Its mass function, $f(M_{\rm p}) = 5.35 \times 10^{-6}$ M$_\odot$, implies a median companion mass of $M_{\rm c} = 0.025$ M$_\odot$, hence it is a black widow.

As for pulsar J, besides improving the measurement of all the parameters and detecting $\ddot{f}$, we detected an intrinsic orbital variability. Indeed, the orbital period of 47 Tuc O shows a constant increase until MJD $\sim$ 54300, which is then followed by a decrease (Fig. 6.1). In this case, only three orbital frequency derivatives were necessary to model the variability. This is in part due to the fact that the timing baseline for this pulsar is shorter than that of 47 Tuc J. We point out that these variations are not caused by any nearby objects, as the motion of the system would be obvious in variations of the observed pulse period.

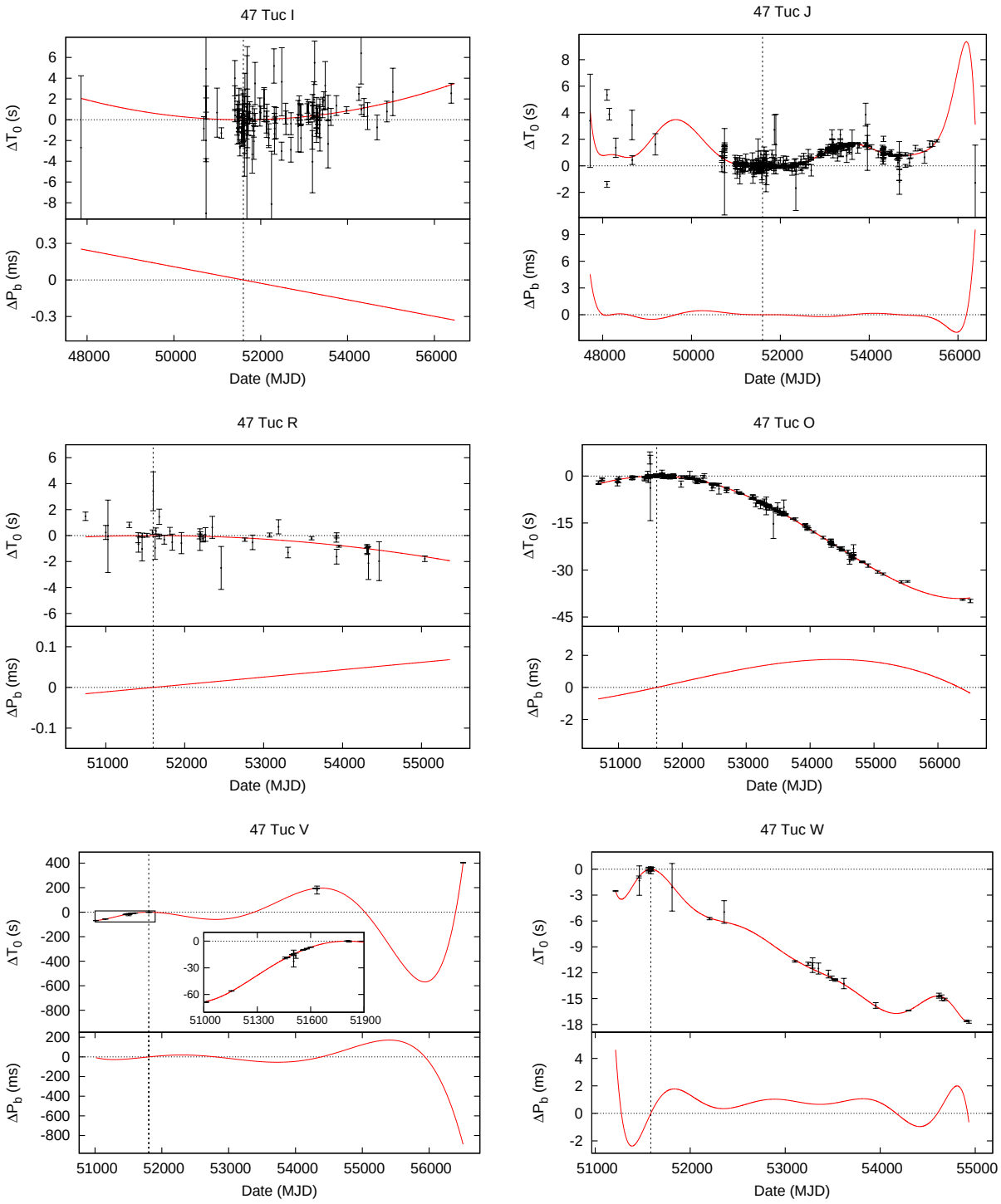

Figure 6.1. Orbital variability for six of the seven "black widow"/"redback" pulsars in 47 Tuc. Top panels: deviation of the epoch of passage at the ascending node from the prediction of a standard Keplerian model as a function of time. The red line is the theoretical prediction of the BTX model, the black points are the values measured with timing (see text for the detailed description of the method). Bottom panels: corresponding change of the orbital period from the reference value as a function of time. Note that the latter is just the time derivative of the red line of the upper panel.

6.3.4 47 Tuc P

47 Tuc P is a 3.64-ms binary pulsar in a 3.5-h orbit that was discovered in a single observation (on MJD 50689) by Camilo et al. (2000). The authors determined the binary parameters by extracting 14 ToAs that covered more than one orbit. Our T_0-search (described in Section 4.4.3) yielded an additional 4 detections (of which only one had high S/N and the other three were relatively faint) from which we were able to extract another 14 ToAs, thus bringing the total number to 28, over a time span of $\sim$9.8 years. Because of the sparsity of the data, we were unable to obtain a phase-connected timing solution. Notwithstanding, we were able to fit for the spin period, spin period derivative, position and binary parameters. We kept the proper motion fixed to the value of global motion of the cluster. The latter was calculated as an unweighted mean of the proper motions of all the 22 pulsars with a timing solution available at the time of the analysis, namely $\mu_\alpha = 4.9 \pm 0.9$ mas yr^{-1} in right ascension and $\mu_\delta = -2.7 \pm 0.7$ mas yr^{-1} in declination. Both the position and spin period derivative are, as expected, rather poorly determined and their values should be taken as just indicative. The orbit is correctly described by a simple Keplerian model, with no evidence of orbital frequency derivatives. This, together with the very low median mass of the companion ($M_c \sim 0.02$ M$_\odot$) and the total absence of radio eclipses, strengthens the hypothesis that 47 Tuc P is a black-widow type system, possibly seen at a low orbital inclination. Indeed, as pointed out by Freire (2005), some black widows have lower mass functions as a result of lower orbital inclinations, which in turn make the display of eclipses less likely. On the contrary, systems seen more edge-on appear to have larger masses and tend to exhibit eclipses.

To measure the DM, we summed in time each of our 4 detections, retaining as many frequency sub-bands as possible, depending on the S/N. From every sub-band we extracted one time-of-arrival, for a total of 12 usable ToAs. The latter were then fitted for the DM only, allowing arbitrary phase jumps between the different epochs. The resulting measured DM was 24.29 ± 0.03 pc cm^{-3}, a value slightly lower than the average, which suggests that the pulsar is on the near side of the cluster. In fact, we can obtain a rough estimate of the distance component along the line of sight, $r_\parallel$, through the linear relation found by Freire et al. (2001c) between the DM and the radial distance from the plane of the sky containing the centre of 47 Tuc. Using this relation and the measured DM, we infer $r_\parallel \simeq -1.36$ pc, with the negative sign indicating that the pulsar is indeed placed between the observer and the cluster centre.

No calibration data are currently available to determine the flux densities of the 47 Tuc pulsars. However, having the lowest detection rate (0.97%) in our dataset, 47 Tuc P is probably the faintest currently known pulsar in the cluster.

6.3.5 47 Tuc R

47 Tuc R is an eclipsing 3.48-ms binary pulsar, originally discovered by Camilo et al. (2000) but no timing solution has been published since then. With an orbital period of only 96 minutes, it was, at the time of discovery, the binary radio pulsar with the shortest orbital period known.

From our timing analysis, we obtained a phase-connected timing solution based on 449 usable ToAs spanning $\sim$ 13 years (Table 4.4).

Its mass function, $f(M_p) = 9.09 \times 10^{-6}$ M$_\odot$, implies a median companion mass of $M_c = 0.031$ M$_\odot$, making the system belong to the black widow class.

In the case of 47 Tuc R, no strong orbital variability emerged from our data, and the orbit was correctly described by a simple Keplerian model together with a single orbital period derivative. Given the high circularity of the system, we opted for an ELL1 binary model, as in the case

of other pulsar-WD systems (see Section 5.8), thanks to which we measured an eccentricity of $e \sim 10^{-4}$.

6.3.6 47 Tuc V

47 Tuc V is a 4.81-ms binary pulsar in a 5.1-h orbit, first presented by Camilo et al. (2000). The pulsar was detected twice in their data (on MJD 51012 and 51055), and the authors were able to give a rough estimate of the orbital parameters by extracting a total of 11 ToAs. At both epochs the pulsar was on the near side of its orbit, as the spin period was increasing during the observations. With the T_0-search, we were able to detect 47 Tuc V in another 7 pointings. Through our timing analysis as described in Section 4.4.5 we were able to obtain an additional 12 (mostly faint) new detections, bringing the total number to 19. After constructing a high-S/N template profile, we carefully extracted 88 usable new ToAs. In total, we had 99 ToAs spanning $\sim$10.7 years. As for pulsar P, we were unable to obtain phase-connection with our timing: in addition to the proper motion (set to the same average value as for P), the large covariances seen also forced us to not fit for the spin period derivative as well as for the position, the latter being set to the nominal cluster centre value. However, allowing arbitrary jumps between groups of ToAs, we derived an incoherent timing solution that enabled us to measure the spin period and the binary parameters with good precision. The parameters are reported in Table 4.5.

Using the same method as described in the previous section, we independently measured the DM, obtaining a value of 24.105 ± 0.008 pc cm^{-3}, the lowest amongst all the 47 Tuc pulsars. For this DM value, the projected distance along the line of sight from the cluster centre, predicted by the linear relation of Freire et al. (2001c), is $r_\parallel \simeq -4.12$ pc.

Eclipses

In the two discovery observations, Camilo et al. (2000) noted that the pulsar signal was being irregularly eclipsed over time scales as short as their 2-minute long sub-integrations. Our new 19 detections allowed us to get a deeper insight into the morphology and, possibly, nature of the eclipses. Not only did we confirm the presence of irregular short-lived eclipses, we also found that the pulsar is *always* invisible for roughly 50% of the orbit around its superior conjunction, likely being enshrouded by the gas that the companion star is losing.

The presence of long and persistent eclipses implies that the system inclination, i, cannot be small and that the companion is likely non-degenerate. Choosing a conservative lower limit of $i \gtrsim 20$ deg and a pulsar mass of $M_\mathrm{c} = 1.4$ M$_\odot$, the mass function implies that the companion has a mass in the range $0.30\ \mathrm{M}_\odot \lesssim M_\mathrm{c} \lesssim 1.17\ \mathrm{M}_\odot$, pointing towards a main sequence type. This range, together with the observed eclipsed fraction of the orbit of $\Delta\phi_\mathrm{b}^\mathrm{ecl} \sim 0.5$, can be used to estimate the rough projected size, R_c, of a supposedly spherical obscuring gas cloud through simple geometrical considerations. In the case of a circular, edge-on ($i = 90$ deg) orbit, this can be expressed by the relation:

$$R_\mathrm{c} = a_\mathrm{p}(1+q)\sin\left(\frac{2\pi\Delta\phi_\mathrm{b}^\mathrm{ecl}}{2}\right) \tag{6.2}$$

where a_p is the radius of the pulsar orbit and $q = M_\mathrm{p}/M_\mathrm{c}$ is the mass ratio. From the previous considerations, $1.19 \lesssim q \lesssim 4.59$, and thus $1.79\ \mathrm{R}_\odot \lesssim R_\mathrm{c} \lesssim 2.05\ \mathrm{R}_\odot$. On the other hand, the inferred Roche-lobe radius R_L of the companion, calculated with the approximate formula by Eggleton (1983), is in the range $0.75\ \mathrm{R}_\odot \gtrsim R_\mathrm{L} \gtrsim 0.46\ \mathrm{R}_\odot$, implying that the gas is extending

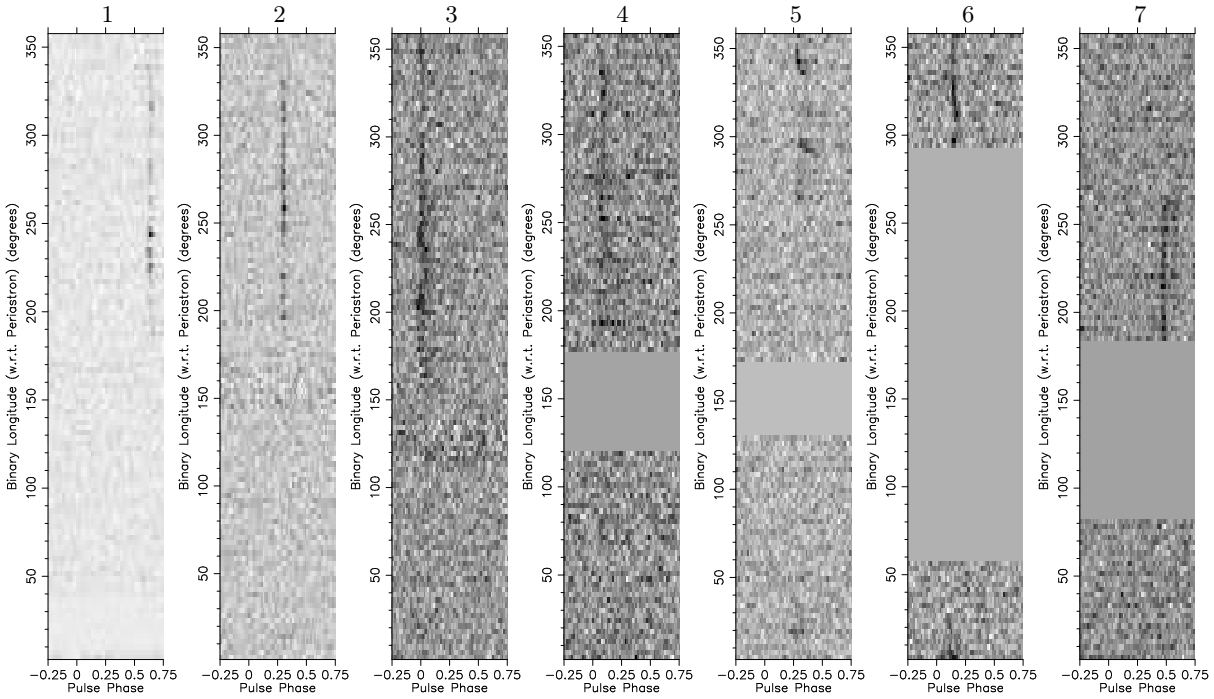

Figure 6.2. Intensity as a function of pulse phase (x-axis) and orbital phase $\phi_{\rm b}$ (y-axis) for 7 sample detections of 47 Tuc V. As can be clearly seen, the pulsar is always eclipsed for about 50% of its orbit around the superior conjunction (i.e. $\phi_{\rm b} = 0.25$). In addition, several short-lived eclipses often occur at other orbital phases, sometimes accompanied by excess time delays (panel 5) and sometimes with a broadening of the pulse (panel 3).

far beyond the gravitational influence of the companion star. Hence, the companion is probably undergoing continuous mass loss through the Roche-lobe overflow of its outer layers. We confirm the presence of frequent, short-lived, eclipses that hide the pulsar over time scales of minutes when the pulsar is on the near side of its orbit (panels 1-2 of Fig. 6.2). Sometimes the signal disappeared even for relatively long times (panels 5 and 7), whereas in another occasion (panel 5), the pulse also underwent a visible delay of roughly ~ 0.5 ms. Very likely, besides the presence of a large gas cloud surrounding the companion, clumps of ionized plasma of smaller size are wandering around the binary, occasionally intercepting the pulsar signal. When the physical characteristics (density and temperature) of the gas clump are such that the optical depth at our observing frequency is low, we still see the signal, but delayed because of the additional contribution to the dispersion measure that the clump introduces. Given our observing frequency of 1390 MHz, in the case of the 0.5-ms delay seen in panel 5 of Fig. 6.2, the inferred extra DM is $\simeq 0.24$ pc cm^{-3}.

The strong orbital variability is a common characteristic among redback binary systems and it thus supports the hypothesis that 47 Tuc V belongs to this class, as already hinted by the mass function and the presence of long eclipses.

It is important to note that, although the five-derivative BTX model used here is able to predict the orbital phase of 47 Tuc V observations within the time spanned by the data, it has no predictive capacity outside that range. Also, the predicted large swing in ΔT_0 between MJD ~ 54500 and ~ 56700 has no data supporting it. For these reasons, we should not consider this BTX binary model as a faithful representation of the binary orbit evolution, especially in

those time intervals where the data points are very sparse. Rather, the model should be seen as a display of the unpredictable orbital variability similar to that observed in other redback systems.

A transitional MSP?

The detections of 47 Tuc V appear clustered in three main groups, separated by two large gaps of $\sim$6.8 (MJD 51815−54298) and $\sim$6.0 years (MJD 54322−56508), respectively, where the pulsar was never visible. A similar behaviour is seen in tMSPs (see Section 1.4.3), which periodically switch between radio-MSP and LMXB phases, over a time scale of a few years.

The strong orbital variability of 47 Tuc V, its persistent and irregular eclipses, the disappearance of its radio pulsations within intervals of a few years, and the mass of the companion of the order of $\sim 0.3-0.4$ M$_\odot$, are all typical characteristics of tMSPs that suggest that pulsar V might indeed be a member of this class. To constrain this hypothesis, we have looked into archival *Chandra* data and the literature on optical studies, to search for signs of an active tMSP. We used two methods: with the *Chandra* data, we searched for X-ray outbursts; from the optical studies, we searched for periodic signals at 47 Tuc V's orbital period.

Transitional MSPs, during their active LMXB states, have X-ray luminosities in the range of $L_{\rm X} = 10^{33} - 10^{34}$ erg s^{-1}; such luminous objects would be easily detected by *Chandra* anywhere in 47 Tuc. The data considered are grouped into four widely separated epochs. The first group of *Chandra* observations took place on MJD 51619−51620 (Grindlay et al., 2001). These observations were only 19 days after a detection of pulsations from 47 Tuc V on MJD 51600. Thus, it seems unlikely that pulsar V would be X-ray active during this *Chandra* observation, and the X-ray sources at 10^{33} erg s^{-1} in this observation can be ruled out. The next two groups of observations were carried out on MJD 52547−52558 and 53723−53743, both in the midst of the first gap in radio pulsation. No new *Chandra* sources significantly brighter than 10^{31} erg s^{-1} were seen in these data. The final *Chandra* observations occurred in the MJD range 56905−57055, after the radio data considered, and also show no new bright sources. We point out that there are at least two caveats that must be considered: a) it is possible that pulsar V was X-ray active during small fractions of the time in the radio detection gaps; b) it is possible that the actual position of 47 Tuc V is beyond the field of view of *Chandra*. Even though both hypotheses appear unlikely, we are currently not able to rule them out.

We make reference to three major optical surveys for periodicities in 47 Tuc: two ground-based, and one using the *HST* over a smaller field of view. The optical light curve of the tMSP PSR J1023+0038, which has a similar orbital period (4.75 h), though slightly lower companion mass (0.24 M$_\odot$) compared to 47 Tuc V, varies between a magnitude of $V_{\rm min} = 17.0$ and $V_{\rm max} = 16.4$ in its active state (Halpern et al., 2013), and between $V_{\rm min} = 17.7$ and $V_{\rm max} = 17.35$ in its passive state (Thorstensen & Armstrong, 2005). Placing PSR J1023+0038 ($d = 1.37$ kpc, Deller et al. 2012) at the distance of 47 Tuc would suggest $V_{\rm min} = 19.7$ and $V_{\rm max} = 19.1$ in the active state, or $V_{\rm min} = 20.3$ and $V_{\rm max} = 20.0$ in the passive state. The B- and V-band photometric variability study of 47 Tuc done by Kaluzny et al. (2013) covered the entire Parkes beam down to about $V = 20.5$, though the core region could not be studied due to confusion. These observations were obtained primarily in 2009 and 2010 and coincide with the second gap in which 47 Tuc V is not detected, suggesting it may have been in the active LMXB state of a tMSP. In the LMXB state, the tMSPs PSR J1023+0038 and XSS J12270−4859 have sinusoidal light curves (Coti Zelati et al., 2014; de Martino et al., 2015), i.e. having a single minimum and maximum per orbital cycle. None of the variables in the study by Kaluzny et al. (2013)

had a period comparable to the 5.1-h orbital period of 47 Tuc V. The range where Kaluzny et al. (2013) found variables with similar orbital periods (the faintest variable detected had $V_{\rm max} = 19.6$) covered the range expected for 47 Tuc V in the active state. This suggests that, if 47 Tuc V was an active tMSP in 2009−2010 with similar properties as PSR J1023+0038, it is likely that it would have been detected by the authors, unless 47 Tuc V resides in the core region.

Weldrake et al. (2004) performed a photometric variability study of 47 Tuc in September 2002 (MJD 52508−52541), during the first gap in radio detections of 47 Tuc V. They observed for 33 continuous nights, for 10 h/night with 6-minute exposure times. The field of view was 52 arcmin per side, using a single filter that covered the Cousins V and R bands, and median seeing of 2.2 arcsec. They detected variables down to a magnitude of $V = 20$, but blending prevented them from studying stars within the central 6 arcmin in radius. Two variables showed interesting periods of 0.2144 (V80) or 0.2155 (V34) days. V80, at 24 arcmin from 47 Tuc's centre, should not be visible in the 14.4-arcmin wide beam of the Parkes radio telescope, while V34, at 9.3 arcmin from 47 Tuc's centre, is not too distant to be plausible, although the period is not an exact match. V34 is (barely) inside the field of view of *Chandra* ACIS-I observations on March 16, 2000 (MJD 51619), and a *Chandra* HRC-S observation on January 8, 2006 (MJD 53743), the latter also during the first gap in radio detections of 47 Tuc V. Neither *Chandra* observation showed a detection, with upper limits of $L_{\rm X} < 3 \times 10^{30}$ erg s^{-1} (during 2000) and $L_{\rm X} < 1 \times 10^{31}$ erg s^{-1} (during 2006). We rule out that any variable detected by Weldrake et al. (2004) is the counterpart of 47 Tuc V, and note that should 47 Tuc V have entered an active state in 2002, it would probably have been detected by this study.

Finally, Albrow et al. (2001) performed a deep search for variable stars in a 8.3-day sequence of *HST* WFPC2 images, covering much of the central region of 47 Tuc (roughly 2.5 × 2.5 arcmin, off-centre). Due to the *HST* sharp point-spread function, this study was mostly complete down to $V = 22$ for $>10\%$ variations. No periodic signals were found that matched the period of 47 Tuc V. Since this study would have been sensitive to a signal from 47 Tuc V even in a passive state, given its predicted optical properties, it is likely that 47 Tuc V is not projected upon the central portion of the cluster investigated by Albrow et al. (2001). We note that 47 Tuc W, with a shorter orbital period of 3.1 h, was identified in this dataset by Edmonds et al. (2002) at $V = 22.3$.

Observational evidence thus suggests that 47 Tuc V did not turn on as an accreting tMSP during its radio disappearances. Even bearing in mind the aforementioned caveats relative to the X-ray analysis, the lack of any compelling signals in the three optical surveys is a strong indication that 47 Tuc V is very likely not a tMSP. If so, the question about what is causing such long stretches of non-detections still holds. Scintillation can be ruled out since it acts over much shorter timescales of hours or days in all 47 Tuc pulsars, and this was also the case for pulsar V during the intervals in which it was visible. A similar consideration applies to the observed eclipses, whose timescales are of the order of minutes for the short-lived events showed in Fig. 6.2, or hours for the regular obscurations seen during about half the orbit. We believe that some more fundamental and long-lived physical process, such as an increase in the rate of mass loss from the companion star, may have occurred. This may have resulted in an engulfment of the pulsar, which thus became invisible until the mass loss switched back to the original rate.

6.3.7 47 Tuc W

47 Tuc W is a 2.35-ms binary pulsar in a 3.2-h orbit. Like pulsars P and V, it was originally discovered by Camilo et al. (2000), who detected it at a single epoch (MJD 51214) during which the favourable scintillation conditions brought the signal far above the detection threshold. On that occasion, the pulsar was also eclipsed for a large portion of the observation. The high S/N of the discovery observation allowed the authors to extract 12 ToAs and derive a first rough orbital solution, which was in turn used by Edmonds et al. (2002) to obtain the first optical identification of the companion of 47 Tuc W. The association with the radio pulsar was validated by the optical photometry, which showed sinusoidal variations at a period consistent with that derived at radio frequencies.

Our T_0-search produced 23 more detections of the radio MSP, from which we built a first incoherent timing solution. This was in turn used to refold the whole dataset, allowing us to spot the pulsar in another 11 pointings. Thanks to the large number of detections, we built a high-S/N template profile that revealed a previously unresolved third peak in the profile (Fig. 4.4), which was instead blended with the major peak in Camilo et al. (2000). With this template, we carefully extracted 187 more ToAs. Our timing data for 47 Tuc W thus consisted of 199 ToAs, spanning $\sim$10.2 years. The high number of ToAs, together with their frequent cadence, allowed us to obtain a phase-connected timing solution. The timing residuals (Fig. 4.3) had an r.m.s. of 10.20 μs. The best-fit parameters are reported in Table 4.5 and will now be discussed in detail.

Astrometric parameters and dispersion measure

Fig. 5.1 shows the radio timing position of 47 Tuc W relative to the nominal centre of the cluster and to the other pulsars in 47 Tuc. With an angular distance of only 0.066 arcmin, it is the closest pulsar to the cluster centre. As expected, the measured right ascension (α) and declination (δ) are both consistent, within 1.1-σ, with the optical position of the companion as measured by Edmonds et al. (2002) on an *Hubble Space Telescope* astrometric frame tied to the positions of the other MSPs in the cluster. The measured proper motion along the same coordinates, $\mu_\alpha = 6.1 \pm 0.5$ mas yr^{-1} and $\mu_\delta = -2.6 \pm 0.3$ mas yr^{-1}, is consistent with the global motion of the cluster, as calculated in Section 6.3.4, within less than 1-σ. The DM was measured using the same method as for pulsars P and V and amounts to 24.367 ± 0.003 pc cm^{-3}, a value that, like in the case of 47 Tuc P, is very close to the average DM of all the 47 Tuc pulsars. According to the Freire et al. (2001c) linear relation, this corresponds to a line-of-sight distance from the cluster centre of just $r_\parallel \simeq -0.21$ pc. This corroborates the hypothesis, already suggested by the position, that the three-dimensional distance of 47 Tuc W from the cluster centre is very small.

Long-term orbital variability

For 47 Tuc W, we needed to use a BTX model to correctly take into account the pulsar orbital motion. In this case the number of orbital frequency derivatives that we had to introduce was nine. We used the same method described in Section 6.2 to study the long-term orbital variability. The resulting plot is shown in Fig. 6.1. The lower panel shows that the orbital period varies with an amplitude of a few milliseconds in a quasi-periodic fashion and with a characteristic timescale of roughly 3 years. Contrary to the case of pulsar V, the coherence (phase-connection) of the timing solution and the frequent cadence of the data guarantee that the fitted BTX model is a reasonably faithful description of the actual changes in the orbital

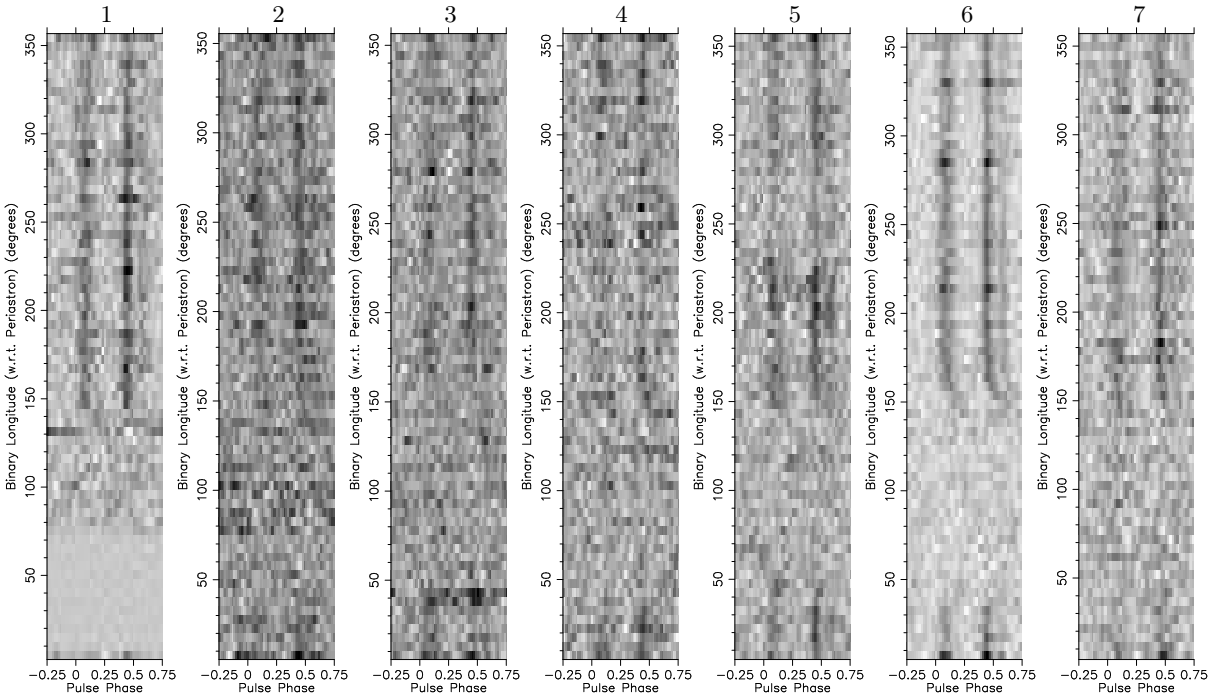

Figure 6.3. Intensity as a function of pulse phase (x-axis) and orbital phase $\phi_{\rm b}$ (y-axis) for 7 sample detections of 47 Tuc W. The pulsar systematically exhibits eclipses between $\phi_{\rm b} \simeq 0.09$ and $\phi_{\rm b} \simeq 0.43$ that appear to be much more regular than those of 47 Tuc V.

dynamics within the time span considered. However, the inability of the model to predict the orbital phase outside that range still holds. The large orbital variability prevents us from using 47 Tuc W as a probe for the cluster gravitational potential in the vicinity of the core.

Eclipses and redback nature

The new 34 detections of 47 Tuc W constitute a good sample for a qualitative study of the eclipses. As shown in Fig. 6.3, the pulsar shows regular eclipses that last for about one third of its orbit. Using our sample of detections, we measured the mean eclipse ingress and egress orbital phases to be $\phi_{\rm b}^{\rm ing} = 0.09$ and $\phi_{\rm b}^{\rm egr} = 0.43$, respectively, resulting in the pulsar not being visible for $\sim$34% of the orbit, on average. The eclipse is thus centered at orbital phase $\phi_{\rm b} = 0.26$, that is about 2 minutes later than the pulsar superior conjunction ($\phi_{\rm b} = 0.25$). Also, the eclipse egress exhibits, on average, a smoother transition that is often accompanied by a delay of the pulses, whereas the ingress transition is generally shorter and more abrupt. These characteristics are very similar to those found at X-ray wavelengths by Bogdanov et al. (2005), who proposed that the X-ray eclipses could be caused by a shock produced by the interaction of the energetic pulsar wind with the gas spilling out from the companion via Roche-lobe overflow, through the inner Lagrangian point (Fig. 2 in Bogdanov et al., 2005). The gas flow would have a "cometary" shape due to the orbital Coriolis forces, from which the observed asymmetry of the X-ray and radio eclipses originate. Our radio observations are thus in support of this model.

Based on the median companion mass of 0.148 $M_\odot$, 47 Tuc W can be classified as a redback system.

6.4 Discussion

From what we have just discussed in Section 6.3, we can see that the black widow and redback pulsars of 47 Tuc can be divided into two groups, based on their orbital beaviour. This can be seen in Fig. 6.1, where we have used the method outlined in Section 6.2 to plot the variation of the orbital period, and the consequent shift in the epoch of passage at the ascending node, as a function of time for six of these pulsars (the four detections of 47 Tuc P are too few to yield any meaningful conclusions, hence it has been excluded).

A first set of pulsars, constituted by 47 Tuc J, O, V and W, is characterized by a strong orbital variability, indicated by the high number of orbital frequency derivatives used in the relative binary models. These are necessary to correctly account for the erratic behaviour of the orbits, which evolve in a semi-chaotic fashion. It is important to recall that the BTX models are only valid in the region for which we have data, i.e. they do not have predictive power and cannot accurately describe the orbital phase evolution outside the timing baseline. This is the reason why the model seems to "explode" around the extrema of the time range.

The second set of pulsars is represented by 47 Tuc I and R. Even with the long timing baseline being considered here, the orbits of these two pulsars could be correctly described without the need of invoking any orbital frequency derivatives higher than the first (which in these cases we report as $\dot{P}_{\rm b,obs}$). This could be due, to some extent, to lack of timing precision. Looking at Fig. 6.1, we can see that the oscillations in ΔT_0 for 47 Tuc J are quite small compared to the dispersion of the data points observed in 47 Tuc I and R. If the latter could be timed with the same precision as 47 Tuc J, it might be possible that subtle oscillations in ΔT_0 (such as those observed for 47 Tuc J) would become detectable. However, the values of $\dot{P}_{\rm b,obs}/P_{\rm b}$ for these two systems are remarkably similar to their $\dot{P}_{\rm obs}/P$ (see Fig. 5.3); they are even slightly smaller as one would expect from a positive intrinsic spin period derivative $\dot{P}_{\rm int}$: for 47 Tuc I, we obtain $\dot{P}_{\rm int} = (9.2 \pm 4.3) \times 10^{-20}\,{\rm s\,s^{-1}}$, and for 47 Tuc R $\dot{P}_{\rm int} = (3.1 \pm 2.2) \times 10^{-20}\,{\rm s\,s^{-1}}$, values that are similar to those of the remaining pulsars. This makes it likely that, as in the case of $\dot{P}_{\rm obs}/P$, the $\dot{P}_{\rm b,obs}/P_{\rm b}$ observed in these systems is mostly caused by the acceleration of the pulsars in the field of the globular cluster, $a_{\rm GC}$. These systems have such short orbital periods that, despite the small companion masses, we must take into account an intrinsic variation of the orbital period caused by the emission of gravitational waves. In this case, Eq. (5.14) becomes:

$$\dot{P}_{\rm int} = \dot{P}_{\rm obs} - \frac{\dot{P}_{\rm b,obs} - \dot{P}_{\rm b,int}}{P_{\rm b}} P. \tag{6.3}$$

Assuming a pulsar mass of 1.4 $M_\odot$ and an orbital inclination of 60 deg for both pulsars, we obtain for the orbital variation $\dot{P}_{\rm b,int} = -4.8 \times 10^{-15}\,{\rm s\,s^{-1}}$ for 47 Tuc I and $\dot{P}_{\rm b,int} = -7.6 \times 10^{-14}\,{\rm s\,s^{-1}}$ for 47 Tuc R. Inserting these terms in Eq. 6.3, we obtain even smaller intrinsic spin period derivatives: $\dot{P}_{\rm int} = (7.8 \pm 4.3) \times 10^{-20}\,{\rm s\,s^{-1}}$ for 47 Tuc I and $\dot{P}_{\rm int} = (-1.6 \pm 2.2) \times 10^{-20}\,{\rm s\,s^{-1}}$ for 47 Tuc R, implying lower limits on the characteristic ages of both systems of 0.33 and 2.0 Gyr respectively. This means that the agreement between the cluster acceleration and the observed orbital period derivative is even more precise when we take the gravitational wave emission into account.

Provisionally, we conclude that the black widow systems come in two flavours, with and without strong orbital variability. It is plausible that this is determined by some physical process, related to the mass loss rate of the companion star, that we do not yet fully understand.

Chapter 7

Polarimetric studies of the pulsars in M15

The work presented in this chapter is part of an ongoing project on the monitoring and the study of the pulsars in the globular cluster M15. I am the lead scientist of the project. I wrote two proposals, made the vast majority of the relative observations, and carried out the data reduction, timing and polarimetric analysis for all the pulsars. When completed, this work will be presented in an article, in which I will be the lead author, with the following provisional author list and title:

- **Ridolfi, A.**; Desvignes, G.; Freire, P. C. C.; Kramer, M.; Wex, N., Venkataraman, A.; Kirsten, F.; *"Long-term observations of the pulsars in M15 - I. Polarimetry properties of five pulsars and relativistic spin precession in PSR B2127+11C"*; To be submitted to MNRAS

Contents

7.1 Introduction

NGC 7078 (also known as M15) is one of the most luminous and most massive Galactic globular clusters known. With an estimated age of $\sim$ 13 Gyr (e.g. McNamara et al., 2004; Monelli et al., 2015), it is also one of the oldest systems of stars in our Galaxy. The very old age is also confirmed by its extremely low measured metallicity (Fe/H $\simeq -2.3$, Carretta et al., 2009). The inferred distance of M15 from the Solar System is $\simeq$ 10.3 kpc (Watkins et al., 2015b), which is more than twice the distance of 47 Tuc. Its position in the sky ($\alpha = 21^{\rm h}\,29^{\rm m}\,58.33^{\rm s}$, $\delta = +12^\circ\,10'\,01''.2$, Goldsbury et al. 2010) near the celestial equator makes M15 visible to the 305-m Arecibo radio telescope, a non-steerable spherical dish located in Puerto Rico.

The interest for M15 mostly stems from the fact that it is in an advanced post-core-collapsed state (Djorgovski & King, 1986), a fact signaled by the observed central cusp in the radial brightness profile. This has led to speculations about the possible presence of an intermediate-mass black hole (IMBH) in the cluster (e.g. Newell et al., 1976). Recent works, however, have challenged this hypothesis by putting stringent constraints on the maximum possible mass of the black hole (e.g. Kirsten & Vlemmings, 2012), and by showing how the observed properties of the cluster could be explained with just a high concentration of stellar remnants in the core (e.g. den Brok et al., 2014).

The presence of a large number of compact objects in the cluster is also supported by direct evidence. Indeed, a series of observations of M15 made with the Arecibo telescope in the years 1989 and 1990 have led to the discovery of 8 radio pulsars residing in the cluster (Wolszczan et al., 1989; Anderson et al., 1990; Middleditch, 1992; Anderson, 1993). Of these, seven are isolated pulsars (four of which being MSPs, Anderson 1993) and one is a mildly recycled pulsar in an eccentric binary system (Prince et al. 1991; Jacoby et al. 2006, see also Section 7.5).

Until circa 2013, all the pulsars were monitored fairly regularly at Arecibo through observations made in total-intensity mode (i.e. summing the two polarization signals). This allowed a very good long-term timing of the pulsars but no polarimetric studies were possible.

In this chapter we exploit the most recent M15 data that we have taken in full-Stokes mode with the Arecibo telescope to investigate the polarimetric properties of the pulsars in the cluster. After giving a detailed description of our whole dataset (Section 7.2) we present the strategy used to calibrate the data in polarization and flux (Section 7.3). Then, in Section 7.4, we report on the measured fluxes, RMs and polarimetric profiles of the five pulsars detectable in our data. Finally, in Section 7.5, we use the polarimetric properties of the binary pulsar M15C to study relativistic spin precession, a secular effect occurring in this system.

7.2 The M15 dataset

Our M15 dataset consisted of about 28 years of observations entirely taken with the Arecibo radio telescope, spanning from 1989 to 2016. The whole dataset can be divided into two main parts. The first (and older) part was taken with three different observing set-ups:

- From April 1989 until January 1994, the cluster was observed at a central frequency of 430 MHz with a bandwidth of 10 MHz, using the 430-MHz line feed and the Arecibo three-level autocorrelation spectrometer (XCOR) as back-end. The latter was providing 128 frequency channels in each of the two circular polarizations and a time resolution of 506.6 ms (Wolszczan et al., 1989; Jacoby et al., 2006). Starting from February 1994,

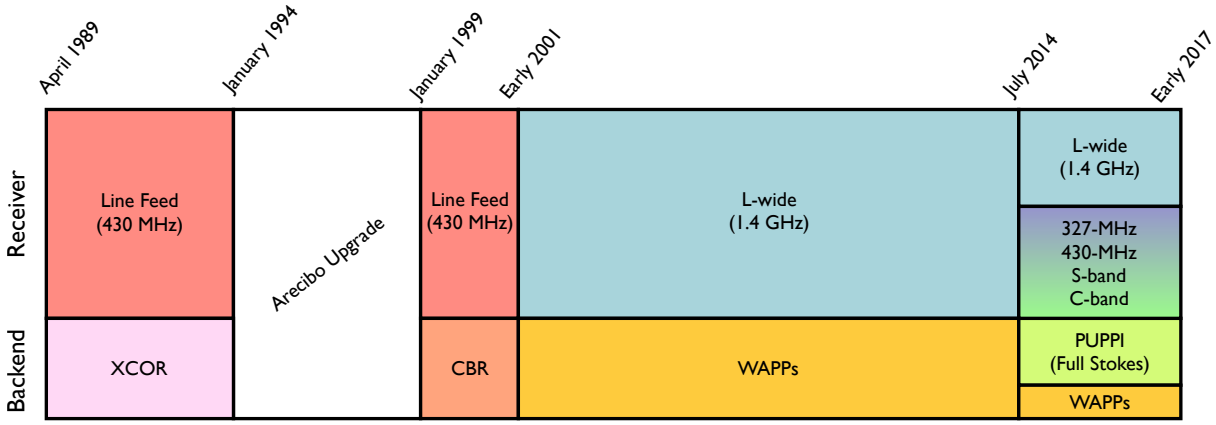

Figure 7.1. Graphical sketch of the different set-ups (receiver+backend) used to observe the globular cluster M15 over the years with the Arecibo radio telescope.

a major upgrade of the Arecibo telescope forced a stop in the observing program until the end of 1998.

- Starting from January 1999, the XCOR was replaced by the newer Caltech Baseband Recorder (CBR, Jenet et al., 1997) as back-end. The CBR was capable of 2-bit digitizing the two polarization signals in quadrature and record the baseband data onto magnetic tapes. Later, the data were converted into 32-channel coherently-dedispersed (at the DM of the pulsar M15C) search-mode filterbank files (see Section 2.3.3.2). This observing set-up was used until early 2001.

- From then, almost all the successive observations of M15 were carried out using the gregorian L-wide receiver, which has a central frequency of 1.4 GHz. This was done until mid-2014, using the four Wideband Arecibo Pulsar Processors (WAPPs, Dowd et al., 2000), each of which is able to process 100 MHz of bandwidth with 256 time-lags (i.e. frequency channels), a sampling time of 64 μs and a 3-level digitization, for a total effective bandwidth of 400 MHz divided into 1024 frequency channels.

The second and newest part of the M15 dataset is composed by observations that have been made specifically in the context of this thesis (Arecibo project P2910, P.I. Ridolfi):

- From July 2014 until December 2016 we observed M15 with a quarterly cadence. The reason of this cadence was to monitor the rapid changes observed in the pulsar M15C (see Section 7.5). For all the observations, we made use of the newest pulsar back-end available at Arecibo, i.e. the Puertorican Ultimate Pulsar Processing Instrument (PUPPI, a clone of the GUPPI back-end in use at the Green Bank Telescope, DuPlain et al. 2008). By using multiple GPUs, PUPPI is capable of producing coherently-dedispersed data, for up to 800 MHz of bandwidth, in real time. The vast majority of the observations were made with the L-wide receiver, with a central frequency of 1.4 GHz. When observing with this receveir, we always used PUPPI in full-Stokes (i.e. retaining the polarization information) coherent-search mode, with a total bandwidth of 800 MHz divided into 512 channels, and a time resolution of 10.24 μs. As for the CBR data, the coherent de-dispersion was made at the DM of M15C. Whenever possible, we also made parallel use of (at least some of) the WAPPs, with exactly the

same configuration as used in the past. This was done to later be able to compare the timing with PUPPI and with the WAPPs and to measure the time offset between the two back-ends. A few observations were also made with the "327-MHz", the Gregorian "430-MHz", the "S-low" and the "C-band" receivers. For the former three, we used only PUPPI in full-Stokes coherent search-mode with a bandwidth of 100, 100 and 800 MHz, respectively. With the "C-band", we instead used only the WAPPs, because PUPPI was not capable of operating with that receiver. To later correctly calibrate each pulsar in polarization and in flux, most of the observing sessions included one or more observations of the receiver noise-diode, and a pair of on-source/off-source observations of the quasar QSO B2209+080, whose radio flux and spectrum is known very accurately (Kuehr et al., 1981).

A schematic diagram summarizing the different observing set-ups used over the years at Arecibo for the observations of M15 is shown in Fig. 7.1. A detailed list of the most recent observations conducted under project P2910 is given in Table 7.1.

We point out that, because the observations of M15 have been made and processed by several people over the years and stored on different storage media, most of the original XCOR, CBR and (partly) WAPP files got lost or could not be retrieved. For some of these early data, and depending on the pulsar of the cluster considered, we only had the ToAs that were extracted by previous astronomers; in some other cases, we managed to retrieve at least the folded archives, from which we were able to extract the ToAs autonomously. However, this is relevant only for the timing analysis, which is beyond the scope of this chapter.

Here we focus only on the most recent full-Stokes PUPPI data taken with the L-wide receiver. The few PUPPI observations taken at different frequencies were excluded from our polarimetric analyses either because the pulsars were too faint or not detected at all, or because RFI contamination was too severe. All the L-wide PUPPI raw data files were folded with `DSPSR` with the most up-to-date ephemeris available for each pulsar. Of the eight known pulsars, only five were actually detectable. These are M15A, M15B, M15C, M15D and M15E. Hence, all the analyses presented in this chapter are relative to these five pulsars only.

7.3 Calibration of the M15 L-wide/PUPPI data

To calibrate the full-Stokes data of M15 taken with the L-wide receiver and PUPPI, we followed the standard NDO procedure, as described in Section 2.6.3.1. For the vast majority of the epochs (see Table 7.1) we had at least one observation of the noise-diode and one pair of on-source/off-source observations of the flux calibrator QSO B2209+80. For these epochs, we were able to perform an NDO calibration in both polarization and absolute flux. The few epochs lacking an associated observation of the flux calibrator made on that day, were calibrated using the available pair of QSO B2209+080 observations that was closest in time. This is justified by the fact the system equivalent flux density of the Arecibo L-wide receiver never changed significantly over time, having a measured average value of 3.0 Jy and a standard deviation of only 0.1 Jy.

7.3.1 Feed cross-coupling in the Arecibo L-wide receiver

To make sure that the polarization calibration of our data done with the NDO method was accurate enough (particularly important in the case of pulsar M15C, see Section 7.5), we investigated the impact of the possible cross-coupling of the two linear receptors in the Arecibo

Table 7.1. List of the recent observations of M15 made with the Arecibo radio telescope, in the context of this thesis, between 2014 and 2016. The (UP) note next to the S-low receiver indicates that the upper part of the receiver available band was used.

Epoch (MJD)	Receiver	Back-end	Noise-Diode Observation	Flux-Calibrator Observation	Notes
56845	L-wide	PUPPI	Yes	No	
56847	327-MHz	PUPPI	Yes	Yes	Only M15A detected
56944	L-wide	PUPPI + WAPP	Yes	Yes	
56965	L-wide	PUPPI + WAPP	Yes	Yes	
56966	430MHz	PUPPI	Yes	Yes	Only M15A detected
57037	L-wide	PUPPI + WAPP	Yes	Yes	
57038	C-band	WAPP	No	No	No pulsar detected
57088	L-wide	PUPPI	Yes	Yes	
57089	430MHz	PUPPI	Yes	Yes	Only M15A detected
57128	L-wide	PUPPI	Yes	No	
57143	L-wide	PUPPI	Yes	No	
57158	S-low	PUPPI	Yes	Yes	Severe RFI
57159	S-low	PUPPI	Yes	No	Severe RFI
57205	S-low	PUPPI	Yes	Yes	Severe RFI
57206	L-wide	PUPPI + WAPP	Yes	Yes	
57248	L-wide	PUPPI + WAPP	Yes	Yes	
57249	S-low (UP)	PUPPI	Yes	No	Severe RFI
57342	L-wide	PUPPI + WAPP	Yes	Yes	
57343	L-wide	PUPPI + WAPP	Yes	Yes	
57403	L-wide	PUPPI + WAPP	Yes	Yes	
57404	L-wide	PUPPI + WAPP	Yes	Yes	
57405	L-wide	PUPPI + WAPP	Yes	No	
57408	S-low (UP)	PUPPI	Yes	No	Severe RFI
57526	L-wide	PUPPI + WAPP	Yes	Yes	
57527	L-wide	PUPPI + WAPP	Yes	Yes	
57528	L-wide	PUPPI + WAPP	Yes	Yes	
57531	L-wide	PUPPI + WAPP	Yes	Yes	
57643	L-wide	PUPPI + WAPP	Yes	Yes	
57644	L-wide	PUPPI + WAPP	Yes	Yes	
57647	L-wide	PUPPI + WAPP	Yes	Yes	
57648	L-wide	PUPPI + WAPP	Yes	Yes	
57730	L-wide	PUPPI + WAPP	Yes	No	
57732	L-wide	PUPPI + WAPP	Yes	Yes	
57734	L-wide	PUPPI + WAPP	Yes	Yes	
57735	L-wide	PUPPI + WAPP	Yes	Yes	
57740	L-wide	PUPPI + WAPP	Yes	Yes	

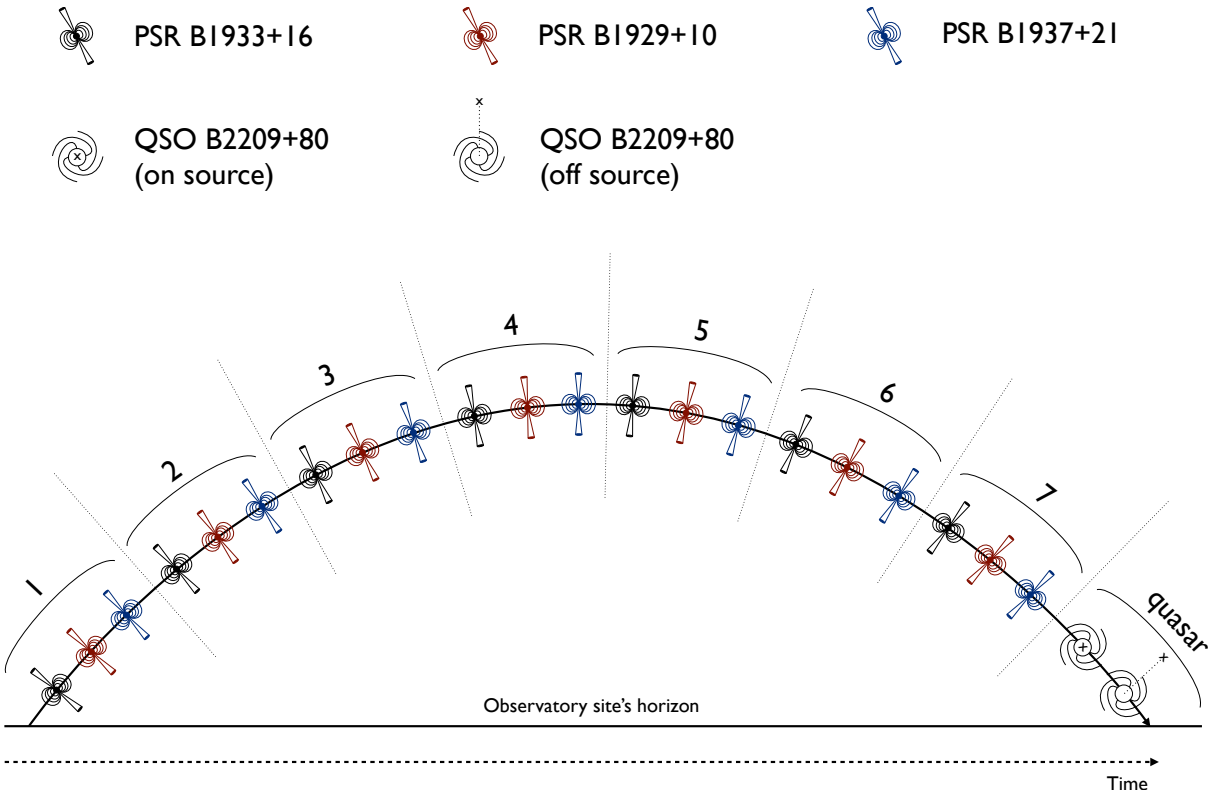

Figure 7.2. Schematic representation of the observing strategy used to investigate the cross-coupling of the two linear receptors in the Arecibo L-wide receiver. Over 3 hours, three bright and highly polarized pulsars (PSR B1933+16, PSR B1929+10 and PSR B1937+21) were alternately observed, every time for 3 minutes each, following an observation of the receiver noise-diode. For each pulsar, this resulted in a total of 7 pointings over a wide range of parallactic angles. After that, a pair of on-source/off-source observations of the quasar QSO B2209+80 was observed to be used as a completely unpolarized flux calibrator.

L-wide receiver.

To do so, we observed three extremely bright and highly polarized pulsars (PSR B1937+21, PSR B1933+16 and PSR B1929+10) over a wide range of parallactic angles, to be able to apply the MEM calibration method (see Section 2.6.3.2). The choice of observing three different pulsars was made to later cross-check the consistency of the results derived for each of them, as a sanity check.

The observations (made under Arecibo project P3113, P.I. Ridolfi) consisted of a single 3-hour long session in which we continuously switched between the three pulsars. This was possible thanks to the very similar right ascensions of the pulsars, which thus had very similar rise and set times at the site. Every time, each pulsar was observed for 3 minutes, following a 90-second long observation of the noise-diode. For each pulsar, this resulted in a total of 7 observations over a wide range of parallactic angles. In addition to that, the quasar QSO B2209+08 (the same observed in each M15 observing session) was observed on-source and off-source, to be later used as a completely unpolarized reference flux calibrator. A sketch of the observing strategy is shown in Fig. 7.2.

The observing set-up was chosen to exactly match that of our regular campaign of M15: we used the L-wide receiver in combination with PUPPI, the latter used in full-Stokes coherent

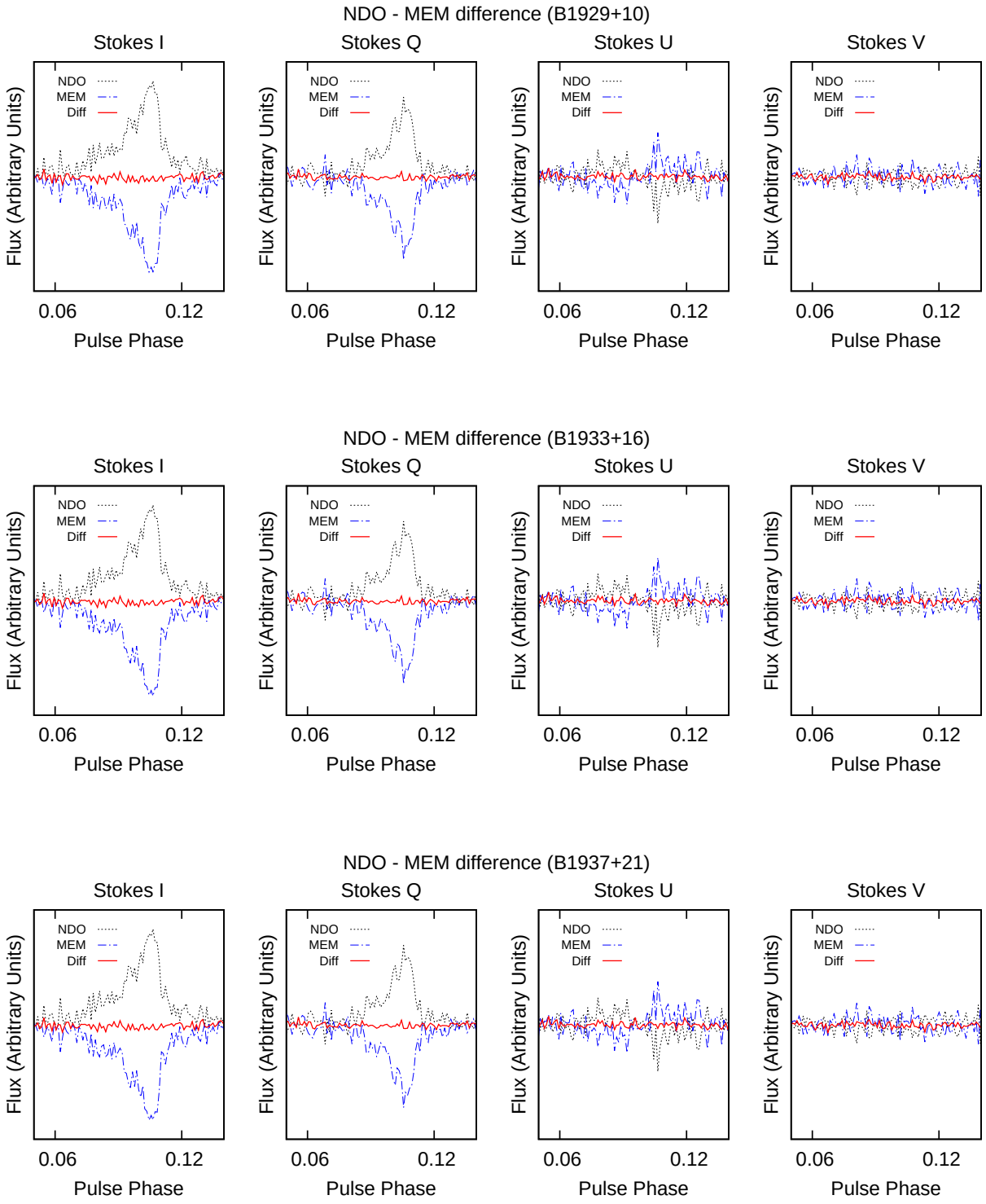

Figure 7.3. Comparison between the NDO and MEM calibration techniques as applied to an observation of M15C taken on MJD 57736. To each NDO-calibrated Stokes profile (black dotted lines) we subtracted the corresponding MEM-calibrated Stokes profile (blue dot-dashed lines, shown flipped for a better visualization), derived from the solution obtained from pulsar B1929+10 (first row), B1933+16 (second row) and B1937+21 (third row). All the resulting residual profiles (red solid lines) are always well within the noise level, indicating a very small cross-coupling in the Arecibo L-wide receiver and, hence, the actual equivalence between the results obtained with the NDO and MEM calibration methods.

Table 7.2. Measured values of the cross-coupling parameters of interest for the Arecibo L-wide receiver, as derived via the MEM calibration technique, using three different pulsars.

Cross-Coupling Parameter	PSR B1933+16	PSR B1929+10	PSR B1937+21
$\langle\epsilon_0\rangle$ (deg)	0.312 ± 0.484	0.003 ± 0.363	-0.219 ± 0.559
$\langle\epsilon_1\rangle$ (deg)	0.375 ± 0.503	0.060 ± 0.360	-0.157 ± 0.623
$\langle\theta_1\rangle$ (deg)	0.171 ± 0.439	-0.479 ± 0.380	0.303 ± 0.488

search-mode, 800 MHz of bandwidth divided into 512 channels and a sampling time of 10.24 μs.

The analysis of the data was carried out as follows. For each of the three pulsars, we used `DSPSR` and the best available ephemeris to fold the 7 search-mode data files acquired during the corresponding pointings. This produced 7 folded archives, which were processed, together with the relative noise-diode and quasar observations, using the `pcm` routine of `PSRCHIVE`. As explained in the documentation page[1], `pcm` uses the noise-diode observations to perform a first NDO calibration on each archive, from which it derives a first guess of the receiver instrumental response. We let the code choose the best 64 profile bins (typically the ones with the highest polarized flux) whose relative Stokes parameters were corrected for the parallactic angle rotation and for the previously derived instrumental response. The on-source quasar observation is instead used to estimate the mixing of Stokes I and V. The variation of the four Stokes parameters, as a function of the parallactic angle, is then fitted simultaneously for the 64 selected bins, to derive the MEM solution, i.e. the complete instrumental response of the system.

The cross-coupling parameters of interest (i.e. ϵ_0, ϵ_1 and θ_1, where the latter represents the relative orientation of the two receptors and not an absolute value) derived with the MEM solutions are reported in Table 7.2. The values of three cross-coupling parameters, averaged over the observing bandwidth, are very small in all the solutions. In the worst case (for PSR B1933+16), we found the ellipticities of the two receptors to be $\epsilon_0 \simeq 0.3$ deg and $\epsilon_1 \simeq 0.4$ deg, corresponding to a mixing of about 1.3% between the linear and circular polarization. This indicates that the cross-coupling in the L-wide receiver is very small and practically negligible for our purposes.

To verify that the extremely small cross-coupling does not indeed make a significant difference in the polarization properties of our data, we took the observation of M15C that was closest (i.e. done the next day) to our P3113 observations and we calibrated it with both the standard NDO method and with each of the three derived MEM solutions. We then subtracted each of the MEM-calibrated Stokes profiles to the ones derived with the NDO calibration and looked at the residual profile. As evident from Fig. 7.3, the residual profiles do not show any significant signals that stand out from the noise, indicating that the NDO and MEM calibrations give equivalent results.

7.4 RMs, polarimetric profiles and mean flux densities

After the data were properly calibrated, we measured the RM for all the five detectable pulsars at L-band. To do so, we applied the `rmfit` routine of `PSRCHIVE` to our folded archives, in which we retained the full frequency resolution. In each archive, we looked for the RM value that maximizes the total linear polarization, spanning a range between -1000 and $+1000$ rad m^{-2}.

For pulsars A, B and C the single observations had, in most cases, enough S/N to be able to

[1] http://psrchive.sourceforge.net/manuals/pcm

Table 7.3. Measured RMs and mean flux densities (S_{1400}) at 1.4 GHz for the five pulsars of M15 detectable in our PUPPI dataset. The reported values are the averages of all the measurements obtained for the single L-wide/PUPPI observations and the associated uncertainties are the relative standard deviations. Exceptions are the RM measurements for M15D and M15E and the flux density measurement for M15C (see notes below).

Pulsar	RM (rad m^{-2})	S_{1400} (μJy)
M15A	−69.6(5.5)	117.9(16.5)
M15B	−73.6(6.3)	22.0(5.4)
M15C	−68.9(5.0)	$< 40^{\star}$
M15D	$-67.7(4.6)^{\dagger}$	9.2(3.4)
M15E	$-72.8(2.4)^{\dagger}$	9.1(2.8)

† Single measurement performed on the sum of all the available observations of the pulsars, necessary to increase the resulting S/N. In this case, the relative uncertainty is calculated through the error propagation formula, with the off-pulse noise standard deviation used as the error for the flux density of the single pulse profile bins.
* Because M15C is precessing, its mean flux density is not steady and it is currently decreasing (see Fig. 7.5).

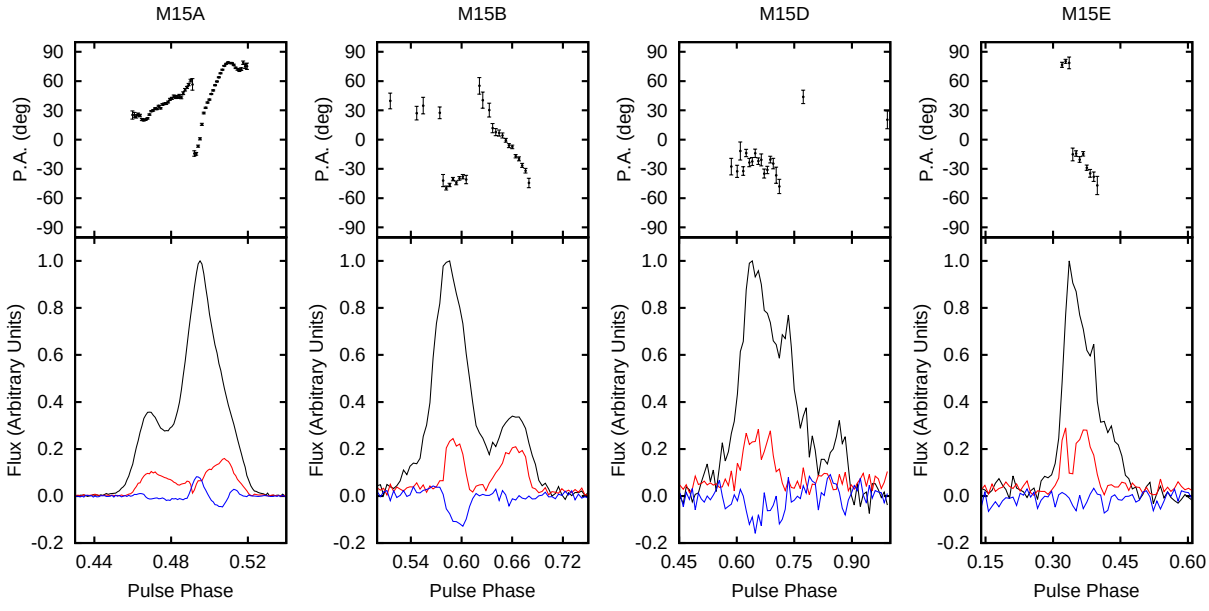

Figure 7.4. Polarimetric properties for pulsars A, B, D and E in M15. Bottom panels: polarization-calibrated total intensity (black lines), linear polarization (red lines) and circular polarization (blue lines) profiles. Top panels: corresponding measured linear polarization angles.

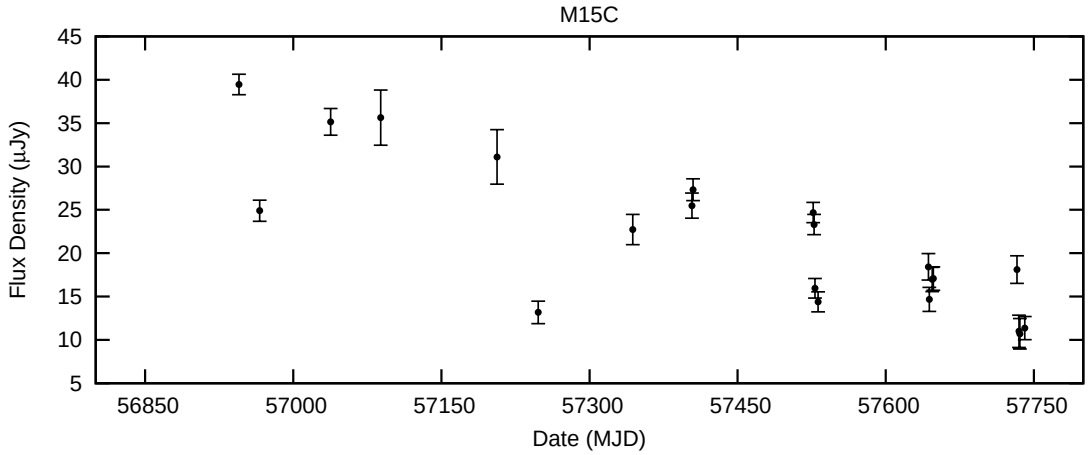

Figure 7.5. Measured mean flux density at 1.4 GHz as a function of time for the precessing binary pulsar M15C.

measure the RM independently on each epoch (i.e. on each folded archive). For pulsars D and E, instead, because of their faintness, it was necessary to sum all the observations together to maximize the resulting S/N. This allowed us to correctly run `rmfit` and derive one single RM measurement for each of the two pulsars.

Table 7.3 shows the RMs associated with all the five pulsars. In the case of pulsars A, B and C, the reported value is an average of all the independent measurements obtained. As can be seen, the measured RMs for the five pulsars are all compatible within 1-σ, with an ensemble weighted average of -71.3 ± 1.1 rad m^{-2}. This sharply contrasts with what has recently been seen in 47 Tuc, where the pulsar RMs span from positive to negative values and show a large gradient along one particular direction (Abbate et al, in prep.). The low dispersion in the measured RMs of the pulsars in M15 thus suggests that the contribution of the cluster to the RMs is very small compared to the contribution of our Galaxy. Hence, it is likely that the M15 intracluster magnetic field is very weak.

For each pulsar, we then used the measured RMs reported in Table 7.3 to correct for the Faraday effect and thus obtain the intrinsic polarimetric profiles. Again, for pulsars A and B, this was done independently on all the single observations, which were later added together to obtain very-high-S/N profiles. For pulsars D and E, instead, we directly corrected the previously-built summed archives. The resulting integrated polarimetric pulse profiles for pulsars A, B, D and E are shown in Fig. 7.4.

Because pulsar C is a precessing pulsar, it constitutes an exceptional case: although its RM is expected to remain roughly constant, so do not its polarimetric properties. Hence, for M15C, we corrected the single observations for the Faraday effect with the average RM of the pulsar (-68.9 rad m^{-2}). The resulting polarimetric profiles, shown in Fig. 7.8, were then used to conduct the study described in the next section.

Finally, being all the observations calibrated in flux, we were also able to measure the mean flux densities, S_{1400}, relative to the central observing frequency (1.4 GHz), for all the five pulsars. In Table 7.3 we report the unweighted average of all the flux density measurements for pulsars A, B, D and E. Pulsar C is treated differently because it has recently becoming fainter and fainter over time and for it we thus report only an upper limit. The detailed actual trend of S_{1400} as a function of time for M15C is shown in Fig. 7.5. Our measurements of the flux densities of the

pulsars in M15 are all in excellent agreement with previously published values (see e.g. Kirsten et al. 2014), with the obvious exception of M15C, for the reasons discussed above.

7.5 Relativistic spin precession in PSR B2127+11C

Relativistic spin precession (RSP) is another effect, predicted by GR and by other relativistic theories of gravity (de Sitter, 1916; Fokker, 1921; Damour & Ruffini, 1974; Barker & O'Connell, 1975), that can have measurable effects on the observables of a pulsar. In a binary system, RSP is the manifestation of relativistic spin-orbit coupling, namely the interaction between the rotational and the orbital motions of the two stars.

Calling $\mathbf{L}$ the orbital angular momentum of the binary, the resulting effect of RSP is that the spin angular momentum of the pulsar, $\mathbf{S}$, will undergo a change in its orientation with respect to a distant observer, by precessing about the total angular momentum of the system, $\mathbf{J} = \mathbf{L} + \mathbf{S}$, at a constant angular rate given by (Barker & O'Connell, 1975):

$$\Omega_{\rm so} = \mathrm{T}_{\odot}^{\frac{2}{3}} \cdot \left(\frac{2\pi}{P_{\rm b}}\right)^{\frac{5}{3}} \cdot \frac{M_{\rm c}(4M_{\rm p} + 3M_{\rm c})}{2(M_{\rm p} + M_{\rm c})^{4/3}} \cdot \frac{1}{1-e^2}, \tag{7.1}$$

with the usual meaning of the quantities involved and $M_{\rm p}$ and $M_{\rm c}$ expressed in solar masses. Because $\mathbf{S}$ is usually much smaller than $\mathbf{L}$, we can safely make the approximation $\mathbf{J} \simeq \mathbf{L}$, so that the precession occurs about the orbital angular momentum. Now, we recall that the pulsar magnetic axis $\mathbf{m}$, along which the emission is beamed, is assumed to be oriented at a constant angle $\alpha_{\rm m}$ with respect to the pulsar spin axis (see Section 1.3). An obvious consequence of RSP is that the observer's line-of-sight cut through the emission beam, will change over time. This results in a slowly time-varying observed pulse profile shape, intensity and polarimetry, as the observer's line of sight will probe different regions of the pulsar beam. Clearly, the larger is the misalignment angle, $\delta_{\rm so}$, between $\mathbf{S}$ and $\mathbf{L}$, the larger the effect will be; on the contrary, if $\mathbf{S} \parallel \mathbf{L}$, there will be no precession at all.

To date, significant evidence of observational changes that can be ascribed to RSP has been seen in PSR B1913+16 (Weisberg et al., 1989; Kramer, 1998; Weisberg & Taylor, 2002, 2005; Clifton & Weisberg, 2008), PSR B1534+12 (Arzoumanian, 1995; Stairs et al., 2004; Fonseca et al., 2014), PSR J0737−3039B (i.e. the double-pulsar system, Manchester et al., 2005b; Breton et al., 2008; Perera et al., 2010; Ferdman et al., 2013; Perera et al., 2014), PSR J1141−6545 (Manchester et al., 2010) and, more recently, PSR J1906+0746 (Desvignes et al., 2013; van Leeuwen et al., 2015). These changes can provide unique insights into several properties of both the pulsar and the binary, such as the pulsar beam structure and emission mechanism, the geometry of the system as well as its formation history. Last but not least, the modelling of RSP can represent an independent test of GR.

7.5.1 Evidence of RSP in M15C

PSR B2127+11C (or M15C, for short) is the only known binary system in M15. It is in a double neutron star system with a very eccentric ($e \simeq 0.68$) orbit and an orbital period of $P_{\rm b} \simeq 8$ h, which make it very similar to PSR B1913+16, the Hulse-Taylor pulsar. After its discovery by Anderson et al. (1990), its subsequent timing (Prince et al., 1991; Anderson, 1993; Deich & Kulkarni, 1996; Jacoby et al., 2006) has led to the precise measurement of three post-Keplerian parameters in the system: the advance of periastron, the Einstein delay and the orbital decay

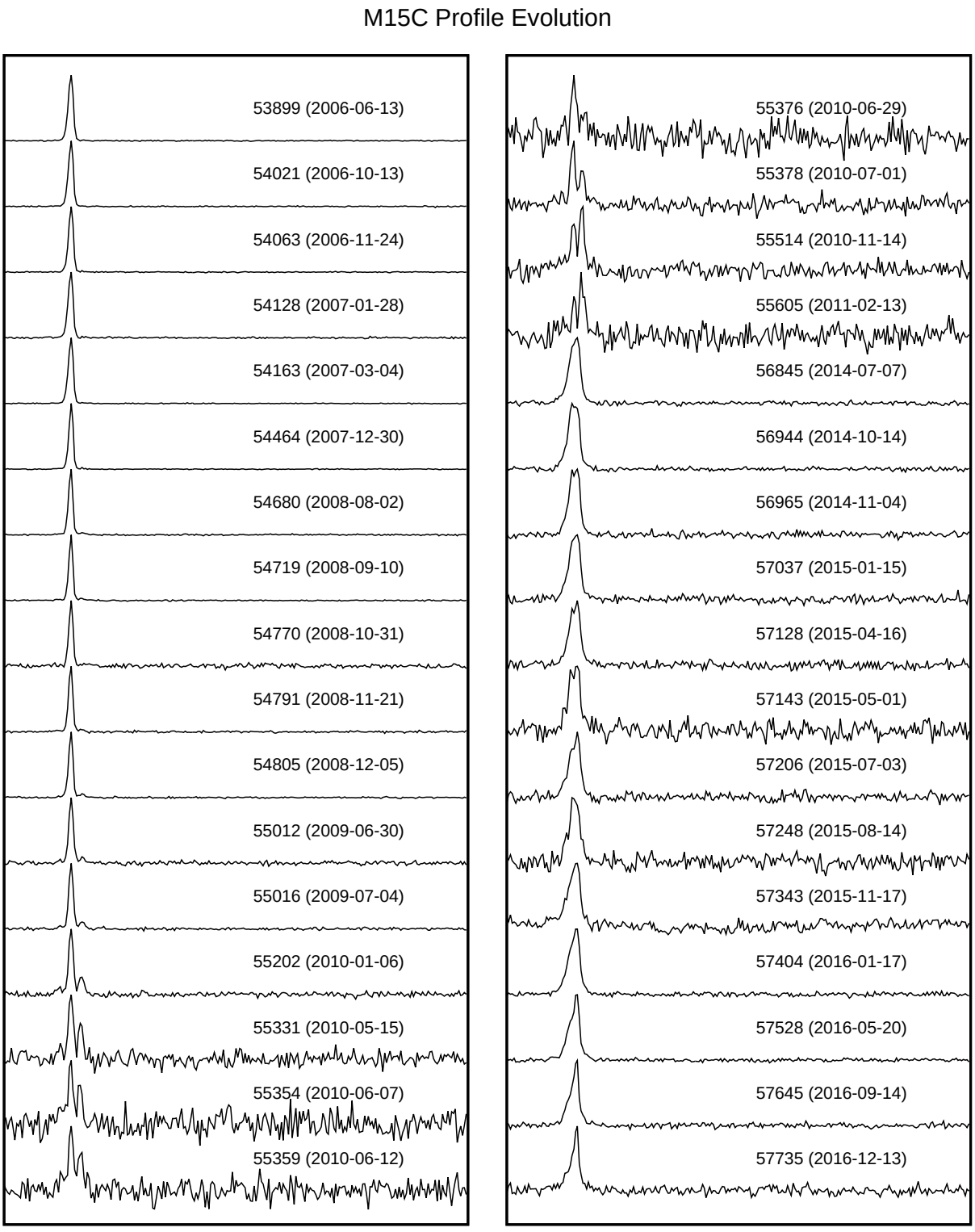

Figure 7.6. Evolution of the total intensity pulse profile of the precessing binary pulsar M15C between the years 2006−2016. The profiles are aligned using the timing solution listed in Table 7.4.

due to the emission of gravitational waves.

Since then, the continuous monitoring campaign (as described in Section 7.2) has resulted in the observation of significant changes in the pulse profile of M15C, as can be seen in Fig. 7.6. Indeed, after 2009, the pulsed signal of M15C became fainter and fainter, and disappeared around 2011. Recent interferometric images made by Kirsten et al. (2014), along with new pulsed observations made in 2013, revealed that M15C became again detectable, although much fainter and with a different pulse profile.

For this reason, starting from mid-2014, we decided to undertake the monitoring campaign described in Section 7.2 with the goal of modelling the ongoing RSP in M15C. The observations have been done in full-Stokes mode in order to exploit the possibly time-varying polarimetric properties of M15C. In particular, as Kramer & Wex (2009) pointed out, one should expect the observed linear polarization angle (PA) curve of the precessing pulsar to change in its shape and absolute value. This is indeed what we see our ~ 2.5 yr of polarimetric data. As can be seen in Fig. 7.8, the S-shape curve of the PA in M15C has become slightly flatter. At the same time, we recorded significant changes in the total intensity, linear polarization and circular polarization profiles of M15C, together with a fast decrease in the brightness of the pulsar. None of such changes are seen in any of the other four pulsars detectable in the same data, therefore the phenomenon has to be intrinsic to M15C. Since the characteristics of M15C closely resemble those of PSR B1913+16, where RSP has been observed and modelled, there was no doubt that RSP had to be responsible for the observed changes in the pulsar.

7.5.2 Updated timing solution

As a preliminary step for the study of RSP, we utilized the additional 10 years of new data available to extend the timing solution of M15C from that last published by Jacoby et al. (2006). The older extant XCOR and CBR datasets (spanning the years 1989−2001) consisted in previously extracted ToAs. For the vast majority of the newer WAPP (2002−2016) and the totality of the PUPPI (2014−2016) data, we had the original raw files. These were folded with `DSPSR` using the most up-to-date ephemeris available, from which we obtained the relative archives. We then followed the usual timing analysis as thoroughly discussed in Section 2.5 and Section 4.3, but with a difference. Because the pulse profile of M15C showed a major change in our PUPPI/WAPP data starting from 2014, with a sharp increase in the pulse width (see Fig. 7.6), we decided to use two different standard profiles: the first one was constructed by adding data taken up to the year 2008, until when the pulse shape was stable narrow; the second one was built adding data taken in the year 2014, when the pulse width had almost doubled and the S/N was still high. In both cases the summed profiles were de-noised using a wavelet smoothing algorithm implemented in the `psrsmooth` routine of `PSRCHIVE`. The resulting noiseless template was then cross-correlated against the data.

The ToAs so obtained for the WAPP and PUPPI data were combined with those of the XCORR and CBR. In total, we had 5648 ToAs, spanning ~ 27.67 years, which we fitted with `TEMPO`. In doing so, we also fitted for arbitrary jumps between groups of ToAs relative to different observing systems. The same was done between groups of ToAs extracted with different templates (as in the case of the WAPP data taken *before* and *after* 2014), as using different templates introduces an arbitrary phase offset due to the different fiducial point chosen in the profiles. Thanks to the parallel use of PUPPI and the WAPPs in most of our post-2014 observations, we were able to measure the time delay between the two back-ends and thus to remove the arbitrary phase jump between these two observing systems.

Table 7.4. Timing parameters for the pulsar in the double neutron star system M15C. The associated 1-σ uncertainties were calculated using a Monte-Carlo bootstrap routine implemented in `TEMPO`. A fixed parallax value of 0.1 mas was assumed; the time units are TDB; the assumed terrestrial time standard is UTC(NIST); the Solar System ephemeris used is the JPL DE421.

Pulsar Name	M15C
Reference Epoch (MJD)	50000.000
Start of Timing Data (MJD)	47632.493
End of Timing Data (MJD)	57740.848
Number of TOAs	5648
Residuals RMS (μs)	5.96
Right Ascension, α (J2000) (hh:mm:ss)	21:30:01.20439(3)
Declination, δ (J2000) (dd:mm:ss)	12:10:38.2031(9)
Proper Motion in α, μ_α (mas yr^{-1})	$-1.10(5)$
Proper Motion in δ, μ_δ (mas yr^{-1})	$-3.28(8)$
Spin Frequency, f (s^{-1})	32.755422697332(1)
1st Spin Frequency derivative, $\dot{f}$ (Hz s^{-2})	$-5.351636(7)\times10^{-15}$
2nd Spin Frequency derivative, $\ddot{f}$ (Hz s^{-3})	$-3.6(4)\times10^{-28}$
Dispersion Measure, DM (pc cm^{-3})	67.1348(2)
Epoch of glitch #1 (MJD)	52000.000
Permanent pulse frequency increment of glitch #1 (Hz)	$1.435(2)\times10^{-9}$
Epoch of glitch #2 (MJD)	56000.000
Permanent pulse frequency increment of glitch #2 (Hz)	$1.276(4)\times10^{-9}$
Binary Parameters	
Binary Model	DDGR
Projected Semi-major Axis, x_p (lt-s)	2.518380(5)
Orbital Eccentricity, e	0.6813901(8)
Longitude of Periastron, ω (deg)	345.30608(10)
Epoch of passage at Periastron, T_0 (MJD)	50000.06434476(6)
Rate of periastron advance, $\dot{\omega}$ (deg/yr)	4.4644772
Orbital Period, P_b (days)	0.335282048243(7)
Orbital Period derivative, $\dot{P}_\mathrm{b}$ (10^{-12} s s^{-1})	-3.9402375
Rate of change of orbital period minus GR prediction (10^{-12} s s^{-1})	$9.6(2)\times10^{-2}$
Einstein Delay, γ (s)	0.004823288
Total Mass, M (M$_\odot$)	2.7129(1)
Companion Mass, M_c (M$_\odot$)	1.3636(8)
Rate of change of projected semi-major axis, $\dot{x}_\mathrm{p}$ (10^{-12} s s^{-1})	$-0.021(6)$
Rate of change of eccentricity, $\dot{e}$ (10^{-12})	0.007(2)
Relativistic deformation of the orbit, δ_θ (10^{-6})	5.836
Relativistic deformation of the orbit, δ_r (10^{-6})	5.584
Derived Parameters	
Spin Period, P (s)	$3.05292961486000(10)\times10^{-2}$
1st Spin Period derivative, $\dot{P}$ (s s^{-1})	$4.987928(7)\times10^{-18}$
Mass Function, $f(M_\mathrm{p})$ (M$_\odot$)	0.153
Surface Magnetic Field, B_s (10^8 G)	167.05
Intrinsic Spin-down, $\dot{P}_\mathrm{int}$ (10^{-21} s s^{-1})	9140.48
Intrinsic Spin-down Luminosity, L_sd (10^{33} erg s^{-1})	12.68
Characteristic Age, τ_c (Gyr)	0.05

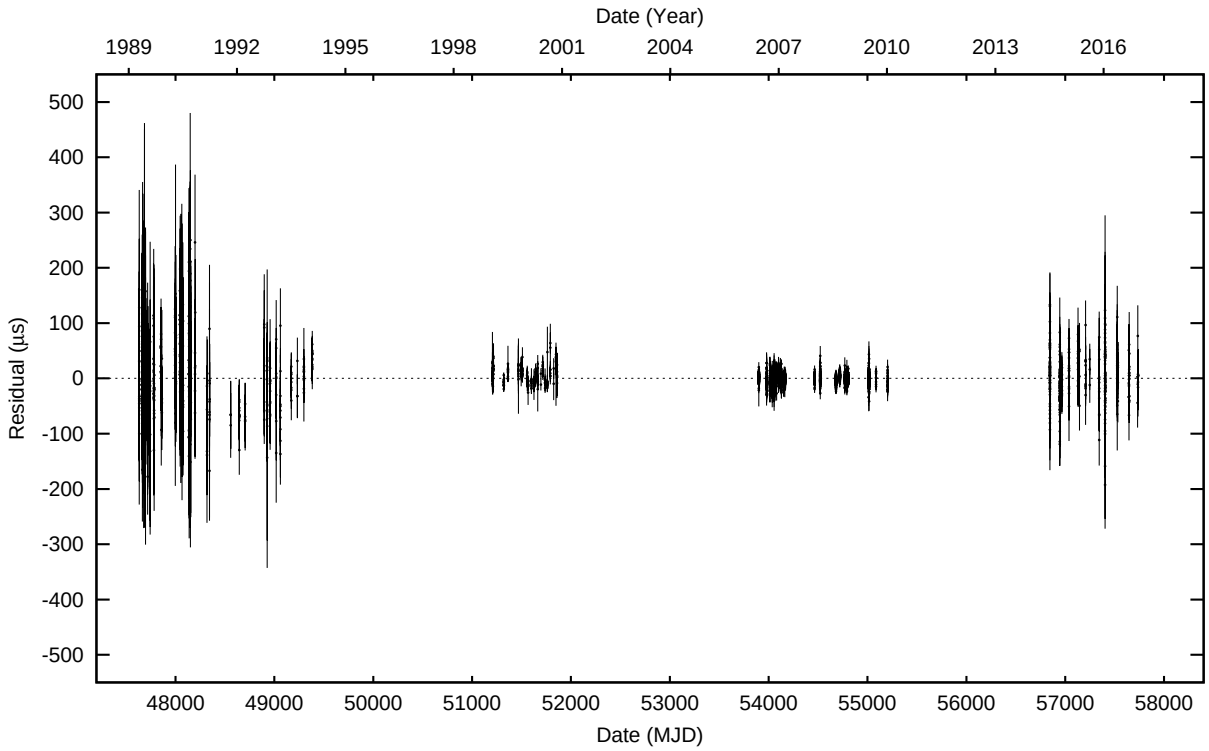

Figure 7.7. Timing residuals associated with the timing solution listed in Table 7.4 for pulsar M15C.

For the orbit of M15C we used the DDGR binary model (e.g. Taylor & Weisberg, 1989), which assumes GR as the correct theory of gravity. In this model, the binary-component masses are fitted and all the PK parameters are then evaluated according to GR.

The resulting timing solution is listed in Table 7.4, whereas the corresponding timing residuals are shown in Fig. 7.7. The greatly increased time span of our data allowed us to measure all the astrometric parameters with a much better precision than reported in Jacoby et al. (2006), in some cases of even one order of magnitude. Besides seeing similar improvements in all the orbital parameters, we were also able to detect, although with low significance, changes in the projected semi-major axis and in the orbital eccentricity. Furthermore, we detected two glitches, occurring sometime between 2002−2006 and between 2010−2014.

A detailed investigation of the two glitches of M15C is beyond the scope of this chapter and will be discussed in a future publication.

7.5.3 Geometry of the precessional RVM

In this section we utilize the PAs, as measured for M15C from our full-Stokes PUPPI data, to constrain the geometry of the pulsar and its binary system, as discussed by Damour & Taylor (1992) and Kramer & Wex (2009). In the following, we use the same conventions as in the latter two papers.

As previously discussed, the *precessional phase*, $\Phi_{\rm so}$, of the rotation axis of M15C about the orbital angular momentum of the binary varies linearly with time, t, as:

$$\Phi_{\rm so}(t) = \Omega_{\rm so}\, t + \Phi_0\,, \tag{7.2}$$

Table 7.5. Parameters involved in the modelling of the precessional RVM of M15C and relative best-fit values with associated 2-σ uncertainties. Similar values (consistent within the 2-σ uncertainties) are obtained when assuming an inclination of $i' = 180\,\mathrm{deg} - i = 130.34$ deg.

Parameter	Symbol	Best-fit value	Notes
Magnetic inclination of the main beam	α_m	115^{+5}_{-4} deg	Free parameter
Spin-orbit misalignment angle	δ_so	76^{+22}_{-20} deg	Free parameter
Reference precessional phase	Φ_0	257^{+21}_{-19} deg	Free parameter
PA constant shift	$\Delta\psi_0$	39^{+30}_{-29} deg	Free parameter
Pulse phase of spin axis closest approach	ϕ_0^i	–	Free parameter, one for each epoch i
Precession rate	Ω_so	1.31 deg/yr	Constant, calculated through GR
Orbital inclination	i	49.66 deg	Constant, calculated through GR

where $\Phi_0 \equiv \Phi_\mathrm{so}(t = t_0)$ is a reference precessional phase at some chosen epoch t_0 and Ω_so is the constant angular precession rate. If we assume GR, the latter is known and can be calculated via Eq. (7.1).

We now introduce the *polar angle* Λ, which is the angle, defined between 0 and π, between the observer's line of sight and the pulsar spin axis **S**. The polar angle depends on the precessional phase through the equation:

$$\cos\Lambda(t) = \cos\delta_\mathrm{so}\,\cos i + \sin\delta_\mathrm{so}\,\sin i\,\cos(\Omega_\mathrm{so}\,t)\,, \tag{7.3}$$

where i is the usual orbital inclination, and δ_so is the misalignment angle introduced in Section 7.5. These two angles are assumed to be constant, as they are not affected by RSP. What is instead affected by RSP is ψ_0, namely the PA corresponding to the inflection point in the PA swing curve. Once referred to infinite frequency, ψ_0 gives the orientation of the pulsar spin axis as projected on the plane of sky. Because of RSP, it is thus a time-varying quantity that can be expressed as:

$$\psi_0(t) = \eta_\mathrm{so}(t) + \Delta\psi_0\,, \tag{7.4}$$

where $\Delta\psi_0 = \Omega_\mathrm{asc} + \Delta\psi_\mathrm{F} + \Delta\psi_\mathrm{A}$ is a constant offset that is the sum of three main contributions, namely the longitude of the ascending node of the pulsar orbit (Ω_asc), the Faraday rotation effect (ψ_F) and the orbital aberration ($\Delta\psi_\mathrm{A}$). The time-varying term, $\eta_\mathrm{so}(t)$, is called *precessional longitude* and embodies the effect of RSP. It can range between 0 and 2π and can be obtained by solving the system of equations:

$$\begin{cases} \cos\eta_\mathrm{so}(t) = \dfrac{\sin\delta_\mathrm{so}\,\sin\Phi_\mathrm{so}(t)}{\sin\Lambda(t)} \\ \\ \sin\eta_\mathrm{so}(t) = \dfrac{\cos\Lambda(t)\,\cos i - \cos\delta_\mathrm{so}}{\sin i\,\sin\Lambda(t)} \end{cases}\,. \tag{7.5}$$

Ultimately, the value of $\psi_0(t)$ is well described by the RVM (Eq. 2.61) which, for convenience, we report again here in its explicit form:

$$\psi_0(t) = \arctan\left\{\frac{\sin\alpha_\mathrm{m}\,\sin(\phi-\phi_0)}{\sin[\pi-\Lambda(t)]\cos\alpha_\mathrm{m} - \cos[\pi-\Lambda(t)]\,\sin\alpha_\mathrm{m}\,\cos(\phi-\phi_0)}\right\} - \psi\,, \tag{7.6}$$

Table 7.6. List of the "epochs" fitted for the precessional RVM of M15C. Due to ever-decreasing brightness of the pulsar, the last four epochs are in fact the addition of multiple observations, made on different days.

Epoch #	Summed MJDs	Total integration time (s)	S/N
1	56845	4221	66.96
2	56944	7200	78.44
3	56965	7200	23.42
4	57037	4664	19.04
5	57088	3157	15.41
6	57128	1433	15.52
7	57143	1172	11.85
8	57206	5098	15.29
9	57248	7278	11.52
10	57342, 57343	14399	30.20
11	57403, 57404, 57405	18135	46.96
12	57526, 57527, 57528, 57531	30406	43.14
13	57643, 57644, 57647, 57648	24388	34.95
14	57730, 57732, 57734, 57735, 57740	28900	11.41

where we have used the relation $\pi - \Lambda(t) = \alpha_{\rm m} + \beta_{\rm m}(t)$.

7.5.4 Analysis and results

The set of Eqs. (7.2)-(7.6) can be used to perform a global fit to the polarization angle values measured in the polarization-calibrated data of M15C. The dataset used for the precessional RVM fit of M15C consisted of a total of 14 "epochs", spanning $\sim$ 2.5 yr, from July 2014 to December 2016. Because of the steady decrease in flux of the pulsar, some of these epochs are in fact constituted by the sum of a few, closely spaced single observations, which were previously independently calibrated and corrected for the Faraday rotation. This was necessary to guarantee a sufficiently high S/N in each resulting profile to be actually informative and, hence, beneficial to our fit. The list of the epochs used in our analysis, with the details of the summed observations, total integration time and resulting S/N is reported in Table 7.6. The corresponding profiles are shown in Fig. 7.8

For the actual fit of our polarimetric data, we used MODELRVM[2] (Desvignes et al., in prep.). This code is able to estimate the precessional RVM parameters using a Bayesian approach, based on the MULTINEST parameter space sampling algorithm (Feroz et al., 2009). As discussed in the previous section, the parameters involved in the precessional RVM are: $\alpha_{\rm m}$, $\delta_{\rm so}$, Φ_0, $\Delta\psi_0$, $\Omega_{\rm so}$, i, and one ϕ_0 for each epoch involved. However, in the case of M15C, both the inclination and the precession rate are known, thanks to the timing measurement of the PK parameters. Hence, we decided to keep these two parameters fixed in our analysis to the values predicted by GR, namely $i = 49.66$ deg and $\Omega_{\rm so} = 1.31$ deg yr^{-1}. In total, our model had 19 free parameters, which were sampled by MODELRVM using uniform priors.

In Fig. 7.9 we show the one- and two-dimensional marginalized posterior distributions for the four parameters of interest in our model. We find $\alpha_{\rm m} = 115^{+5}_{-4}$ deg, $\delta_{\rm so} = 76^{+22}_{-20}$ deg,

[2] https://github.com/gdesvignes/modelRVM

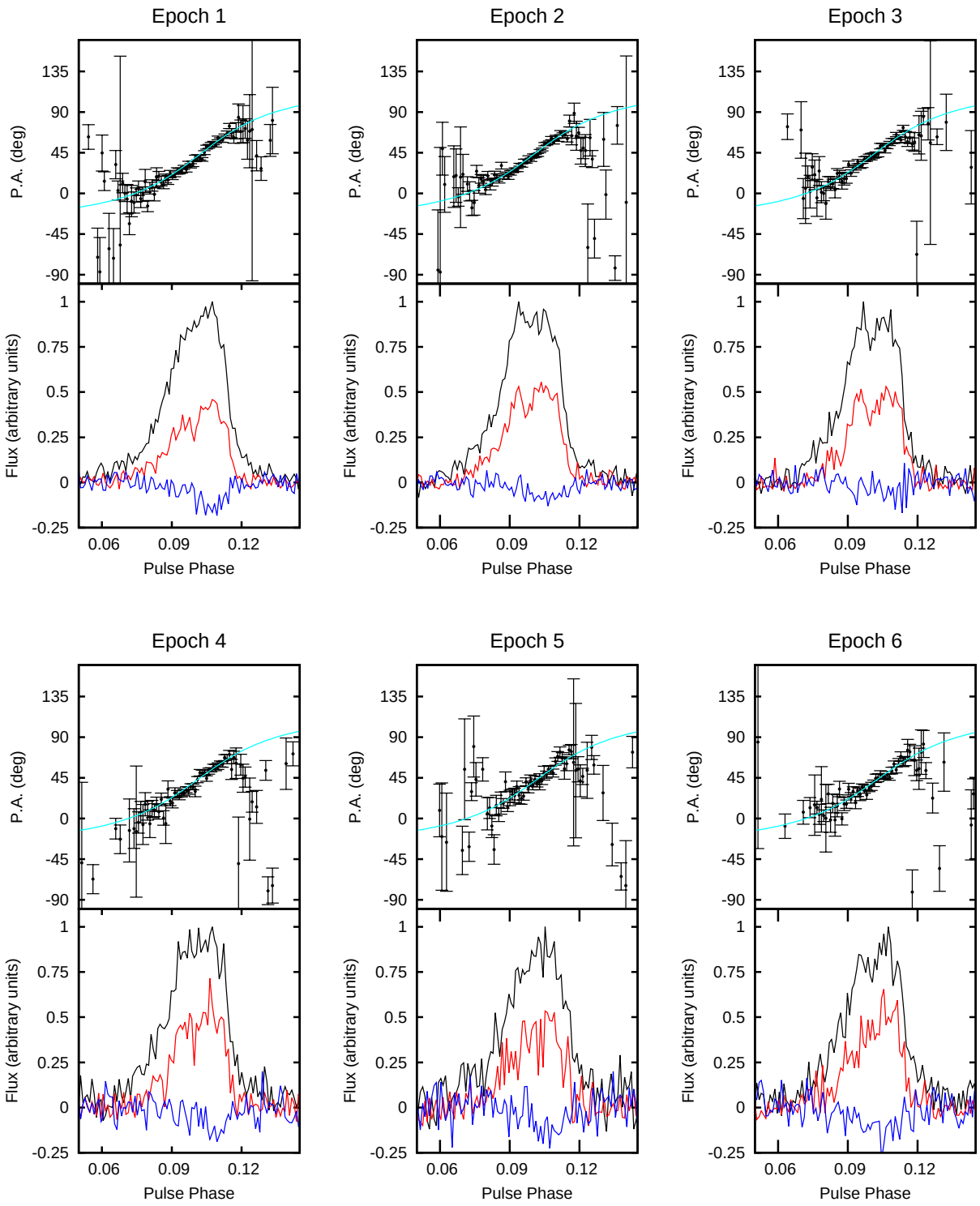

Figure 7.8. Bottom panels: polarization calibrated total intensity (black lines), linear polarization (red lines) and circular polarization (blue lines) M15C profiles of the 14 epochs fitted to the precessional RVM. Top panels: theoretical polarization angle swing (light blue lines), as predicted by the best-fit solution of the precessional RVM, plotted over the measured polarization angles (black bars).

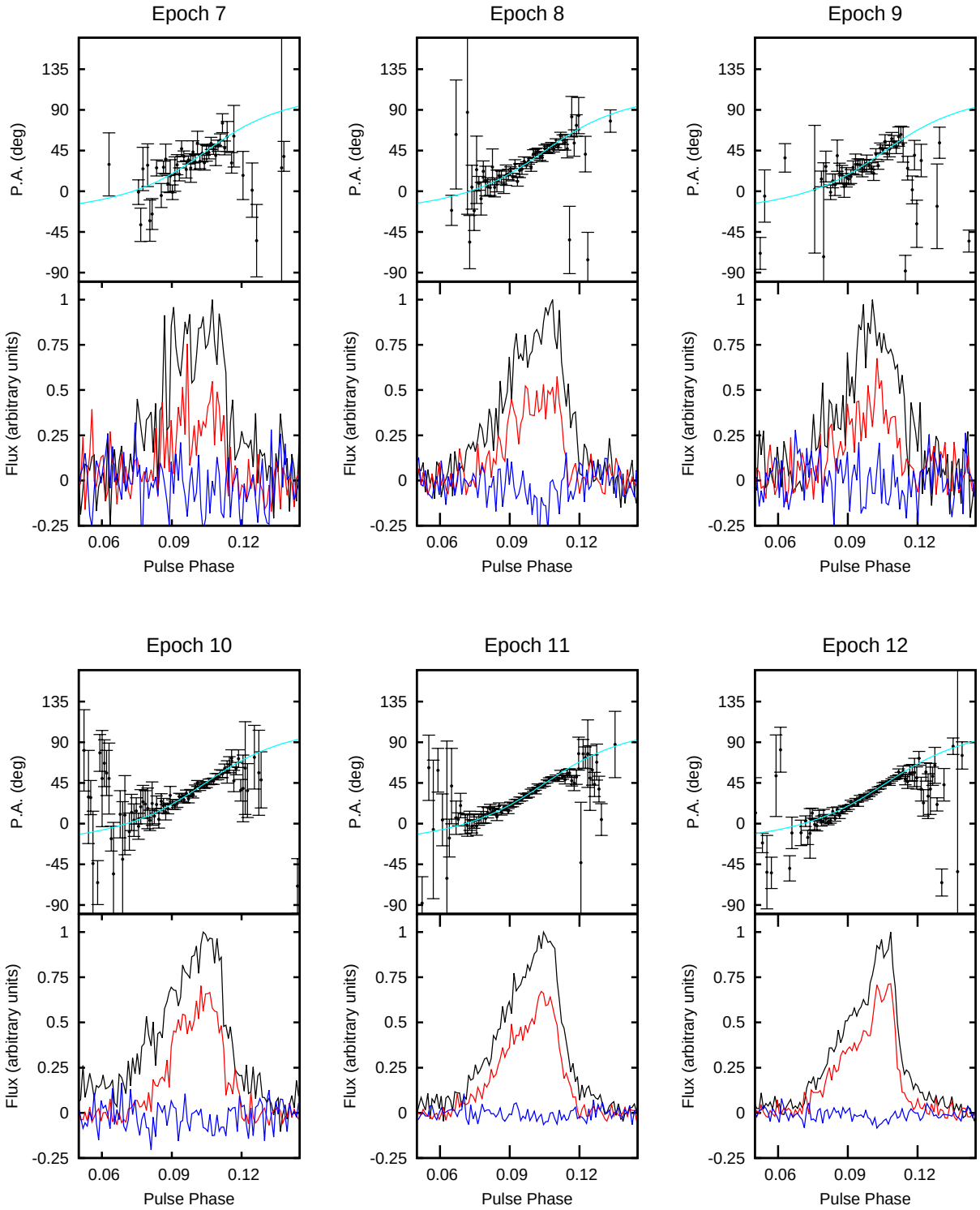

Figure 7.8 – *continued*

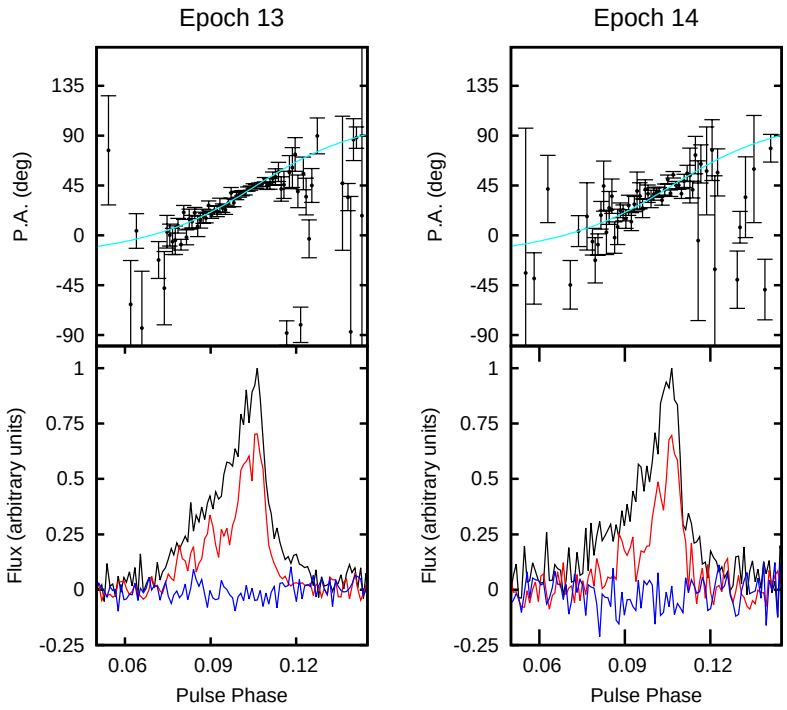

Figure 7.8 – *continued*

$\Phi_0 = 257^{+21}_{-19}$ deg and $\Delta\psi_0 = 39^{+30}_{-29}$ deg, at the 2-σ level. Although an assumed inclination of $i = 180$ deg $- i = 130.34$ deg is also possible, our results do not change significantly, being consistent with the aforementioned values within the 2-σ uncertainties. This is very likely due to the small time span of our data (2.5 yr) with respect to the precession cycle (275 yr), which is too short to allow us to break the degeneracy between the two inclinations.

Regardless of the true value of the inclination, the solution found predicts a magnetic inclination angle larger than 90 deg, meaning that we are currently observing the pulsar "southern" beam. The misalignment angle $\delta_{\rm so}$, although not very well constrained, is also large, as we were indeed expecting given the very fast profile changes observed. The fact that the pulsar spin axis is not aligned with the orbital angular momentum is not surprising: as Prince et al. (1991) discussed in detail, M15C is, in all probability, the result of chaotic exchange encounters. Hence, the pulsar rotation axis has no *a priori* preferred direction.

The precessional RVM solution can be used to make important predictions about the future behaviour of the pulsar. In particular, we can calculate the values of the impact parameter of the main beam, $\beta_{\rm m}$, as a function of time. The same can be done for the secondary beam from the opposite magnetic pole, assuming a perfectly dipolar magnetic field, the magnetic inclination of the main beam, $\alpha_{\rm m}$, and that of the secondary beam, $\alpha_{\rm s}$, are related simply by:

$$\alpha_{\rm s} = \pi - \alpha_{\rm m}. \tag{7.7}$$

Calling $\beta_{\rm m}$ the impact parameter of the secondary beam, it is also easy to see that (Fig. 7.10):

$$\alpha_{\rm m} + \beta_{\rm m} = \alpha_{\rm s} + \beta_{\rm s}. \tag{7.8}$$

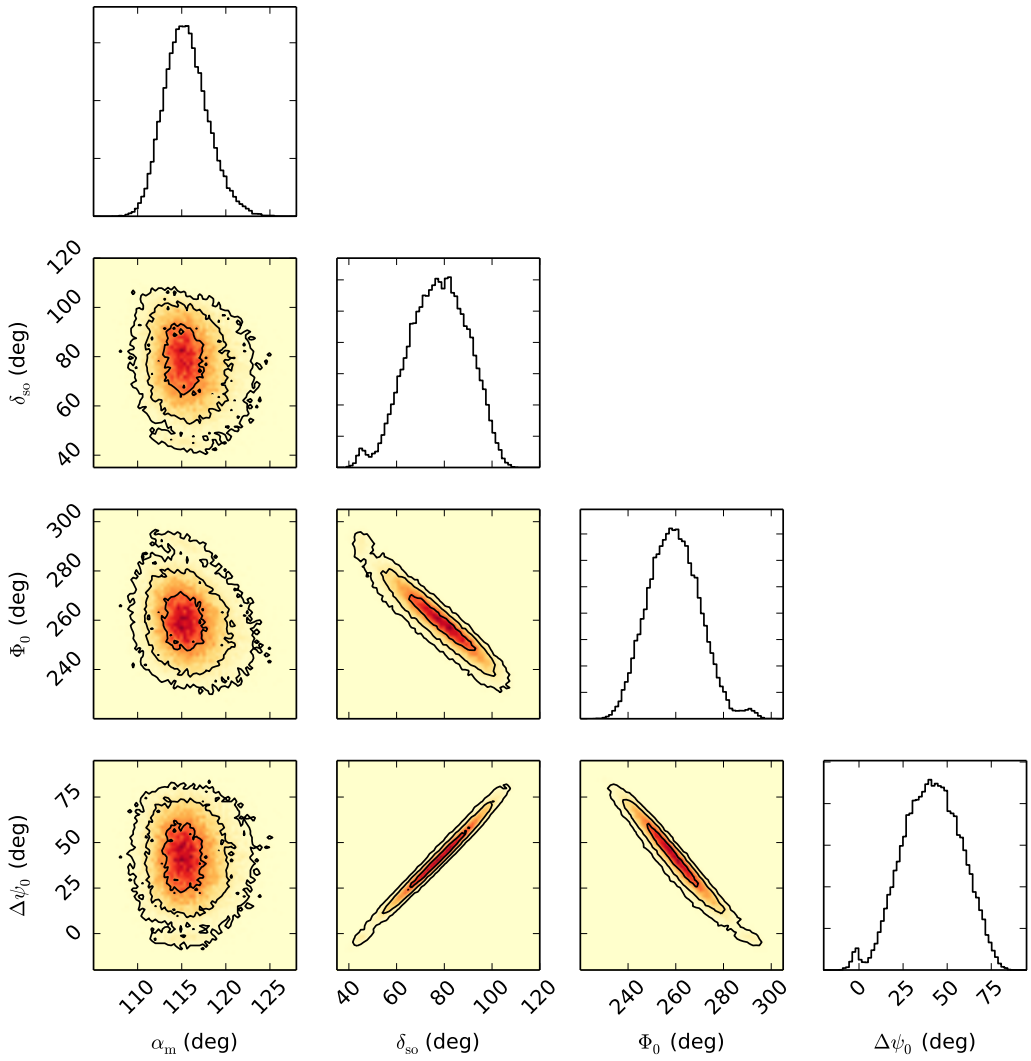

Figure 7.9. One and two-dimensional marginalized posterior distribution functions for the four parameters of interest of M15C, as computed by MODELRVM. From top to bottom and left to right, the represented parameters are the angle between the rotation axis and the magnetic axis, $\alpha_{\rm m}$, the misalignment angle, $\delta_{\rm so}$, the reference precessional phase, Φ_0 and the constant PA offset, $\Delta\psi_0$. In the analysis, we fixed the inclination $i = 49.66$ deg and the precession angular rate, $\Omega_{\rm so} = 1.31$ deg yr^{-1}, namely to the values predicted by GR as derived from our timing analysis. Although an inclination of $i' = 180$ deg $- i = 130.34$ deg is also possible, our results do not change significantly when using the latter value.

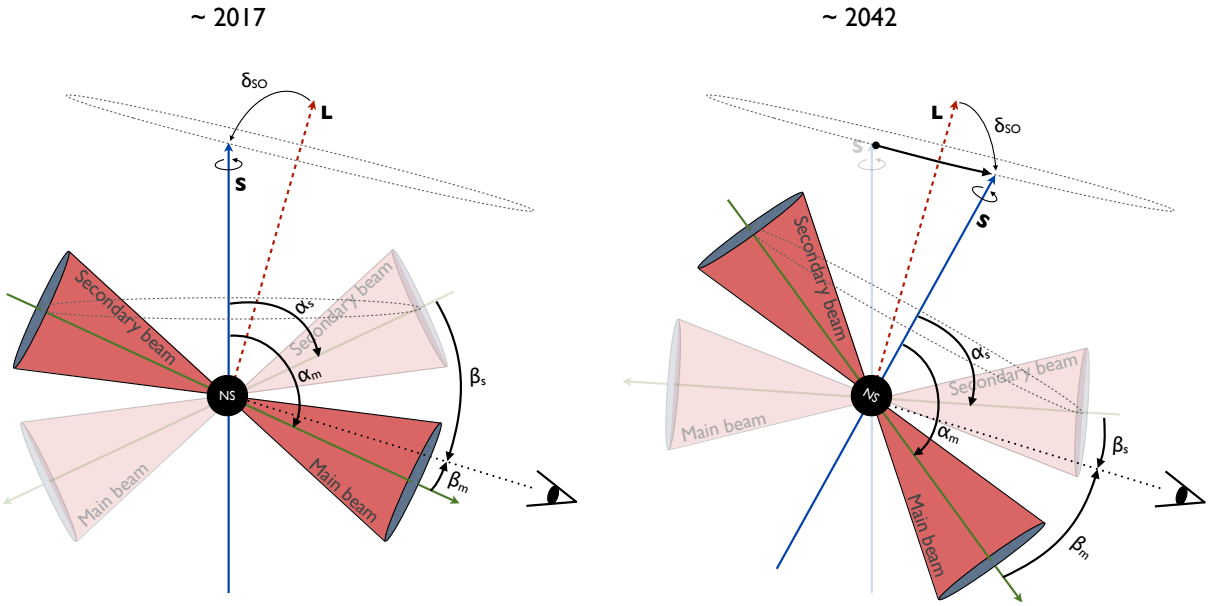

Figure 7.10. Graphical representation of the present (left) and future (right) geometry of the precessing pulsar M15C with respect to the distant observer. Currently, our line of sight falls between the magnetic and the spin axis, with a minimum angular distance of $\beta_{\rm m} \simeq -12$ deg. Over time, the relativistic spin precession will cause this distance to increase in its absolute value until our line of sight will completely move away from the main beam. However, in a few decades, it may be possible that the secondary beam will approach the observer's line of sight enough, so that we may be able to see the interpulse.

Combining Eq. (7.7) and (7.8), we can thus relate $\beta_{\rm s}$ to the main beam parameters:

$$\beta_{\rm s}(t) = 2\alpha_{\rm m} + \beta_{\rm m}(t) - \pi\,, \tag{7.9}$$

where the dependence of both impact parameters on time has been made explicit.

The predictions on $\beta_{\rm m}(t)$ and $\beta_{\rm s}(t)$ calculated by our best-fit model of the precessional RVM can be seen in Fig. 7.11. The estimated values are $\beta_{\rm m} \simeq -12$ deg and $\beta_{\rm s} \simeq 38$ deg in early 2017, both decreasing over time.

The knowledge of $\alpha_{\rm m}$ and $\beta_{\rm m}$, together with the pulse duty cycle W, also enables us to estimate the angular radius $\rho_{\rm m}$ of the conical beam envelope, which can be calculated as (Gil et al., 1984; Lorimer & Kramer, 2004):

$$\rho_{\rm m} = \arccos\left[\cos\alpha_{\rm m}\cos(\alpha_{\rm m}+\beta_{\rm m}) + \sin\alpha_{\rm m}\sin(\alpha_{\rm m}+\beta_{\rm m})\cos\left(\frac{W}{2}\right)\right], \tag{7.10}$$

where W is measured in units of longitude of rotation. Given that our line of sight is moving away form the magnetic axis over time, the best estimate for $\rho_{\rm m}$ is obtained using the values relative to the most recent epoch available. These are $\beta_{\rm m} \simeq -11.9$ deg and $W_{10} \simeq 22.3$ deg (where the subscript indicates that the M15C pulse duty cycle is measured at the 10% intensity level), from which we derive $\rho_{\rm m} \simeq 13.0$ deg.

The beam angular radius can in turn be used to make predictions on the future disappearance of the M15C main pulse and on the possible appearance of the interpulse from the secondary beam. Indeed, a condition necessary for a beam to be detectable is that its impact parameter

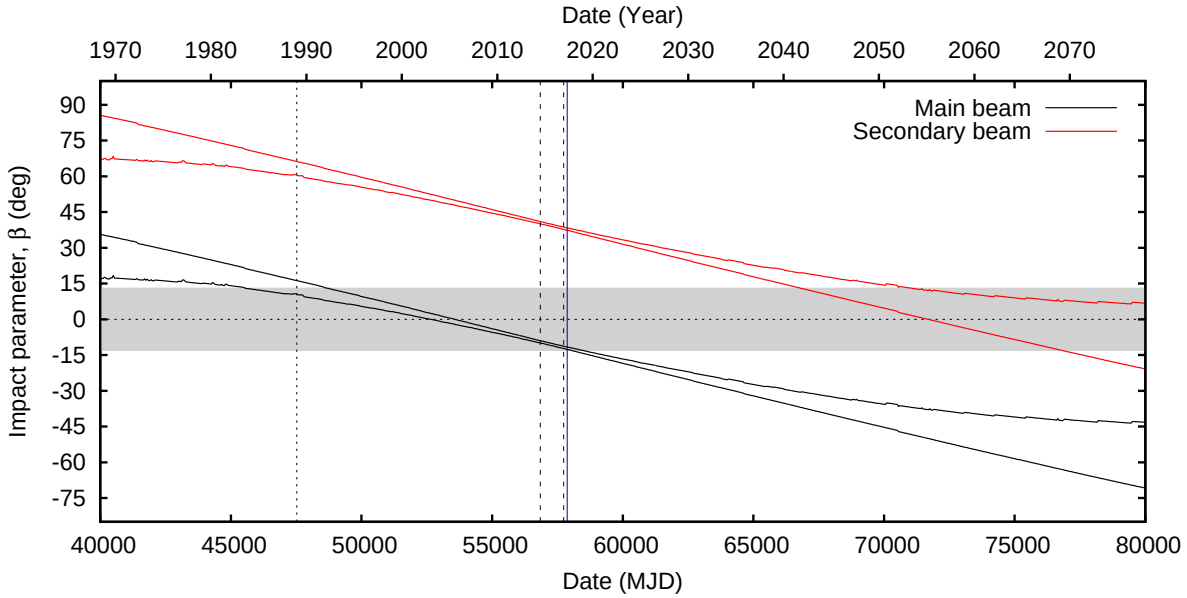

Figure 7.11. Predicted evolution of the impact parameter of the main (black solid line) and secondary beam (red solid line) as a function of time. The black and red solid lines delimit the 2-σ credible intervals for the solution found, whereas the two vertical dashed lines delimit the time range covered by our polarimetric data, to which the model has been fitted. The vertical blue line indicates the current date (May 1, 2017). Assuming a beam conal envelope of opening angle $\rho_{\rm m} = 13$ deg, we expect to see the emission (i.e. a pulse) when the impact parameter is smaller than that value. This condition is verified when the impact parameter falls within the grey horizontal band. The vertical dotted line indicates the date of discovery of M15C.

$|\beta| \lesssim \rho$. From $\beta_{\rm m}(t)$ and $\beta_{\rm s}(t)$, we can thus predict that the main pulse of M15C may become undetectable any time between late 2017 and late 2018. Correspondingly, assuming it to have the same angular size of the main beam, we expect the secondary beam to become detectable roughly between the year 2041 and 2053.

We note that such predictions are based on the assumption that $\rho_{\rm m} = 13.0$ deg. However, this value can be considered as a lower limit. If M15C continues to be detectable in the coming months or years, $\beta_{\rm m}$ will become more and more negative, implying a larger $\rho_{\rm m}$ and thus, different predicted ranges.

7.5.5 Beam map

Another interesting application of the precessional RVM result is the possibility of obtaining a "tomography" of the currently visible beam of M15C, over the range of impact parameter values spanned by our data.

To do this properly, all epochs should in principle be calibrated in flux. This is necessary to have the correct relative scale of intensities for the different emission regions of the beam. For all the PUPPI data, we correctly performed the flux calibration as described in Section 7.3.

For the older WAPP data, we did not have any flux calibrator nor noise-diode observations. Hence, for these data, we calculated the mean flux density by using the radiometer equation (Eq. 2.18). Being the latter method different from the proper flux calibration procedure, we investigated possible systematic errors by using the most recent data taken simultaneously with PUPPI and the WAPPs. Specifically, we compared the mean flux density obtained from the

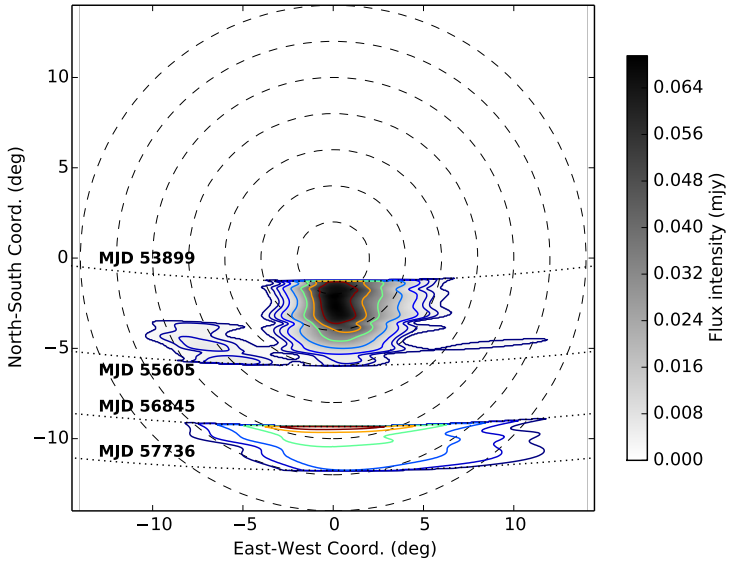

Figure 7.12. Reconstructed morphology of the currently visible beam of M15C. We remark that we did not correct for possible aberration/retardation effects (Blaskiewicz et al., 1991), hence this is just the observed emission pattern. The dashed circles represent 2-deg steps in the beams radius. The dotted lines mark the cuts of the observer's line of sight through the emission beam on the days reported next to them. The gap between MJD 55605 and 56845 corresponds to a period in which M15C was extremely faint, and hence very often undetectable.

proper flux-calibration of the PUPPI data, with that obtained from the radiometer equation on the corresponding WAPP data. We found that the radiometer equation method was underestimating the flux by a factor of ~ 4.3, on average. This factor was then used to rescale all the WAPP observations accordingly.

Once the mean flux density for all the PUPPI and WAPP data was estimated, each total-intensity profile was fitted with a number of Gaussian functions, which were used to have an analytic representation of the pulse profiles. These profiles were then aligned in phase: for the PUPPI data, we used the best-fit ϕ_0^i values, i.e. the pulse longitude of the PA swing inflection point of each epoch; for the WAPP data, we aligned the profiles using the phase of the timing solution. We note that the PA swing can in principle be shifted in pulse longitude by relativistic effects such as aberration and retardation (Blaskiewicz et al., 1991), which depend on the emission height of the observed radiation. However, given that most of our data (WAPP) is lacking polarimetric information, we preferred to reconstruct just the *observed* emission pattern, without correcting for the aforementioned effect.

The intensities of the analytic profiles were put in a two-dimensional grid with the axes being pulse longitude and latitude, and a 2D spline interpolation was performed. The resulting beam pattern obtained was finally plotted in polar coordinates with the y-axis being the North-South direction (i.e. aligned with the pulsar spin axis) and x-axis the orthogonal East-West direction. The final beam map so obtained can be seen in Fig. 7.12.

Chapter 8

Summary and future work

Contents

8.1 Summary

Radio pulsars are strongly magnetized neutron stars that act like cosmic "lighthouses" and that, while spinning extremely fast, are characterized by an extraordinary rotational stability. This is particularly true for the so-called *recycled* (or *millisecond*) pulsars (MSPs), which have been spun-up by the accretion of matter and angular momentum from a companion star, thus reaching spin periods of only a few milliseconds. Recycled pulsars are very common in globular clusters, because the latter provide very dense environments where the probability for a star to gravitationally interact with other objects is much higher than in the Galactic plane. This greatly promotes the formation (and the disruption) of binary systems composed by an old, "dead" neutron star and a main sequence star. When the latter evolves into a giant it fills its Roche lobe and transfers its mass to the neutron star, thus "recycling" it.

In this thesis, we have studied the radio pulsars located in two different globular clusters, 47 Tuc and M15, and we have exploited them to investigate a number of astrophysical issues. The main tool utilized was the *pulsar timing* technique, described in Chapter 2. We explained that a *timing solution* is a model that describes the rotational behaviour of the pulsar and that a timing solution is said to be *phase-connected* if it is able to account for every single rotation of the neutron star. Timing thus allows us to precisely measure those physical parameters that are affecting the propagation time of the pulsar radiation.

The first part of the thesis was about the pulsars in 47 Tuc (Chapter 4). To begin, we have analyzed about two decades of data taken with the Australian Parkes radio telescope. In particular, we have presented phase-connected timing solutions for 23 of the 25 pulsars known to reside in the cluster. In some cases, which involved some exceptionally faint binary pulsars, this has required the development and the application of time-domain search techniques specifically devised for the purpose. For some of the previously known pulsars (47 Tuc R, W, X, Y), we managed to obtain phase-connected solutions for the first time, finally unveiling their physical characteristics, which had remained unknown for more than a decade. The same is true for another three recently discovered isolated pulsars, namely 47 Tuc Z, aa and ab. The derived

characteristics of these three pulsars are largely consistent with those of the other isolated millisecond pulsars in 47 Tuc. For many other pulsars, the solutions presented here constitute a major update, since we included an additional 10 years of data, almost doubling their timing baseline. This has allowed us to determine the pulsar proper motions with a precision significantly better than those previously published, as well as higher order spin period derivatives. For nine binary systems, we also measured changes in the orbital period which, in eight cases, are solely due to the acceleration of the binary in the globular cluster; these have allowed, for the first time, the measurement of real accelerations along the line of sight, which we have in turn been used to estimate the pulsar characteristic ages, magnetic fields and spin-down luminosities. For the only two pulsars that still lack a phase-connected solution, namely 47 Tuc P and V, we have greatly improved the measurement of their orbital parameters. Pulsar V is particularly interesting because it behaves like one of the so-called *transitional millisecond pulsars*, which are known to swing between a radio pulsar and a low-mass X-ray binary state. However, our analysis of optical and X-ray data seems to exclude this hypothesis.

The new and extended timing solutions of the pulsars in 47 Tuc have also enabled a wealth of additional scientific investigations. One of these is the possibility of studying the cluster dynamics (Chapter 5). First, we have used the much more precise proper motion measurements of the 47 Tuc pulsars to infer the proper motion of the cluster as a whole, for which we found a value of 5.16 mas yr^{-1} in right ascension and -2.85 mas yr^{-1} in declination. The same proper motions have also been used to investigate the intriguing positional coincidence of two pulsar pairs, namely that of 47 Tuc I and G, and that of 47 Tuc F and S. We concluded that the former pair is unlikely to be a bound system, whereas the latter is probably in a temporarily bound status. We have also provided an estimate of the cluster distance by showing how our measurements of the real line-of-sight accelerations can be accounted for by an analytic King model only if the cluster is about 4.69 kpc away. Furthermore, we have pointed out how such a model is also able to correctly account for the observed acceleration derivatives (jerks), for the pulsars near the core, without the need of invoking the existence of an intermediate-mass black hole at the centre of the cluster. The latter, however, cannot be ruled out yet and further investigations are needed in order to constrain this hypothesis. Regarding the evolution of the cluster, the wide range of characteristic ages measured by our timing suggests that the pulsars in 47 Tuc have probably been forming at a near-constant rate throughout the age of the cluster.

Although 47 Tuc has a high stellar interaction rate, Γ_{GC} (which favours the recycling of straggling neutron stars and, thus, the formation of MSPs), its interaction rate *per binary*, γ_{b} is rather low (Verbunt & Freire, 2014). This implies that the vast majority of the formed binaries can evolve completely undisturbed, thus producing systems whose characteristics closely resemble those observed in the Galaxy. This is supported by the fact that almost all the pulsars are found very close to the cluster core, an expected consequence of *mass segregation* and the low probability of three-body exchange interactions, which would cause the hurling towards the outskirts of the cluster. The only exception is constituted by 47 Tuc X, a binary MSP that is more than three times farther away than any other pulsar. We discussed how this system is peculiar also for its characteristics, having by far the widest and the least eccentric orbit of all the 47 Tuc binaries. We have studied this system in detail at multiple wavelengths and we have discussed two different formation scenarios.

Another important application of the derived timing solutions is related to the population of black widow and redback binary pulsars of 47 Tuc (Chapter 6). The long-term timing has allowed us to detect, in four such objects, a strong orbital variability, which is instead absent in the other two systems where we have a good orbital model, despite the very similar orbital

characteristics. The orbital variability is, in all probability, related to the mass outflow from the low-mass companion star; however, we were unable to find any obvious correlation with particular characteristics of the pulsar and/or of the system. Provisionally, we concluded that black widow pulsars seem to have a bimodal behaviour, with some of them showing a stable orbit and some other showing chaotic orbital dynamics. This may have important implications for the possible inclusion of this class of binaries in pulsar timing arrays.

The second part of the thesis dealt with the pulsars in M15 (Chapter 7), a globular cluster known to host seven isolated pulsars and one binary pulsar. Such a different population, compared to that of 47 Tuc, reflects the very different dynamical state of this cluster, which has a core-collapsed core. In this case, polarimetry was the chief tool used for our analysis. Our dataset consisted of 27 years of observations made with the Arecibo telescope, which we have used to update the timing solutions of the five detectable pulsars, namely pulsars A, B, C, D and E. We then focused on the most recent full-Stokes data, taken over the last 2.5 years, to do the first polarimetric study of the pulsars in this cluster. After accurately calibrating these data, we have obtained the rotation measures (RMs), the full-polarimetric integrated pulse profiles and the mean flux densities, for all the five pulsars. We have noted how the RMs are all consistent within 1-σ, suggesting the absence of a significant intra-cluster magnetization. After that we focused on M15C, a mildly recycled binary pulsar in a double neutron star system where the relativistic spin precession effect is causing the pulsar spin axis to precess about the total angular momentum of the binary, with a periodicity of ~ 275 years. We have used M15C's time-varying polarimetric properties to model the precession effect and constrain the system geometry. We found that the angle between the pulsar spin axis and the total angular momentum is large (~ 76 deg). The currently visible beam of M15C is moving away from our line of sight and it might become undetectable already in 2018. On the other hand, the secondary beam, from the opposite magnetic pole, is approaching us and we expect it to become detectable sometime between 2041 and 2053. Finally, the long-term timing and the polarimetry have been jointly used to reconstruct the morphology of the currently visible beam of M15C.

8.2 Future work

47 Tuc and M15 are certainly among the most studied globular clusters known to host pulsars. The work presented here represents an additional contribution to our knowledge and understanding of these two stellar systems and their pulsars. However, many scientific issues are still open and several additional studies can be done. A large fraction of these can already be done with the same data used in this thesis. Here we list the most relevant ones.

8.2.1 Improving the models for the dynamics and gas content of 47 Tuc

The long-term timing of the pulsars in 47 Tuc paves the way for a more accurate analysis of the physical characteristics of the cluster. Prager et al. (2016) exploited the long-term timing of 36 MSPs in the globular cluster Terzan 5 by modelling the observed spin period and spin period derivative of all the pulsars, to derive independent measurements of the key parameters of the cluster. In the paper, they also applied the analysis to 47 Tuc using the previously published timing parameters of the pulsars, which did not include our measurements of the jerks and were obviously less precise than those derived in this thesis. It will thus be very interesting to include our new measurements in their model to improve the characterization of the physical parameters of 47 Tuc. In a similar way, the Freire et al. (2001c) gas model of 47 Tuc can be further improved

by including the newly timed pulsars and by using our more accurate parameters for the older pulsars. The RMs obtained by Abbate et al. (in prep.) from recent observations taken in full-Stokes mode with the Parkes telescope for many of the 47 Tuc pulsars can also be combined with the gas model to look for a possible intra-cluster magnetic field.

8.2.2 Continuing the monitoring campaign of M15

The precession effect is currently making M15C fainter and fainter and we predict that the pulsar might very soon become undetectable. The follow-up of M15C in the next few months is thus of utmost importance to be able to monitor the rapid changes seen in the emission properties of the pulsar before this is not any longer possible. A larger data span will also allow us to further constrain our precessional model and thus make more accurate predictions on when the secondary beam may become visible.

The same data will be very valuable for the timing of the other four detectable pulsars in the cluster, for which we expect to detect higher order spin frequency derivatives, exactly as we did for the pulsars in 47 Tuc.

8.2.3 Searching for the companion radio pulsar of M15C

Relativistic spin precession affects not only the spin axis orientation of M15C, but also that of its companion NS. If the latter is also a radio pulsar, it might thus become observable in the future, thanks to the change in its orientation due to the precession. If so, the system would be the second double pulsar system known, after PSR J0737−3039A/B. The different orbital characteristics, though, could in theory enable new and even more stringent tests of General Relativity. For this reason, it is our highest priority to conduct a deep search for the companion pulsar in our recent high-resolution data that we have taken with the Arecibo telescope. In doing this, we will exploit the large number of observations taken with PUPPI at 1.4 GHz, to combine them together to increase our sensitivity. This will be achieved by using a code, part of the `PSRALEX` software package developed in the context of this thesis, which is able to remove the orbital modulation in the data. This has the effect of making both M15C and its companion look as if they were isolated pulsars, thus greatly simplifying the search. The same PUPPI data taken at different observing frequencies will also be helpful, given that we have no prior knowledge of how steep the radio spectrum of the companion may be.

8.2.4 Searching for new pulsars in both clusters

The same multi-year search-mode data that we have used for our timing and polarimetric analysis is perfectly suitable for conducting new deep searches for new pulsars in both 47 Tuc and M15. Pan et al. (2016) has already shown how reprocessing archival globular cluster data with a novel stack-search pipeline can be fruitful in detecting faint new pulsars. However they have worked on only ~ 1100 h of 47 Tuc data, which is less than two thirds of our whole 47 Tuc dataset. On the other hand, we have utilized a newly-developed GPU-based accelerated search pipeline that proved to be extremely effective in re-detecting faint millisecond pulsars in extremely compact binaries.

Although we do not expect a large number of new discoveries, applying these two pipelines on the remaining part of the 47 Tuc dataset and on the new high-resolution search-mode PUPPI data of M15, has the potential of detecting new faint pulsars that may have been missed in previous searches.

8.3 Prospects with the new upcoming radio telescopes

Many of the objectives listed above will become much easier to achieve with the new generation of radio telescopes coming online soon.

One of these is the *Five-hundred-meter Aperture Spherical Telescope*[1] (FAST, Nan et al. 2011), a spherical reflector 500 meters across located in the Guizhou Province, Southwest China, which began operations in September 2016. Although its design is very similar to that of Arecibo, FAST is able to observe as far as 40 degrees from the zenith, thus covering about twice as much sky as the Puertorican dish. This is possible thanks to its active surface, which is able to dynamically synthesize an effective 300-m wide paraboloid on different parts of the reflector. Such a huge collecting area allows FAST to reach unprecedented sensitivities over very short time scales, making the telescope an ideal instrument for searching for highly relativistic binary systems. Because Arecibo and FAST are located at very similar latitudes, all the sky visible to the former is also entirely visible to the latter. Therefore, the globular cluster M15 is certainly a possible FAST observing target. Apart from conducting even deeper searches in this and other globular clusters, the Chinese telescope might be very useful to follow up the geodetic precession of M15C when the flux density of the pulsar will go below the Arecibo detectability threshold. Similarly, FAST might be sensitive enough to detect pulsars F, G and H in single observations. This would allow us to extend their timing solutions, which would in turn be useful for the study of the dynamics of M15.

Being very far south, 47 Tuc is instead not observable by FAST. However, two new other facilities will soon be able to observe this cluster. The first one is *MeerKAT*[2] (Booth & Jonas, 2012), an array of 64 dishes, each 13.5-m across, located in South Africa. The telescope construction was completed in 2016 and it is slated to become fully operational by the end of 2017. Thanks to its large collecting area, wide observing bandwidth and position in the Southern Hemisphere, MeerKAT will become the paramount facility with which to follow up 47 Tuc. Its much greater sensitivity, compared to the Parkes telescope, will very likely allow us to discover many more pulsars in the cluster, as well as re-detecting those already known with a much higher rate. This should eventually enable us to find phase-connected timing solutions for 47 Tuc P and V, the only two pulsars, currently known in the cluster, that are left to be solved.

MeerKAT will be the most sensitive radio telescope in the Southern Hemisphere until with completion of the *Square Kilometre Array*[3] (SKA), a telescope composed by thousands of small antennas, which will be located across two continents (precisely in South Africa and Australia). The SKA will provide a huge leap in sensitivity and will thus likely produce major advances in many scientific areas, including astrophysics of pulsars. Regarding pulsars in globular cluster, the SKA is expected to double or even triple the currently known population during its first phase, whereas, when fully operational, the number of cluster pulsars discovered might be of the order of a few hundreds or thousands (Hessels et al., 2015). Not only will this allow us to study a large number of potentially very interesting single objects, it will also give us a unique opportunity to better understand the history, dynamics and evolution of these peculiar systems of stars.

[1] http://fast.bao.ac.cn
[2] http://public.ska.ac.za/meerkat
[3] http://skatelescope.org

Bibliography

Aarseth S. J., 1999, PASP, 111, 1333 (Cited on page 79.)

Aarseth S. J., 2003, Gravitational N-Body Simulations (Cited on page 79.)

Albrow M. D., Gilliland R. L., Brown T. M., Edmonds P. D., Guhathakurta P., Sarajedini A., 2001, ApJ, 559, 1060 (Cited on page 137.)

Alpar M. A., Cheng A. F., Ruderman M. A., Shaham J., 1982, Nature, 300, 728 (Cited on page 20.)

Anderson S. B., 1993, PhD thesis, California Institute of Technology, Pasadena. (Cited on pages 142 and 151.)

Anderson S. B., Gorham P. W., Kulkarni S. R., Prince T. A., Wolszczan A., 1990, Nature, 346, 42 (Cited on pages 142 and 151.)

Antoniadis J., 2014, ApJ, 797, L24 (Cited on page 27.)

Antoniadis J., et al., 2013, Science, 340, 448 (Cited on pages 25 and 58.)

Antoniadis J., Kaplan D. L., Stovall K., Freire P. C. C., Deneva J. S., Koester D., Jenet F., Martinez J. G., 2016, ApJ, 830, 36 (Cited on page 22.)

Antonov V. A., 1962, Solution of the problem of stability of stellar system Emden's density law and the spherical distribution of velocities (Cited on page 80.)

Archibald A. M., et al., 2009, Science, 324, 1411 (Cited on page 20.)

Arnaud K. A., 1996, in Jacoby G. H., Barnes J., eds, Astronomical Society of the Pacific Conference Series Vol. 101, Astronomical Data Analysis Software and Systems V. p. 17 (Cited on page 120.)

Arnett D., 1996, Supernovae and Nucleosynthesis (Cited on page 15.)

Arzoumanian Z., 1995, PhD thesis, Princeton University. (Cited on page 151.)

Athanasiadis D., Kramer M., Stairs I. H., Lyne A. G., 2003, in Bailes M., Nice D. J., Thorsett S. E., eds, Astronomical Society of the Pacific Conference Series Vol. 302, Radio Pulsars. p. 187 (arXiv:astro-ph/0301167) (Cited on page 72.)

Baade W., Zwicky F., 1934, Proceedings of the National Academy of Science, 20, 259 (Cited on page 13.)

Backer D. C., Hellings R. W., 1986, ARA&A, 24, 537 (Cited on pages 52 and 53.)

Backer D. C., Rankin J. M., Campbell D. B., 1976, Nature, 263, 202 (Cited on page 66.)

Backer D. C., Kulkarni S. R., Heiles C., Davis M. M., Goss W. M., 1982, Nature, 300, 615 (Cited on page 23.)

Backer D. C., Hama S., van Hook S., Foster R. S., 1993, ApJ, 404, 636 (Cited on page 54.)

Bahramian A., Heinke C. O., Sivakoff G. R., Gladstone J. C., 2013, ApJ, 766, 136 (Cited on page 124.)

Barker B. M., O'Connell R. F., 1975, Phys. Rev. D, 12, 329 (Cited on pages 25 and 151.)

Barr E. D., Freire P. C. C., Kramer M., Champion D. J., Berezina M., Bassa C. G., Lyne A. G., Stappers B. W., 2017, MNRAS, 465, 1711 (Cited on page 22.)

Bassa C. G., van Kerkwijk M. H., Koester D., Verbunt F., 2006, A&A, 456, 295 (Cited on page 126.)

Bassa C. G., et al., 2014, MNRAS, 441, 1825 (Cited on page 22.)

Bassa C. G., et al., 2016, MNRAS, 456, 2196 (Cited on page 39.)

Becker W., Aschenbach B., 2002, in Becker W., Lesch H., Trümper J., eds, Neutron Stars, Pulsars, and Supernova Remnants. p. 64 (arXiv:astro-ph/0208466) (Cited on page 120.)
Bhattacharya D., van den Heuvel E. P. J., 1991, Phys. Rep., 203, 1 (Cited on page 19.)
Binney J., Tremaine S., 2008, Galactic Dynamics: Second Edition. Princeton University Press (Cited on pages 79 and 80.)
Blandford R., Teukolsky S. A., 1976, ApJ, 205, 580 (Cited on pages 58 and 92.)
Blaskiewicz M., Cordes J. M., Wasserman I., 1991, ApJ, 370, 643 (Cited on page 164.)
Bogdanov S., Grindlay J. E., van den Berg M., 2005, ApJ, 630, 1029 (Cited on pages 86, 120 and 139.)
Bogdanov S., Grindlay J. E., Heinke C. O., Camilo F., Freire P. C. C., Becker W., 2006, ApJ, 646, 1104 (Cited on pages 86, 120 and 121.)
Bogdanov S., van den Berg M., Heinke C. O., Cohn H. N., Lugger P. M., Grindlay J. E., 2010, ApJ, 709, 241 (Cited on page 120.)
Bogdanov S., Patruno A., Archibald A. M., Bassa C., Hessels J. W. T., Janssen G. H., Stappers B. W., 2014, ApJ, 789, 40 (Cited on page 22.)
Bogdanov S., Heinke C. O., Özel F., Güver T., 2016, ApJ, 831, 184 (Cited on pages 86, 104 and 124.)
Bond H. E., White R. L., Becker R. H., O'Brien M. S., 2002, PASP, 114, 1359 (Cited on page 20.)
Booth R. S., Jonas J. L., 2012, African Skies, 16, 101 (Cited on page 169.)
Brans C., Dicke R. H., 1961, Physical Review, 124, 925 (Cited on page 26.)
Breton R. P., et al., 2008, Science, 321, 104 (Cited on page 151.)
Britton M. C., 2000, ApJ, 532, 1240 (Cited on pages 65 and 69.)
Brogaard K., VandenBerg D. A., Bedin L. R., Milone A. P., Thygesen A., Grundahl F., 2017, preprint, (arXiv:1702.03421) (Cited on page 104.)
Burbidge G. R., Strittmatter P. A., 1968, Nature, 218, 433 (Cited on page 14.)
Burgay M., et al., 2003, Nature, 426, 531 (Cited on pages 22 and 25.)
Caballero R. N., et al., 2016, MNRAS, 457, 4421 (Cited on page 61.)
Cadelano M., Pallanca C., Ferraro F. R., Salaris M., Dalessandro E., Lanzoni B., Freire P. C. C., 2015, ApJ, 812, 63 (Cited on pages 86, 116 and 119.)
Camilo F., Lorimer D. R., Freire P., Lyne A. G., Manchester R. N., 2000, ApJ, 535, 975 (Cited on pages 86, 87, 131, 133, 134 and 138.)
Campana S., Coti Zelati F., Papitto A., Rea N., Torres D. F., Baglio M. C., D'Avanzo P., 2016, preprint, (arXiv:1607.06245) (Cited on page 20.)
Capderou M., 2005, Satellites: Orbits and missions (Cited on page 57.)
Carretta E., Bragaglia A., Gratton R., D'Orazi V., Lucatello S., 2009, A&A, 508, 695 (Cited on page 142.)
Cash W., 1979, ApJ, 228, 939 (Cited on page 120.)
Chandrasekhar S., 1931, MNRAS, 91, 456 (Cited on page 15.)
Chandrasekhar S., 1935, MNRAS, 95, 207 (Cited on page 15.)
Chen K., Ruderman M., 1993, ApJ, 402, 264 (Cited on page 19.)
Chernoff D. F., Weinberg M. D., 1990, ApJ, 351, 121 (Cited on page 79.)
Clark G. W., 1975, ApJ, 199, L143 (Cited on page 82.)
Clifton T., Weisberg J. M., 2008, ApJ, 679, 687 (Cited on page 151.)

Cohn H., 1979, ApJ, 234, 1036 (Cited on page 79.)
Colgate S. A., White R. H., 1966, ApJ, 143, 626 (Cited on page 13.)
Comella J. M., Craft H. D., Lovelace R. V. E., Sutton J. M., 1969, Nature, 221, 453 (Cited on page 14.)
Cooley J. W., Tukey J. W., 1965, Math. Comput., 19, 297 (Cited on page 42.)
Cordes J. M., 1978, ApJ, 222, 1006 (Cited on page 23.)
Cordes J. M., Lazio T. J. W., 2002, ArXiv Astrophysics e-prints, (Cited on pages 24 and 31.)
Cordes J. M., Lazio T. J. W., 2003, ArXiv Astrophysics e-prints, (Cited on pages 24 and 32.)
Cordes J. M., Weisberg J. M., Frail D. A., Spangler S. R., Ryan M., 1991, Nature, 354, 121 (Cited on page 24.)
Corongiu A., Possenti A., Lyne A. G., Manchester R. N., Camilo F., D'Amico N., Sarkissian J. M., 2006, ApJ, 653, 1417 (Cited on page 125.)
Corongiu A., et al., 2012, ApJ, 760, 100 (Cited on page 126.)
Coti Zelati F., et al., 2014, MNRAS, 444, 1783 (Cited on page 136.)
D'Amico N., Possenti A., Fici L., Manchester R. N., Lyne A. G., Camilo F., Sarkissian J., 2002, ApJ, 570, L89 (Cited on page 125.)
Damour T., Deruelle N., 1985, Ann. Inst. Henri Poincaré Phys. Théor., Vol. 43, No. 1, p. 107 - 132, 43, 107 (Cited on page 58.)
Damour T., Deruelle N., 1986, Ann. Inst. Henri Poincaré Phys. Théor., Vol. 44, No. 3, p. 263 - 292, 44, 263 (Cited on pages 58 and 60.)
Damour T., Esposito-Farese G., 1992, Classical and Quantum Gravity, 9, 2093 (Cited on page 26.)
Damour T., Ruffini R., 1974, Academie des Sciences Paris Comptes Rendus Serie Sciences Mathematiques, 279, 971 (Cited on page 151.)
Damour T., Taylor J. H., 1991, ApJ, 366, 501 (Cited on page 115.)
Damour T., Taylor J. H., 1992, Phys. Rev. D, 45, 1840 (Cited on pages 55, 59 and 155.)
Davies M. B., 2013, Globular Cluster Dynamical Evolution. p. 879, doi:10.1007/978-94-007-5612-0-17 (Cited on page 79.)
De K., Gupta Y., 2016, Experimental Astronomy, 41, 67 (Cited on page 38.)
De Vito M. A., Benvenuto O. G., 2010, MNRAS, 401, 2552 (Cited on page 124.)
Deich W. T. S., Kulkarni S. R., 1996, in van Paradijs J., van den Heuvel E. P. J., Kuulkers E., eds, IAU Symposium Vol. 165, Compact Stars in Binaries. p. 279 (Cited on page 151.)
Deller A. T., et al., 2012, ApJ, 756, L25 (Cited on page 136.)
Deller A. T., et al., 2015, ApJ, 809, 13 (Cited on page 20.)
Demorest P. B., Pennucci T., Ransom S. M., Roberts M. S. E., Hessels J. W. T., 2010, Nature, 467, 1081 (Cited on page 25.)
Demorest P. B., et al., 2013, ApJ, 762, 94 (Cited on page 48.)
Desvignes G., Kramer M., Cognard I., Kasian L., van Leeuwen J., Stairs I., Theureau G., 2013, in van Leeuwen J., ed., IAU Symposium Vol. 291, Neutron Stars and Pulsars: Challenges and Opportunities after 80 years. pp 199–202 (arXiv:1211.3937), doi:10.1017/S1743921312023630 (Cited on page 151.)
Dewey R., Stokes G., Segelstein D., Taylor J., Weisberg J., 1984, in Reynolds S. P., Stinebring D. R., eds, Birth and Evolution of Neutron Stars: Issues Raised by Millisecond Pulsars. p. 234 (Cited on page 39.)
Djorgovski S., King I. R., 1986, ApJ, 305, L61 (Cited on page 142.)

Dowd A., Sisk W., Hagen J., 2000, in Kramer M., Wex N., Wielebinski R., eds, Astronomical Society of the Pacific Conference Series Vol. 202, IAU Colloq. 177: Pulsar Astronomy - 2000 and Beyond. pp 275–276 (Cited on page 143.)

Drukier G. A., 1995, ApJS, 100, 347 (Cited on page 79.)

DuPlain R., Benson J., Sessoms E., 2008, in Advanced Software and Control for Astronomy II. p. 70191A, doi:10.1117/12.789402 (Cited on pages 49 and 143.)

Eatough R. P., Keane E. F., Lyne A. G., 2009, MNRAS, 395, 410 (Cited on page 41.)

Eatough R. P., Molkenthin N., Kramer M., Noutsos A., Keith M. J., Stappers B. W., Lyne A. G., 2010, MNRAS, 407, 2443 (Cited on page 44.)

Eddington A. S., 1919, The Observatory, 42, 119 (Cited on page 25.)

Edmonds P. D., Gilliland R. L., Heinke C. O., Grindlay J. E., Camilo F., 2001, ApJ, 557, L57 (Cited on pages 86 and 116.)

Edmonds P. D., Gilliland R. L., Camilo F., Heinke C. O., Grindlay J. E., 2002, ApJ, 579, 741 (Cited on pages 86, 116, 119, 137 and 138.)

Edwards R. T., Hobbs G. B., Manchester R. N., 2006, MNRAS, 372, 1549 (Cited on pages 47, 49, 50, 51, 52 and 60.)

Eggleton P. P., 1983, ApJ, 268, 368 (Cited on page 134.)

Einstein A., 1915, Sitzungsberichte der Königlich Preußischen Akademie der Wissenschaften (Berlin), Seite 844-847., (Cited on page 25.)

Everett J. E., Weisberg J. M., 2001, ApJ, 553, 341 (Cited on page 66.)

Fabian A. C., Pringle J. E., Rees M. J., 1975, MNRAS, 172, 15p (Cited on page 81.)

Fall S. M., Rees M. J., 1988, in Grindlay J. E., Philip A. G. D., eds, IAU Symposium Vol. 126, The Harlow-Shapley Symposium on Globular Cluster Systems in Galaxies. pp 323–330 (Cited on page 76.)

Ferdman R. D., et al., 2013, ApJ, 767, 85 (Cited on page 151.)

Feroz F., Hobson M. P., Bridges M., 2009, MNRAS, 398, 1601 (Cited on page 157.)

Ferraro F. R., Lanzoni B., Dalessandro E., Mucciarelli A., Lovisi L., 2015, Blue Straggler Stars in Globular Clusters: A Powerful Tool to Probe the Internal Dynamical Evolution of Stellar Systems. p. 99, doi:10.1007/978-3-662-44434-4-5 (Cited on page 76.)

Fokker A. D., 1921, Koninklijke Nederlandse Akademie van Wetenschappen Proceedings Series B Physical Sciences, 23, 729 (Cited on page 151.)

Folkner W. M., Williams J. G., Boggs D. H., 2009, Interplanetary Network Progress Report, 178, 1 (Cited on pages 52 and 88.)

Folkner W. M., Williams J. G., Boggs D. H., Park R. S., Kuchynka P., 2014, Interplanetary Network Progress Report, 196, 1 (Cited on page 52.)

Fonseca E., Stairs I. H., Thorsett S. E., 2014, ApJ, 787, 82 (Cited on page 151.)

Forestell L. M., Heinke C. O., Cohn H. N., Lugger P. M., Sivakoff G. R., Bogdanov S., Cool A. M., Anderson J., 2014, MNRAS, 441, 757 (Cited on page 121.)

Fregeau J. M., Gürkan M. A., Joshi K. J., Rasio F. A., 2003, ApJ, 593, 772 (Cited on page 79.)

Freire P. C. C., 2005, in Rasio F. A., Stairs I. H., eds, Astronomical Society of the Pacific Conference Series Vol. 328, Binary Radio Pulsars. p. 405 (arXiv:astro-ph/0404105) (Cited on pages 20 and 133.)

Freire P. C. C., Tauris T. M., 2014, MNRAS, 438, L86 (Cited on page 27.)

Freire P. C., Kramer M., Lyne A. G., 2001a, MNRAS, 322, 885 (Cited on pages 44, 89 and 92.)

Freire P. C., Camilo F., Lorimer D. R., Lyne A. G., Manchester R. N., D'Amico N., 2001b,

MNRAS, 326, 901 (Cited on pages 83, 86, 87, 105, 107, 109, 116 and 131.)
Freire P. C., Kramer M., Lyne A. G., Camilo F., Manchester R. N., D'Amico N., 2001c, ApJ, 557, L105 (Cited on pages 86, 119, 133, 134, 138 and 167.)
Freire P. C., Camilo F., Kramer M., Lorimer D. R., Lyne A. G., Manchester R. N., D'Amico N., 2003, MNRAS, 340, 1359 (Cited on pages 86, 87, 104, 105, 107, 111, 112, 114, 116, 118, 127 and 131.)
Freire P. C. C., Hessels J. W. T., Nice D. J., Ransom S. M., Lorimer D. R., Stairs I. H., 2005, ApJ, 621, 959 (Cited on pages 78, 109 and 127.)
Freire P. C. C., Ransom S. M., Bégin S., Stairs I. H., Hessels J. W. T., Frey L. H., Camilo F., 2008, ApJ, 675, 670 (Cited on page 82.)
Freire P. C. C., et al., 2011, MNRAS, 412, 2763 (Cited on pages 26, 116 and 124.)
Freire P. C. C., et al., 2012, MNRAS, 423, 3328 (Cited on page 26.)
Fruchter A. S., Stinebring D. R., Taylor J. H., 1988, Nature, 333, 237 (Cited on page 20.)
Fukushima T., 1995, A&A, 294, 895 (Cited on page 52.)
Giersz M., Heggie D. C., 2009, MNRAS, 395, 1173 (Cited on page 79.)
Gil J., Gronkowski P., Rudnicki W., 1984, A&A, 132, 312 (Cited on page 162.)
Gold T., 1968, Nature, 218, 731 (Cited on page 14.)
Gold T., 1969, Nature, 221, 25 (Cited on page 14.)
Goldreich P., Julian W. H., 1969, ApJ, 157, 869 (Cited on page 15.)
Goldsbury R., Richer H. B., Anderson J., Dotter A., Sarajedini A., Woodley K., 2010, AJ, 140, 1830 (Cited on page 142.)
Gonzaga S., Hack W., Fruchter A., Mack J., eds. 2012, The DrizzlePac Handbook. (Baltimore, STScI) (Cited on page 122.)
Gratton R. G., Bragaglia A., Carretta E., Clementini G., Desidera S., Grundahl F., Lucatello S., 2003, A&A, 408, 529 (Cited on pages 120 and 123.)
Gratton R., Sneden C., Carretta E., 2004, ARA&A, 42, 385 (Cited on page 76.)
Grindlay J. E., Heinke C., Edmonds P. D., Murray S. S., 2001, Science, 292, 2290 (Cited on pages 86 and 136.)
Grindlay J. E., Camilo F., Heinke C. O., Edmonds P. D., Cohn H., Lugger P., 2002, ApJ, 581, 470 (Cited on page 86.)
Guhathakurta P., Yanny B., Schneider D. P., Bahcall J. N., 1996, AJ, 111, 267 (Cited on page 80.)
Halpern J. P., Gaidos E., Sheffield A., Price-Whelan A. M., Bogdanov S., 2013, The Astronomer's Telegram, 5514 (Cited on page 136.)
Hamaker J. P., Bregman J. D., 1996, A&AS, 117, 161 (Cited on page 61.)
Hankins T. H., 1971, ApJ, 169, 487 (Cited on page 37.)
Hankins T. H., Rickett B. J., 1975, in Alder B., Fernbach S., Rotenberg M., eds, Vol. 14, Methods in Computational Physics. Volume 14 - Radio astronomy. pp 55–129 (Cited on page 37.)
Hansen B. M. S., et al., 2013, Nature, 500, 51 (Cited on pages 104 and 121.)
Harris W. E., 1996, AJ, 112, 1487 (Cited on pages 75, 86 and 104.)
Harris W. E., 2009, ApJ, 703, 939 (Cited on page 76.)
Heggie D. C., 1975, MNRAS, 173, 729 (Cited on page 80.)
Heggie D., Hut P., 2003, The Gravitational Million-Body Problem: A Multidisciplinary Approach to Star Cluster Dynamics (Cited on page 79.)

Heiles C., et al., 2001, PASP, 113, 1274 (Cited on pages 66, 67 and 68.)
Heinke C. O., Grindlay J. E., Edmonds P. D., Cohn H. N., Lugger P. M., Camilo F., Bogdanov S., Freire P. C., 2005, ApJ, 625, 796 (Cited on pages 86, 120, 125 and 126.)
Heinke C. O., Rybicki G. B., Narayan R., Grindlay J. E., 2006, ApJ, 644, 1090 (Cited on page 120.)
Helfand D. J., Manchester R. N., Taylor J. H., 1975, ApJ, 198, 661 (Cited on page 23.)
Hellings R. W., Downs G. S., 1983, ApJ, 265, L39 (Cited on page 26.)
Hénon M., 1971a, Ap&SS, 13, 284 (Cited on page 79.)
Hénon M. H., 1971b, Ap&SS, 14, 151 (Cited on page 79.)
Hessels J. W. T., Ransom S. M., Stairs I. H., Freire P. C. C., Kaspi V. M., Camilo F., 2006, Science, 311, 1901 (Cited on page 83.)
Hessels J. W. T., Ransom S. M., Stairs I. H., Kaspi V. M., Freire P. C. C., 2007, ApJ, 670, 363 (Cited on page 127.)
Hessels J., et al., 2015, Advancing Astrophysics with the Square Kilometre Array (AASKA14), p. 47 (Cited on pages 27, 82, 83 and 169.)
Hewish A., Bell S. J., Pilkington J. D. H., Scott P. F., Collins R. A., 1968, Nature, 217, 709 (Cited on page 14.)
Hills J. G., 1975, AJ, 80, 809 (Cited on page 81.)
Ho A., Ransom S. M., Demorest P., 2014, in American Astronomical Society Meeting Abstracts #223. p. 153.18 (Cited on page 83.)
Hobbs G., 2013, Classical and Quantum Gravity, 30, 224007 (Cited on page 26.)
Hobbs G., Edwards R., Manchester R., 2006, Chinese Journal of Astronomy and Astrophysics Supplement, 6, 189 (Cited on pages 47 and 61.)
Hobbs G., et al., 2012, MNRAS, 427, 2780 (Cited on page 51.)
Homer L., Szkody P., Chen B., Henden A., Schmidt G., Anderson S. F., Silvestri N. M., Brinkmann J., 2006, AJ, 131, 562 (Cited on page 20.)
Hotan A. W., van Straten W., Manchester R. N., 2004, PASA, 21, 302 (Cited on pages 12, 47 and 87.)
Hořava P., 2009, Phys. Rev. D, 79, 084008 (Cited on page 26.)
Hoyle F., Narlikar J. V., Wheeler J. A., 1964, Nature, 203, 914 (Cited on page 14.)
Hulse R. A., Taylor J. H., 1975, ApJ, 195, L51 (Cited on pages 22 and 25.)
Hurley J. R., Pols O. R., Aarseth S. J., Tout C. A., 2005, MNRAS, 363, 293 (Cited on page 79.)
Hut P., Bahcall J. N., 1983, ApJ, 268, 319 (Cited on page 80.)
Irwin A. W., Fukushima T., 1999, A&A, 348, 642 (Cited on page 52.)
Issautier K., Meyer-Vernet N., Moncuquet M., Hoang S., 1998, J. Geophysical Research, 103, 1969 (Cited on pages 51 and 52.)
Issautier K., Hoang S., Moncuquet M., Meyer-Vernet N., 2001, Space Sci. Rev., 97, 105 (Cited on page 52.)
Jackson J. D., 1962, Classical Electrodynamics (Cited on page 16.)
Jacoby B. A., Cameron P. B., Jenet F. A., Anderson S. B., Murty R. N., Kulkarni S. R., 2006, ApJ, 644, L113 (Cited on pages 118, 142, 151, 153 and 155.)
Janka H.-T., 2007, Astronomische Nachrichten, 328, 683 (Cited on page 26.)
Jenet F. A., Cook W. R., Prince T. A., Unwin S. C., 1997, PASP, 109, 707 (Cited on page 143.)
Jenet F. A., Lommen A., Larson S. L., Wen L., 2004, ApJ, 606, 799 (Cited on page 26.)

Jenet F. A., Hobbs G. B., Lee K. J., Manchester R. N., 2005, ApJ, 625, L123 (Cited on page 26.)
Johnson T. J., et al., 2013, ApJ, 778, 106 (Cited on page 116.)
Johnston S., Weisberg J. M., 2006, MNRAS, 368, 1856 (Cited on page 66.)
Johnston S., Karastergiou A., Mitra D., Gupta Y., 2008, MNRAS, 388, 261 (Cited on page 66.)
Joshi K. J., Rasio F. A., 1997, ApJ, 479, 948 (Cited on pages 111 and 114.)
Kaluzny J., Rozyczka M., Pych W., Krzeminski W., Zloczewski K., Narloch W., Thompson I. B., 2013, Acta Astron., 63, 309 (Cited on pages 136 and 137.)
Karuppusamy R., 2009, PhD thesis, University of Amsterdam (Cited on page 39.)
Keith M. J., et al., 2013, MNRAS, 429, 2161 (Cited on page 54.)
Kijak J., Lewandowski W., Maron O., Gupta Y., Jessner A., 2011, A&A, 531, A16 (Cited on page 24.)
King I., 1962, AJ, 67, 471 (Cited on pages 78 and 109.)
King I. R., 1966, AJ, 71, 64 (Cited on page 78.)
Kirsten F., Vlemmings W. H. T., 2012, A&A, 542, A44 (Cited on page 142.)
Kirsten F., Vlemmings W., Freire P., Kramer M., Rottmann H., Campbell R. M., 2014, A&A, 565, A43 (Cited on pages 151 and 153.)
Kızıltan B., Baumgardt H., Loeb A., 2017, Nature, 542, 203 (Cited on page 127.)
Knigge C., Leigh N., Sills A., 2009, Nature, 457, 288 (Cited on page 76.)
Knight H. S., 2007, MNRAS, 378, 723 (Cited on pages 86 and 93.)
Komesaroff M. M., 1970, Nature, 225, 612 (Cited on pages 23, 24 and 66.)
Kopeikin S. M., 1995, ApJ, 439, L5 (Cited on page 60.)
Kopeikin S. M., 1996, ApJ, 467, L93 (Cited on page 60.)
Kramer M., 1994, A&AS, 107 (Cited on page 48.)
Kramer M., 1998, ApJ, 509, 856 (Cited on page 151.)
Kramer M., Champion D. J., 2013, Classical and Quantum Gravity, 30, 224009 (Cited on page 26.)
Kramer M., Wex N., 2009, Classical and Quantum Gravity, 26, 073001 (Cited on pages 153 and 155.)
Kramer M., Wielebinski R., Jessner A., Gil J. A., Seiradakis J. H., 1994, A&AS, 107 (Cited on page 48.)
Kramer M., Xilouris K. M., Jessner A., Lorimer D. R., Wielebinski R., Lyne A. G., 1997, A&A, 322, 846 (Cited on page 25.)
Kramer M., Xilouris K. M., Lorimer D. R., Doroshenko O., Jessner A., Wielebinski R., Wolszczan A., Camilo F., 1998, ApJ, 501, 270 (Cited on page 24.)
Kramer M., et al., 2006, Science, 314, 97 (Cited on page 25.)
Krauss L. M., Chaboyer B., 2003, Science, 299, 65 (Cited on page 77.)
Kuehr H., Witzel A., Pauliny-Toth I. I. K., Nauber U., 1981, A&AS, 45, 367 (Cited on page 144.)
Kuniyoshi M., Verbiest J. P. W., Lee K. J., Adebahr B., Kramer M., Noutsos A., 2015, MNRAS, 453, 828 (Cited on page 24.)
Lam M. T., Cordes J. M., Chatterjee S., Jones M. L., McLaughlin M. A., Armstrong J. W., 2016, ApJ, 821, 66 (Cited on page 54.)
Lange C., Camilo F., Wex N., Kramer M., Backer D. C., Lyne A. G., Doroshenko O., 2001,

MNRAS, 326, 274 (Cited on page 119.)
Large M. I., Vaughan A. E., Mills B. Y., 1968, Nature, 220, 340 (Cited on page 14.)
Larson R. B., 1970a, MNRAS, 147, 323 (Cited on page 79.)
Larson R. B., 1970b, MNRAS, 150, 93 (Cited on page 79.)
Lattimer J. M., Prakash M., 2001, ApJ, 550, 426 (Cited on page 15.)
Lattimer J. M., Prakash M., 2004, Science, 304, 536 (Cited on page 25.)
Lazarus P., et al., 2014, MNRAS, 437, 1485 (Cited on page 61.)
Lazarus P., et al., 2015, ApJ, 812, 81 (Cited on page 41.)
Lee K. J., et al., 2013, MNRAS, 433, 688 (Cited on page 44.)
Lee K. J., et al., 2014, MNRAS, 441, 2831 (Cited on page 54.)
Lentati L., Alexander P., Hobson M. P., Feroz F., van Haasteren R., Lee K. J., Shannon R. M., 2014, MNRAS, 437, 3004 (Cited on page 61.)
Liu K., et al., 2014, MNRAS, 443, 3752 (Cited on page 49.)
Lorimer D. R., 2011, SIGPROC: Pulsar Signal Processing Programs, Astrophysics Source Code Library (ascl:1107.016) (Cited on pages 39 and 87.)
Lorimer D. R., Kramer M., 2004, Handbook of Pulsar Astronomy (Cited on pages 18, 22, 23, 31, 32, 33, 34, 42, 48, 49, 58, 59, 66, 67, 69, 70, 121 and 162.)
Lorimer D. R., Bailes M., McLaughlin M. A., Narkevic D. J., Crawford F., 2007, Science, 318, 777 (Cited on page 25.)
Lynch R. S., Ransom S. M., Freire P. C. C., Stairs I. H., 2011, ArXiv:1101.1467, (Cited on page 127.)
Lynch R. S., Freire P. C. C., Ransom S. M., Jacoby B. A., 2012, ApJ, 745, 109 (Cited on pages 82, 118, 124 and 127.)
Lynden-Bell D., Eggleton P. P., 1980, MNRAS, 191, 483 (Cited on page 79.)
Lyne A. G., Rickett B. J., 1968, Nature, 219, 1339 (Cited on page 34.)
Lyne A. G., Biggs J. D., Harrison P. A., Bailes M., 1993, Nature, 361, 47 (Cited on page 82.)
Lyne A. G., et al., 2004, Science, 303, 1153 (Cited on pages 22 and 25.)
Manchester R. N., 2013, Classical and Quantum Gravity, 30, 224010 (Cited on page 26.)
Manchester R. N., 2015, IAU General Assembly, 22, 2256190 (Cited on page 49.)
Manchester R. N., Taylor J. H., Huguenin G. R., 1975, ApJ, 196, 83 (Cited on page 66.)
Manchester R. N., Lyne A. G., Johnston S., D'Amico N., Lim J., Kniffen D. A., 1990, Nature, 345, 598 (Cited on page 86.)
Manchester R. N., Lyne A. G., Robinson C., Bailes M., D'Amico N., 1991, Nature, 352, 219 (Cited on pages 86 and 131.)
Manchester R. N., Hobbs G. B., Teoh A., Hobbs M., 2005a, AJ, 129, 1993 (Cited on page 18.)
Manchester R. N., et al., 2005b, ApJ, 621, L49 (Cited on page 151.)
Manchester R. N., et al., 2010, ApJ, 710, 1694 (Cited on page 151.)
Maron O., Kijak J., Kramer M., Wielebinski R., 2000, A&AS, 147, 195 (Cited on page 24.)
McLaughlin M. A., 2013, Classical and Quantum Gravity, 30, 224008 (Cited on page 26.)
McLaughlin D. E., Anderson J., Meylan G., Gebhardt K., Pryor C., Minniti D., Phinney S., 2006, ApJS, 166, 249 (Cited on pages 86, 104, 106 and 107.)
McNamara B. J., Harrison T. E., Baumgardt H., 2004, ApJ, 602, 264 (Cited on page 142.)
Michie R. W., 1963, MNRAS, 125, 127 (Cited on page 78.)
Middleditch J., 1992, in American Astronomical Society Meeting Abstracts. p. 1275 (Cited on

page 142.)
Monelli M., et al., 2015, ApJ, 812, 25 (Cited on page 142.)
Morello V., Barr E. D., Bailes M., Flynn C. M., Keane E. F., van Straten W., 2014, MNRAS, 443, 1651 (Cited on page 44.)
Müller H., 1948, J. Opt. Soc. Am., 38, 661 (Cited on page 65.)
Nan R., et al., 2011, International Journal of Modern Physics D, 20, 989 (Cited on page 169.)
Newell B., Da Costa G. S., Norris J., 1976, ApJ, 208, L55 (Cited on page 142.)
Ng C., et al., 2014, MNRAS, 439, 1865 (Cited on page 130.)
Ng C., et al., 2015, MNRAS, 450, 2922 (Cited on page 43.)
Noutsos A., Johnston S., Kramer M., Karastergiou A., 2008, MNRAS, 386, 1881 (Cited on page 25.)
Noutsos A., Kramer M., Carr P., Johnston S., 2012, MNRAS, 423, 2736 (Cited on page 26.)
Nyquist H., 1928, Transactions of the American Institute of Electrical Engineers, Volume 47, Issue 2, pp. 617-624, 47, 617 (Cited on page 36.)
Oppenheimer J. R., Volkoff G. M., 1939, Physical Review, 55, 374 (Cited on pages 13 and 15.)
Ostriker J., 1968, Nature, 217, 1227 (Cited on page 14.)
Özel F., Freire P., 2016, ARA&A, 54, 401 (Cited on page 118.)
Pacini F., 1967, Nature, 216, 567 (Cited on page 14.)
Pan Z., Hobbs G., Li D., Ridolfi A., Wang P., Freire P., 2016, MNRAS, 459, L26 (Cited on pages 86, 89, 93 and 168.)
Papitto A., et al., 2013, Nature, 501, 517 (Cited on pages 22, 26 and 83.)
Pennucci T. T., Demorest P. B., Ransom S. M., 2014, ApJ, 790, 93 (Cited on page 49.)
Perera B. B. P., et al., 2010, ApJ, 721, 1193 (Cited on page 151.)
Perera B. B. P., Kim C., McLaughlin M. A., Ferdman R. D., Kramer M., Stairs I. H., Freire P. C. C., Possenti A., 2014, ApJ, 787, 51 (Cited on page 151.)
Perets H. B., Fabrycky D. C., 2009, ApJ, 697, 1048 (Cited on page 76.)
Phinney E. S., 1992, Philosophical Transactions of the Royal Society of London Series A, 341, 39 (Cited on pages 83, 111, 118 and 126.)
Phinney E. S., 1993, in Djorgovski S. G., Meylan G., eds, Astronomical Society of the Pacific Conference Series Vol. 50, Structure and Dynamics of Globular Clusters. p. 141 (Cited on pages 83, 109, 111, 112 and 118.)
Pilkington J. D. H., Hewish A., Bell S. J., Cole T. W., 1968, Nature, 218, 126 (Cited on page 14.)
Podsiadlowski P., Rappaport S., Pfahl E. D., 2002, ApJ, 565, 1107 (Cited on page 19.)
Portegies Zwart S., van den Heuvel E. P. J., van Leeuwen J., Nelemans G., 2011, ApJ, 734, 55 (Cited on page 26.)
Prager B., Ransom S., Freire P., Hessels J., Stairs I., Arras P., Cadelano M., 2016, preprint, (`arXiv:1612.04395`) (Cited on page 167.)
Predehl P., Schmitt J. H. M. M., 1995, A&A, 293, 889 (Cited on page 120.)
Press W. H., Teukolsky S. A., 1977, ApJ, 213, 183 (Cited on page 81.)
Press W. H., Teukolsky S. A., Vetterling W. T., Flannery B. P., 1992, Numerical recipes in FORTRAN. The art of scientific computing (Cited on page 42.)
Prince T. A., Anderson S. B., Kulkarni S. R., Wolszczan A., 1991, ApJ, 374, L41 (Cited on pages 82, 142, 151 and 160.)

Pryor C., Meylan G., 1993, in Djorgovski S. G., Meylan G., eds, Astronomical Society of the Pacific Conference Series Vol. 50, Structure and Dynamics of Globular Clusters. p. 357 (Cited on page 86.)
Radhakrishnan V., Cooke D. J., 1969, Astrophys. Lett., 3, 225 (Cited on pages 24 and 66.)
Radhakrishnan V., Srinivasan G., 1982, Current Science, 51, 1096 (Cited on page 19.)
Rajwade K., Lorimer D. R., Anderson L. D., 2016, MNRAS, 455, 493 (Cited on page 24.)
Rankin J. M., 1983a, ApJ, 274, 333 (Cited on page 25.)
Rankin J. M., 1983b, ApJ, 274, 359 (Cited on page 25.)
Rankin J. M., 1986, ApJ, 301, 901 (Cited on page 25.)
Rankin J. M., 1990, ApJ, 352, 247 (Cited on page 25.)
Ransom S. M., 2001, PhD thesis, Harvard University (Cited on pages 12 and 39.)
Ransom S. M., Eikenberry S. S., Middleditch J., 2002, AJ, 124, 1788 (Cited on page 43.)
Ransom S. M., Cordes J. M., Eikenberry S. S., 2003, ApJ, 589, 911 (Cited on pages 43 and 90.)
Ransom S. M., et al., 2014, Nature, 505, 520 (Cited on page 22.)
Rasio F. A., Pfahl E. D., Rappaport S., 2000, ApJ, 532, L47 (Cited on page 86.)
Ray P. S., et al., 2012, preprint, (arXiv:1205.3089) (Cited on page 20.)
Reid M. J., et al., 2014, ApJ, 783, 130 (Cited on page 109.)
Rivera-Sandoval L. E., et al., 2015, MNRAS, 453, 2707 (Cited on pages 86, 116, 118, 119, 123 and 124.)
Roberts M. S. E., 2013, in van Leeuwen J., ed., IAU Symposium Vol. 291, Neutron Stars and Pulsars: Challenges and Opportunities after 80 years. pp 127–132 (arXiv:1210.6903), doi:10.1017/S174392131202337X (Cited on page 20.)
Robinson C., Lyne A. G., Manchester R. N., Bailes M., D'Amico N., Johnston S., 1995, MNRAS, 274, 547 (Cited on pages 86, 87 and 131.)
Roy J., Bhattacharyya B., Ray P. S., 2014, The Astronomer's Telegram, 5890 (Cited on page 22.)
Roy J., et al., 2015, ApJ, 800, L12 (Cited on page 22.)
Russell H. N., 1931, MNRAS, 91, 951 (Cited on page 14.)
Rybicki G. B., Lightman A. P., 1979, Radiative processes in astrophysics (Cited on page 61.)
Sanidas S. A., Battye R. A., Stappers B. W., 2012, Phys. Rev. D, 85, 122003 (Cited on page 26.)
Saslaw W. C., Faulkner J., Strittmatter P. A., 1968, Nature, 217, 1222 (Cited on page 14.)
Sazhin M. V., 1978, Soviet Ast., 22, 36 (Cited on page 26.)
Scheuer P. A. G., 1968, Nature, 218, 920 (Cited on page 33.)
Schnitzeler D. H. F. M., 2012, MNRAS, 427, 664 (Cited on page 24.)
Shaifullah G., et al., 2016, MNRAS, 462, 1029 (Cited on pages 115 and 130.)
Shannon C. E., 1949, IEEE Proceedings, 37, 10 (Cited on page 36.)
Shao L., Caballero R. N., Kramer M., Wex N., Champion D. J., Jessner A., 2013, Classical and Quantum Gravity, 30, 165019 (Cited on page 26.)
Shapiro I. I., 1964, Physical Review Letters, 13, 789 (Cited on page 52.)
Shklovskii I. S., 1970, Soviet Ast., 13, 562 (Cited on page 109.)
Sieber W., 1973, A&A, 28, 237 (Cited on page 24.)
Sigurdsson S., Phinney E. S., 1995, ApJS, 99, 609 (Cited on page 80.)
Sigurdsson S., Richer H. B., Hansen B. M., Stairs I. H., Thorsett S. E., 2003, Science, 301, 193 (Cited on pages 22 and 114.)

Spitzer L., 1987, Dynamical evolution of globular clusters (Cited on pages 78 and 104.)
Splaver E. M., Nice D. J., Stairs I. H., Lommen A. N., Backer D. C., 2005, ApJ, 620, 405 (Cited on page 52.)
Spruit H., Phinney E. S., 1998, Nature, 393, 139 (Cited on page 26.)
Staelin D. H., Reifenstein III E. C., 1968, Science, 162, 1481 (Cited on pages 14 and 19.)
Stairs I. H., Thorsett S. E., Arzoumanian Z., 2004, Physical Review Letters, 93, 141101 (Cited on page 151.)
Stappers B. W., et al., 2014, ApJ, 790, 39 (Cited on page 20.)
Staveley-Smith L., et al., 1996, PASA, 13, 243 (Cited on page 87.)
Stokes G. G., 1851, Transactions of the Cambridge Philosophical Society, 9, 399 (Cited on page 62.)
Tamura N., Sharples R. M., Arimoto N., Onodera M., Ohta K., Yamada Y., 2006, MNRAS, 373, 588 (Cited on page 76.)
Tauris T. M., Savonije G. J., 1999, A&A, 350, 928 (Cited on pages 26, 124 and 126.)
Tauris T. M., van den Heuvel E. P. J., 2006, Formation and evolution of compact stellar X-ray sources. pp 623–665 (Cited on pages 19 and 22.)
Tauris T. M., van den Heuvel E. P. J., Savonije G. J., 2000, ApJ, 530, L93 (Cited on pages 22 and 26.)
Tauris T. M., Langer N., Kramer M., 2011, MNRAS, 416, 2130 (Cited on pages 22 and 26.)
Tauris T. M., Langer N., Kramer M., 2012, MNRAS, 425, 1601 (Cited on pages 22 and 26.)
Taylor J. H., 1992, Philosophical Transactions of the Royal Society of London Series A, 341, 117 (Cited on page 48.)
Taylor J. H., Weisberg J. M., 1982, ApJ, 253, 908 (Cited on pages 25 and 26.)
Taylor J. H., Weisberg J. M., 1989, ApJ, 345, 434 (Cited on pages 25, 60 and 155.)
Thornton D., et al., 2013, Science, 341, 53 (Cited on page 25.)
Thorsett S. E., Arzoumanian Z., Camilo F., Lyne A. G., 1999, ApJ, 523, 763 (Cited on page 114.)
Thorstensen J. R., Armstrong E., 2005, AJ, 130, 759 (Cited on pages 20 and 136.)
Tolman R. C., 1939, Physical Review, 55, 364 (Cited on page 15.)
Toscano M., Bailes M., Manchester R. N., Sandhu J. S., 1998, ApJ, 506, 863 (Cited on page 24.)
Turk P. J., Lorimer D. R., 2013, MNRAS, 436, 3720 (Cited on page 81.)
Verbiest J. P. W., et al., 2016, MNRAS, 458, 1267 (Cited on page 49.)
Verbunt F., Freire P. C. C., 2014, A&A, 561, A11 (Cited on pages 82, 83, 86, 116, 125 and 166.)
Verbunt F., Hut P., 1987, in Helfand D. J., Huang J.-H., eds, IAU Symposium Vol. 125, The Origin and Evolution of Neutron Stars. p. 187 (Cited on page 124.)
Verner D. A., Ferland G. J., Korista K. T., Yakovlev D. G., 1996, ApJ, 465, 487 (Cited on page 120.)
Vogt H., 1926, Astronomische Nachrichten, 226, 301 (Cited on page 14.)
Watkins L. L., van der Marel R. P., 2016, preprint, (arXiv:1611.03170) (Cited on page 107.)
Watkins L. L., van der Marel R. P., Bellini A., Anderson J., 2015a, ApJ, 803, 29 (Cited on pages 104 and 107.)
Watkins L. L., van der Marel R. P., Bellini A., Anderson J., 2015b, ApJ, 812, 149 (Cited on pages 104, 105 and 142.)
Weisberg J. M., Taylor J. H., 2002, ApJ, 576, 942 (Cited on page 151.)

Weisberg J. M., Taylor J. H., 2005, in Rasio F. A., Stairs I. H., eds, Astronomical Society of the Pacific Conference Series Vol. 328, Binary Radio Pulsars. p. 25 (arXiv:astro-ph/0407149) (Cited on page 151.)
Weisberg J. M., Romani R. W., Taylor J. H., 1989, ApJ, 347, 1030 (Cited on page 151.)
Weldrake D. T. F., Sackett P. D., Bridges T. J., Freeman K. C., 2004, AJ, 128, 736 (Cited on page 137.)
Will C., 2001, Living Reviews in Relativity, 4 (Cited on page 25.)
Will C. M., Zaglauer H. W., 1989, ApJ, 346, 366 (Cited on page 58.)
Wilms J., Allen A., McCray R., 2000, ApJ, 542, 914 (Cited on page 120.)
Wolszczan A., Kulkarni S. R., Middleditch J., Backer D. C., Fruchter A. S., Dewey R. J., 1989, Nature, 337, 531 (Cited on page 142.)
Woodley K. A., et al., 2012, AJ, 143, 50 (Cited on pages 86, 88, 104, 105, 119, 121, 123 and 124.)
Xilouris K. M., Kramer M., Jessner A., von Hoensbroech A., Lorimer D. R., Wielebinski R., Wolszczan A., Camilo F., 1998, ApJ, 501, 286 (Cited on page 66.)
Yao J. M., Manchester R. N., Wang N., 2016, preprint, (arXiv:1610.09448) (Cited on pages 24 and 32.)
You X. P., et al., 2007, MNRAS, 378, 493 (Cited on page 54.)
Zacharias N., Urban S. E., Zacharias M. I., Wycoff G. L., Hall D. M., Monet D. G., Rafferty T. J., 2004, AJ, 127, 3043 (Cited on pages 122 and 123.)
Zavlin V. E., 2006, ApJ, 638, 951 (Cited on page 120.)
Zavlin V. E., Pavlov G. G., Sanwal D., Manchester R. N., Trümper J., Halpern J. P., Becker W., 2002, ApJ, 569, 894 (Cited on page 120.)
Zhu W. W., et al., 2014, ApJ, 781, 117 (Cited on page 44.)
de Martino D., et al., 2014, MNRAS, 444, 3004 (Cited on page 22.)
de Martino D., et al., 2015, MNRAS, 454, 2190 (Cited on page 136.)
de Sitter W., 1916, MNRAS, 76, 699 (Cited on page 151.)
den Brok M., van de Ven G., van den Bosch R., Watkins L., 2014, MNRAS, 438, 487 (Cited on page 142.)
van Leeuwen J., et al., 2015, ApJ, 798, 118 (Cited on page 151.)
van Straten W., 2004, ApJS, 152, 129 (Cited on pages 70 and 72.)
van Straten W., 2006, ApJ, 642, 1004 (Cited on page 68.)
van Straten W., 2013, ApJS, 204, 13 (Cited on page 72.)
van Straten W., Bailes M., 2011, PASA, 28, 1 (Cited on pages 12, 47 and 87.)
van Straten W., Manchester R. N., Johnston S., Reynolds J. E., 2010, PASA, 27, 104 (Cited on page 61.)
van Straten W., Demorest P., Oslowski S., 2012, Astronomical Research and Technology, 9, 237 (Cited on pages 12, 47 and 87.)

List of Figures

List of Tables

Erklärung

Ich versichere, dass ich die von mir vorgelegte Dissertation selbständig angefertigt, die benutzten Quellen und Hilfsmittel vollständig angegeben und die Stellen der Arbeiteinschlielich Tabellen, Karten und Abbildungen –, die anderen Werken im Wortlaut oder dem Sinn nach entnommen sind, in jedem Einzelfall als Entlehnung kenntlich gemacht habe; dass diese Dissertation noch keiner anderen Fakultät oder Universität zur Prfung vorgelegen hat; dass sie noch nicht verffentlicht worden ist sowie, da ich eine solche Veröffentlichung vor Abschluss des Promotionsverfahrens nicht vornehmen werde. Die Bestimmungen dieser Promotionsordnung sind mir bekannt. Die von mir vorgelegte Dissertation ist von Prof. Dr. Michael Kramer betreut worden.

Unterschift:

_____

Datum:

_____